Large-Scale Dynamic Testing of Rocking Cross Laminated Timber Walls

Sarah Wichman

A thesis
submitted in partial fulfillment of the
requirements for the degree of

Master of Science in Civil Engineering

University of Washington

2018

Committee:
Jeffrey W. Berman
Richard Wiebe
Paolo M. Calvi

Program Authorized to Offer Degree:
Civil and Environmental Engineering

University of Washington

Abstract

Large-Scale Dynamic Testing of Rocking Cross Laminated Timber Walls

Sarah Wichman

Chair of the Supervisory Committee:
Professor Jeffrey W. Berman
Civil and Environmental Engineering

With the recent development of engineered wood products such as cross laminated timber (CLT), tall mass timber buildings are becoming a feasible and attractive alternative to using nonrenewable materials such as concrete and steel. Using CLT panels in a post-tensioned rocking wall system shows great potential for creating reliable, cost-effective, and rapidly constructible ductile seismic load resisting systems. The design of these systems are supplemented with replaceable steel U-shaped flexural plate energy dissipation devices (UFPs). This system has opened the door to creating seismic resilience systems that sustain minor damage during large earthquakes.

With this in mind, the NHERI TallWood Project funded by the National Science Foundation, is developing a rocking cross laminated timber wall seismic force resisting system and design procedure for tall timber buildings that enables seismic resilience by meeting rigorous performance requirements. The system is designed to have no damage during a frequent hazard (such as a 50% probability of exceedance in 50 years), limits damage to the easily replaceable UFP devices in less frequent earthquakes (such as a 10% probability of exceedance in 50 years), and has more considerable damage that may require CLT repair and PT replacement in an even less frequent hazard (such as a 2% probability of exceedance in 50 years). Experiments conducted by the NHERI TallWood group tested a full-scale two-story

mass timer building, with CLT post-tensioned rocking walls as the lateral system, on the world's largest outdoor shake table in San Diego, California at the NHERI@UCSD facility. Fourteen dynamic ground motion tests were conducted on the specimen and experimental results showed a ductile response with low levels of damage. In addition, the performance-based design procedure and performance objectives for the specimen matched well with the observed and instrumented response.

TABLE OF CONTENTS

Page

LIST OF FIGURES

LIST OF TABLES

ACKNOWLEDGMENTS

I would like to fist acknowledge and thank my advisor, Professor Jeffrey Berman. He has truly been a supportive advisor and has always expressed great confidence in my abilities. His guidance and support over the past two years has been critical to the completion of this work and has helped me develop many skills necessary to becoming a better researcher. I would also like to thank Professor Richard Wiebe and Professor Paolo Calvi for serving on my committee.

I would also like to extend my gratitude to my entire research team including, but not limited to: Professor Shiling Pei of Colorado School of Mines; Professor John van de Lindt of Colorado State University; Professor Dan Dolan of Washington State University; Professor Keri Ryan of University of Nevada, Reno; Professor Richard Sause of Lehigh University; Professor Andre Barbosa of Oregon State University; Eric McDonnell and Reid Zimmerman of KPFF; and Hans-Erik Blomgren of Katerra. I would also like to thank the staff at the NHERI@UCSD lab, including Darren McKay, Alex Sherman, and Jeremy Fitcher for all their help and patience during the crazy construction process and experimental tests. A thank you to my fellow research students on this project for working hard during construction and data processing. Special thanks to Brian DeMeza and Aleesha Busch for their company during our many outings to The Taco Stand in San Diego.

Monetary support from the National Science Foundation (Awards CMMI: 1636164, 1634204, 1635363, 1635227, 1635156, and 1634628) is much appreciated. Additional thanks to our other sponsors including: Simpson Strong-Tie, the Tall Wood Design Institute, SmartLam, DR Johnson Lumber Co., Softwood Lumber Board, Forest Products Lab, and City of Springfield, OR.

I would not have been able to complete my Master's degree without the help and support from many students at the University of Washington. Thank you to Andy Sen, Nasser Marafi, and my fellow office mates in More 236 for their willingness to help and answer my questions. Their assistance has been an invaluable resource. A special thank you to my classmates to whom I have gained wonderful friendships from. In particular, thank you to Tasha Tardieu, Jakob Sumearll, Samar Kenkre, Cassie Gills, and Sarah Ibarra.

Most importantly, I would like to thank all my family and friends. Specifically, my parents for their unconditional love and support and my sisters, Katie and Laura, for being amazing role models and for providing compassion and love from so far away. Finally, I would like to thank my boyfriend, Chris for believing in me, showing unbelievable patience, and for providing a constant supply of gummy bears during stressful times. I wouldn't have been able to do it without him or the bears.

Chapter 1

INTRODUCTION

1.1 Overview

Urban areas face many competing challenges such as accommodating increasing urban populations, minimizing urban sprawl, and supporting global sustainability to fight climate change. To address these concerns, there is a growing need for 8 to 14 story buildings for residential and commercial use. Steel and concrete are most often the answer for buildings in this height range, however tall timber building construction is a green building solution because material for timber structural elements can be produced from well-managed sustainable forests, and the CO_2 emissions and embodied energy is far superior to steel and concrete construction as found in several studies. For example, a Skidmore, Owings, and Merrill team compared a 40-story reinforced concrete building in Chicago to a 40-story timber redesign and found the overall carbon footprint of the timber design was 60% to 70% lower than the reinforced concrete building [SOM, 2013].

In the past, timber has not been a viable option for buildings in this height range because of it's lack in strength and stiffness. In addition, current light-frame design and construction methods are not adequate for heights taller than 6 stories in areas of high seismicity. However, with recent developments of engineered wood products such as cross-laminated timber (CLT), tall timber construction is becoming a feasible option for high seismic regions and offers benefits such as faster construction and the use of sustainable building materials.

CLT is an engineered wood product created by glue laminating timber boards in orthogonal directions to create the panalized product shown in Figure 1.1. Timber alone only has high strength in the parallel to grain direction, however the orthogonal pattern allows for CLT to have relatively high strength and stiffness in both the in-plane directions. The

result is a product ideal for walls and slabs. Coupling the use of CLT with a glulam gravity frame to create tall timber buildings can provide solutions to accommodate increasing urban density while enabling the use of rapid prefabricated construction techniques. Other potential broader impacts for tall timber building construction include helping struggling rural economies by reinvigorating the timber industry and providing jobs in CLT and other timber product manufacturing.

(a) CLT concept (b) CLT panel

Figure 1.1: Panelized CLT product

Today, the tallest CLT mass-timber building in the world, Brock Commons Tallwood House (shown in Figure 1.2), is a student resident space at the University of British Columbia in Vancouver, BC. The structure has a concrete core with 17-stories of CLT floors and glulam columns. With a crew of only nine, the mass timber construction was completed in less than 70 days using the prefabricated material [Naturally:wood, 2018]. The Framework building, a mixed-use structure which has be approved for construction in Portland, OR will be the United State's tallest CLT building. The 12-story building is designed with a glulam gravity frame and a rocking post-tensioned CLT planer shear wall lateral system and CLT floor panels [Zimmerman and McDonnell, 2018]. The building was permitted through the alternative means and methods provision of the International Building Code. However, a

codified design procedure for tall timber is necessary to fully utilize the potential of CLT construction.

(a) Brock Commons in Vancouver, BC [Naturally:wood, 2018]

(b) Framework building in Portland, OR [Zimmerman and McDonnell, 2018]

Figure 1.2: CLT mass timber buildings today

The limiting factor with CLT design is the low deformation capacity and low energy dissipation capabilities of the CLT panels when used as the main lateral force resisting system. To combat this issue, unbonded post-tension (PT) connections can be used to achieve a more ductile response and U-shaped flexural plate energy dissipation devices (UFPs) can be used in the system to dissipate energy and reduce accelerations. This results in an efficient structural system that can undergo large inelastic displacements while assuring recentering capabilities because of the PT bars. The UFPs allow for limited, localized damage to specific components that can be replaced after a large seismic events. The concept for this system, typically referred to as the hybrid system, was originally developed for precast concrete

structures [Stanton et al., 1997].

In this thesis, the use of post-tensioned rocking CLT wall panels coupled together with UFP energy dissipation devices, as shown in Figure 1.3, is investigated for the lateral force resisting system in tall timber buildings using large-scale dynamic testing. The concept is to have the system recenter after seismic events and to only have minimal, but repairable damage during high level seismic events.

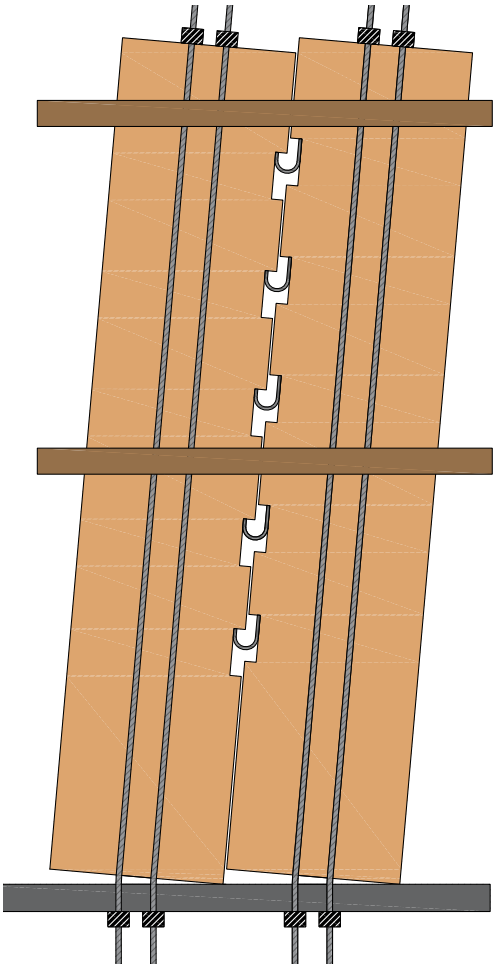

Figure 1.3: Schematic of post-tensioned rocking wall system being investigated

1.2 NHERI Tall Wood Project

The research presented in this thesis is part of the NHERI TallWood Project supported by the National Science Foundation through a number of collaborative awards including: CMMI: 1636164, 1634204, 1635363, 1635227, 1635156, and 1634628. The use of the NHERI facility is supported by the Nation Science Foundation's Natural Hazard Research Institute Program.

The rocking CLT wall research presented here builds on previous and ongoing research with the the NHERI TallWood Project on mass-timber construction and performance based design. An overview of the whole project is shown in Figure 1.4. The research presented here is part of Task 4: Sub-Assembly Testing, in which a full-scale two story test specimen was design, tested, and analyzed to work towards an ultimate goal of developing a design methodology for resilient tall wood buildings in high seismic regions. The NHERI TallWood Project is a collaboration with multiple universities and firms from industry. The main collaborators included: University of Washington, Colorado School of Mines, Colorado State University, Washington State University, Lehigh University, Oregon State University, and KPFF Consulting Engineers from Portland, Oregon.

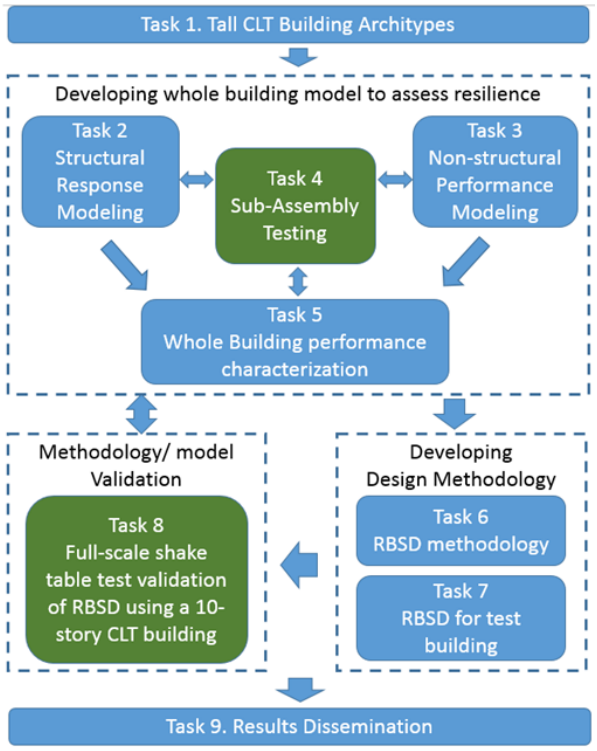

Figure 1.4: NHERI TallWood Project Overview

1.3 Research Objectives

The Objectives of this research are outlined here:

- Develop an understanding of the performance and behavior of the rocking CLT wall system and the proposed performance based design procedure used to design the system
- Adapt the design procedure to design the CLT rocking wall lateral system for experimental tests
- Perform an experimental investigation of the designed CLT rocking wall lateral system
- Analyze data from the experimental investigation to evaluate the performance

- Compare the experimental performance to the proposed design procedure and assess the performance objectives

- Consider the future research necessary to develop design code provisions

1.4 Organization of Thesis

To address the stated research objectives, this thesis is separated into six remaining chapters. The remaining chapters are organized as follows:

- *Chapter 2: Literature Review*, provides an overview of existing research on CLT and rocking wall systems in CLT and other materials.

- *Chapter 3: Behavior and Design of Rocking CLT Walls*, provides a detailed explanation of the CLT rocking wall systems and a set of proposed performance objectives for the system. This chapter also explains the performance base design procedure used to design the test specimen in Chapter 4.

- *Chapter 4: Experimental Specimen Design and Test Setup*, explains the design of the full-scale two-story test specimen with emphasis on the design of the CLT rocking wall lateral system. This chapter also includes an explanation of the test setup including the instrumentation plan, testing plan, and ground motion records used for the dynamic testing sequence.

- *Chapter 5: Experimental Observations*, contains observations made during the dynamic testing of the specimen, with emphasis on modifications made during testing and observed damage.

- *Chapter 6: Experimental Data Analysis*, documents the data analysis performed for the dynamic tests. The data analysis includes: evaluation of the buildings fundamental period, estimation of the damping coefficient, analysis of the global response (including

drifts, base shear, and torsional response), and evaluation of the the PT bar response, deformation at the base of the wall panels, and UFP response.

- *Chapter 7: Conclusion*, contains a summary of the research completed and key results and findings from the tests. Recommendations for future work are also included.

In addition to the chapters outlined above, Appendix A includes sample design calculations used for designing the test specimen described in Chapter 4. Appendix B includes additional figures from the data analysis performed in Chapter 6.

Chapter 2

LITERATURE REVIEW

2.1 Overview

Using CLT rocking walls as the main lateral force resisting system in buildings located in areas with high seismicity is a relatively new idea in structural engineering, but it builds upon previous research in timber and base rocking systems. This chapter will review previous studies which the research presented in this thesis builds upon. The use of CLT as a building material will first be reviewed followed by relevant research projects that tested the use of CLT for buildings in seismic regions. Finally, the development of base rocking systems in precast concrete and mass timber base rocking systems will be summarized.

2.2 CLT as a Building Material

Originally developed in Austria in the mid-1990's, CLT is a relatively new building material that falls into the class of timber products called "mass" timber. CLT has been gaining popularity across Europe for mid-rise residential and commercial applications. The European market has shown that CLT construction can be competitive, can offer shorter construction times, and is helping drive the green building movement [Karacabeyli and Douglas, 2013]. CLT is created by gluing layers of laminated boards into a panel where each layer is orientated orthogonal to the adjacent layers as seen in Figure 2.1. The panels are typically fabricated with an odd number of layers, typically three, five, or seven layers (called plys), with a total thickness limit of up to 20 inches. The typical panel sizes vary by manufacturer and transportation regulations can also dictate the sizes of panels [Karacabeyli and Douglas, 2013]. Because the CLT layers are orientated perpendicular to each other, CLT panels exhibit high strength and stiffness in both in-plane directions, resulting in two-way action

capabilities, similar to a concrete slab. This differs from laminated veneer lumber (LVL) and glue laminated timber (glulam), which only show high strength in one direction.

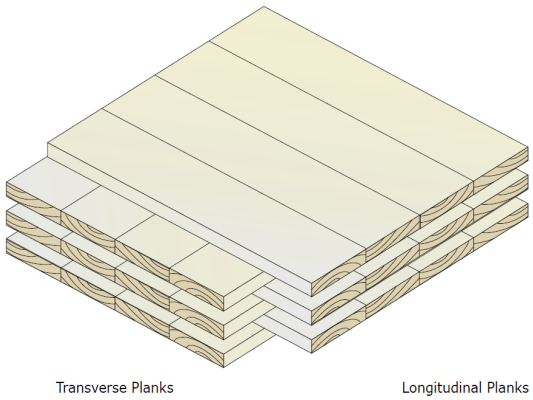

Figure 2.1: CLT panel configuration [Karacabeyli and Douglas, 2013]

CLT can be made from any Softwood lumber species that has a specific gravity greater than 0.35 and is recognized by either the United States National Design Specification for Wood Construction (NDS) or the Canadian CSA O86. All lumber pieces in a single layer of CLT must be made of the same species, but adjacent layers are permitted to be made of different species [APA, 2017]. Layers orientated in the parallel to grain direction of the panel must have a minimum grade of 1200f-1.2E MSR or visual grade No. 2. Layers in the perpendicular direction must have a minimum visual grade of No. 3 [APA, 2017]. The lumber is kiln dried prior to assembly to prevent dimensional variations and surface cracking. The adhesives used to laminate the timber have the same qualifications as adhesives used for glulam. Adhesives must be qualified polyurethane, melamine, and phenolic-based adhesives. The total assembly process can take 15 to 60 minutes and starts by selecting lumber and grouping them in to layers for planing. The layers are then set up and pressed with a hydraulic press. After pressing, the panel product is cut and the surface is machined and marked for packaging [Karacabeyli and Douglas, 2013].

In 2012 a CLT product standard was developed and published by the American National

Standards Institute and the Engineered Wood Association, ANSI/APA CLT standard Committee [APA, 2017]. In 2013, FPInnovations, a non-profit Canadian organization that carries out scientific research for the forest industry, released a CLT handbook that summarizes the design and construction procedure for CLT markets in the U.S. and Canada [Karacabeyli and Douglas, 2013]. In 2015, CLT was incorporated into the NDS, allowing CLT to be recognized as a code complaint construction material [AWC, 2015].

2.3 CLT Used for Buildings in Seismic Regions

Using mass timber as a building material for structures in seismic regions is a relatively new idea and the research is limited when compared to that of other materials. This section will summarize major research completed on using mass timber materials to create the main lateral system for buildings in areas of high seismicity.

2.3.1 Green and Karsh [2012]

Green and Karsh [2012] created a technical report highlighting the potential for mass timber buildings. Their study showed that with growing populations there is an increasing demand for taller buildings. In the past steel and concrete have been used and there has been no reason to challenge the use of those materials. However, with climate change a switch needs to be made to make buildings more environmentally sustainable. It was stated that concrete production represents roughly 5% of the worlds carbon dioxide emissions, more than five times the carbon footprint of the airline industry as a whole. The report argues that when harvested responsibly, wood is one of the best tools for engineers and architects to reduce greenhouse gas emissions in the construction of buildings. In this study, Green and Karsh [2012] show that 10 to 30 story buildings can be achieved using the new mass timber techniques. This was shown through presenting conceptual design solutions that with time and additional design and engineering can become a reality. The study shows how mass timber structures can meet relevant structural design criteria and fire and life safety needs and it can do so in a cost competitive marketplace.

In addition, Green and Karsh [2012] introduces a new design concept called Finding the Forest Through the Trees (FFTT) to assist in shifting the way we approach building construction. The system has been engineered to address the seismic codes for markets in Vancouver, BC. The system consists predominately of wood with a solid wood central elevator core and wood floor slabs. Steel beams provide the ductility and concrete is used for the below grade areas.

Green and Karsh [2012] also conducted a cost analysis comparison on a 12-story and 20-story mass timber building. For this study concrete construction was used as the benchmark building and fire protection techniques were taken into account in the analysis. The costs were estimated based on the presented preliminary design drawings and the results concluded that with development and evolution of the FFTT buildings, there could be a significant reduction in the costs of construction for this type of system. Finally, Green and Karsh [2012] found that it is possible to design tall timber buildings with the FFTT system that are equivalent to concrete structures and this can be achieved through facilitating additional research with structural analysis studies, structural testing, fire assessment, etc.

2.3.2 Djuic et al. [2004 and 2006]

One of the first experimental tests studying the lateral resistance of CLT panels was conducted at the University of Ljubljana in Ljubljana, Slovenia by Dujic et al. [2004]. At the time, earthquakes and strong winds were too demanding on the conventional timber lateral systems in use for support applications in taller buildings, so the potential of using CLT instead of basic lumber was investigated. Fifteen CLT panels with different anchoring systems were tested under monotonous and cyclic horizontal load in combination with constant vertical load to study the influence of the anchoring systems on the shear stiffness and strength of the CLT wall panels. The results of the tests showed that the load bearing capacity of the wall was governed by the anchors connecting the panels to the building foundation.

The importance of studying boundary conditions and the influence of vertical loading on the behavior of CLT panels was tested in Dujic and Zarnic [2006]. This test was completed

to show the importance of simulating realistic boundary conditions that may occur during earthquakes as well as the changes in boundary conditions that may occur during an earthquake due to damage. Panels were tested using a custom machine that mimicked the three different sets of boundary conditions shown in Figure 2.2: Case A) a shear cantilever mechanism where the base is fully connected and the other end is free to rotate and translate; Case B) a condition where the base is also fully connected and the other end is free to translate without rotation; and Case C) a condition where the base is fully connected and the other end is restrained only against rotation. Case A and Case B were exposed to constant vertical load while Case C experienced increased vertical load where the panel wanted to uplift due to displacements. Results showed that boundary conditions had a significant impact on the lateral resistance of the panels. A shear mechanism was only reached when boundary conditions were set to Case C. Varying boundary conditions between Case A and Case B did not develop the shear mechanism, but the load bearing capacity more than doubled when moving from Case A to Case C.

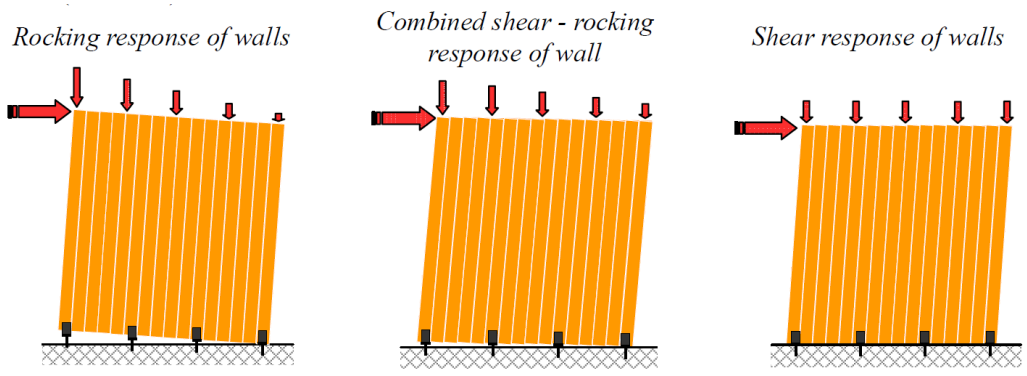

Figure 2.2: Boundary condition configurations tested in Dujic and Zarnic [2006]

Dujic and Zarnic [2006] also constructed two full-scale models and tested them on the shake table at the IZIIS Laboratory in Skopje, Macedonia to validate the cyclic tests results discussed above and to make a correlation between the results. During this test two single-story box CLT wall assemblies were tested. Specimen 1 consisted of two one-unit wall

elements and specimen 2 consisted of two wall elements of half width screwed together. Each panel was 2.44 m x 2.72 m x 9.4 cm and each specimen had a roof element that was 2.44 m x 2.10 m x 16.2 cm. The panels were anchored to the RC foundation through a series of ribbed angle irons. A series of dynamic tests were performed on both the specimens to investigate the behavior under dynamic conditions. Maximum accelerations reached 0.6g for specimen 1 and 0.5g for specimen 2. Results showed that the anchorage connections were the main source of non-linearity in the system and were also the main source of energy dissipation. In addition, both systems behaved as expected and saw no visible damage. In the end, the test results showed that the system exhibited very ductile behavior and there was good correlation to the cyclic testing presented above.

2.3.3 SOFIE Project

The SOFIE project is one of the largest research projects studying CLT buildings and was carried out by the IVALSA Institute of the Italian National Research Council with the support of Trento Province of Italy. The overall project consisted of connection tests [Gavric et al., 2012], CLT panel shear wall tests [Lauriola and Sandhaas, 2006], and several full-scale shake table building tests [Ceccotti et al., 2013].

Gavric et al. [2012] performed many tests on different connections used with CLT panels with the overall goal of providing a better understanding of the performance of these connections during seismic events. In-plane monotonic and cyclic shear tests were performed on different configurations of screwed connections between CLT panels. Configurations included, parallel wall to wall, perpendicular wall to wall, floor to floor, and wall to floor details. Properties such as strength, stiffness, energy dissipation, and ductility were all evaluated. In addition, overstrength factors were also determined as they had not been studied for CLT walls before. Defined as the ratio between the 95^{th} percentile of the connection strength distribution and the analytical prediction of the design connection strength, overstrength values ranging from 1.2 to 1.9 with an average value of 1.74 were determined. Results of these tests also provided insight on spacing, edge distances, and panel thickness that are

required to prevent brittle failure. It was also determined that the screw head penetration was more critical than the withdrawal of the screw from the panel.

Within the SOFIE project, Lauriola and Sandhaas [2006] performed quasi-static in-plane cyclic tests on CLT walls and pseudo-dynamic tests on a full-scale building. The quasi-static tests looked at the influence of the uplift and shear anchoring systems, the opening layout within a panel, the magnitude of vertical loads, and the inter-story connection. Fourteen tests were conducted with varying conditions and expected results were observed. Stiffer hold-down connections lead to higher lateral load carrying capacity but lower ultimate displacement and a less ductile behavior. Overall, it was determined that the connection joints strongly influenced the behavior of the system and forces were concentrated at small regions in the timber, leading to the failure shown in Figure 2.3. Lauriola and Sandhaas [2006] also conducted pseudo-dynamic tests carried out on a 7 m x 7 m single story specimen. Three different opening layout configurations were tested and two earthquake motions were applied at two different peak ground accelerations. The results of these tests showed that the walls were stiff while the connections provided the ductility. Figure 2.4 shows the resulting pinched hysteric behavior from the three opening configurations under the same earthquake motion.

Also within the SOFIE project, Ceccotti et al. [2013] conducted both 3-story and 7-story shake table tests. Both buildings were designed according to the European seismic standard, Eurocode 8. The full-scale 1D tests on the 3-story test specimen made of CLT was performed at the NIED shake table in Tsukuba, Japan. The CLT building was 3-stories with a total height of 10 meters and had a 7 m x 7 m floor plan. The specimen was designed according to the simplified lateral force procedure in Eurocode 8 with a peak ground acceleration of 0.35g which is representative of the most hazardous seismic region in Italy. Eurocode 8 uses a behavior factor, q, in the design procedure which is equivalent to the response modification factor, R, used the U.S. code, ASCE 7-10. Ceccotti et al. [2013] defied q as $PGA_{near-collapse}$ / PGA_{design}, where $PGA_{near-collapse}$ is the peak ground acceleration recorded at the defined near-collapse state, and PGA_{design} is the design peak ground acceleration which was equal to 0.35g in this test. For the design of the 3-story test specimen, a q factor of 1.0 was

(a) (b)

Figure 2.3: Localized failure observed in quasi-static cyclic tests [Lauriola and Sandhaas, 2006]

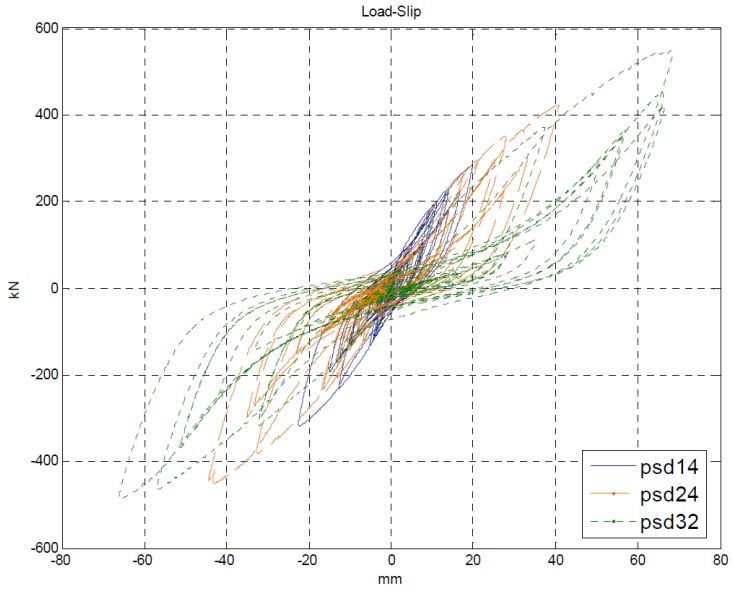

Figure 2.4: Response of the three configurations from the Kobe earthquake with a 0.5g PGA [Lauriola and Sandhaas, 2006]

used meaning it was designed to be purely elastic and ignored overstrength and any energy dissipation. Three different floor plan configuration were tested in which the last was not symmetric. The specimen was then exposed to 3 different ground motion events with varying peak ground accelerations. For the third floor plan configuration, a near-collapse peak ground acceleration, $PGA_{near-collapse}$, of 1.20g was observed. This resulted in a q factor of 3.4 which was rounded to 3, showing relatively good energy dissipation and ductility. In the end the building did not collapse and did not sustain significant residual drifts.

Ceccotti et al. [2013] then used the q factor of 3 to design the 7-story test specimen which was also performed under the SOFIE project. The 23.5 meter tall, 7-story test specimen shown in Figure 2.5 had a 7.5 m x 13.5 m floor plan and was made of spruce wood CLT. The wall to floor joint connections were designed based on the design shear forces per story and consisted of hold-downs, angle brackets, and self-drilling screws. During this test, only one configuration was tested and fewer earthquakes were applied. For each ground motion, the larger earthquake component was applied along the longer, Y direction and the smaller component was applied along the shorter, X length of the building. The specimen in the 7-story tests in Ceccotti et al. [2013] remained upright and only easy to repair damages, such as tightening loose hold-downs and replacing bent and sheared screws, were necessary. Figure 2.6 shows the maximum story shears measured with the design values from Eurocode 8, which resulted in errors between 20% and 25%. These are considered acceptable levels which validate the force-based approach from Eurocode 8 for the design of these CLT specimens. Outcomes from both tests by Ceccotti et al. [2013] showed that the buildings demonstrated recentering capabilities with high stiffness and sufficient ductility to prevent brittle failure.

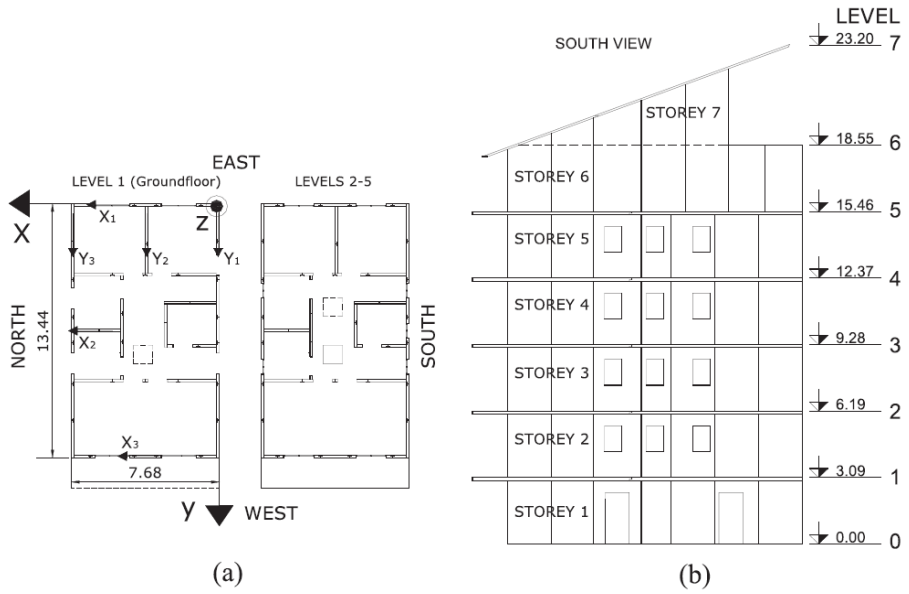

Figure 2.5: (a) Plan and (b) Elevation view of the 7-story test specimen tested in Ceccotti et al. [2013]

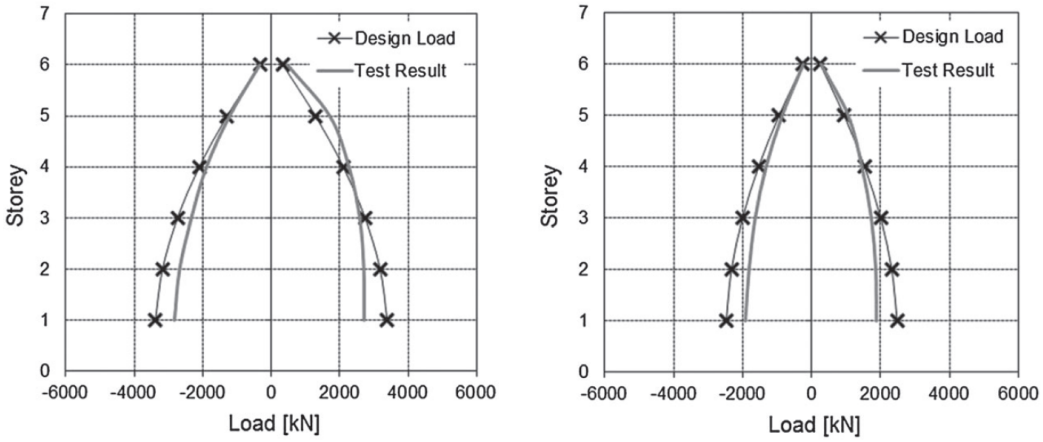

Figure 2.6: Story shear forces per sotyr verses the design load for (a) the long direction, Y, and (b) the short direction, X Ceccotti et al. [2013]

2.3.4 Popovski et al. [2010]

Research on the seismic behavior or CLT systems in North American was initiated by FPInnovations to address the moderate seismicity in British Colombia, Canada. Popovski et al. [2010] conducted one of the first tests on CLT shear walls. Popovski et al. [2010] tested a total of 32 shear walls under monotonic and cyclic loading. All panels were 3-ply European spruce CLT panels with a total thickness of 94 mm. A total of 12 different configurations, both one and two stories, were tested. One story specimens were all 2.3 meters tall with an aspect ratio of either 1:1 or 1:1.5. Two story specimens had a total height of 4.9 meters with an aspect ratio of 2.1:1 and were made of either a single panel or two 1:1 single story panels. Four different types of brackets, as shown in Figure 2.7, were used for connecting the CLT walls to the foundation. Two of the brackets (Brackets A and B) were commercial Simpson Strong Tie brackets that are commonly used in Europe and the other two brackets (Brackets C and D) were custom brackets that accommodated timber rivets. Some panel configurations also included the use of hold-downs with nails at the ends of the wall. In addition, two different types of foundations, steel or a CLT panel, were used to investigate the effect of the foundation stiffness on the response of the specimen.

Walls were loaded vertically with either a 10 $\frac{kN}{m}$ load to represent the wall being at the bottom of a two story structure, or a 20 $\frac{kN}{m}$ load to represent the wall being at the bottom of a four story structure, and were loaded horizontally using a 110 kN hydrolic actuator. Results from the tests showed that the panels behaved almost rigidly with very small shear deformations measured, while majority of the deformations occurred at the joints connecting the wall to the foundation. As seen in Figure 2.8, connections with spiral nails exhibited bearing failures combined with withdrawal, while ring nails mainly saw withdrawal failures with small chucks of wood breaking away. Connections with timber rivets experienced fastener pull-out combined with with wood shear plug failure as seen in Figure 2.9 (a), however once spacing of the timber rivets was increased, the desired failure mode of rivet yielding was observed, as seen in Figure 2.9 (b).

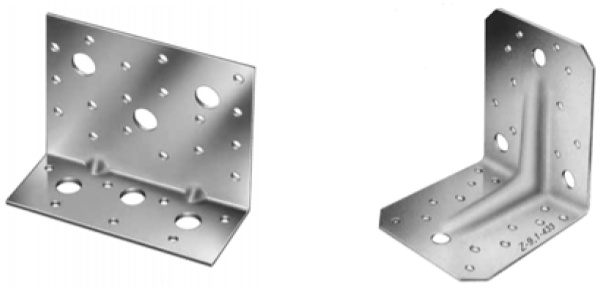

a) Bracket A

b) Bracket B

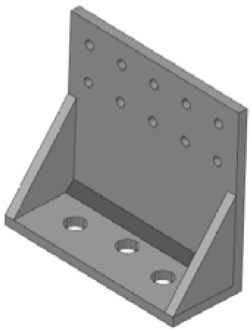

c) Bracket C

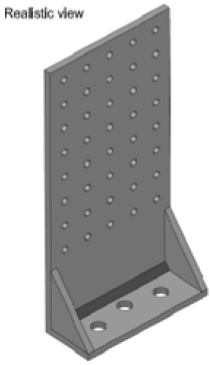

d) Bracket D

Figure 2.7: Four different brackets tested for the CLT walls Popovski et al. [2010]

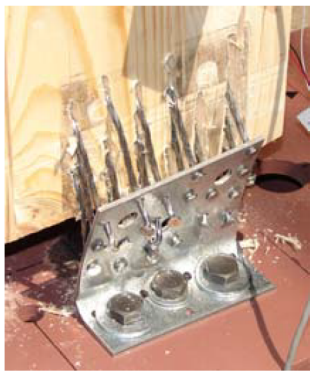

a)

b)

Figure 2.8: Failure modes of the bracket connection for a) spiral nails and b) ring nails Popovski et al. [2010]

Figure 2.9: Timber rivit failure in brackets a) showing undesired failure, and b) showing the desired rivit yielding Popovski et al. [2010]

The results of the tests from Popovski et al. [2010] showed that CLT wall panels have adequate seismic performance for low ductility demand applications in regions of moderate seismicity and that the bracket connections are the main source of ductility in the system. The wall panels that used either screws or nails had similar strength capacity, but the screw connections lost strength faster. However, the walls with timber rivets showed a higher capacity than both the nails and the screws and these specimens also saw higher stiffness. Finally, the specimens with hold-downs on the ends showed the highest stiffness and ductility capacity.

2.3.5 Pei et al. [2013]

Pei et al. [2013] conducted a performance-based seismic design (PBSD) for a 6-story apartment building utilizing data from the tests discussed form Popovski et al. [2010]. The performance was verified through a nonlinear time history simulation and an approximated CLT response modification factor (R-factor) for use in force-based design procedures was estimated.

A performance-based seismic design (PBSD) procedure originally developed by Pang et al. [2010] for midrise, wood-frame buildings was used to for a 6-story building located

near Los Angeles, California. For this design procedure, three performance levels (PL) were used: PL 1) 50% nonexceedance probability for 1% drift during a 50% in 50 year hazard level event; PL 2) 50% nonexceedance probability for 2% drift during a 10% in 50 year hazard level event; and PL 3) 80% nonexceedance probability for 4% drift during a 2% in 50 year hazard level event. The procedure was conducted using direct displacement design (DDD) where given a performance target and story weight and height, the target lateral resistance at specific inter-story drift levels were calculated based on DDD.

For the tests presented in Pei et al. [2013], three wall designs were used with three different types of connections. The model used for this study was the simplified model shown in Figure 2.10 from van de Lindt et al. [2010] where all lateral wall deformation results from CLT panel rotation. The lateral resistance of the panel can be calculated as the summation of the load-slip resistance for all the connections. The load-slip resistance model for the connections was a hysteric model from Filiatrault and Folz [2002] as shown in Figure 2.11 where the 10 parameters were obtained through calibration of test results from van de Lindt et al. [2010].

Connection force resistances were calculated base on this procedure and the results were validated through nonlinear, time history analysis of the models. 22 bi-axial far-field ground motions scaled to the three hazard levels were used on the models. Peak inter-story drifts from any story level and in any direction were recorded for each analysis. The recorded values were ranked and plotted as an empirical cumulative distribution function (CDF) as shown in Figure 2.12. As seen in this figure, performance requirements were met for performance levels 2 and 3. Level 1 only approximately satisfied the objective, but the overall performance of the building should not be affected because the damage to the building was minimal.

The final part of the study by Pei et al. [2013] consisted of calculating an appropriate R-factor for used in ASCE 7-10 using the equivalent lateral force procedure design method. Using the simplified ASCE 7-10 approximate period calculation, the building period was 0.4 seconds for the building located near Los Angeles, California. Short and long period spectral acceleration values for the design response spectra equaled 1.62g and 0.57g respectively from the USGS design maps. The value of R was calculated by trying different values until the

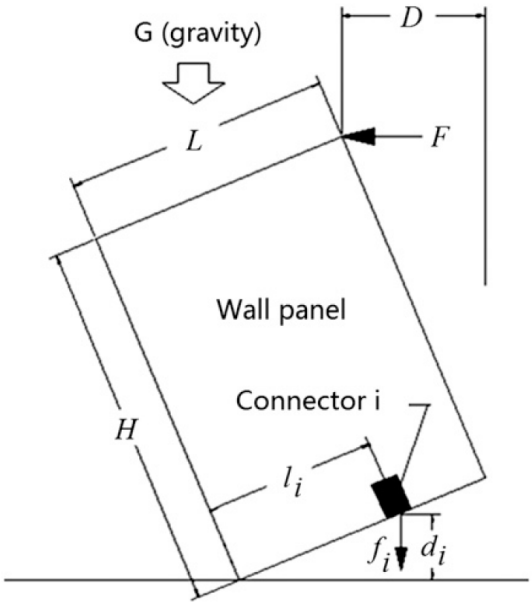

Figure 2.10: Simplifed kimematics model for CLT wall lateral resistance from van de Lindt et al. [2010]

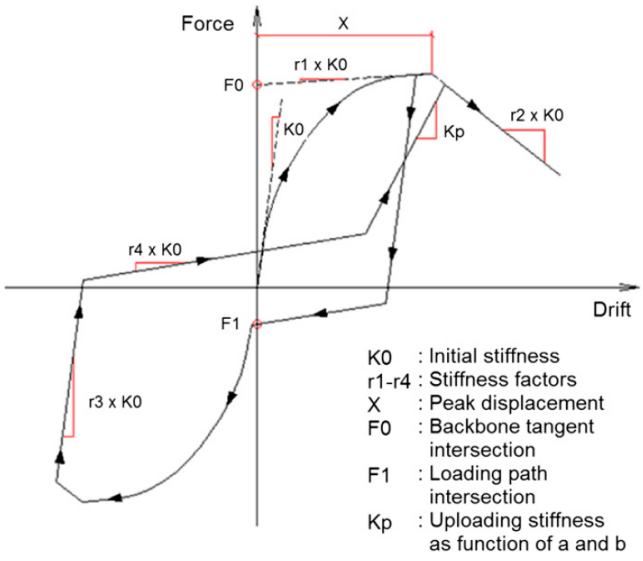

Figure 2.11: Ten-parameter hysteretic model for connections from Filiatrault and Folz [2002]

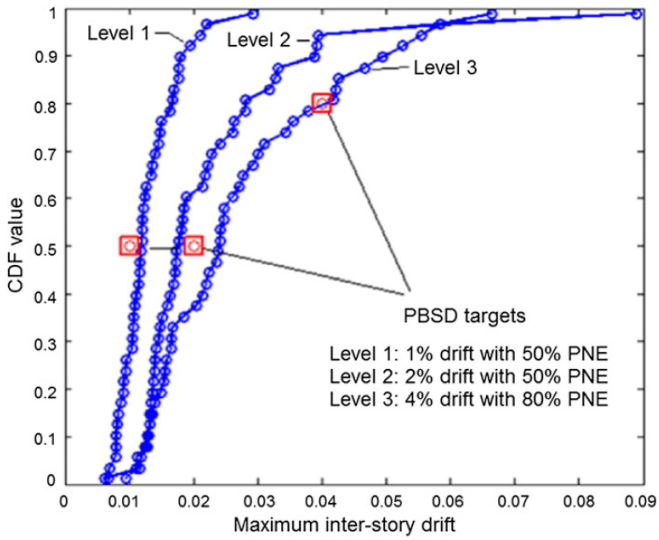

Figure 2.12: CDF of the maximum inter-story drift from the design CLT building simulation [Pei et al., 2013]

final lateral resistance demand distribution along the height of the structure matched the design target. The results of the investigation showed that the R factor for CLT walls is likely between 3.4 and 5.5. It concluded with a suggestion of using 4.5 for the value of R, but it was noted that this was just approximate and should be verified with more research.

2.4 Previous Base Rocking Systems

Controlled rocking timber walls are based on hybrid concrete Precast Seismic Structural Systems (PRESSS). This system has been used in concrete and rocking braced frames before being adapted for timber and CLT.

2.4.1 PRESSS

The PRESSS Program, coordinated by Priestley [1991] was a combined research program between the United States and Japan on the seismic design and performance of precast concrete structural systems. The goal of the project was to develop an effective seismic structural

system for precast buildings, called the hybrid system, and to make design recommendations for incorporation into building codes. This program was the first proposed rocking hybrid system and introduced the concept and design procedure for the used in other materials such as steel and timber. The hybrid system combines unbonded post-tensioned connections with mild steel energy dissipating devices as shown in Figure 2.13a. The unbonded tendons provide recentering capabilities for the system as seen in the nonlinear elastic hysteresis in Figure 2.13b, however a system with unbonded tendons alone dissipates little to no energy. The mild steel energy dissipating devices are added to provide the energy dissipation needs as shown by the damping hysteresis in Figure 2.13b. The resulting hysteretic behavior for the hybrid system with recentering capabilities as well as energy dissipation abilities can be seen in the third hysteresis in Figure 2.13b.

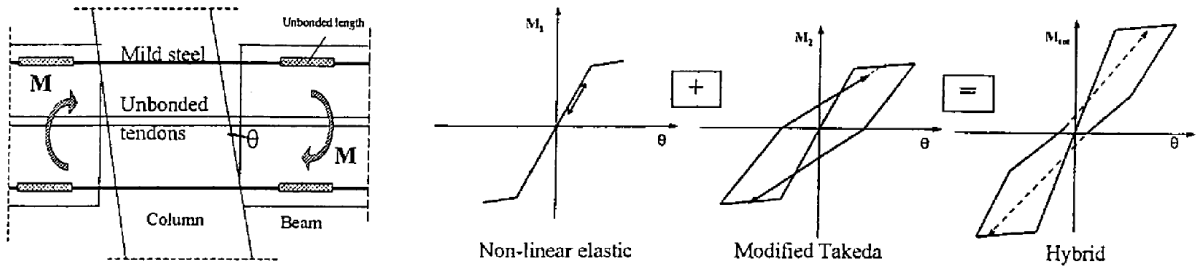

(a) Rocking motion of connection

(b) Hysteretic behavior

Figure 2.13: Beam-column hybrid joint from the PRESSS program [Pampanin et al., 2001]

Kurama et al. [1999] characterized the behavior the the hybrid system and developed a performance-based seismic design approach in which the walls are required to resist design level ground motions with little damage and resist larger earthquakes with more damage but without failure. The behavior of the system was characterized into four states shown in Figure 2.14: 1) decompression state, defined by the initiation of a gap opening along the horizontal joint between the wall and the foundation; 2) softening state, defined by the beginning of significant reduction in lateral stiffness due to the gap opening; 3) yielding state, defined by the point at which the post-tensioning steel reaches it's yield limit; and

4) failure state, identified by axial-flexural failure of the wall which occurs as a result of concrete crushing.

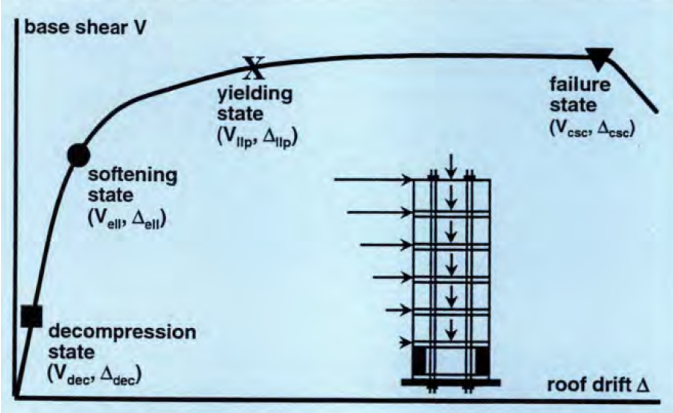

Figure 2.14: Base shear roof drift relationship for an unbounded post-tensioned wall with the four behavior states identified [Kurama et al., 1999]

Kurama et al. [1999] uses the four behavior states to create design objectives and design criteria for the proposed seismic design approach. Figure 2.15a shows the three design objectives. The three design objectives are: 1) immediate occupancy performance under a low level earthquake where limited damage occurs in the structural and non-structural elements; 2) life safety performance under a design based earthquake where significant damage is made but some margin against total or partial collapse remains; and 3) collapse prevention under a survival level ground motion where the building is on the verge of collapse. Figure 2.15b shows the design criteria for the proposed seismic design approach where force and displacement capacities are computed for the wall that exceed estimated demands.

To validate the seismic design procedure, Kurama et al. [1999] designed six 6-story prototype walls using the design approach and design procedure. The prototypes were subjected to more than 200 nonlinear dynamic time history analyses using 15 design level and 15 survival level ground motions. Results showed the desired flag shaped hysteretic behavior with self-centering capabilities and high amounts of energy dissipation. It was concluded that the unbonded PT hybrid system for precast walls provide a more desired behavior than that of

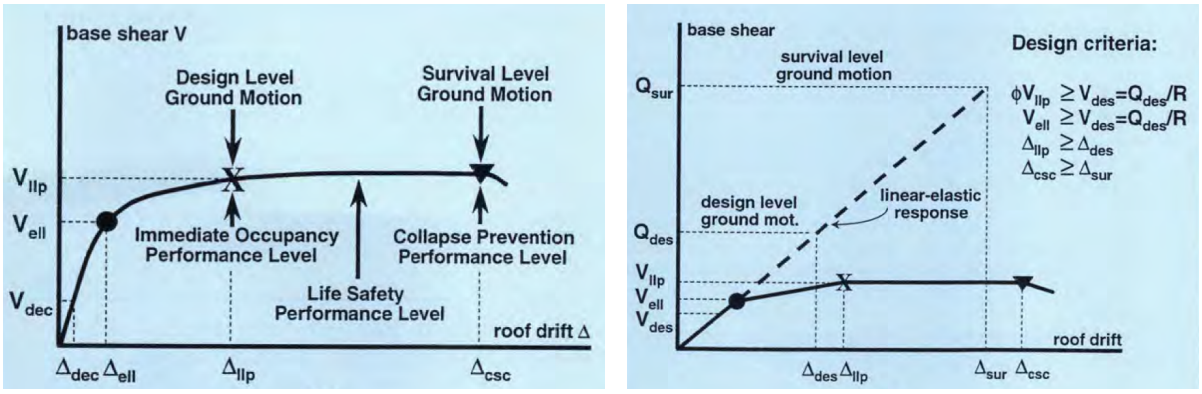

(a) Design objectives (b) Design criteria

Figure 2.15: Proposed seismic dsign approach [Kurama et al., 1999]

a typical monolithic concrete shear wall in seismic regions.

Pampanin et al. [2001] expanded on the work done by Kurama et al. [1999] and further developed the design procedure for the hybrid rocking walls. Pampanin et al. [2001] developed a section analysis method that can be used with precast members through an analogy with an equivalent cast-in-place solution called the "monolithic beam analogy". The result of the cross section procedure provides a moment-rotation response for the ductile connections. The steps of the procedure are as follows: 1) fix the rotation θ; 2) guess the initial neutral axis depth c for the beam; 3) evaluate the strain in the unbonded PT tendons; 4) estimate the strain in the mild steel and concrete; and 5) section equilibrium to determine a the new neutral axis depth c. As part of step 4, a second procedure called the "monolithic beam analogy" was defined to solve the problem of strain compatibility where the neutral axis position, c and the strain in the concrete, ϵ_c are both unknown. Pampanin et al. [2001] defines the procedure by relating the local parameters of the rocking wall to the local parameters of an equivalent monolithic wall by equating the global behavior of each wall as seen in Figure 2.16.

Pampanin et al. [2001] validated the proposed procedure with experimental data from tests on beam-to-column hybrid assemblies from Stanton et al. [1997]. The connections were

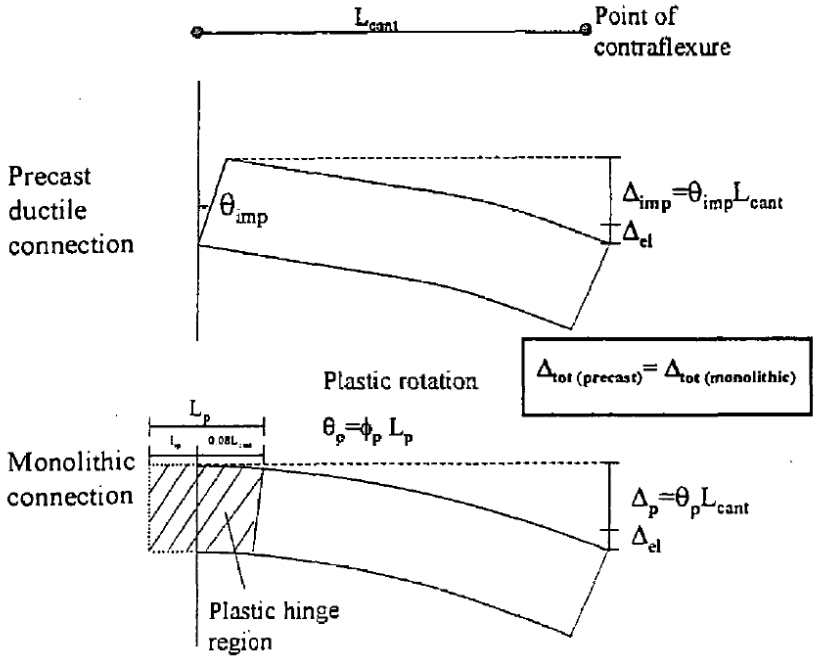

Figure 2.16: Monolithic beam analogy from [Pampanin et al., 2001]

$\frac{1}{3}$ scales with PT steel at the center of the section. During the tests, the PT steel did not yield or fracture leading to failure, failure was typically due to fracture of the mild steel energy dissipation devices. Results showed satisfactory agreement between the analytical and experimental results, verifying the suggested methodology.

2.5 Mass Timber Base Rocking Systems

In recent research, the hybrid base rocking system from PRESSS has been applied to timber structures to create a more sustainable way of building tall buildings quickly. This section highlights some of the big research projects focusing on timber structures with base rocking systems.

2.5.1 Pres-Lam

Pres-Lam was a seismic resistant timber research program based at the University of Canterbury in Christchurch, New Zealand in which a timber system for seismic loading was developed based off the PRESSS research program. With the new structural system, ductile post-tensioned beam-to-column, wall-to-foundation, and column-to-foundation connections made from laminated veneer lumber (LVL) were developed and tested. Information focusing on the wall-to-foundation tests will be summarized here.

As part of of the Pres-Lam project, Palermo et al. [2006] performed experimental cyclic quasi-static and pseudo-dynamic tests on connections in two systems. One system with only unbonded PT bars and one system with hybrid connections that included both unbonded PT bars and a type of energy dissipater. First, quasi-static cyclic tests were performed on three wall-to-foundation hybrid specimens. Figure 2.17 shows the general test setup for the specimens and the geometry details. The first two specimens (HY1 and HY2) had internal dissipaters while, the third specimen (HY3) had external dissipaters. The PT bar force verses drift response for HY1 can be seen in Figure 2.18 (a) and the top lateral applied load verse drift response for HY1 can be seen in Figure 2.18 (b). During the tests, no visible wall damage occurred on specimens HY1 and HY2 at their peak drifts of 3.5% and no visible wall damage occurred on specimen HY3 at it's maximum drift of 4.4% drift. In addition, no PT bar yielding was observed during any of the three tests. Tests HY1 and HY2 were ended at smaller drifts due to buckling failures of the energy dissiption devices at 3.5% drift.

Palermo et al. [2006] also conducted pseudo-dynamic cyclic testing on pure unbonded (without energy dissipaters) post-tensioned walls. The effect of three different levels of initial post-tensioning (0.2, 0.3, and 0.4 f_{py}) was tested and the PT bar force verse drift response is shown in Figure 2.19. These tests showed that increasing the initial PT force increased the drift at which yielding occurs. More specifically, ranging from an initial PT force of $0.4f_{py}$ to $0.2f_{py}$ correlates to a reduction of 30% in terms of maximum drift demand. Overall, the research conducted by Palermo et al. [2006] showed that the Pres-Lam system results in an

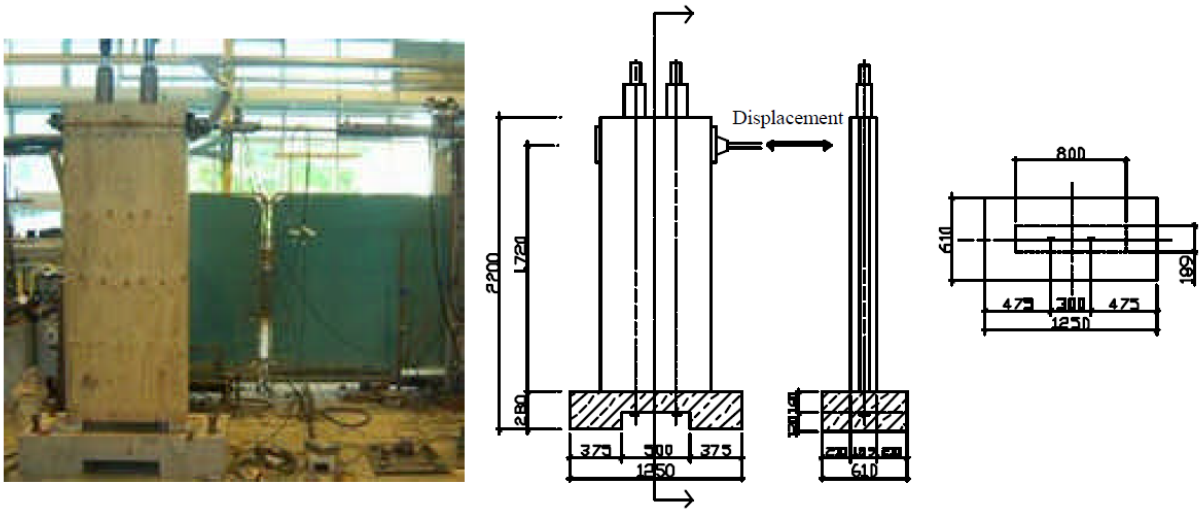

Figure 2.17: Test setup and geometry detials for quasi-static cyclic tests on wall-to-foundation connections [Palermo et al., 2006]

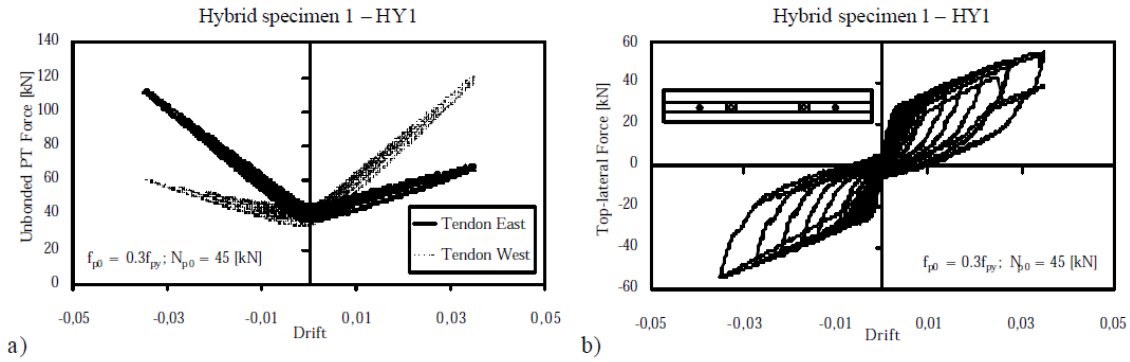

Figure 2.18: (a) Unbonded PT force vs. drift and (b) lateral force vs. drift for hybrid specimen 1 - HY1 [Palermo et al., 2006]

enhanced seismic performance with little to no damage to the structural elements and a flag shaped hysteretic behavior that shows self-centering and energy dissipating capabilities. It should be noted that internal and external dissipaters resulted in similar performance and both solutions could be adopted, but the external dissipaters may be preferred because they are easier to replace.

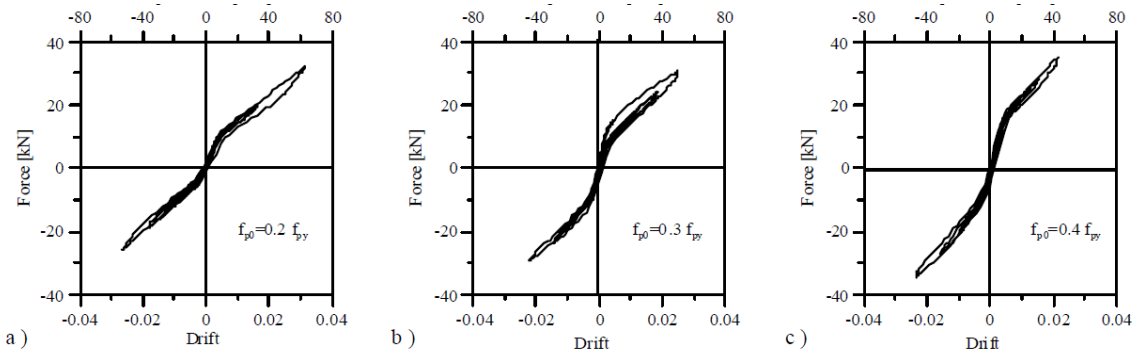

Figure 2.19: Unbonded PT speciments (a) $f_{po} = 0.2f_{py}$, (b) $f_{po} = 0.3f_{py}$, and (c) $f_{po} = 0.4f_{py}$ [Palermo et al., 2006]

Also part of the Pres-Lam project, Smith et al. [2008] performed a case study on the feasibility of implementing a Pres-Lam system into a real building. Smith et al. [2008] redesigned a 6-story reinforced concrete building located in New Zealand with the Pres-Lam system. The building was redesigned with frames in one direction and walls in the other direction as the lateral system and a gravity system with beams sitting on central and exterior columns. The building was designed with 2% inter-story drift limits in the frame direction and 1% inter-story drift limits in the wall direction.

The case study building in Smith et al. [2008] had a timber LVL panel and concrete composite deck, supported by LVL floor joists on steel joist hangers. The LVL beams transferred gravity load to the LVL columns through corbels. During seismic events, shear forces from the diaphragm would transfer to the brace lateral system through coach screws that are cast into the concrete topping and then inserted into the side face of the beam. In the other direction, shear forces would transfer to the wall lateral system through reinforcing

bars that connect the concrete deck to the wall through fixed bolts with threaded wall couplers. At the base, internal steel dissipaters were fixed to the foundation and connected to the columns or walls with epoxy. A cost estimate was then completed for the building to determine it's feasibility in construction and implementation. The estimated construction costs for the equivalent timber, steel, and concrete buildings were $10,020,000, $9,370,000, and $9,430,000 respectively. The breakdown for the timber construction costs is shown in Figure 2.20. Smith et al. [2008] argued that while the cost of timber construction was larger, it is by a very small margin and construction costs are just a small portion of the overall building cost so the different is very minimal. In addition, timber construction allows for prefabrication off sight which could lead to faster construction and the sustainability benefits of building with wood are much higher than in steel or concrete construction.

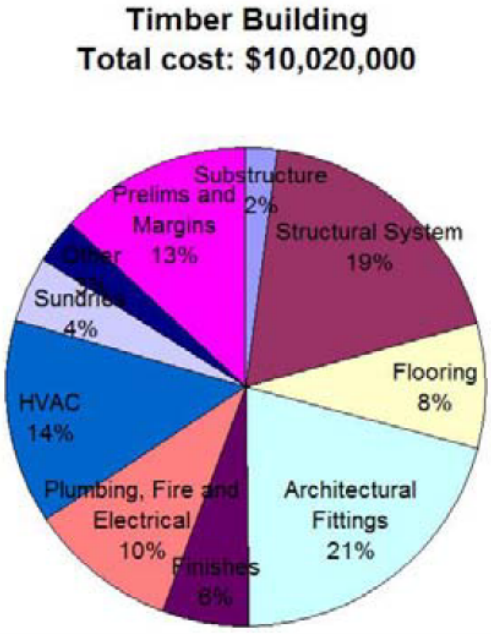

Figure 2.20: Cost breakdown of timber building [Smith et al., 2008]

2.5.2 Achieving Energy Dissipation in Rocking Timber Systems Using UFPs

U-shaped flexural plates (UFPs) are often used in rocking coupled timber wall systems because they are simple and relatively easy to construct and model. They were initially proposed by Kelly et al. [1972] and started gaining popularity due to the successful implementation of the devices in the PRESSS project and Pres-Lam project. With the gain in popularity, Baird et al. [2014] performed parametric studies on UFPs to determine important design characteristics such as the initial and post-yield stiffness, the dissipative capacity, and the maximum possible force developed by the UFPs. A series of displacement controlled test were performed by testing two UFPs in parallel to achieve symmetric loading, as shown in Figure 2.21a. Figure 2.21b shows the force verse displacement behavior for a single UFP in the tests.

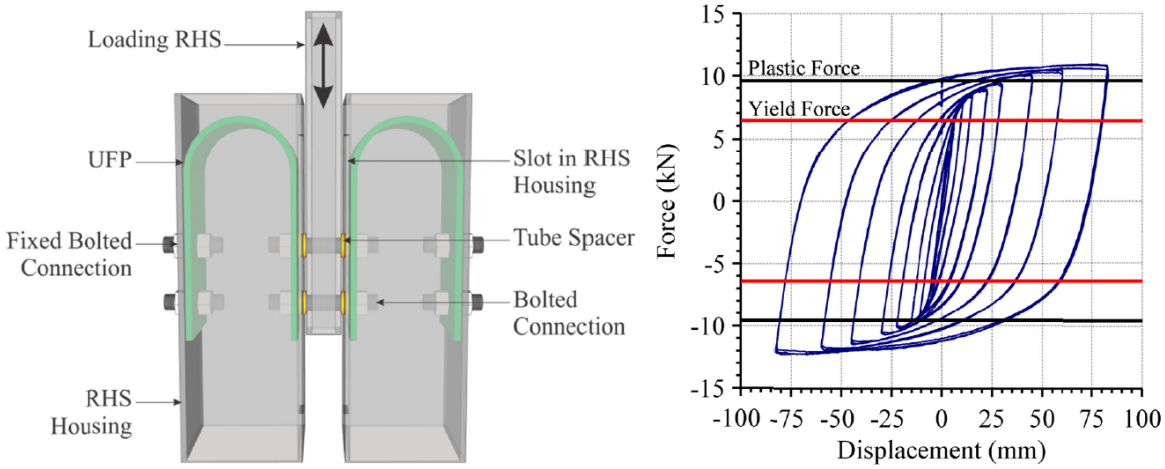

(a) UFP test setup

(b) Experimental hysteresis loop

Figure 2.21: UFP tests performed by [Baird et al., 2014]

Baird et al. [2014] also created numerical models for the tests to calibrate UFP properties to the test results and made recommendations for the yield force, initial stiffness, and Ramberg-Osgood R factor. The recommended equations modeling yield force, initial stiffness, and the Ramberg-Osgood R factor are given in Equations 2.1, 2.2, and 2.3 respectively.

$$F_y = \frac{\sigma_y b_u t_u^2}{2D_u} \tag{2.1}$$

$$k_o = \frac{16Eb_u}{27\pi}\left(\frac{t_u}{D_u}\right)^3 \tag{2.2}$$

$$R = 7.1ln\left(\frac{t_u}{D_u}\right) + 29.5 \tag{2.3}$$

where, b_u is the widht of the UFP plate section, t_u is the thickness of the UFP plate section, D_u is the diameter of the UFP bend, σ_y is the yield stress of the UFP, and E is the elastic modulus of the UFP mild steel.

Iqbal et al. [2015] performed quasi-static cyclic and pseudo-dynamic tests on post-tensioned timber LVL walls coupled together with UFPs. The coupled LVL walls were designed as part of a structural system for a multi-story prototype timber building. The prototype building had bay spacing of 10 meters and story heights of 3 meters, and each wall had a tributary area of 50 square meters and a total vertical load of 5 $\frac{kN}{m^2}$ was assumed for the whole floor. The UFPs were first tested without the wall (similar to the setup from Baird et al. [2014]) in order to better calibrate the cyclic behavior and yielding of the UFPs.

For the panel tests, the UFPs were connected to welded brackets that connected to the panels using self-drilling screws. For testing, the walls were loaded at a height of 2 meters above the foundation as seen in Figure 2.22. Six total specimens were tested under quasi-static and pseudo-dynamic loading. All specimens had the same panel sizes and PT bar properties with the same initial PT force. The first specimen (PT1) had no UFPs and the other five specimens (HU1 - HU5) had varying sizes of UFPs. Figure 2.23 shows the force-displacement curve for the couple wall system with a 5 mm thick UFP and the response from the PT1 specimen. From the figure it is clear that the typical nonlinear, elastic hysteresis loop was observed for the post-tensioned only specimen and the flag shape hysteresis loops with full recentering and energy dissipation was observed for the hybrid solutions. The pseudo-dynamic tests showed very similar results and virtually no damage

was observed in the structural members for both tests. Results of the tests showed that the UFPs provided stable energy dissipation characteristics and in combination with the post-tensioning, a desirable flag-shaped hysteresis was achieved.

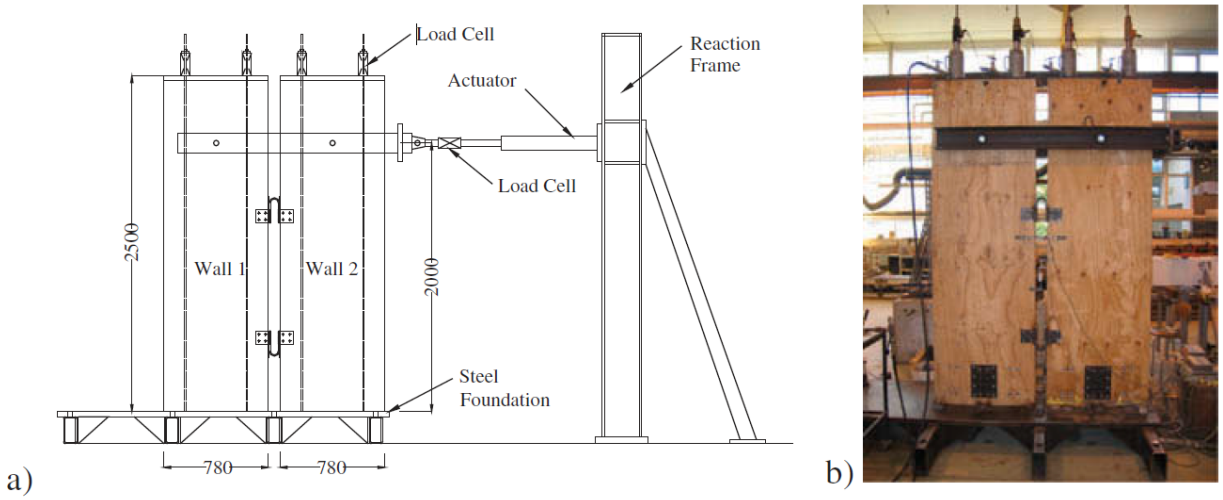

Figure 2.22: (a) Schematic details and (b) view of the coupled wall system test set-up [Iqbal et al., 2015]

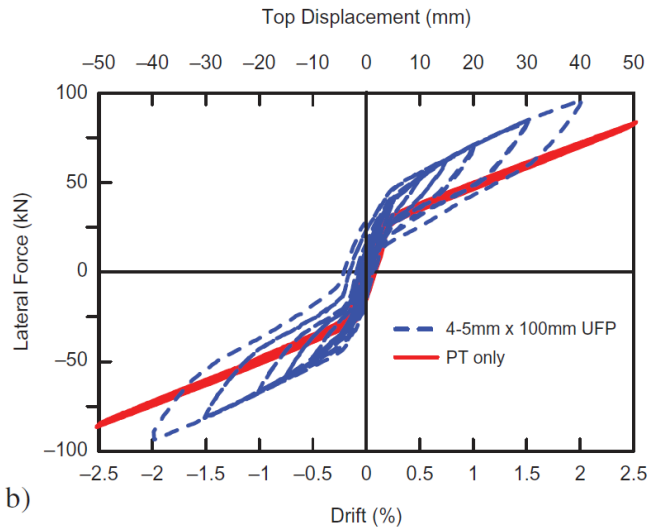

Figure 2.23: Force-displacement plot of specimen HU1 with comparison to specimen PT1 [Iqbal et al., 2015]

2.5.3 Ganey et al. [2017] and Akbas et al. [2017]

Ganey et al. [2017] and Akbas et al. [2017] conducted quasi-static experiments on post-tensioned CLT rocking walls with UFP energy dissipating devices and created the foundation for the research presented in this thesis. The specimens were designed to achieve a set of structural limit states presented by Akbas et al. [2017] to help understand the lateral load response of the rocking CLT walls based on the level of damage to the CLT panels, PT bars, and UFP devices. The limit states shown in Figure 2.24 on an idealized base shear verses drift curve are: 1) decompression at the base of the wall (DEC); 2) UFP yielding (EDP); 3) the effective linear limit that corresponds to the initiation of a visible gap at the base of the wall (ELL); 4) splitting of the CLT panel at the base (SCLT); 5) crushing of the CLT panel at the base (CCLT); and 6) yielding of the PT bars (LLP).

The quasi-static testing completed by Ganey et al. [2017] and Akbas et al. [2017] consisted of six different CLT specimens with the same wall thickness, length, and loading height. Post-tensioning properties such as the PT bar area and initial PT stress were varied for each of

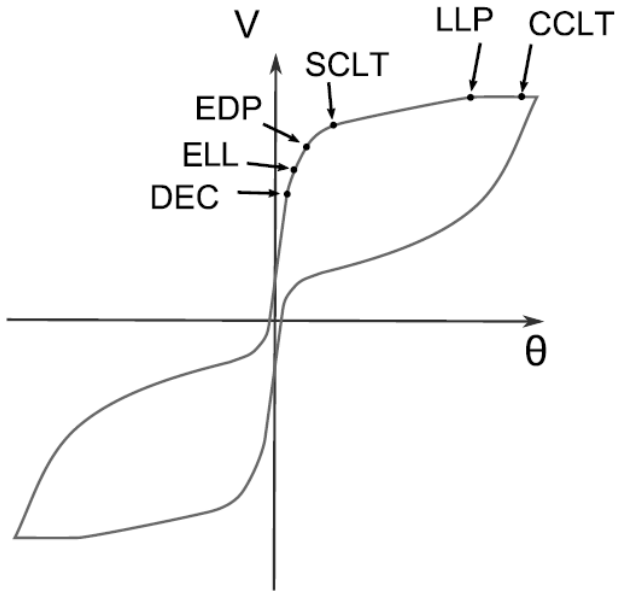

Figure 2.24: Idealized response of a rocking CLT wall with labeled limit states [Ganey et al., 2017]

the tests to determine the effect of changing these properties on the overall response of the system. The first 5 tests were single panel walls and the 6^{th} test was a coupled CLT wall coupled together with UFP energy dissipaters. The general test setup for the specimens is shown in Figure 2.25.

The resulting hysteretic response showed significant pinching at large drifts due to PT bar yielding and CLT crushing as seen in Figure 2.26, the hysteretic response for the coupled CLT wall (test 6). Looking at the PT bar design parameters, it was concluded that the higher the initial prestress force, the higher the decompression moment and the lower drifts at which CLT damage occurred. In addition, the larger the PT bar area, the larger the post-decompression stiffness. So the initial stress for the PT bars should be large enough to provided the needed capacity at the ELL, but small enough to prevent excessive CLT damage and small enough to push PT yielding off until higher drifts are reached. Overall, results

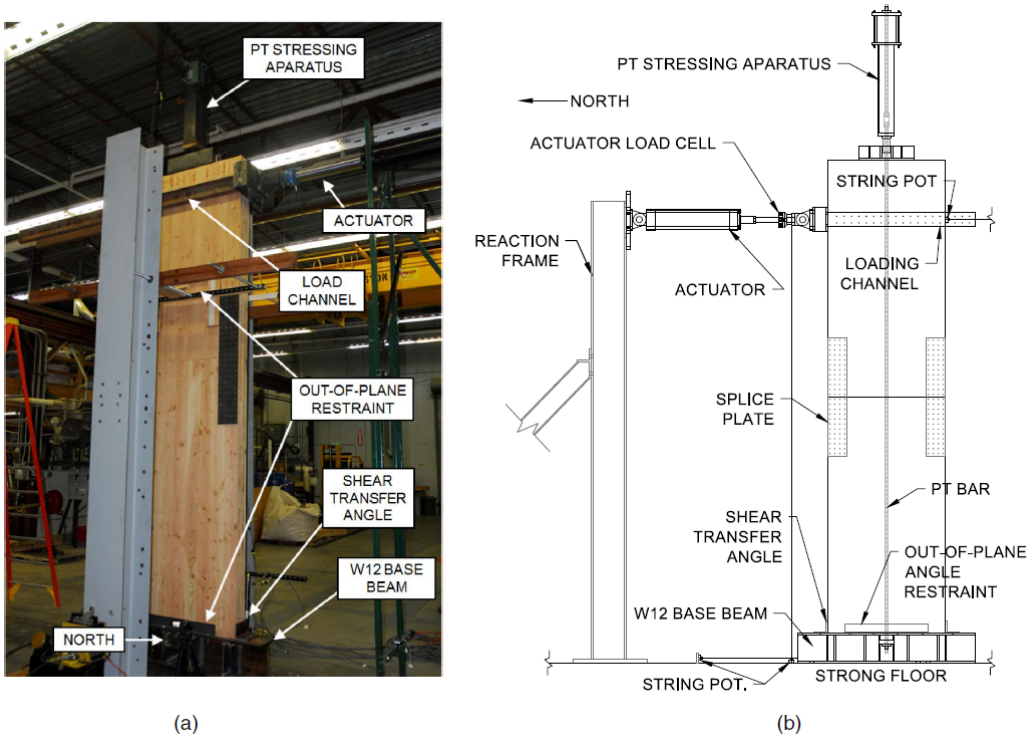

Figure 2.25: General test set-up for quasi-static tets (a) photograph and (b) schematic [Ganey et al., 2017]

from the tests conducted by Ganey et al. [2017] showed that rocking CLT walls have a ductile response, recentering capabilities, and good strength and energy dissipation capabilities.

In addition, Ganey et al. [2017] performed a series of material tests to determine CLT response under axial compression. Axial compression tests on short CLT columns were performed on ten 278 mm tall 3-ply CLT specimens, two 510 mm tall 5-ply CLT specimens, and one 510 mm tall CLT specimen with a structural composite lumber (SCL) core. The results and test set up of these compression tests can be seen in Figure 2.27. The average elastic modulus calculated from the stress strain plot for the CLT and SCL were 441.33 ksi and 842.27 ksi respectively, and the yield stresses were 3.60 ksi and 6.20 ksi respectively. The high variability in the response lead to the conclusion that carefully considered design procedures should be established to account for this variability.

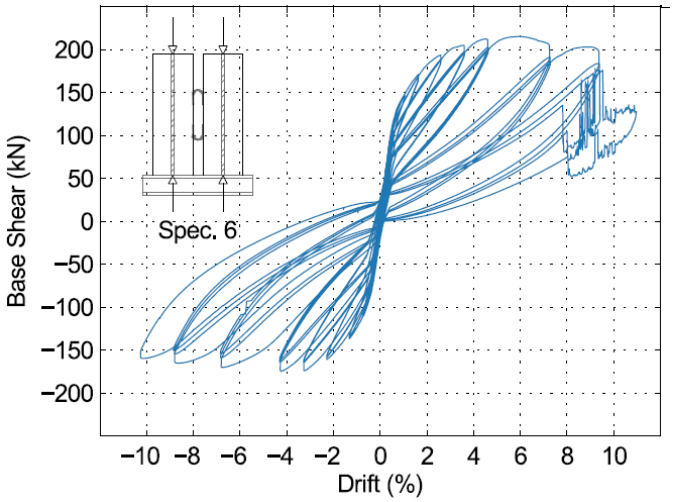

Figure 2.26: Base shear force verse drift repsone for test specimen 6 [Ganey et al., 2017]

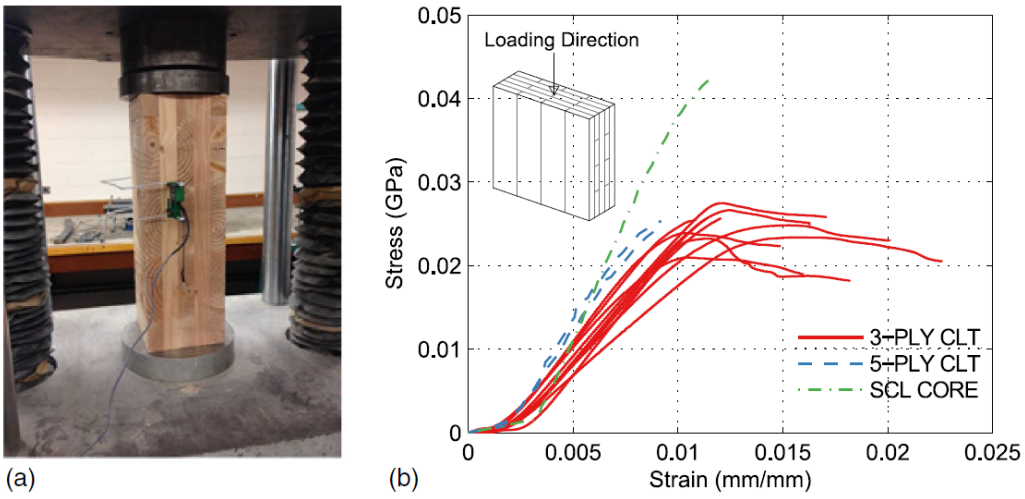

Figure 2.27: CLT material tests (a) test setup and (b) results [Ganey et al., 2017]

2.6 Conclusions and Research Needs

The research shown in this section has come to the following conclusions:

- CLT and mass timber construction is a strong building material that is also a renewable resource and has the potential to greatly decrease the carbon footprint of construction.
- CLT shear walls with mechanical connections are good for low level seismic regions where the system can remain elastic. The only ductility from these systems come from the mechanical connections which is not sufficient for areas that can experience high accelerations.
- Through quasi-static and pseudo-dynamic tests, post-tensioned base rocking connections in concrete and timber systems with energy dissipaters have shown ductile behavior, good energy dissipation, and recentering capabilities for areas of high seiscmicity.
- An established design procedure with limit states has been developed for base rocking systems and has been validated through quasi-static and pseudo-dynamic tests.

The research presented in this section all shows promising success for the implementation of CLT rocking walls. Also, building with CLT can meet the demands of the world's growing population and the need for a greener construction material that can lead to a lower carbon footprint and faster construction. However, limited dynamic testing as been conducted on precast rocking systems, and no large scale dynamic testing has been done with CLT rocking systems to validate the design procedures and performance. The research presented in this thesis is aiming to validate the performance of these systems in dynamic tests.

Chapter 3

BEHAVIOR AND DESIGN OF ROCKING CLT WALLS

3.1 Overview

In this chapter the behavior of post-tensioned CLT rocking walls coupled together with UFP energy dissipation devices will be discussed in detail. A set of performance objectives will be presented along with an outlined design methodology. The design procedure uses an iterative process with a cross-sectional analysis method to determine the moment-drift response of the system. This chapter will first discuss the basic structural behavior of the components in the post-tensioned CLT rocking wall system, it will discuss the hysteretic behavior of the system, and it will finish by explaining the performance-based design procedure that is used to design the system, including a discussion on the iterative cross-sectional analysis procedure.

3.2 Rocking CLT Wall Component Behavior and Analysis Considerations

This section discusses the structural behavior of different components in the rocking wall system and considerations for analysis and design. This includes the simplified constitutive models that will be used for the cross sectional analysis procedure in section 3.5 to develop the moment-drift response of the system. The component behavior of the CLT and UFPs will be discussed first, followed by a brief discussion on the wall to diaphragm connections. Finally, the self-centering response of the rocking walls due to the post-tensioning bars will be presented.

3.2.1 CLT Wall Panel Behavior

Properties of wood vary more than most materials because it is a natural material and is subject to constantly changing conditions such as moisture, soil conditions, and growing space. The tabulated mechanical properties provided by the NDS are averaged results from test data [AWC, 2015]. Because some properties have not been tested extensively, they may be more uncertain than others. In addition, growth features in wood such as knots and the slope of the grain in swan lumber can also change the properties of the wood. Wood can be described as an orthotropic material, meaning the mechanical properties in the three orthogonal directions will all be independent. Figure 3.1 [Kretschmann, 2013] shows the three directions that are typically used when discussing the mechanical properties of timber: 1) the longitudinal (parallel to the grain fiber) direction; 2) the tangential (perpendicular to grain and tangent to the growth rings) direction; and 3) the radial direction (perpendicular to the grains) direction. The orthotropic nature of the material results in twelve constants that are needed to describe the elastic behavior of wood, nine of which are independent. The cell structure of wood is comprised of cylindrical tubes or vessels. These vessels transport water and sap through the wood and provide majority of the strength. When cut from a tree log, lumber is cut in the longitudinal direction so the grains run along the length of the wood, which is also the direction parallel the the main cell structure. This is done because lumber is much stronger in the longitudinal, parallel to grain direction, than in the tangential or radial directions.

In CLT, the layers (or plys) of sawn lumber are placed in orthogonal directions so their material properties are more similar in the orthogonal directions relative to plain sawn lumber. An odd number of plys are always used to make CLT panels so the plys on either face of the panel are the same. Similarly to sawn lumber, the mechanical properties of CLT can also be described in three orthogonal directions where the strong, parallel direction of the panel is defined based on the orientation of the plys on the exterior of the panel. Due to the irregular nature of the wood used to make the CLT panels, the material properties have

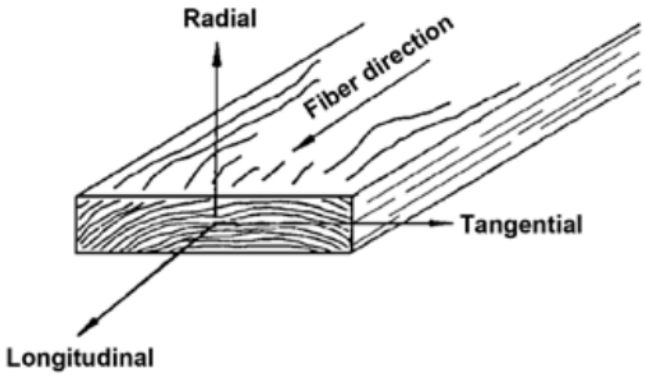

Figure 3.1: Three principal axes of wood [Kretschmann, 2013]

large variability like sawn lumber.

Research has been done to explore the response of sawn lumber, although results vary with wood species, moisture content, and other factors. Figure 3.2a shows the typical stress-strain relationship for sawn lumber [Buchanan, 1990]. In tension the material behaves linear elastically until brittle failure at the maximum load. In compression the material is more ductile with an initial linear-elastic region, followed by a region of reduced stiffness and a yield plateau. From Figure 3.2a, a clear difference in the behavior of lumber tested parallel verse perpendicular to grain is present. More recently, the material response of CLT panels has been studied ([Serrano and Enquist, 2010] and [Flaig and Bla, 2013] among others). Figure 3.2b shows an example of experimental results for the stress-strain response of CLT panels in compression [He et al., 2018]. A similar response to sawn lumber is present and the differences between the two major orthogonal directions is seen. Note the difference in behavior between the major and minor strength directions of the CLT panels is less than the difference in behavior between the parallel and perpendicular to grain directions in sawn lumber.

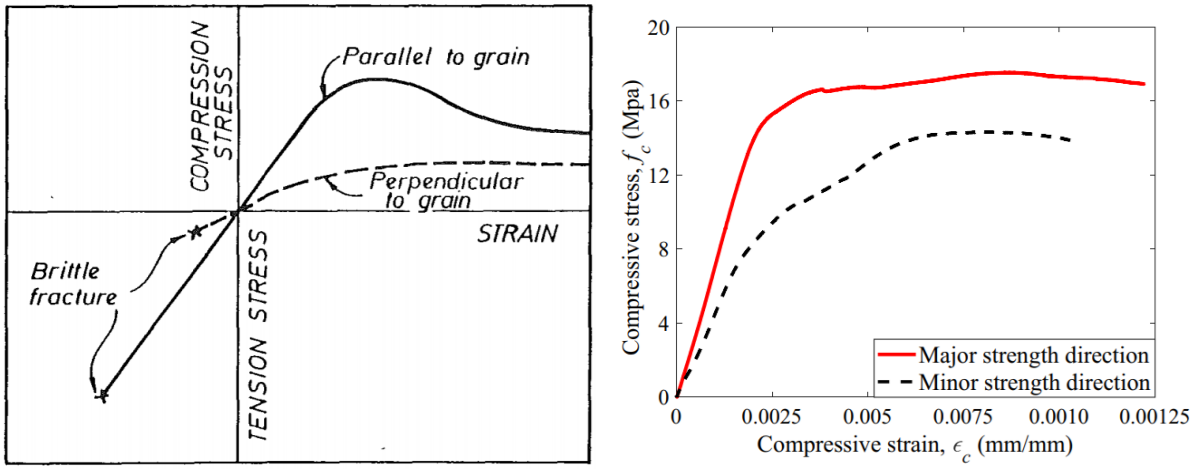

(a) Sawn lumber [Buchanan, 1990] (b) CLT panels [He et al., 2018]

Figure 3.2: Typical stress-strain response

3.2.2 UFP Energy Dissipating Devices

Initially proposed by Kelly et al. [1972], U-shaped flexural plates (UFPs) are made by bending a mild steel plate to form a 'U' shape. For the coupled rocking CLT wall system studied here, the UFPs are used as the primary source of energy dissipation. When the coupled walls undergo large, inelastic deformations, the walls compress resulting in some minor energy dissipation, however it is so small when compared to the dissipation provided by the UFPs and is often neglected.

Figure 3.3a shows a schematic of the UFP with the typical dimensions where t_u is the thickness of the plate, b_u is the width of the UFP, and D_u is the inside diameter of the UFP. The UFPs can be attached to the two walls in a variety of ways including the saddles shown in Figure 3.3b. The saddles wrap around both walls and the UFP can be attached to both the saddles with bolts. This allows for easy replacement after large earthquakes that result in UFP yielding.

To make UFPs, the mild steel is heated before bending into the 'U' shape to prevent stress concentrations from being present in the final configuration. The UFP dissipates energy

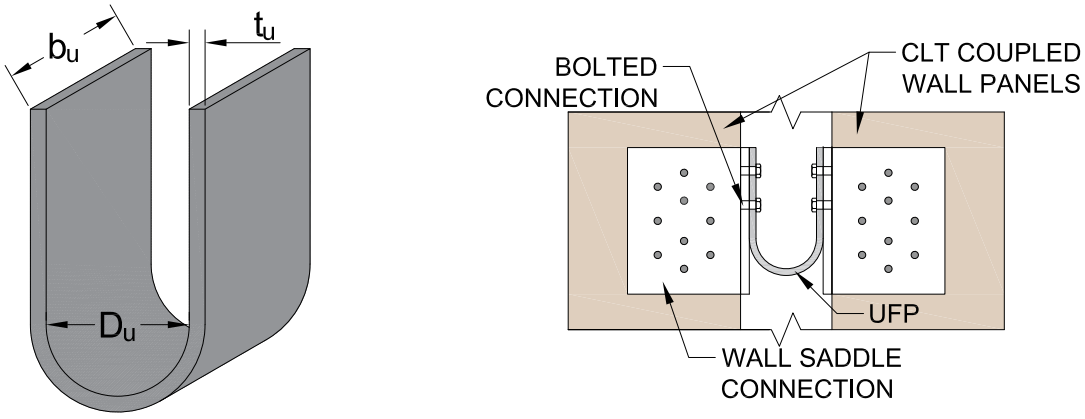

(a) Typical dimensions

(b) Typical mounting detail

Figure 3.3: UFP details

when one end of the UFP moves relative to the other end. During this process the radius of curvature changes from straight to curved and vice versa. This causes the plate to yield back and forth along the plate, dissipating energy [Baird et al., 2014]. Figure 3.4 shows the resulting free body diagram of the UFP once the entire section has yielded, creating plastic moments. The plastic moment, M_p, is determined through basic mechanics by multiplying the yield stress, f_y by the section modulus, Z (Equation 3.1). Kelly et al. [1972] derived the magnitude of force, F_p, that can be provided by the UFP by equating the shear couple to the sum of the plastic moments, M_p (Equation 3.2).

$$M_p = f_y Z = \frac{1}{4} f_y b_u t_u^2 \tag{3.1}$$

$$F_p = \frac{2M_p}{D_u} = \frac{f_y b_u t_u^2}{2D_u} \tag{3.2}$$

To model the UFPs, the initial stiffness, k_o, is needed. This can be found by finding the yield displacement through strain energy methods and solving for stiffness as seen in the

following equation [Baird et al., 2014]:

$$k_o = \frac{F_y}{\Delta_y} = \frac{16Eb_u}{27\pi}\left(\frac{t_u}{D_u}\right)^3 \tag{3.3}$$

where E is the elastic modulus of the mild steel.

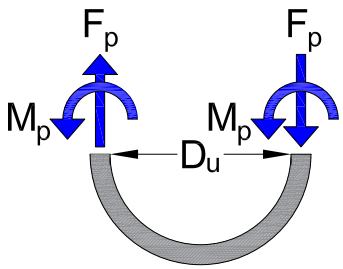

Figure 3.4: Free body diagram of yielded UFP

3.2.3 Diaphragm and Wall to Diaphragm Shear Transfer

Different diaphragm options have been studied for structures with rocking CLT walls. Concrete slabs can be used for a more rigid diaphragm, or the diaphragm can be made more flexible by using a plain CLT slab, or a combination of a CLT diaphragm with a composite concrete topping could also be used to achieve a semi-rigid diaphragm. The latter two options were used in the test set up discussed in Chapter 4. It should be noted that the response of the diaphragm is beyond the scope of work presented here. A more detailed analysis of the diaphragm design and response for the tests described in this thesis can be found in DeMeza [2018].

To achieve the performance objectives desired for the rocking CLT wall systems, a connection between the wall and diaphragm that transfers the horizontal shear force while accommodating the displacements is necessary. Moroder et al. [2017] tests several different

wall to diaphragm connection design concepts with varying degrees of rotational and transnational deformation decoupling. Four of the connections studied are shown in Figure 3.5. In situations where a more flexible diaphragm is present, it was shown that more economical connections such as the one shown in Figure 3.5 (a) or Figure 3.5 (b) a sufficient. With a more rigid diaphragm, a more complicated connections such as the one shown in Figure 3.5 (c) are recommended. When rotations need to remain small, end columns can be used to transfer the shear forces indirectly as shown in Figure 3.5 (d).

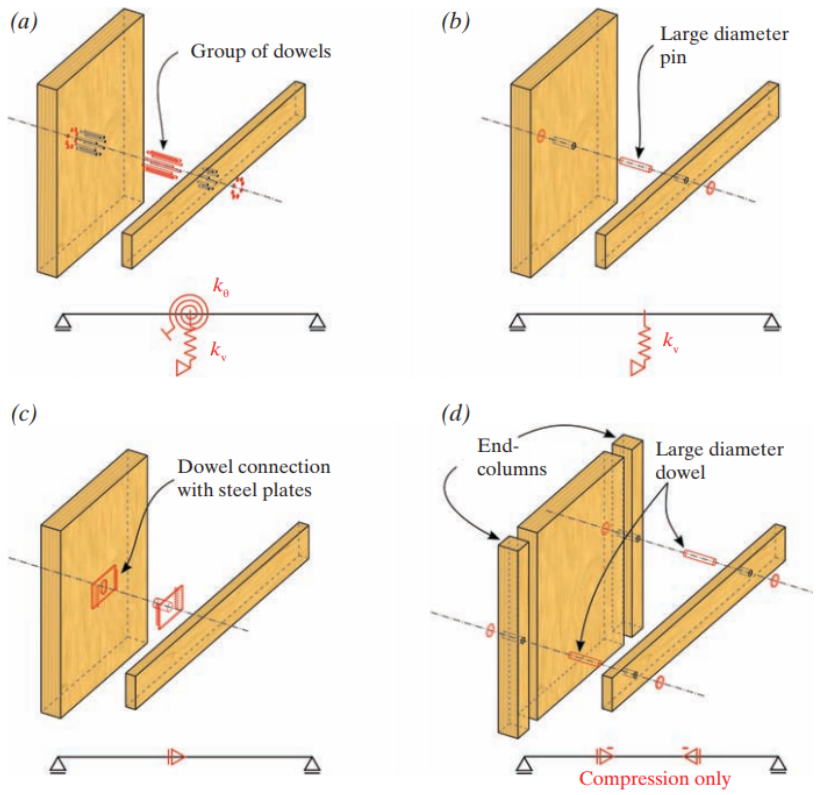

Figure 3.5: Different wall to diaphragm shear transfer connections: (a) vertical and rotational restraint; (b) vertial restraint; (c) horizontal restraint; and (d) use of end columns for no restrains in the walls [Moroder et al., 2017]

3.2.4 Post-Tensioned Connections

In this system, the CLT rocking walls are anchored to the foundation using unbonded steel post-tensioning bars instead of mechanical brackets that are used in typical timber shear walls (see Figure 2.8). The bars are fixed to the foundation or floor diaphragm at the base of the wall. The PT bars then run along the total height of the wall. Multiple bars can be placed symmetrically about the center line of the wall length or just one bar can be placed in the center of the wall thickness. In addition, the bars may run through a pre-cut cavity in the wall or they can run externally on both sides of the walls so the system remains symmetric and balanced. The bars are placed close to the center line of the wall to minimize the increase in strain caused by wall rotation. The connection of the PT bars at the top of the walls determine if the walls can be classified as a single or dual PT connection. With a single PT connection, the bars attach to the top of the wall, typically through a saddle-like connection and the walls are typically balloon framed. In a dual PT connection, the top of the PT bars are connected to the diaphragm at the top of the wall. With the dual PT connection, both the top and bottom of the wall are rocking surfaces. This study will focus on the single PT connection but more information about the dual PT connections can be found in Ganey [2015]. With both connection types, the post-tensioning bars are initially stressed to provide the recentering capabilities of the system. The initial stress in the bars initially puts the whole wall in compression. Figure 3.6 shows a schematic of the walls and PT bar configuration for a CLT rocking wall system with a rocking plane at the base. It should be noted that with this PT bar configuration, two bars could run in the exterior of the wall panel or two bars could be on either side of each panel. In the tests presented in this research, this configuration was used with two PT bars on either side of each panel.

Under small lateral loads and before rocking, the walls behave elastically. During this phase, the lateral load is resisted fully by the elastic deformations of the wall panels, similar to that of a fixed-base shear wall. The system changes stiffness once it reaches the decompression moment, M_{dec}. At the decompression moment, all the force from the gravity load and the

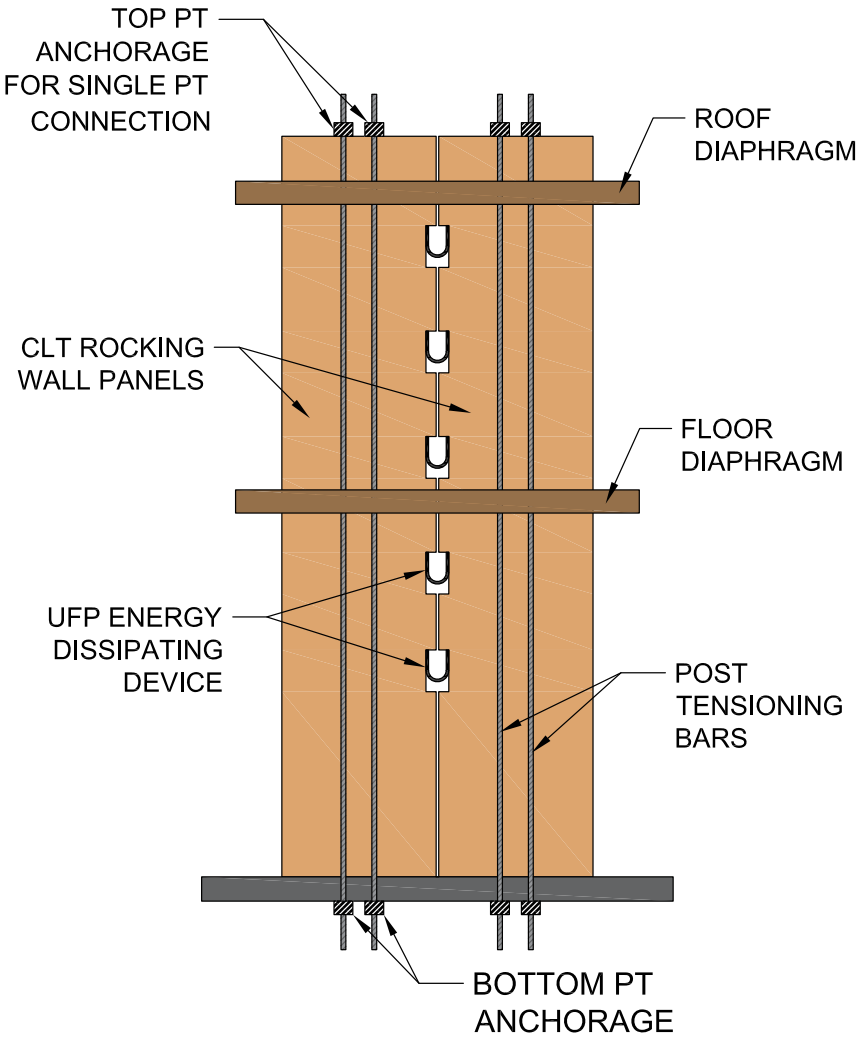

Figure 3.6: Coupled post-tensioned rocking wall schematic with single PT connection

PT bars travels though the wall panels and go to the foundation through the portions of the wall panel bases in compression. At this point, the moment from the lateral load is fully resisted by the couple formed between the gravity and the initial PT load force and the compression force. After the decompression moment, the wall panels begin to rock, forming a gap at the base of each panel, θ_{gap}, as shown in Figure 3.7.

Beyond the decompression moment, the moment due to the lateral load is limited to the

moment induced by the gravity load, W, and the force in the post-tensioning for each panel, T, plus the moment from the UFP forces, V_p. Using the dimensions in Figure 3.7 the base moment at and after decompression is calculated by summing moments about the centroid of the compression zone (at the location of force C) as follows:

$$M = \sum_{1}^{n_w} (T + W)\, d + \sum_{1}^{n_{UFPs}} F_p L_w \tag{3.4}$$

where d is the moment arm length between the sum of the PT tension force and the gravity load at the top of the wall and the centroid of the CLT compression force. At decompression, Equation 3.4 can also be used where the tension force is T_o, the initial PT force. If UFPs are small enough and are expected to yield a very small drifts, then the UFP forces can be included in the calculation of the decompression moment. If the UFPs are larger, the UFP term in the moment equation can be removed. When the wall rocks, the PT bars are stretched and extend, increasing their tension force and the resisting moment. During this phase, the UFPs deform, increasing the resisting moment, as shown in Equation 3.4, but the moment from the UFPs is typically small when compared to that generated by the PT bars. Upon unloading, the wall panels start to rock back downward. As θ_{gap} decreases, the bars shorten and their initial PT force causes the walls to recenter. While the walls are rocking, the force from the gravity load and PT bars travels through the wall and into the foundation. This occurs along the portion of the base of the wall that is in compression. This length changes constantly as the wall rocks and the CLT deforms. To solve for this compression zone length, also called the neutral axis depth c, the cross sectional analysis procedure described in Section 3.5 is used.

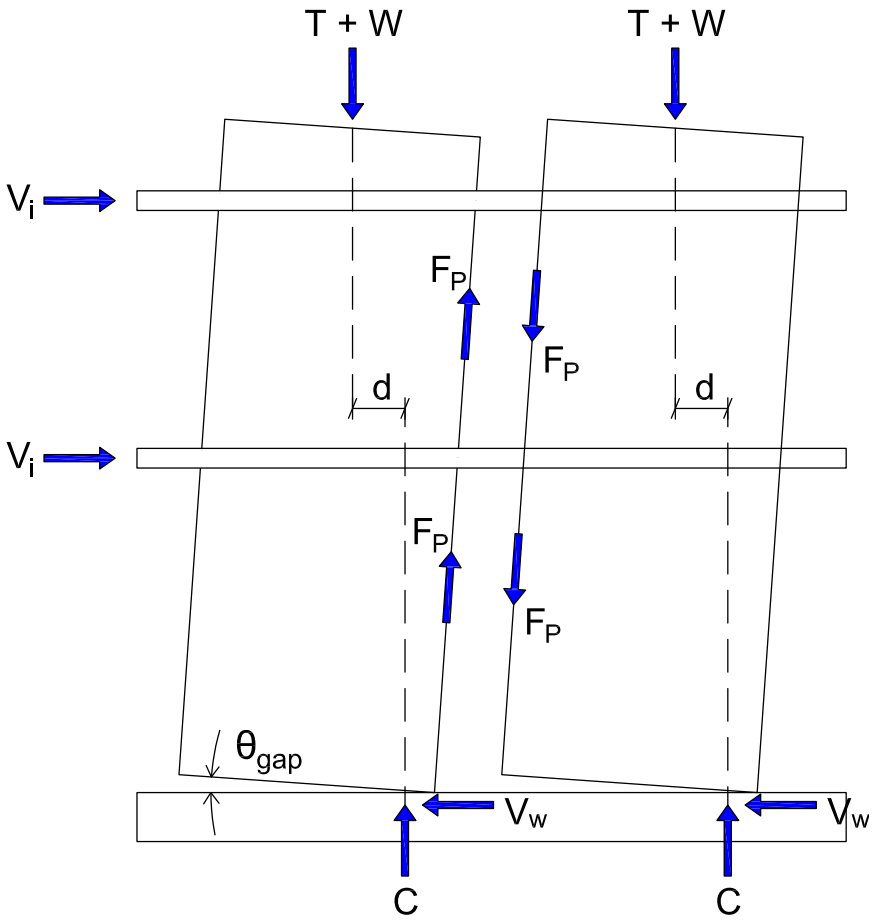

Figure 3.7: Coupled post-tensioned rocking wall free body diagram with single PT connection connection and a single PT bar the the center of each panel

3.3 Rocking Wall Response and Cyclic Behavior

As mentioned earlier, the concept of combining unbonded post-tensioning tendons with damping or energy dissipating devices was first investigated in precast concrete structures and is typically called a hybrid system [Stanton et al., 1997]. The goal was to create a system that could undergo large inelastic displacements while still assuring recentering and minimizing damage. As seen in Figure 3.8 (a) the PT bars provide an elastic but nonlinear response that results in recentering capabilities. As the system rocks, the PT bars load and

unload along the same path resulting in no energy dissipation, but the response is nonlinear due to the gap opening at the base of the wall. The hysteretic behavior of the energy dissipaters, seen in Figure 3.8 (b) provides the dissipation needs for the system. This also allows for localized damage in the system, meaning the dissipaters damage and act as structural fuses for the system, leaving the rest of the structure in fairly good condition. Adding the response from the unbonded PT bars and the energy dissipating devices, results in the flag shaped hysteresis for a hybrid system shown in Figure 3.8 (c).

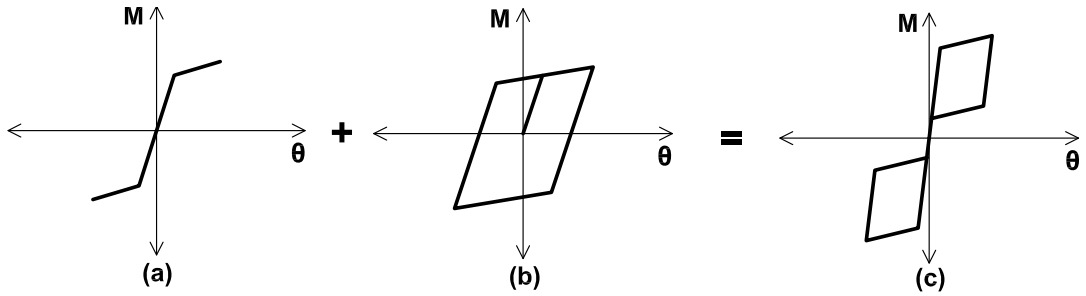

Figure 3.8: (a) Self-centering hysteresis from PT bars and (b) energy dissipating hysteresis combined to get the (c) idealized flag-shape hysteresis loop [Stanton et al., 1997]

The CLT rocking wall concept and system response is very similar to that of the hybrid system. The hysteresis shown in Figure 3.9 is the resulting hysteresis of combining a PT self-centering system in CLT rocking walls with UFP energy dissipaters. There are four main components to this system that need to be considered: 1) decompression; 2) yielding of the UFPs; 3) crushing of the CLT panels; and 4) yielding of the PT bars.

Under small lateral forces, the wall remains linear and elastic until the decompression moment is reached. During the linear elastic region, the stiffness of the system is equal to the elastic shear and flexural stiffness of the CLT panels alone. After the decompression point the stiffness decreases, increasing the period of the system. As the lateral forces increase future, the UFP reach their maximum force and yield, further decreasing the stiffness of the system. However, because the UFPs yield at such small deformations, the point of decompression and UFP yield are almost the same. Next, the system is designed for the CLT panels to

begin crushing at their corners prior to PT yielding, this behavior will further reduce the stiffness of the system. Finally, the PT bars will yield and if toe crushing is not severe, the system will reach it's maximum capacity. If no PT yielding has occurred, or if yielding is limited, as the lateral forces start to decrease the PT bars will help the walls recenter.

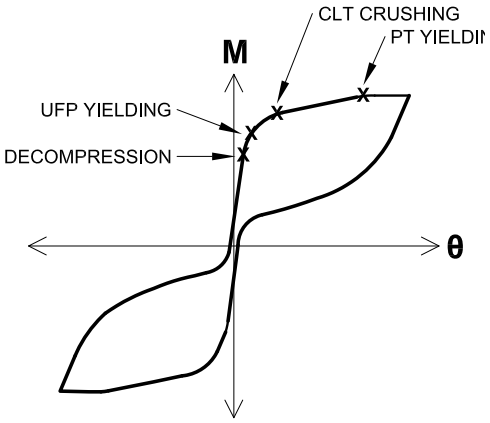

Figure 3.9: Hysteretic behavior of rocking CLT wall system [Ganey, 2015]

3.4 Performance Based Design Procedure for Rocking CLT Walls

There are three main components in the CLT rocking wall system presented in this study, each with limit states to be considered in design. The three main components and their limit states are: 1) CLT rocking wall panels with limit states of yielding and crushing at the rocking base; 2) PT bars with the limit states of yielding and fracture; and 3) UFPs with the limit states of yielding and fracture (although fracture occurs at such large deformations it will not be considered). Each component is designed for limit states to occur at different seismic demands associated with different hazard levels. This section presents a description of the seismic hazards for design, an explanation of the target performance objectives, and a performance-based seismic design procedure for designing this system.

3.4.1 Seismic Hazard Levels

The system is designed to have specific performance at three seismic hazard levels. The first is the service level earthquake (SLE) which refers to earthquakes with a 50% probability of exceedance in 50 years (a earthquake with a 72 year return period). The second is the design based earthquake (DBE) which refers to earthquakes with a 10% probability of exceedance in 50 years (an earthquake with a 475 year return period). The final hazard level is a maximum considered earthquake (MCE) which refers to earthquakes with a 2% probability of exceedance in 50 years (an earthquake with a 2475 year return period).

3.4.2 Performance Objectives

The performance objectives for this design methodology are based on the performance objectives from Ganey [2015]. This section will discuss those performance objectives which are summarized in Figure 3.10. It should be noted that the performance objectives for the two-story shake table testing were modified as discussed in Section 4.2.3.

PO 1: Wind Loading

> *No wall decompression under design wind loading.*

PO 2: Immediate Occupancy

> *No repair of the system is required after a 50% in 50 year hazard level earthquake.* In order for no required repairs, the UFPs and PT bars must not reach their yield strengths. In addition, the system must recenter according to the out-of-plumb limits in construction [ATC, 2009], which specify the residual drifts to be less than 0.2%. However, if PT bars have not yielded, residual drifts should not be an issue.

PO 3: Limited Repair

UFP replacement is required and system fully recenters after an 10% in 50 year hazard level earthquake. The UFPs and their connections can be designed for easily replacement, so under DBE shaking the UFPs are allowed to yield fully. However, PT bars should not yield and the rocking CLT wall panels should not crush, ensuring recentring behavior with residual drifts less than 0.2%. In addition, according to code-based drift limits, the story drifts should be limited to 2% [ASCE, 2010].

PO 4: Collapse Prevention

Damage to the system is limited to prevent building collapse after a 2% in 50 year hazard level earthquake. Damage should still be limited to prevent any major loss of stiffness or strength, so CLT wall panels can crush, however PT bars should not yield or only experience minor yielding. The story drift limit for this performance objective is set at 4% based on engineering judgment of when the PT bar strains become large. After any event larger than a 2% in 50 year hazard level earthquake, the building is expected to see excessive damage including significant PT yielding and large amounts of CLT wall crushing at the base. In addition, story drifts may exceed 4%.

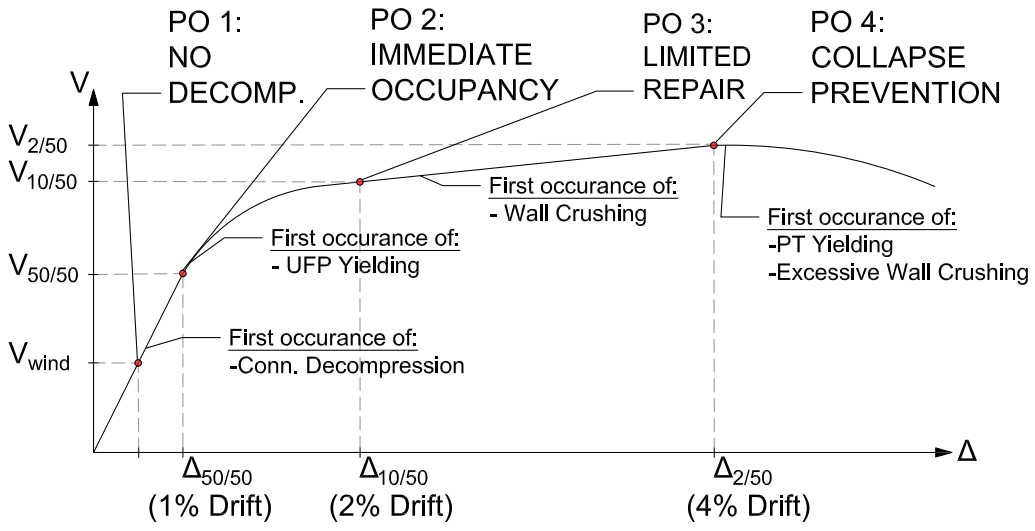

Figure 3.10: Summarized performance objectives [Ganey, 2015]

3.4.3 Design Procedure

The proposed design procedure for post-tensioned CLT rocking walls, coupled with UFP energy dissipaters is described in the following section and summarized in Figure 3.11. The design procedure presented is a slightly modified version of the design procedure presented in Ganey [2015].

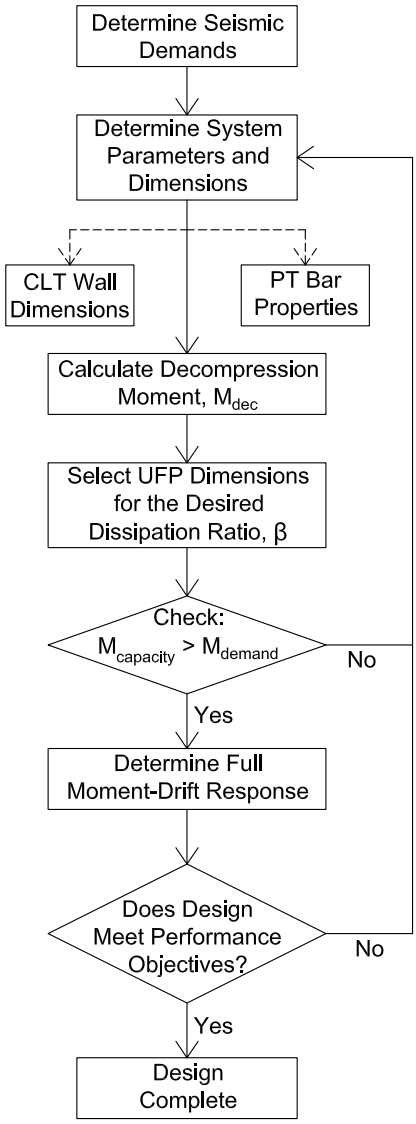

Figure 3.11: Summary of the proposed performanc-based design procedure

Calculate Seismic Demands

The first step of the design procedure is to calculate the elastic seismic demands on the structure. This step is based on the ASCE 7-10 equivalent lateral force procedure using the ASCE 7-10 design response spectra. First the building's approximate fundamental period, T_a, is calculated from the equation in ASCE 7-10 [ASCE, 2010]. The design response spectrum from ASCE 7-10 is then used to determine the spectral acceleration for the calculated T_a. The spectral acceleration is divided by the response modification factor, R, and then multiplied by the seismic mass to get the seismic base shear for elastic design. For CLT shear walls that use typical mechanical connectors, Pei et al. [2013] recommends using an R factor of 4.5. However, because the rocking system with self-centering post-tensioning bars is much more ductile, an R factor of 6 is assumed. The equivalent lateral force procedure from ASCE 7-10 is then used to determine the distribution of lateral forces. Using the lateral forces, the base overturning moment demand, M_{demand} is determined. This is the elastic demand moment.

Determine System Parameters and Dimensions

Once the seismic demands have been calculated, the preliminary system parameters and dimensions are chosen for the rocking walls and the post-tensioning bars. These preliminary parameters may be modified during the design procedure to meet design requirements and performance objectives. The following parameters and dimensions should be chosen:

- CLT rocking wall panel dimensions should be chosen. This also includes the overall configuration of the rocking walls and the material properties of the CLT. The specific wall panel dimension that need to be selected include:
  - CLT wall panel length, L_w
  - CLT wall panel thickness, b_w
  - CLT wall panel height, h_w
- The PT dimensions should also be chosen. This also includes the configuration of the

PT bars, how many PT bars will be included in the design, and the material properties of the PT bars. The specific dimensions that need to be selected include:

- PT bar area, A_p
- PT bar length, L_p
- Initial PT bar force, T_o

Calculate Decompression Moment

As mentioned earlier, the decompression moment, M_{dec} is the point at which the lateral force creates an overturning moment causing the wall to just begin to lift up and rock. Per recommendation by, Akbas et al. [2017], M_{dec} is defined as occurring when the portion of the wall at the base in compression, also called the neutral axis depth, c, is equal to $\frac{3}{8}$ of the total length of the wall panel, L_w. It should be noted that this neutral axis depth at decompression may vary slightly with different parameters such as the initial post-tensioning force, panel size and strength, and gravity load, however in this study and design procedure a consistent value of $\frac{3}{8}L_w$ will be assumed for the neutral axis depth at decompression.

As seen in Figure 3.12, at decompression a linear stress distribution for the CLT along the neutral axis depth, c, is assumed. Because the stress distribution is linear, the total equivalent compression force, C, acts at a distance, $\overline{c}$, from the corner of the wall panel, where the distance $\overline{c}$ is equal to $\frac{1}{3}$ of the neutral axis depth, c. As seen in Figure 3.12, to satisfy equilibrium, the total compression force C is equal to the sum of the total initial post-tensioning force, ΣT_o from all the PT bars and any gravity load, W on the system. The resulting decompression moment for one wall panel is:

$$M_{dec} = \left(\sum_{1}^{n_{PT}} T_o + W \right) d \tag{3.5}$$

where d is the moment arm between the equivalent compression force, C, and the centroid of the vertical loads. Because no uplift has occurred at the decompression moment, the PT bars experience their initial PT forces, and the centroid of the vertical loads is assumed to

act at the centroid of the wall length. Therefore, the decompression moment arm, d can be calculated by subtracting, $\bar{c}$ from $\frac{L_w}{2}$. To calculate the total decompression moment for the wall, the decompression moment per panel is multiplied by the number of panels in the wall (assuming all panels are equal). Additionally, it is typically assumed that the UFPs have not deformed significantly and their contribution to the moment is zero at decompression. However, if they are small enough their contribution could be added into the total decompression moment, resulting in the equation:

$$M_{dec} = n_w \left(\sum_{1}^{n_{PT}} T_o + W \right) d + \sum_{1}^{n_{UFPs}} F_p L_w \tag{3.6}$$

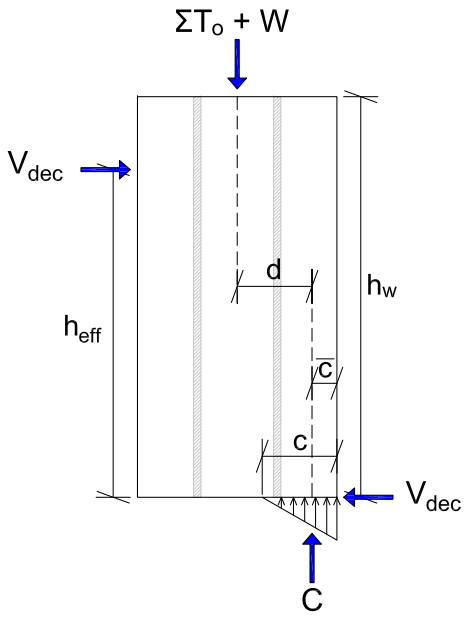

Figure 3.12: Wall panel equilibrium at the deompression point

At the decompression moment, the system is fully elastic and there is no gap opening under the wall. All lateral forces are resisted by the stiffness of the wall panels and any

lateral deformation is due to the elastic deformations in the wall. Both flexural stiffness and shear stiffness should be included in the calculation of the total wall stiffness. The flexural stiffness and shear stiffness can be combined through a simply adding their effects in series as seen in the following equation for the total stiffness of the wall panels, k_w:

$$k_w = \left(\frac{1}{k_{flex}} + \frac{1}{k_{shear}} \right)^{-1} \tag{3.7}$$

where k_{flex} is the flexural stiffness of the wall panel and k_{shear} is the shear stiffness of the wall panel. These values are calculated based on the stiffness of a cantilever beam with a single point load applied at an effective height, h_{eff}:

$$k_{flex} = \frac{2E_w I_w}{h_{eff}^2 \left(h_w - \frac{h_{eff}}{3} \right)} \tag{3.8}$$

$$k_{shear} = \frac{G_w A_w}{h_{eff}} \tag{3.9}$$

where E_w is the modulus of elasticity of the CLT panel, I_w is the second moment of inertia of the CLT panel, h_w is the total height of the CLT panel, G_w is the shear modulus of the CLT panel, and A_w is the cross section area of the CLT panel which is equal to L_w multiplied by b_w. For the case where the walls are used for just one floor and the total shear force, V_{dec} is transfer at the top of the wall system, then h_{eff} is equal to h_w. However, for the case of a wall being used for multiple stories, like the case in this study, h_{eff} is taken as the effective height a single equivalent lateral shear force would act so the base shear and moment are equivalent to the system with multiple story shear forces as shown in Figure 3.13.

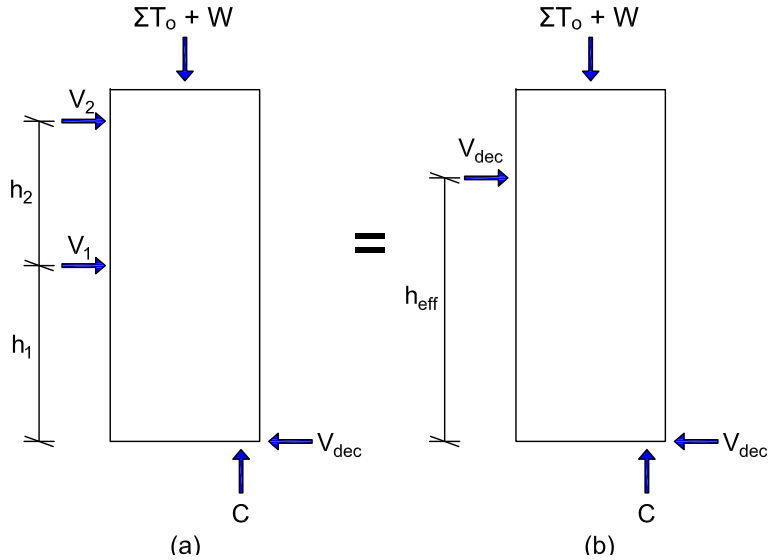

Figure 3.13: Equivalent force systems (a) and (b) where (b) can be easily used for calculating the CLT wall panel stiffness

At the decompression point, the elastic displacement at the location of the equivalent lateral load height, h_{eff}, is:

$$\Delta_e = \frac{M_{dec}}{k_w h_{eff}} \tag{3.10}$$

Select UFP Dimensions and Desired Dissipation Ratio

The energy dissipated by the UFPs, is represented by the ratio of the area of the flag-shape damping hysteresis (Figure 3.14 (a)) and the area of the full elastic-plastic hysteresis (Figure 3.14 (b)) [Seo and Sause, 2005]. This ratio, β can be calculated as:

$$\beta = \frac{n_{UFPs} M_{UFP}}{2M_{dec}} \tag{3.11}$$

where n_{UFPs} is the number of UFPs coupling the walls together, M_{dec} is the decompression moment of the whole wall calculated in Equation 3.5, and M_{UFP} is the moment in each UFP calculated by multiplying V_{UFP} by the panel length, L_w.

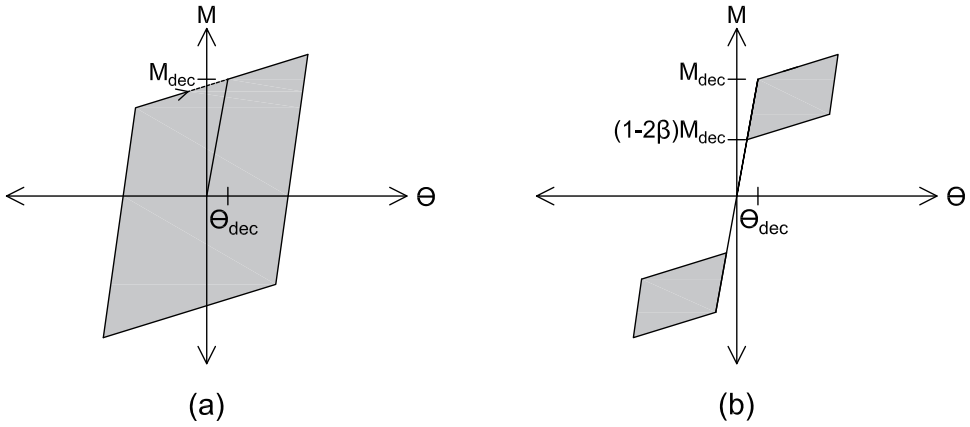

Figure 3.14: (a) the full elastic-plastic hysteresis and (b) the flag-shaped damping hysteresis used to represent the energy dissipation ratio [Seo and Sause, 2005]

In this step of the design procedure the dimensions of the UFPs and the number of the UFPs in the system are determined based on the desired dissipation ratio of the UFPs, β. The three UFP dimensions that need to be selected are the ones discussed in Section 3.2.2, D_u, b_u, and t_u. Equation 3.11 is then used to determine the the number of required UFPs needed to achieve the desired dissipation ratio, β.

Check that Capacity is Greater than Demand

At this point the walls are checked to see if the elastic capacity of the wall is larger than the elastic demand. The demand forces are intended to be the elastic design forces calculated in section 3.4.3 considering the response modification factor R. The capacity of the walls should be taken as the elastic forces at the decompression point. The decompression point is used because this is the maximum elastic and linear portion of the behavior. After the decompression point, the system becomes nonlinear.

With this check, if the decompression moment, M_{dec} is not larger than the moment demand, M_{demand} then the system parameters and dimensions from 3.4.3 should be modified to meet this design check before continuing with the procedure.

Perform Cross Section Analysis Procedure for a Full Moment-Drift Response

The next step of the design procedure is to determine the complete moment-drift response for the wall using the cross section analysis procedure described in section 3.5. The cross section analysis procedure is explained for only one panel, so the procedure should be completed including the additional moment from the plastic capacity of the UFPs and two panels if analyzing a coupled wall. The procedure gives a means of calculating the overturning moment for a given building drift, so the procedure can be repeated for a range a drifts to determine the overall response. The moment-drift response will be used to check performance objectives in the next section.

Check if Performance Objectives are Met

To complete the design procedure, the results from the previous section should be used to determine if all performance objectives are achieved. To do so, for each drift that corresponds to the performance objective, the maximum strain in the CLT panels, the maximum forces in the PT bars, and the forces in the UFPs should be checked to make sure they have not exceeded any limits outlined in section 3.4.2. If all performance objectives are met, the design is complete. If any are not satisfied, the design parameters in Section 3.4.3 should be modified and the design should be repeated.

3.5 Cross Sectional Analysis for Design

As discussed in previous sections, a relatively simple procedure called the cross-sectional analysis procedure has been developed to assist in solving for the neutral axis location at the base of the wall panels in the rocking wall system. This is an iterative procedure to

calculate the length of the compression neutral axis at the base of the wall for any given drift limit. This procedure was originally developed by Pampanin et al. [2001] for precast concrete frames. Since then it has been adapted and modified by Newcombe et al. [2008] for LVL walls and Ganey [2015] for CLT walls. The procedure developed is for single rocking wall and is presented first in this section. Explanation for adapting the procedure to couple walls with UFPs is presented in Section 3.5.7. Figure 3.15 summarizes the procedure.

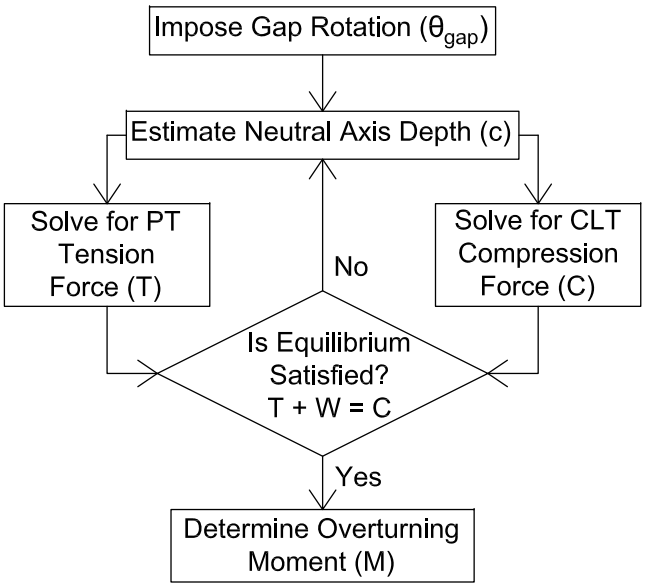

Figure 3.15: Summary of the cross sectional analysis procedure

3.5.1 Impose Gap Rotation

The first step of the cross sectional analysis procedure is to impose a gap rotation, θ_{gap} at the base of the wall. As show in Figure 3.16, θ_{gap} is the rotation angle at the base of the wall that occurs after the wall has fully decompressed and reached it's decompression moment. The imposed gap rotation is used to calculate the total story drift by adding the elastic rotation due to wall deformations, which is calculated using the following equation:

$$\theta_{drift} = \theta_{gap} + \frac{\Delta_e}{h_{eff}} \tag{3.12}$$

The above equation can also be rearranged so θ_{gap} can be solved for given a total story drift, θ_{drift}.

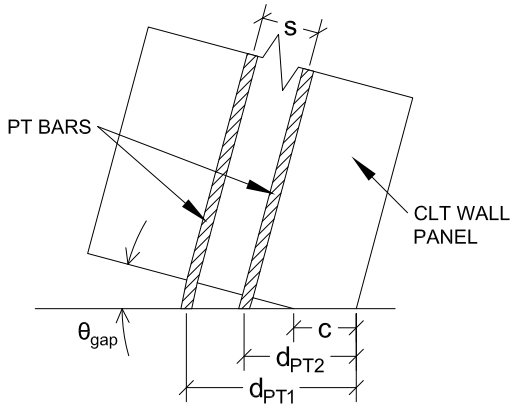

Figure 3.16: Gap rotation at base of wall after the decompression phase

3.5.2 Estimate Neutral Axis Depth

The next step of the cross-sectional analysis procedure is the estimate the neutral axis depth, c shown in Figure 3.16. This distance is iterated on until equilibrium in satisfied in the last step of the procedure (Section 3.5.5).

3.5.3 Solve for PT Tension Force

The next step is to solve for the new post-tensioning forces resulting from the gap rotation, θ_{gap} at the base of the wall. When the gap opens up at the base, the bars stretch by Δ_{PT}. To calculate the change in length, the small angle approximation is used with the equation:

$$\Delta_{PT} = \theta_{gap}(d_{PT} - c) \tag{3.13}$$

where d_{PT} is the distance between the corner of the wall and the location of the PT bars. It should be noted that if there are multiple PT bar locations, like that shown in Figure 3.16, then d_{PT} is different for each bar. In Figure 3.16, d_{PT1} would equal $\frac{1}{2}(L_w + s)$ and d_{PT2} would equal $\frac{1}{2}(L_w - s)$. The increase in length of the PT bars, increases the forces in the bars by, Δ_T. The increase in force is calculated by relating the change in length of the bars to the bar stiffness, k_{PT} with the following equations:

$$\Delta T = k_{PT}\Delta_{PT} \tag{3.14}$$

$$k_{PT} = \frac{A_{PT}E_{PT}}{L_{PT}} \tag{3.15}$$

where A_{PT} is the cross sectional area of the bars, E_{PT} is the modulus of elasticity of the PT bars, and L_{PT} is the length of the PT bars. Finally, the total force in each bar is calculated by adding the change in force to the initial PT force, T_o as shown in the following equation:

$$T = T_o + \Delta T \tag{3.16}$$

It should be noted that the set of equations presented in this section should be done for each location of the PT bar relative to the corner edge of the wall. Each location will experience a different change in length of the bars, resulting in a different total force. The total vertical force on the wall is then equal to the sum of all the PT forces, ΣT plus any additional gravity load.

3.5.4 Solve for CLT Compression Force

To determine the total CLT compression force, C the maximum strain experienced at the rocking corners of the wall panels is first determined using the monolithic beam analogy, originally developed by Pampanin et al. [2001]. The ultimate goal of this analogy is to determine a relationship between the maximum compression strain at the outermost fiber of the wall, ϵ_c and the neutral axis depth, c. The analogy relates the unbonded rocking behavior (Figure 3.17a) to the behavior of a typical monolithic wall with a plastic hinge (Figure 3.17b). Both the wall models have the same geometry and material properties so the analogy can relate the local unknown parameters of the walls to the equal global displacement behavior of the walls.

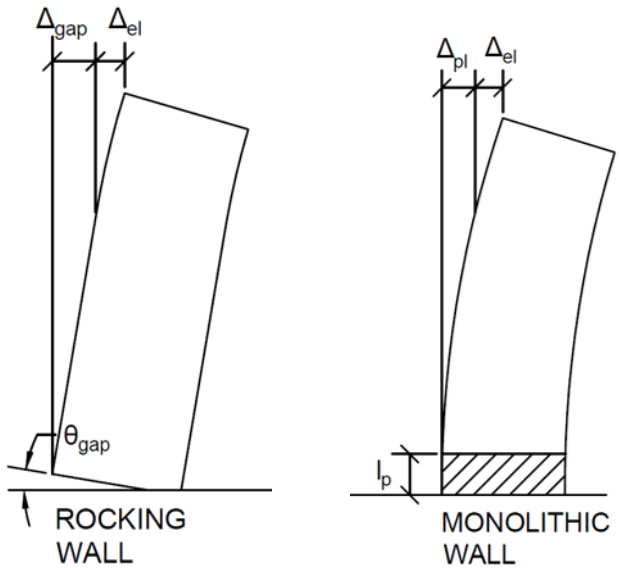

(a) Unbonded rocking wall (b) Monolithic wall

Figure 3.17: Monolithic beam analogy [Ganey, 2015]

As seen in Figure 3.17, an equal displacement is applied to the top of both walls (Equation 3.17). For both these walls, the total deflection is composed of an elastic and a plastic displacement (Equation 3.18). Because the geometry and material properties of the walls

are identical, the elastic deformations are assumed to be equal. This means the plastic deformation of the rocking wall, Δ_{gap} and the monolithic wall, Δ_{pl} are equal (Equation 3.19).

$$\Delta_{total(rocking)} = \Delta_{total(monolithic)} \tag{3.17}$$

$$\Delta_{gap} + \Delta_e = \Delta_{pl} + \Delta_e \tag{3.18}$$

$$\Delta_{gap} = \Delta_{pl} \tag{3.19}$$

The plastic displacement of the rocking wall, Δ_{gap} is determined by multiplying the gap rotation at the base by the height of the wall (Equation 3.20):

$$\Delta_{gap} = \theta_{gap} h_w \tag{3.20}$$

To determine the plastic deformation of the monolithic wall, a plastic hinge analysis is used. The plastic hinge length on the wall is defined as $2d_w$ as recommend by Akbas et al. [2017], where d_w is the thickness of the wall panels. The plastic displacement is defined as the plastic rotation, θ_{pl} multiplied by the distance between the top of the wall and the midpoint of the plastic hinge length (Equation 3.21), where θ_{pl} is the plastic curvature, ϕ_{pl} multiplied by the plastic hinge length (Equation 3.22). The ϕ_{pl} is defined as the total curvature, ϕ_{total}, minus the elastic curvature, ϕ_e (Equation 3.23). The total curvature is determined by dividing the unknown ϵ_c by the neutral axis depth (Equation 3.24). The elastic curvature is determined through basic mechanics by dividing the decompression moment by the modulus of elasticity of the wall, E_w and the moment of inertia of the wall, I_w (Equation 3.25). Finally, the previous five equations are combined to present an equation for the plastic deformation of the monolithic wall in terms of ϵ_c and c (Equation 3.26).

$$\Delta_{pl} = \theta_{pl}\left(h_w - \frac{l_p}{2}\right) \tag{3.21}$$

$$\theta_{pl} = \phi_{pl} l_p \tag{3.22}$$

$$\phi_{pl} = \phi_{total} - \phi_e \tag{3.23}$$

$$\phi_{total} = \frac{\epsilon_c}{c} \tag{3.24}$$

$$\phi_e = \frac{M_{dec}}{E_w I_w} \tag{3.25}$$

$$\Delta_{pl} = \left(\frac{\epsilon_c}{c} - \phi_e\right) l_p \left(h_w - \frac{l_p}{2}\right) \tag{3.26}$$

The next step of the monolithic wall analogy procedure is to combine the previous equations (Equations 3.19, 3.20, and 3.26) to get the final equation for ϵ_c in terms of the neutral axis depth as shown in Equations 3.27 - 3.29.

$$\theta_{gap} h_w = \left(\frac{\epsilon_c}{c} - \phi_e\right) l_p \left(h_w - \frac{l_p}{2}\right) \tag{3.27}$$

$$\frac{\epsilon_c}{c} - \phi_e = \frac{\theta_{gap} h_w}{l_p\left(h_w - \frac{l_p}{2}\right)} \tag{3.28}$$

$$\epsilon_c = \left(\frac{\theta_{gap} h_w}{l_p(h_w - \frac{l_p}{2})} + \phi_e\right) c \tag{3.29}$$

Now, with the maximum compression strain, ϵ_c at the outermost fiver of the CLT wall panel, the strain decreases linearly over the neutral axis depth until the strain equals zero at the decompression point. As discussed in 4.2.3, an elastic-perfectly plastic stress-strain relationship will be assumed over the neutral axis depth. The constitutive relationship between stress and strain is shown in 3.18 and represented by the piecewise function:

$$f_c(\epsilon_c) = \begin{cases} E_w \epsilon_c & \text{if } \epsilon_c \leq \epsilon_y \\ \epsilon_y & \text{if } \epsilon_c \geq \epsilon_y \end{cases} \tag{3.30}$$

where, E_w is the elastic modulus of the CLT panels, f_y is the yielding stress of the CLT panels, and ϵ_y is the yielding strain defined by the equation:

$$\epsilon_y = \frac{f_y}{E_w} \tag{3.31}$$

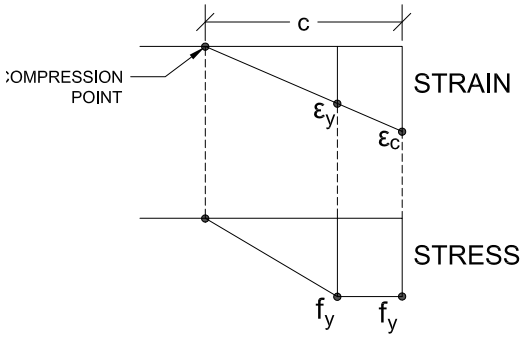

Figure 3.18: Stress and strain distrubtion present in the neutral axis depth

To compute the final compression force at the base of the wall, the stress curve in Figure 3.18 can be integrated under, over the length of the neutral axis depth, c, and multiplied by the thickness of the wall, b_w:

$$C = \int_0^c f_c(c) b_w dx \tag{3.32}$$

3.5.5 Satisfy Equilibrium

The final step of the cross sectional analysis procedure is to check for equilibrium and iterate on the neutral axis depth, c from Section 3.5.2 until equilibrium is satisfied. Figure 3.19 shows a free body diagram of the wall. The equilibrium equation in the vertical direction that must be satisfied is calculated as follows:

$$\sum_{1}^{n_{PT}} T + W = C \tag{3.33}$$

where n_{PT} is equal to the number of PT bars in the wall panel and T is the force in each bar. For each gap rotation, θ_{gap} the corresponding neutral axis depth, c is not correct until the equilibrium equation is satisfied. With the initial guess of c, both the compression force, C and the PT bar force, ΣT should be calculated, if equilibrium is not satisfied, then c should be adjusted until it is satisfied.

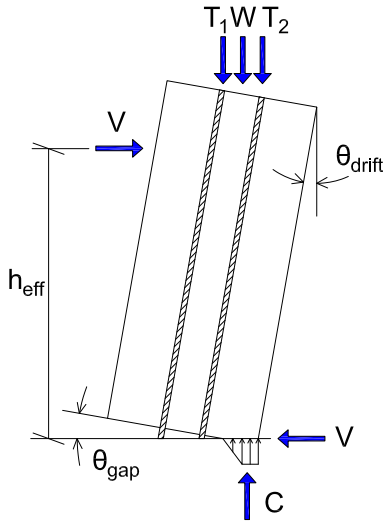

Figure 3.19: Equilibrium configuration of CLT rocking wall Panels

3.5.6 Determine Overturning Moment

Using the results of the cross-sectional analysis procedure, the resulting overturning moment for each imposed gap rotation, θ_{gap} can be determined through equilibrium. The resulting panel moment, M_{panel} is equal to the induced moment due to the PT forces, ΣT, the gravity load, W, and the compression force, C. This is calculated by summing the moments about the location of the compression force, C, as seen in Equation 3.34:

$$M_{panel} = \sum_{1}^{n_{PT}} T\left(d_{PT} - \overline{c}\right) + Wd \tag{3.34}$$

where d_{PT} is the distance from each bar to the corner of the wall as shown in Figure 3.16, $\overline{c}$ is the distance from the corner of the wall to the centroid of the compression zone, and d is the distance from the centroid of the wall to the centroid of the compression zone (i.e. $\left(\frac{L_w}{2} - \overline{c}\right)$).

An approximation for the base shear can be calculated by dividing base moment by the effective load height, h_{eff} as shown in the following equation:

$$V_{base} = \frac{M}{h_{eff}} \tag{3.35}$$

3.5.7 Application to Coupled Walls with UFPs

When using the cross-sectional analysis procedure with couple walls with UFPs, a few modifications and assumptions must be made to the presented procedure. With UFP coupled walls, the compression force at the base of the two walls will be slightly different because the force from the UFPs will increase the compression force in one wall, but decrease the compression force in the other wall. However, the force in the UFPs are significantly smaller than that of the PT bars, so the difference isn't very significant. Therefore, it will be assumed that the compression forces in the two walls are equal to simplify calculations. For

calculation purposes, this means the compression force, the PT forces, and the overall panel drift will be equal for the two panels as shown in the free body diagram in Figure 3.20. This process will be explained for two panels coupled together, but can be used for any number of panels coupled together.

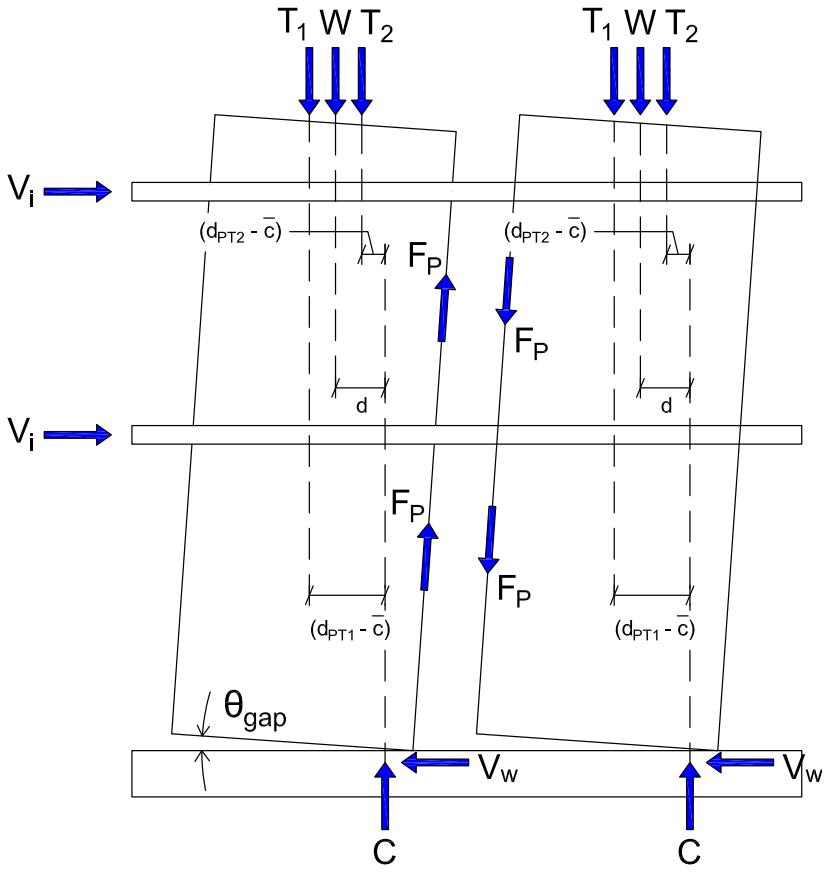

Figure 3.20: Coupled post-tensioned rocking wall free body diagram with single PT connection connection and multiple PT bars per panel

The first few steps of the cross-sectional analysis procedure will not change for coupled walls. A gap rotation can be imposed on one wall and the neutral axis depth can be estimated. The PT forces and the CLT compression force can be calculated as done before. The results from these steps can then be applied to both wall panels. To satisfy equilibrium, the force from the UFPs should be included in Equation 3.34, giving the new equation as shown:

$$\sum_{1}^{n_{PT}} T + W + \sum_{1}^{n_{UFPs}} F_P = C \tag{3.36}$$

The total moment in the wall can then be calculated by summing the base moments in each panel, M_{panel} and adding to that the additional moment from the UFPs which is calculated by summing the plastic force of the UFPs, F_p and multiplying by the width of the wall panel, L_w, as seen in the following equation:

$$M_{wall} = \sum_{1}^{n_w} M_{panel} + \sum_{1}^{n_{UFPs}} F_p L_w \tag{3.37}$$

Chapter 4

EXPERIMENTAL SPECIMEN DESIGN AND TEST SETUP

4.1 Overview

To better understand the performance and behavior of using rocking CLT walls as a lateral system in tall timber buildings, a full-scale two-story mass timber building with CLT rocking walls was tested at the NHERI@UCSD shake table at the University of California San Diego. The testing was performed as part of the sub-assembly testing task in the NHERI TallWood Project that is developing a seismic design methodology for tall wood buildings that will be validated through full-scale shake table testing of a ten-story CLT specimen in the summer of 2020. A key objective of this two-story test was to generate data on the behavior of important components that can be used to calibrate numerical models for future numerical simulation of the 10-story test specimen. In this chapter, the design and test setup will be discussed with emphasis on the rocking walls. Then, the construction and instrumentation of the specimen will be explained, followed by the testing plan used on the specimen.

4.1.1 Test Location and Shake Table Details

The full-scale two-story specimen was tested at the National Hazard Education Research Institute at University of California San Diego (NHERI@UCSD) uniaxial outdoor shake table. This laboratory hosts the largest outdoor shake table in the world, making it ideal for conducting a one of a kind test for the tall timber industry. The table measures 24.9 feet in the north-south direction and 40 feet in the east-west direction and shakes in the east-west direction. With the table empty, the table can reach a peak acceleration of 4.2g and with a 400 ton payload the table can reach a peak acceleration of 1.2g. The table has a total stroke length of +/- 2.5 feet.

4.1.2 Test Specimen Design Considerations

At the beginning of the NHERI TallWood Project, the researches collaborated with architects and practicing structural engineers to evaluate the potential market for tall wood buildings. The results of this discussion showed there is a market for mix use buildings for residential and commercial use with open floor plans that could be reconfigured with nonstructural walls. The overall geometry of the test specimen was not only controlled by the need for an open floor plan, but also by the desired aspect ratio of the diaphragm, and the size limitations of the shake table at UCSD. The aspect ratio of the diaphragm and CLT walls was designed to have a similar aspect ratio to a tall building.

Taking into account the design constraints, there were four key components of the test building as shown in Figure 4.1, that the research team wanted to investigate. Those components included: 1) a gravity framing design that could tolerate large lateral drifts without damage; 2) CLT diaphragms with and without a composite concrete deck; 3) resilient post-tensioned rocking CLT wall lateral system; and 4) a shear transfer mechanism connecting the rocking walls to the diaphragms. The overall structural design configuration was such that the lateral elements and the gravity systems were separated, as commonly adopted for concrete and steel high-rise buildings.

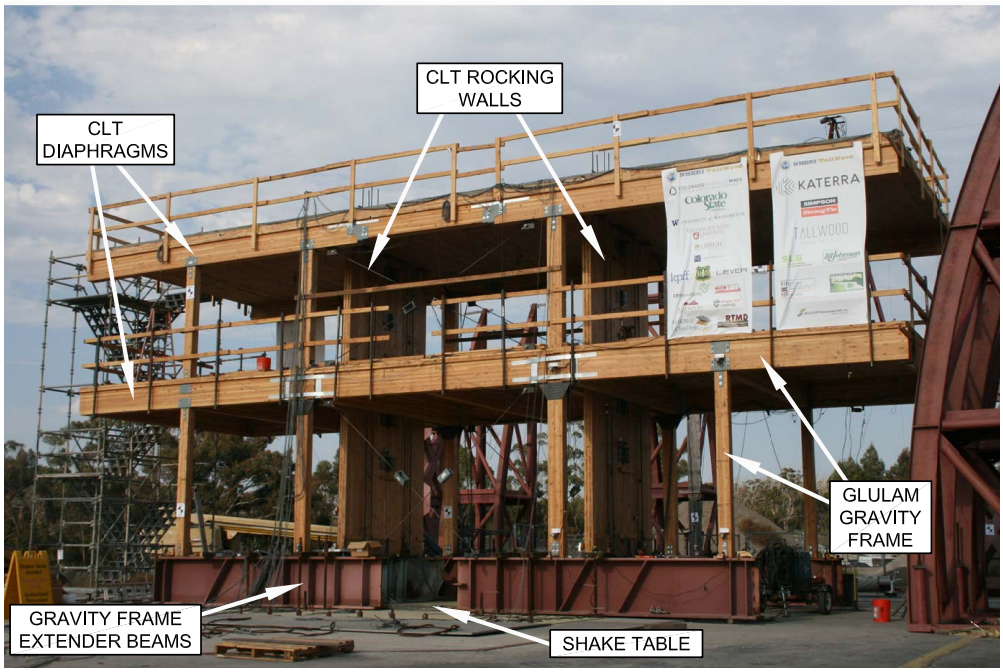

Figure 4.1: Photo of test building

4.2 Specimen Design and Test Setup

As seen in Figure 4.2, four steel foundation extender beams were connected to the shake table and cantilevered perpendicular to the direction of shaking to extend the width of table, allowing the structure to be larger in the direction perpendicular to shaking. The beams were securely anchored to the table using $1\frac{3}{4}$" Dywidag rods and additional braces were welded to the end of the cantilevers and braced back to the table to further prevent any motion of the extender beams. The columns were placed on top of these beams, raising the structure up. Because the gravity frame was raised the CLT rocking walls were placed on top of steel foundation base beams so the base of the walls could be at the same elevation as the base of the gravity frame. The wall base beams were also securely anchored to the shake table using post-tensioned rods and welding the bottom of the base beam to the table. The extender beams, the wall base beams, and the angled cantilever braces were used in previous projects at the shake table and were not fabricated specifically for this test.

(a) Plan view of layout

(b) Pieces used

Figure 4.2: Steel foundation pieces

As seen in Figure 4.3 the gravity frame consisted of glulam columns and beams with modified slotted pin connections to accommodate the increased drifts from the rocking walls. The first floor elevation was 12 feet from the foundation and the roof height was 10 feet from the first floor, giving a total roof elevation of 22 feet. The flexible first floor 3-ply CLT diaphragm and the 5-ply CLT and $2\frac{1}{4}$ inch concrete composite roof diaphragms measured 20 ft x 58 ft, each with two slots for the CLT post-tensioned rocking wall lateral system. The two 24 foot rocking walls each had two CLT panels, coupled together with five U-shaped flexural plate (UFP) energy dissipaters. The walls were connect to the diaphragm with a slotted shear key connection which allowed for rotational and vertical movement to decouple the diaphragm from the rocking walls. The walls were balloon framed and extended 2 feet above the roof diaphragm.

4.2.1 Gravity Frame

The gravity frame was designed in accordance to the U.S. National Design Specification for Wood Construction and consisted of glulam beams and columns. All structural timber

for the gravity frame was provide by the U.S. CLT manufacturer, DR. Johnson Lumber in Riddle, Oregon. The columns were all grade L2 and the beams were either 24F-Vf or 24F-V8. The gravity frame design was for typical office live loading of 50 psf and 20 psf for partitions. A dead load of 64 psf and 79 psf was used on the floor and roof respectively, to design the gravity system. Table 4.1 shows the load break down of the dead load. It should be noted that the same dead load was used as the seismic weight for design.

Table 4.1: Load break down of the seismic dead loads used for design

Load Description	Floor Seismic (psf)	Load Description	Roof Seismic (psf)
2" Gypcrete	19	2.25" Concrete	30
3-ply CLT panels	12	5-ply CLT panels	20
Glulam beams	8	Glulam beams	4
Glulam columns	1	Glulam columns	1
CLT walls	0	CLT walls	0
Partitions	10	Partitions	10
Miscellaneous	14	Miscellaneous	14
Total	64	Total	79

A total of eight columns supported the gravity load of the structure that were designed using both balloon and platform framing concepts to investigate the feasibility of connections for both framing techniques. Column A and column B in Figure 4.3 show the balloon and platform style framing respectively. The four columns closest to the center of the building were continuous through the diaphragm, demonstrating platform framing, while the others were separated by the floor diaphragm, demonstrating platform framing.

Figure 4.4 shows the layout of the glulam beams and columns that made up the gravity frame of the structure. Table 4.2 lists and describes each of the members used. The glulam beam grid under the CLT floor had six 10 foot spans that spanned in the direction of shaking. The glulam beam grid under the concrete CLT composite roof had just one 20 foot span, spanning the width of the building in the direction perpendicular to the direction of shaking.

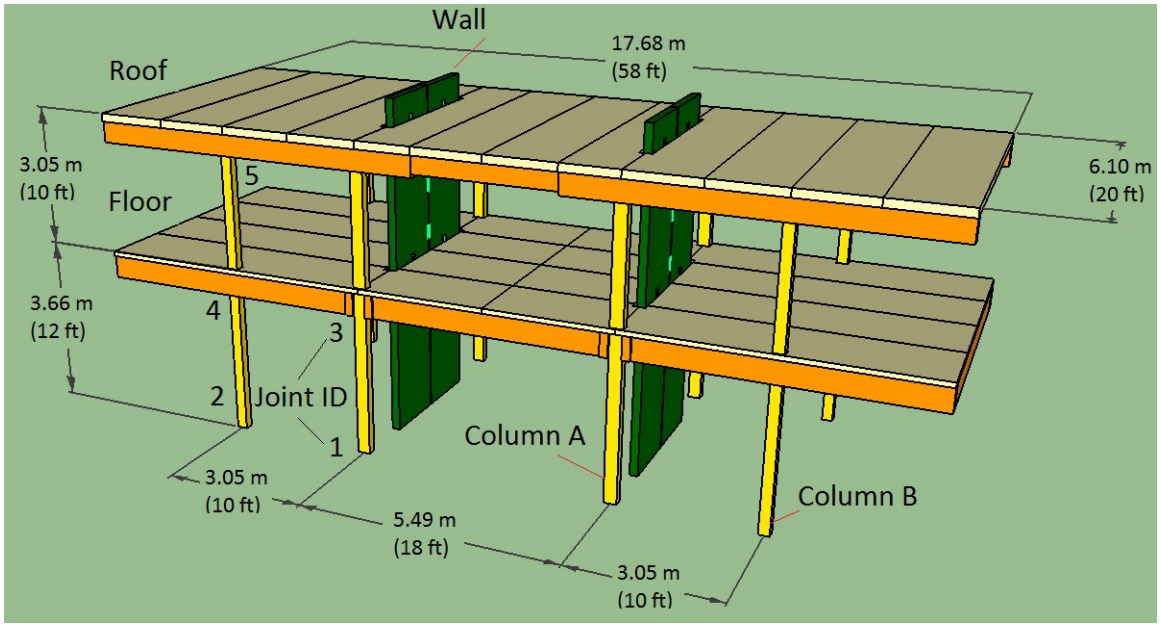

Figure 4.3: Design configuration of test structure [Pei et al., 2018]

These spans were determined to satisfy defection and vibration requirements in the CLT floors for the design office occupancy. CLT strength requirements typically do not control the design.

The gravity frame connections between beams and columns and at column bases and tops utilized vertically slotted details to prevent the gravity frame from engaging in moment transfer, minimizing the damage to columns, beams, and joints under large lateral drifts. Five different types of gravity frame connections were used in the structure, most of which utilized commercially available connectors with some modifications to accommodate joint rotation during earthquakes. The locations of these different joints can be seen in Figure 4.3 and each will be described in detail next. It should be noted that considerations for joint fire protection was not incorporated into these details as that was outside the scope of this study.

As seen in Figure 4.3, two types of column base connections, denoted with joint ID 1 and 2, were used in the test building. Figures 4.5 and 4.6 show the connections for joint 1 and

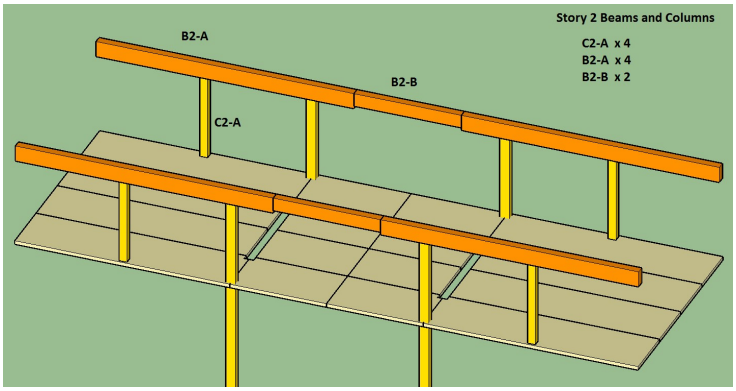

(a) Roof

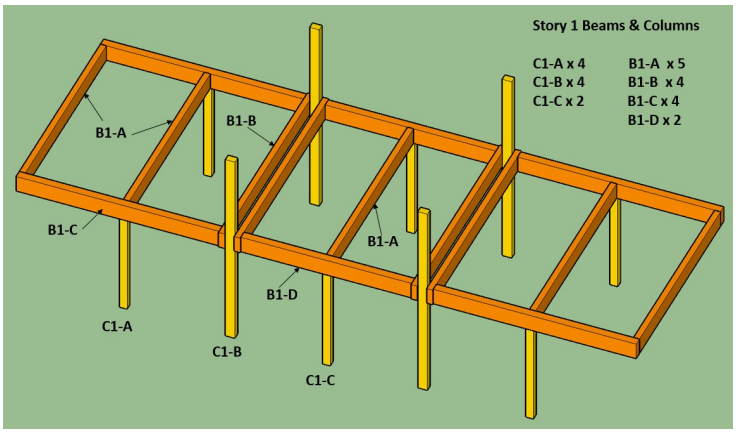

(b) Floor

Figure 4.4: Glulam column and beam layout

Table 4.2: Glulam gravity frame members used in the test structure

Type	Name	Quantity	Level	Grade	Dimensions
Column	C1-A	4	Floor	L2	7.5” x 8.75” x 10’ 3/8”
	C1-B	4	Floor	L2	7.5” x 10.75” x 19’ 11 1/8”
	C1-C	2	Floor	L2	7.5” x 8.75” x 10’ 2 7/8”
	C2-A	4	Roof	L2	7.5” x 8.75” x 7’ 11 1/8”
Beam	B1-A	5	Floor	24F-V4	6.75” x 19.5” x 18’ 3 1/4”
	B1-B	4	Floor	24F-V4	6.75” x 19.5” x 20’
	B1-C	4	Floor	24F-V8	8.75” x 19.5” x 18’ 11 7/8”
	B1-D	2	Floor	24F-V8	8.75” x 19.5” x 15’ 11 3/4”
	B2-A	4	Roof	24F-V8	8.75” x 18” x 24’
	B2-B	2	Roof	24F-V4	8.75” x 15” x 10’

and joint 2 respectively. These column base connections consisted of a $\frac{3}{8}$” steel plates, fillet welded to the gravity frame extender beams on all sides. Simpson Strong-Tie 3 gauge side straps with 1-$\frac{1}{2}$” long vertically slotted holes were fillet welded to two sides of the base plate. $\frac{3}{4}$” A325 through bolts were installed at the bottom of the four or two vertically slotted holes for joints 1 and 2 respectively to prevent moment transfer.

As mentioned before, the gravity framing connections were designed to rock at the beam-column joints to accommodate the larger inter-story drifts and both balloon and platform framing techniques were used. From Figure 4.3 joint 3 is a balloon framed beam-column joint for the two story continuous columns. Figure 4.7 shows this connection in detail. This connection consisted of a custom designed through column platform paired beam seating connection. This connection has two trapezoidal steel plate that connect to either side of the columns with $\frac{1}{4}$” Simpson Strong Tie screws. steel plates are welded to the trapezoidal pieces and act as a platform for the collector beams that end at the column face. Steel rods welded to the steel plates, extrude into the beams to prevent the beams for falling off the platform. In addition, typical Simpson Strong-Tie girder hangers were installed, connecting the collector beams to the exterior beams. This connection was inspired by a design by

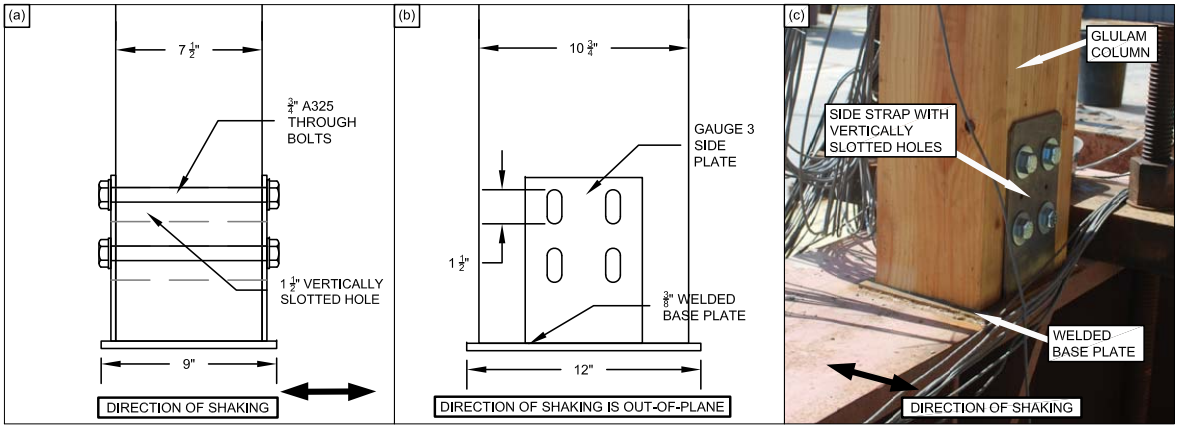

Figure 4.5: Gravity frame connection joint 1 (a) side view schematic (b) exterior view schematic (c) photo showing constructed connection

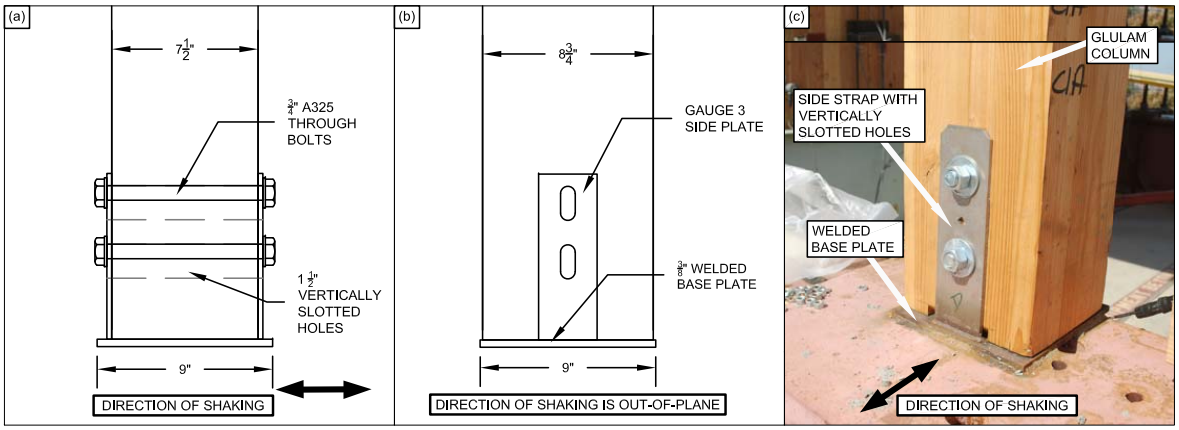

Figure 4.6: Gravity frame connection joint 2 (a) side view schematic (b) exterior view schematic (c) photo showing constructed connection

KPFF Consulting Engineers, an industry partner on the project, for the proposed Glenwood CLT Parking Garage project in Springfiled, Oregon and the proposed Framework Project in Portland, Oregon [Zimmerman and McDonnell, 2018]. This connection was designed to permit shear transfer of diaphragm forces during simultaneous uplift of the CLT rocking walls. Note that in Figure 4.7 the direction of shaking is indicated. Connection rocking (or relatively free rotation between the beams and columns) occurs between the collector beams and the columns in the direction of shaking. In the orthogonal direction, rotation is more restrained to provided some resistance to accidental torsion.

From Figure 4.3 joint 4 is a platform framed beam-column connection for the first floor non-continuous columns. This joint can be seen in detail in Figure 4.8. These connections are modified standard Simpson String-Tie column caps with extended side straps. The extended side straps each have two 1-$\frac{1}{2}$" long vertically slotted holes for $\frac{3}{4}$" A325 through bolts. The through bolts connecting the second floor column were installed at the bottom of the slotted holes and bolts for the first floor column were installed at the top of the vertically slotted holes to allow for joint rotation at the top of the column. To connect the collector beam to the exterior beam, $\frac{3}{4}$" bolts were installed into non-slotted holes in the column cap. Joint 5 is also a platform framed beam-column connection as seen in Figure 4.9 and is used at the top of all the columns on the roof. This connection consists of the same column cap configuration from the second floor column in joint 4, but an additional angle brace is added. The angle brace connects to side of the column cap and braces to the bottom of the roof diaphragm to prevent the beam from falling. It is connected to the diaphragm using $\frac{1}{4}$" Simpson Strong-Tie SDS screws.

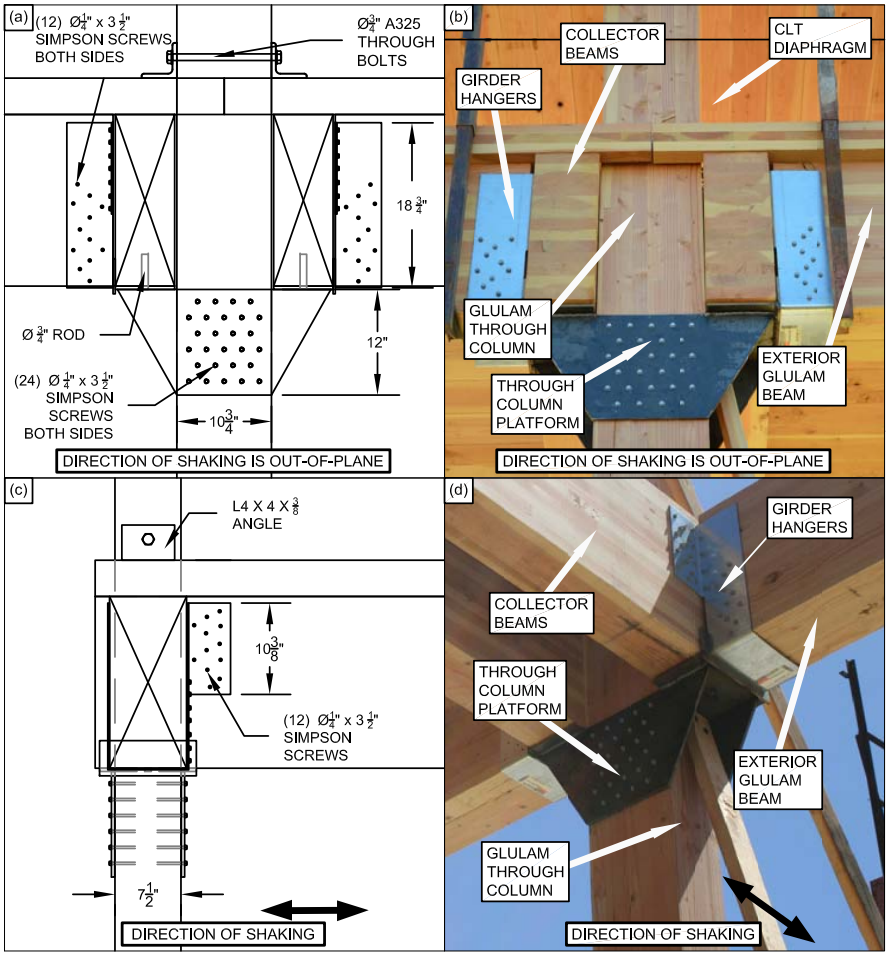

Figure 4.7: Gravity frame connection joint 3 (a) exterior view schematic (b) exterior view photo (c) side view schematic (d) side view photo

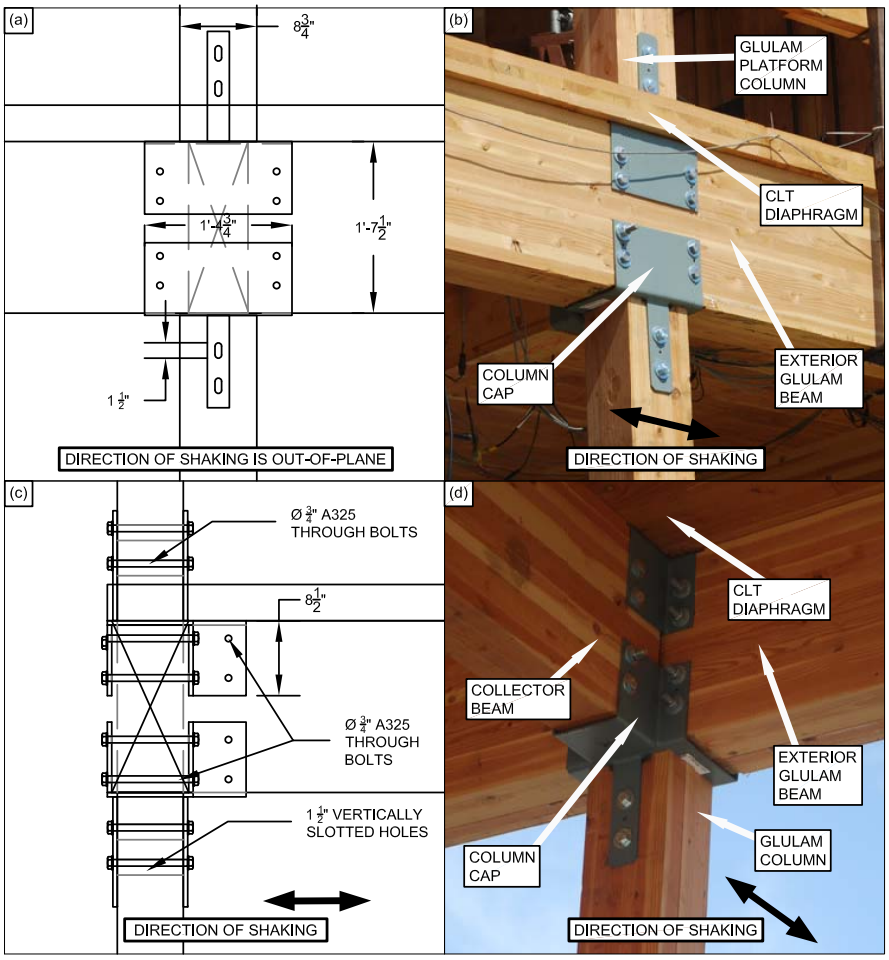

Figure 4.8: Gravity frame connection joint 4 (a) exterior view schematic (b) exterior view photo (c) side view schematic (d) side view photo

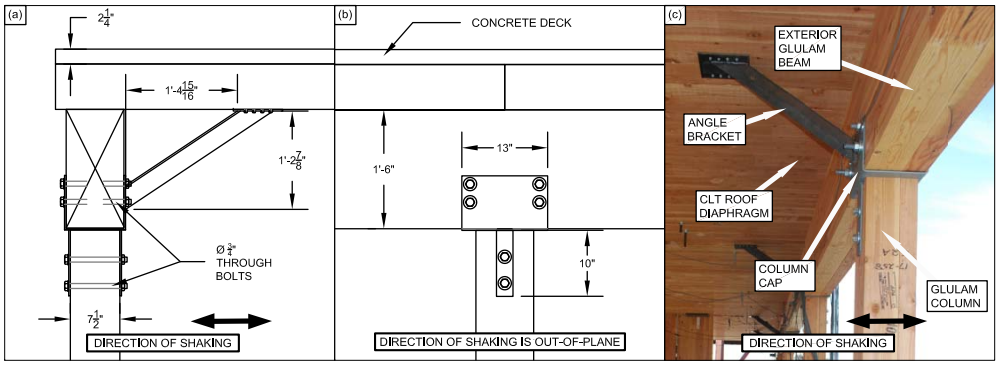

Figure 4.9: Gravity frame connection joint 5 (a) side view schematic (b) exterior view schematic (c) photo

4.2.2 Diaphragm

The CLT used for the diaphragm panels was also supplied by DR Johnson. The panels were certified as Grade V1 base on APA standard PRG320 [APA, 2017]. The floor and roof diaphragms were designed to be damage-free under the planned seismic excitations. As seen in the diaphragm panel layout in Figure 4.10, the panels on the roof spanned the whole 20 foot width of the structure, in the direction of shaking. On the floor, the panels spanned in the direction perpendicular to shaking. The two spans on each end were 10 feet and the two middle spans were each nine feet. Different panel sizes were created to create these layouts. Table 4.3 summarizes each of the sizes of CLT panels used for the diaphragms. A brief discussion of the diaphragm design and details will be presented in this section. A more detailed discussion is presented in DeMeza [2018].

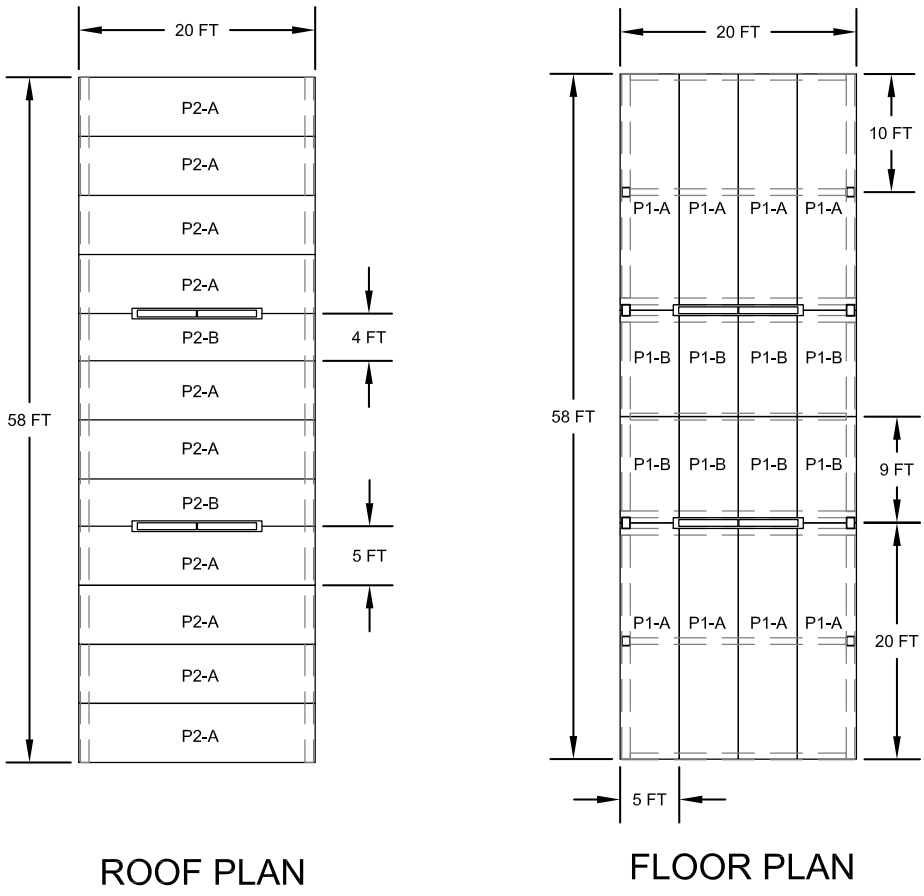

Figure 4.10: CLT panel layout on roof and floor levels

Table 4.3: CLT diaphragm panels used in test structure

Name	Quantity	Level	Ply	Grade	Dimensions
P1-A	8	Floor	3 ply	V1	20’ x 5’
P1-B	8	Floor	3 ply	V1	9’ x 5’
P2-A	10	Roof	5 ply	V1	20’ x 5’
P2-B	2	Roof	5 ply	V1	20’ x 4’

The roof and floor CLT diaphragm panels were fastened to the glulam girders below

through a series of Simpson Strong-Tie structural screws. The CLT panel joints were constructed following typical CLT top spline floor splice details with pre-routed panel edges covered with plywood strips with shear transfer from structural screws as seen in Figure 4.11. A shear demand calculation was conducted to determine the number of Simpson Strong-Tie structural screws needed for shear transfer across the panel splices. Chord connectors were placed perpendicular to the panel splines to transfer the chord tensile forces over the panel joints. The chord connectors were custom sized ASTM A36 steel straps fasted to the CLT using Simpson Strong-Tie self-tapping screws. These straps were designed in accordance with principles of mechanics using values of fastener and member strength in accordance with test results available in the US 2015 Nation Design Specification (NDS) for Wood Construction. To meet the requirements for continuity of the diaphragm tension chords, only the strength of the fasteners in the chord straps were considered, the fasteners in the roof and floor spline joints and floor to beam connections were not included.

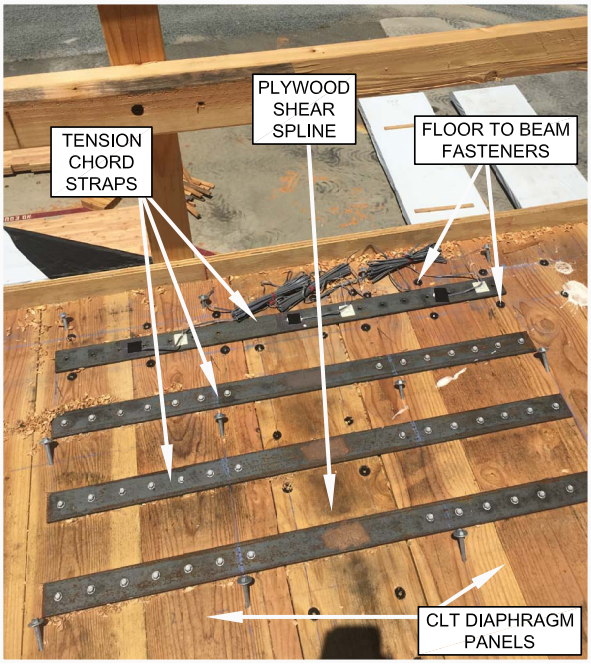

Figure 4.11: Typical detail for diaphragm panel spline

The design of the concrete CLT composite roof diaphragm was conducted based on earlier testing of similar composite floors at Oregon State University [Higgins et al., 2017] and with basic principles of mechanics. The shear transfer between the 2-$\frac{1}{4}$ inch concrete topping and the 5-ply CLT diaphragm was achieved using Simpson String-Tie wood screws installed at 45° and protruding from the CLT floor by approximately 1-$\frac{3}{8}$ inches as shown in Figure 4.12. These shear studs were designed to ensure composite action between the concrete and CLT in order to handle the larger 20 foot span on the roof. In addition to the shear studs, the concrete topping was reinforced to prevent shrinkage cracks. A large space near the walls was left without concrete in order for the wall to diaphragm connection to be installed.

Figure 4.12: Shear screws used for CLT concrete composite deck on the roof

4.2.3 Post-Tensioned CLT Rocking Walls

The designs of the two walls in the structure were identical. Each wall consisted of two CLT rocking wall panels coupled together with five UFP energy dissipating devices and were post-tensioned with four bars on each wall panel. The CLT post-tensioned rocking walls were designed using the performance-based design procedure outlined in Chapter 3, but used the the modified performance objectives described below. The walls were designed to meet the seismic demands computed per ASCE 7-10 [ASCE, 2010] for a Class B soil site in San Francisco, California. Figure 4.13 shows the resulting design spectrum used. A seismic force reduction factor, R of 6, an importance factor of 1.0, and the approximate period per ASCE 7-10 were used to complete the calculation of equivalent lateral force demands used in the design procedure in Chapter 3. It should be noted that accidental torsion was not included in this calculation. The design values used were:

- Mapped spectral acceleration parameters: $S_S = 1.77g$ $S_1 = 0.67g$
- MCE_R spectral acceleration parameters: $S_{MS} = 1.59g$ $S_{M1} = 0.54g$
- Design spectral acceleration parameters: $S_{DS} = 1.06g$ $S_{D1} = 0.34g$
- Approximate Fundamental Period: $T_a = 0.20s$

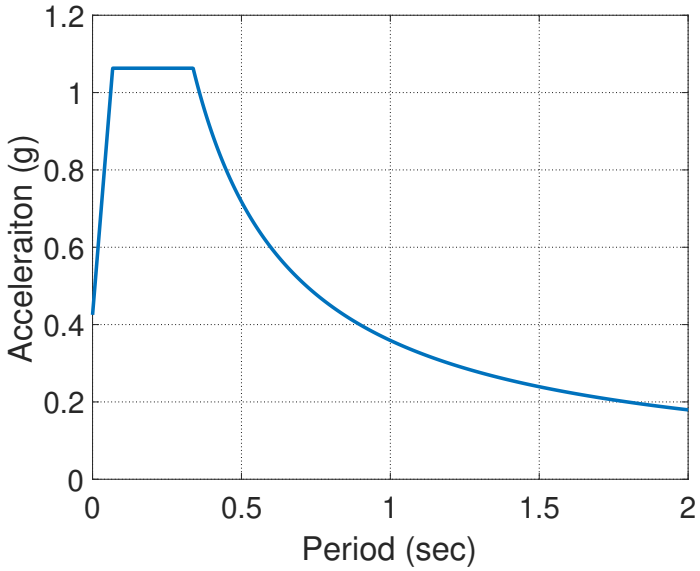

Figure 4.13: Design spectrum used to complete the seismic demands per ASCE 7-10

Modified Performance Objectives

Chapter 3 discusses the suggested performance objectives for the design of post-tensioned, rocking CLT walls per Ganey [2015]. Figure 4.14 summarizes the modified performance objectives that have been changed from the original performance objectives presented in Figure 3.10. For the design of the CLT rocking walls in the full-scale two-story test, these performance objectives were slightly modified. First, the earthquake hazard levels at two performance objective were modified, in order to conform to the recently released alternative design procedure for tall buildings in Los Angeles, California [LATBSDC, 2018]. The hazard level for performance objective 2 (immediate occupancy) was changed to an earthquake representing a 50% probability of exceedence in 30 years (43 year return period) and the hazard level for performance objective 4 (collapse prevention) was changed to an earthquake representing, MCE_R, the maximum considered earthquake per ASCE 7-10 [ASCE, 2010].

Other modifications made to the performance objectives were related to when the first occurrence of UFP yielding, PT yielding, and CLT wall crushing happens. First, because

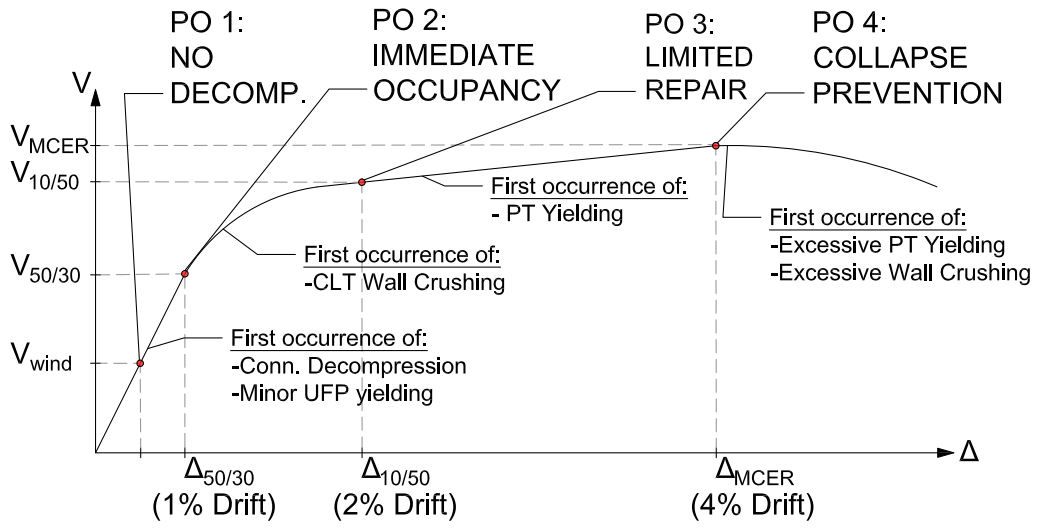

Figure 4.14: Modified performance objectives used for the design of the rocking walls in the full-scale two-story shake table test

the structure is smaller relative to a typical building, the UFPs were also smaller so minor UFP yielding was allowed at lower drifts and during SLE tests. It was expected for UFPs to yielding around the same time as decompression. Second, in the original performance objectives, it is suggested that CLT wall crushing precedes PT bar yielding and both occur after 4% drift. However, because the walls were only 24 feet tall and the structure was small relative to a typical building, PT bar yielding after 4% drift was unrealistic. Due to this constraint, the performance objectives were modified for the design of this test. The new performance objectives were to still have CLT crushing precede PT bar yielding, but to allow the first occurrence of minor CLT wall crushing to happen after the SLE tests at 1% drifts and to have the first occurrence of PT bar yielding after DBE tests at 2% drift.

Predicted Performance of the CLT Rocking Walls

For the design details described below, the behavior of the CLT rocking walls was predicted, using the methods described in Chapter 3, to have a response that met the modified performance objectives. Table 4.4 shows the general predicted moment-drift response of the

specimen with major events called out and Figure 4.15 shows the corresponding plot with the major events identified. A detailed example of the design calculations completed for the response of the building at 1% drift can be seen in Appendix A. Similar calculations for a full range of drifts between 0% and 5.5% to determine the response.

Table 4.4: Summary of perdicted design moment-drift response

Roof Drift	M_{wall} (kip-in)	V_{base} (kip)	Event
0.1%	3365	14.7	M_{demand}
0.2%	3731	16.3	M_{dec}
1.0%	5805	25.3	-
1.3%	6326	27.6	Onset of CLT crushing
2.0%	7490	32.7	-
2.1%	7573	33.1	Onset of PT yielding
3.0%	7999	34.9	-
4.0%	8052	35.2	-
5.0%	8053	35.2	-

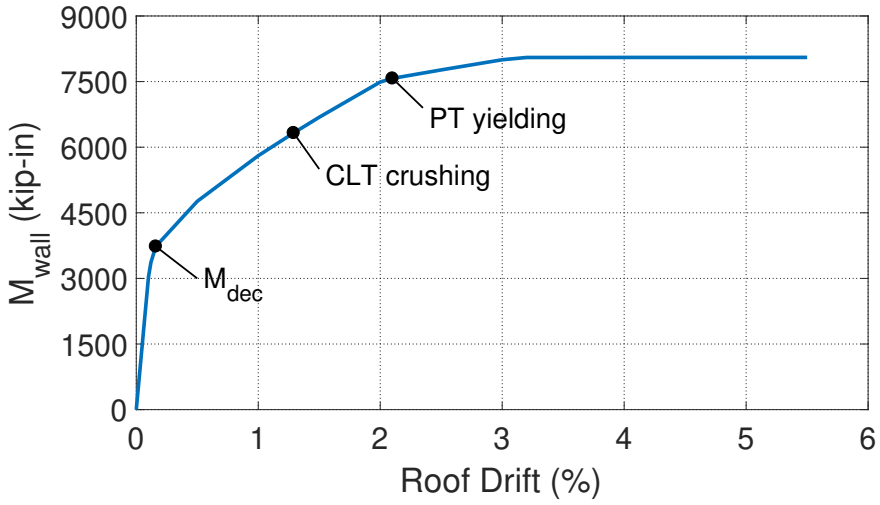

Figure 4.15: Predicted design performance of rocking CLT wall system based on design calculations

CLT Wall Panels

The 24 foot tall post-tensioned rocking walls were balloon framed such that they extended 2 feet above the roof elevation to allow for easy installation of the post-tensioning. The four CLT wall panels were also manufactured by DR. Johnson and were all 5-ply grade E2-M1. Each wall panel was 5 ft x 24 ft and were manufactured with both the shear key transfer slots and the cutouts for the UFP connections.

The material properties used for the CLT panels in design were based off results from compression testing on DR. Johnson CLT panels at at Oregon State University [Barbosa et al., 2018]. Five 5-ply Douglas-fir Larch CLT panels (18 inches wide, 6.8 inches thick, and 60 inches long) were tested under compression loading. Load and displacement data over a 48 inch gauge length were recorded at the first onset of yielding, the peak load, and the onset of delamination, which will be taken as crushing. Table 4.5 shows the mean results from the in-plane compression tests.

Table 4.5: Summary of compression test results from Barbosa et al. [2018]

	Load (kips)	Disp. (in)[a]
Yielding	444	0.141
Peak Load	473	0.181
Crushing	434	0.268

[a]Measured over 48" gauge length

The results from the test can be used to characterize an equivalent stress-strain relationship of the panels. Even though the results show a slight decrease in stiffness after yield as seen in Figure 4.16, an assumed elastic perfectly plastic relationship was used for a simplified design. From these results, the material properties used for the constitutive model of the CLT wall panels were as follows:

- Modulus of elasticity: $E_w = 1238\ ksi$

- Yield stress: $f_y = 3.627\ ksi$
- Crushing strain: $\epsilon_{crush} = 0.0056\ \frac{in}{in}$

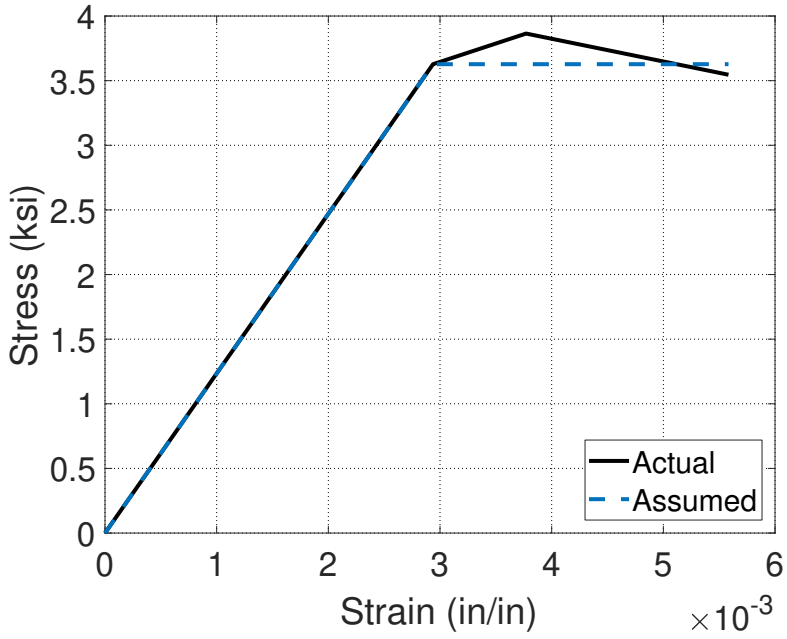

Figure 4.16: Stress-strain relationship for CLT panels based on test data from Barbosa et al. [2018]

Post-Tensioning Bars

The PT bars used were ATS high-strength, fully-threaded, 3/4" diameter rods manufactured by Simpson Strong-Tie. The listed yield stress and ultimate stress were 92 ksi and 120 ksi respectively. A combination of 8 foot and 10 foot long bar segments were used to span the whole length of the wall. CNW3/4 ATS-HSC66 high strength coupler nuts were used to attach the rod segments. The coupler nuts had the same material properties as the PT bars and were designed so even yielding could occur over the whole length of the bar assembly.

Each bar was initially stressed to $0.39f_{pu}$ which results in an initial PT bar force of 12 kips per bar.

The PT bars were anchored to the top of the wall with a fabricated A572 steel post-tensioning saddle. The saddle was constructed out of a 1 inch thick, 36 inch long, and 16 inch wide steel anchor plate with four $\frac{13}{16}$" diameter holes for the PT bars. A $\frac{1}{2}$" thick steel top plate was filet welded perpendicular to the top of the plate and $\frac{1}{2}$" stiffeners were filet welded to these pieces to create a strong bearing box that would not yield from the PT forces. Four $\frac{1}{2}$" hanger plates were CJP welded perpendicular to the other face of the anchor plate to form the saddle for the top of the wall. Each hanger plate had 14 holes used to attach the saddle to the face of the wall with Simpson Strong-Tie structural screws. At each hole location, a load cell was placed around the PT bars and between two $\frac{7}{8}$" thick 5" x 8.5" Simpson Strong-Tie bearing plate on the top of the anchor plate in the saddle. A nut and washer secured the top of the PT bar. At the base of the wall, a 4 inch thick steel post-tensioning plate was welded on all sides to the base plate. The post-tensioning plate had two tapped holes to anchor the PT bars. A $\frac{1}{2}$" steel guide plate was CJP welded to the top of the post-tensioning plate to ensure the wall would not get caught on the top face of the plate if it lifted far enough up. The welds and thickness of the plate were all calculated to resist the max forces expected in the PT bars with a safety factor.

UFP Energy Dissipation Devices

The two CLT wall panels were coupled together with five UFP energy dissipating devices. Figure 4.17 shows the details of each UFP connection. The edge of each wall panel had five small cutouts for the UFP. The bottom cutout started six feet from the base of the wall and the top cutout started 3'-1" from the top of the wall and the three other cutouts were spaced roughly evenly between. The locations of the UFPs were chosen so they were spaced as evenly as possible while avoiding diaphragm locations to make installation easier. To attach each UFP to the wall, a saddle was created by filet welding two $\frac{1}{2}$" side plates perpendicular to a $\frac{3}{4}$" in UFP plate. The saddle was mounted to the CLT wall panels with 45° MyTiCon

self-tapping timber screws and washers ($\frac{5}{16}$" diameter 6-$\frac{1}{4}$" long SWG ASSY VG CSK Screws and $\frac{5}{16}$" VG CSK 45° wedge washers). Once the saddles were secured to the wall, the walls were lifted into the building, then the UFPs were attached with non-structural $\frac{1}{2}$" diameter bolts to the UFP plate that had four tapped holes. The number and dimensions of the UFP plates were chosen to provide a minimum energy dissipation ratio, β, or 0.3, which is consistent with recommendations from Seo and Sause [2005]. The dimensions of the UFPs used (shown in Figure 3.3a) were as follows:

- Diameter: $D_u = 3\frac{5}{8}$ inches
- Width: $b_u = 4\frac{1}{2}$ inches
- Thickness: $t_u = \frac{3}{8}$ inches

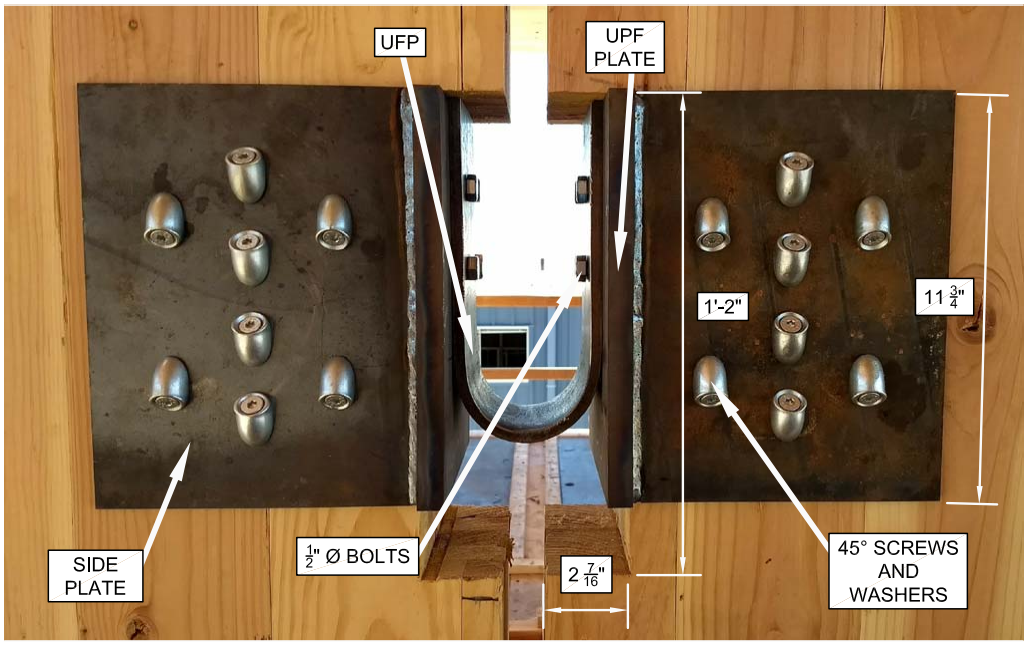

Figure 4.17: UFP energy dissipater connection

Base Beam Setup

Figure 4.18 shows the setup of the rocking wall base beam. During the tests, when the wall rocked, shear force was transferred from the wall panels to the base beam though two shear transfer angles located on both ends of the wall. The shear transfer angles were custom angles made of two 5-$\frac{1}{2}$" x 10" x $\frac{1}{2}$" steel plates welded along the longer edges to form a 75° angle to prevent the wall panels from hitting against the face of the angles while rocking. The shear transfer angles were connected to the base beam with a filet weld on the three faces of the angle not in contact with the wall. To prevent out-of-plane movement of the CLT walls at the base, 6 inch long L4x4x$\frac{1}{2}$ steel angles were filet welded longitudinally to the base beam along all sides except the one in contact with the wall. An out-of-plane angle was placed on either side of the PT bar connection on each face of the wall panel. Finally, a 10 inch long 3" x $\frac{1}{2}$" plate was filet welded in the 1 inch gap between the walls to prevent any possible movement of the walls during the test.

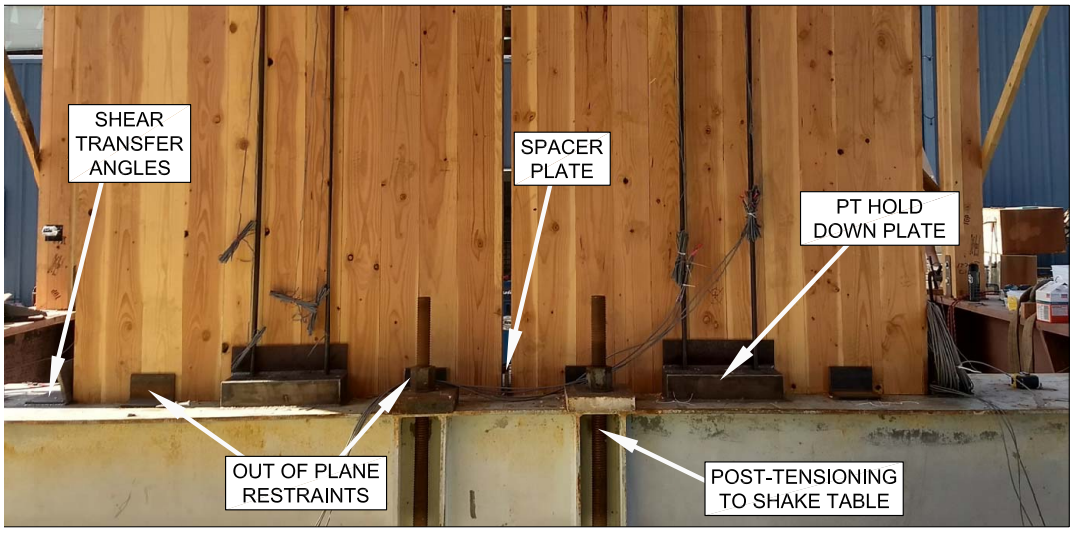

Figure 4.18: UFP energy dissipater connection

4.2.4 Wall to Diaphragm Connection

The rocking wall lateral system was connected to the diaphragm using the shear key connection detail shown in Figure 4.19. This connection was design to be similar to that shown in Figure 3.5 (c). This connection was originally designed for the proposed Framework project in Portland, OR [Zimmerman and McDonnell, 2018]. This connection was designed to transfer shear forces between the diaphragms and the rocking shear walls while keeping the diaphragm level at all times by allowing uplift of the wall panel relative to the diaphragm. The connection was designed based on the estimated rocking wall capacity at 4% drift with an additional safety factor of 1.5. As seen in the figure, the steel tongue plate was inserted into a vertically slotted hole to create a slotted pin connection which allowed for vertical and rotational movement to decouple the diaphragm from the rocking walls. The steel shear key was fabricated A572 steel and with rounded edges to accommodate the rocking motion. To transfer the load from the tongue plate to the diaphragm, the steel tongue plate was bolted with A490 bolts to a thick steel wing plate with tapped holes. The A572 steel wing plate was connected to the CLT diaphragm with 45° MyTiCon timber screws and washers to prevent torsional rotation of the wing plate. In addition to the 45° screws, Simpson Strong-Tie self-tapping screws were used to secure the plate to the diaphragm. $\frac{1}{4}$ inch thick A572 steel collector plates ran along the whole width of the diaphragm, parallel to the walls were attached to the diaphragm using Simpson Strong-Tie screws.

The tongue plate was inserted into a vertically slotted hole in the wall which was surrounded by A572 steel edge plates. Side plates were field PFP welded to the two sides of the edge plate and attached to the walls with Simpson Strong-Tie screws. The portion of the steel tongue inserted into the wall was wrapped in a thin teflon sheet to limit the potential for friction at the interface. The overall assembly was designed to be snug to prevent any slip between the tongue plate and the edge plate, but lose enough to allow the rotation of the walls. It was designed to have only a $\frac{1}{16}$ inch gap. On the other side of the wall, the tongue plate was not connected to the diaphragm. The end of the tongue plate had two tapped

holes where a cap plate was bolted with A490 bolts onto the end to prevent any sliding out of the tongue plate from the slot. This connection was designed as a cantilevered system to represent the worst-case scenario for the shear keys. This configuration represents a condition where the wall are placed on the exterior of the building, therefore, the connections used are larger relative to those needed for the case of the shear key connected to the diaphragm edges on each side of the wall panels.

At the intersection of the roof and floor diaphragms and the rocking shear walls, out-of-plane bracing of the walls was also provided through a series of angles to reduce the unbraced length of the walls and prevent buckling. Several 15 inch long 6x4x$\frac{1}{2}$" A36 steel angles were lined with stainless steel on the 4 inch side and placed at the edge of the diaphragm so the stainless steel face of the angle was snug against the face of the CLT panel which was lined with a teflon strip. The interface between the stainless steel and the teflon was greased to limit friction and the angles were attached to the diaphragm with at least seven self-tapping MyTiCon screws ($\frac{5}{16}$" diameter x 4-$\frac{3}{4}$" SWG ASSY VG CSK). The strength of these braces were designed so the screws resist a shear strength equal to 5% of the total maximum estimated compression force from the PT bars. 5% of the max compressive strength was used as a conservative estimate from the 2% suggested by AISC in steel design. Each wall panel required two out-of-plane brace angles on each side at each diaphragm level, resulting in 32 total angles used in the test specimen. At the floor diaphragm level, these angles were installed on the top of the CLT diaphragm panels, but because of the concrete deck on the roof, the angles were installed on the bottom of the CLT diaphragm panels.

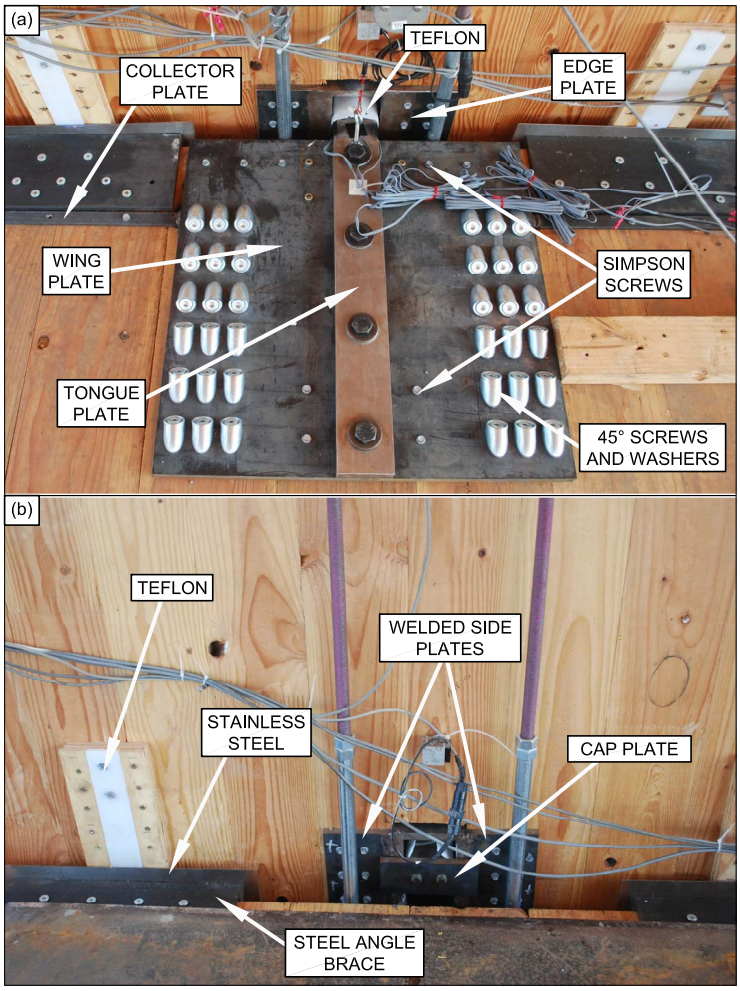

Figure 4.19: Photos of shear key connection (a) front view (b) back view with out-of-plane restraint details

4.2.5 Seismic Mass

Because the test building did not include non-structural components, the self weight of the CLT and concrete was not enough to achieve the intended design seismic mass. Figure 4.21 shows the additional mass that was added in the form of large steel trench plates. Each plate was approximately 4 ft x 8 ft x 1 in and weighed about 1.6 kips. To bring the total weight of the building up to the design weight, 22 plates were added and secured to the roof diaphragm and 48 plates were added and secured to the floor diaphragm. The plates were secured to the diaphragms using a grid built by dimension lumber. The wood grid was cut across the diaphragm splices to avoid artificially strengthening the diaphragm. The process was used previously used in large scale timber tests [van de Lindt et al., 2010] and was proven to be successful. The layout of the seismic mass plates can be seen in Figure 4.21.

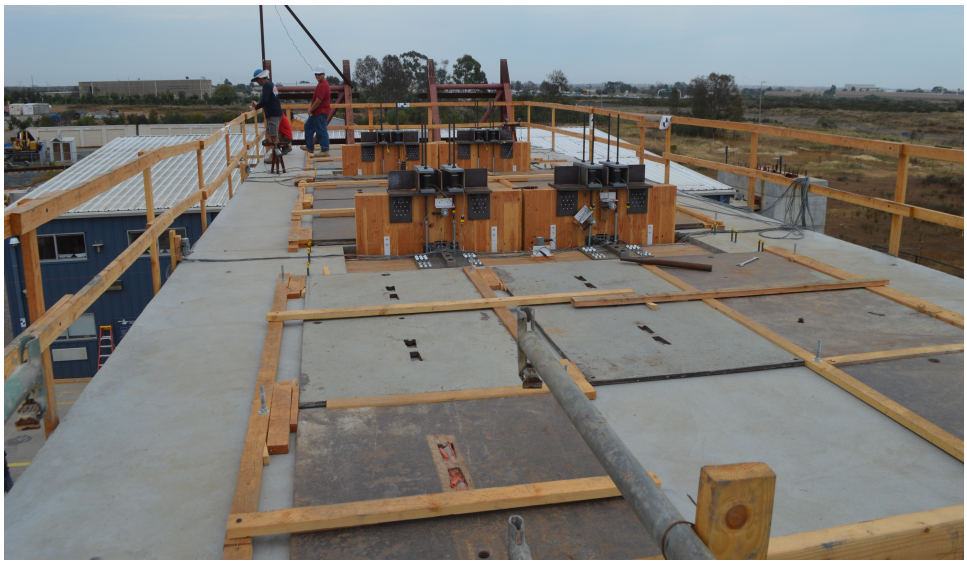

Figure 4.20: Photo of additional seismic mass on the roof held down by the wood grid

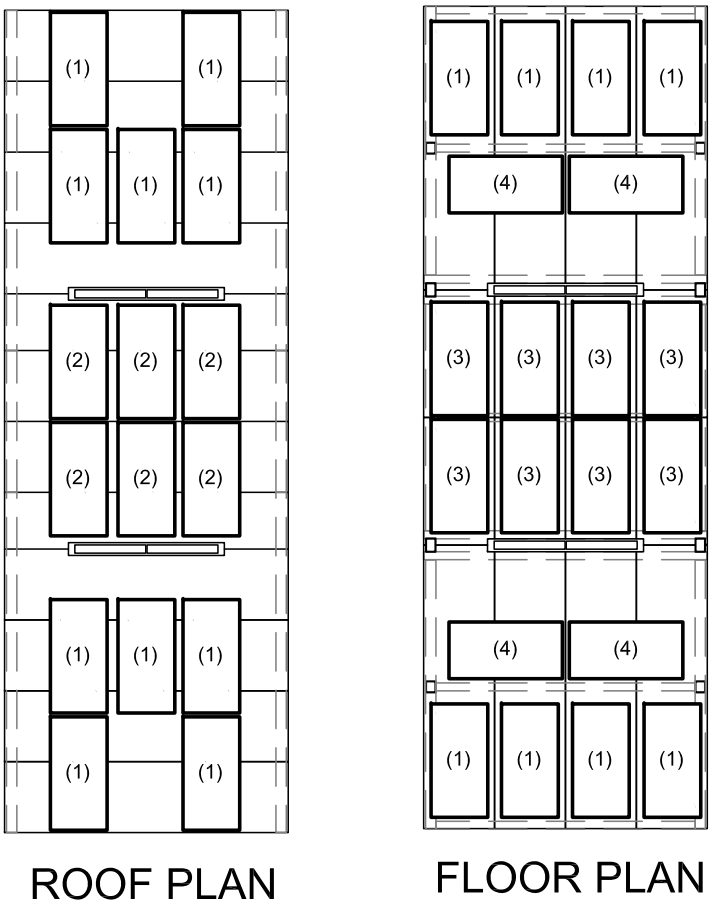

Figure 4.21: Arrangement of the additional seismic mass on the roof and the floor

4.3 Construction of Test Building and Walls

Because the CLT wall and diaphragm panels and the glulam beams and columns were all prefabricated and arrived on site precut to the correct dimensions, the overall installation was relatively fast. Figure 4.22 shows the constriction sequence of the first phase of construction, gravity frame and placement of the steel seismic mass plates. This first phase of construction took only four days to complete with a very small construction crew of about four people. The precut beams and columns were all lifted into place with an on site crane, and the connections were installed. Next, the CLT floor diaphragm panels were lifted in place and installed with the correct spline and tie details and then the floor seismic mass plates were placed on top of the CLT and secured. Finally, the remaining roof columns and roof CLT diaphragm panels were lifted into place. Figure 4.23 shows a brief outline of the second phase of construction, the diaphragm preparation and concrete work for the composite roof deck which took about one week to complete. Once all the splines and ties were complete on the roof, the 45° composite screws were installed. Next, a contracted concrete crew installed the concrete rebar and pour the concrete deck. Once the concrete had cured, seismic mass plates were lifted into place with the crane and secured to the roof trough a series of holes that were left in the concrete deck.

Figure 4.24 shows the construction sequence for the final phase of construction, the post-tensioned CLT rocking wall installation. First, all the base beam connections were welded to the base beam prior to lifting the walls into place with the crane. Next, the PT bar saddles were put into the place, the PT bars were connected to the base and strung the length of the wall, and the tongue was put into place. When the walls were lifted into place, the UFP saddles were already installed on the walls, but the actually UFP plates were not attached until the wall panels were in the specimen. Finally, once all the wall connections were complete, the instrumentation was installed, and the walls were post-tensioned. The initial PT force was small enough to be tensioned by hand with a large wrench. The bars were tensioned two at a time, on opposite faces of the wall to avoid creating torsion in the

building. In addition, all bars were first tensioned to 50% of their full stress, once all bars were at 50%, they were stressed fully and the specimen was ready for testing. The final phase of construction, not including the instrumentation set up, took only about two days to complete.

Figure 4.22: Gravity frame construction sequence (a) beam and column gravity frame (b) floor diaphragm panels (c) floor seismic mass (d) roof diaphragm panels

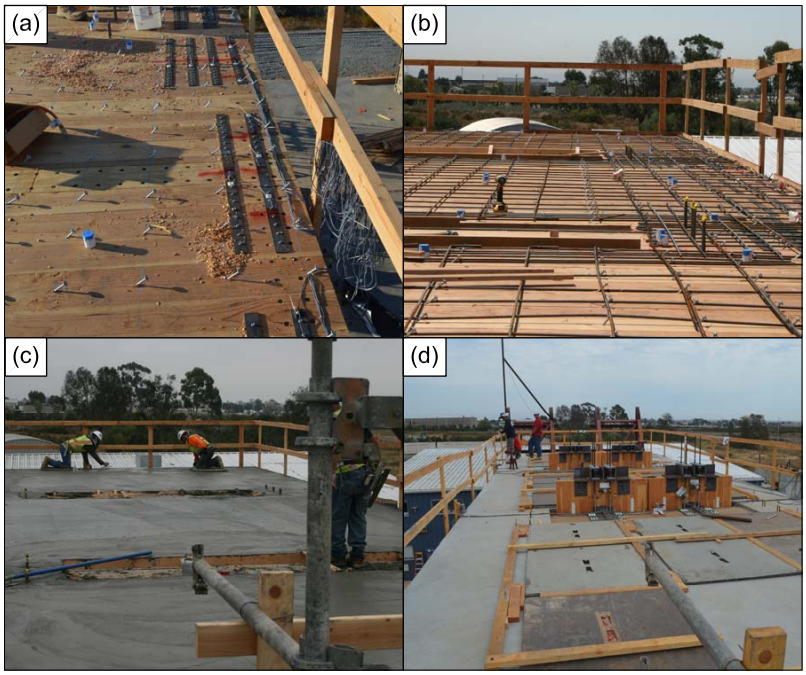

Figure 4.23: Concrete composite deck construction sequence (a) shear studs and diaphragm splines and ties (b) rebar (c) concrete pour (d) finalized deck with seismic mass

Figure 4.24: Rocking wall construction sequence (a) base beam connections (b) wall installation (c) PT saddle and tongue connection (d) wall without UFPs installed (e) post-tensioning (f) completed specimen

4.4 Instrumentation

A total of 357 instruments were used on the structure for data collection. About 250 of these instruments were used to measure either the overall movement of the structure or measure the movement of the walls specifically. The other instruments were used to measure diaphragm movements and will only be discussed briefly. Table 4.6 summarizes all the instruments used during the test.

The NHERI@UCSD facilities were equipped with a data acquisition system based on the National Instruments PXI platform. The facility had eight SCXI-1520 Signal Conditioning modules that each had 64 channels, resulting in a total of 512 available for use. However, one of the modules was not working while conducting the test, limiting the total number of channels available for use. Because of this, all of the desired measurements could not done. In addition to limited equipment, some of the sensors and recorders malfunctioned during the test, causing some loss in data for the tests. The data acquisition system described is controlled with a Windows XP software running the LabView application. The whole system was synchronized with the shake table controller and the PC based video recording system. With a 16-bit differential analog to digital converter, the National Instruments data acquisition system used LabView to convert measured voltages to displacements and strains. Instrument calibration factors were already calculated by the crew at UCSD and were inputted into the system. Data was recorded and stored at 240 Hz (240 measurements per second). A combination of load cells, linear potentiometers, Duncan potentiometers, string potentiometers, strain gauges, and accelerometers were used to measure the movements of the specimen.

The load cells used to monitor the PT bar forces were noncommercial and provided by Lehigh University. The linear potentiometers were MLS130 sealed linear sensors made by Penny and Giles. Multiple lengths, including 50, 100, 150, and 200 millimeter stroke potentiometers were used depending on what the instrument was being used for. The typical accuracy of the linear potentiometers ranged between 0.15% for shorter stroke potentiometers

to 0.07% for longer stroke potentiometers. The Duncan Potentiometers were model 9600 Miniature Spring Return Linear Motion Position Sensors made by the Duncan Electronics Division at BEI Technologies, inc. The available stroke lengths were 10, 22.8 and 39.6 mm and had an accuracy of about 2%. The string potentiometer were PT8101 Cable-Extension Position Transducers made by Celesco Transducer Products. 2, 5, 10, 20, 25, 30, and 50 inch stroke string potentiometers were available for use and had an accuracy of 0.25%. The strain gauge models were YFLA-5-7LT from Tokyo Sokki Kenkyujo CO. Ltd. They had a gauge length of 5 millimeters and a gauge factor of 2.11 with an accuracy of 2%. Finally, the accelerometers were 4000A Silicon Mems accelerometers with a full range of 10G from measurement specialties and had an accuracy of 5%.

Table 4.6: Summary of instrumentation on test building

Location	Instrument Type	Quantity	Measurement
Global	String pot.	10	Absolute horizontal displacement of diaphragms
Global	String pot.	12	Absolute vertical displacement of diaphragms
Global	String pot.	8	Displacement between wall panels and diaphragms
Global	Accelerometer	39	Floor and roof acceleration
Global	Accelerometer	24	Rocking wall acceleration
Global	Accelerometer	11	Base of structure and table acceleration
Wall	Load cell	16	PT bar load
Wall	Strain gauge	24	PT bar strain
Wall	Linear pot.	20	Wall panel uplift at base
Wall	String pot.	8	Wall deformation/ Uplift
Wall	String pot.	4	Wall deformation/ Axial
Wall	String pot.	4	Wall deformation/ Shear
Wall	String pot.	12	Shear key movement within wall panels
Wall	Strain gauge	24	Shear key strain
Wall	String pot.	6	UFP deformation
Wall	Linear Pot.	10	Wall panel spacing
Column	String pot.	16	Column rocking
Diaphragm	Linear pot.	14	Relative slip between diaphragm and glulam gravity frame
Diaphragm	Linear pot.	25	Relative disp. between adjacent CLT diaphragm panels
Diaphragm	Linear pot.	14	Relative slip between adjacent CLT diaphragm panels
Diaphragm	String pot.	2	CLT diaphragm deformation
Diaphragm	Strain gauge	40	Diaphragm shear transfer strap strain
Diaphragm	Duncan pot.	12	Slip between CLT diaphragm and concrete deck
Diaphragm	Strain gauge	2	Concrete rebar strain

4.4.1 Global Response of the Building

To measure the global response of the structure, as seen in Figure 4.25a, long stroke string potentiometers were used to measure the displacement between the diaphragm and fixed structures located off the shake table. Only six long stroke string potentiometers were available on site so three were spaced along each of the two diaphragms levels to measure global displacement in the direction of shaking. Two shorter stroke string potentiometers were placed on the other side of each of the diaphragms to measured global displacement in the direction perpendicular to shaking. These were also connected to fixed structures located off the shake table. Because of the limited long stroke potentiometers, the global displacement of the walls could not be measured directly, but string potentiometers measuring in the direction of shaking and perpendicular to shaking were used to measure the relative displacement between the wall panels and the diaphragm. In addition to the string potentiometers described above, accelerometers were used to measure the global response of the structure. As seen in Figure 4.25b, accelerometers were placed at seven locations on the roof and the floor diaphragms. Each of these locations had accelerometers measuring in the direction parallel and perpendicular to the shaking to capture the horizontal movement of the structure and any torsional movement that occurred. Vertical accelerometers were also placed at each of the corners of the diaphragm to capture any flapping motion at the ends of the cantilevered diaphragms.

Figure 4.26 shows the typical layout accelerometer layout for the wall panels. Each wall panel had five accelerometers spaced relatively even along the height of the structure to measure horizontal movement of the walls. The accelerometers at the base of the wall also had an accelerometer measuring vertical movement. Finally, a triaxial accelerometer was placed on the table to verify table feedback readings and horizontal accelerometers were placed on top of the beams supporting the wall to capture any movement or rocking that could have occurred.

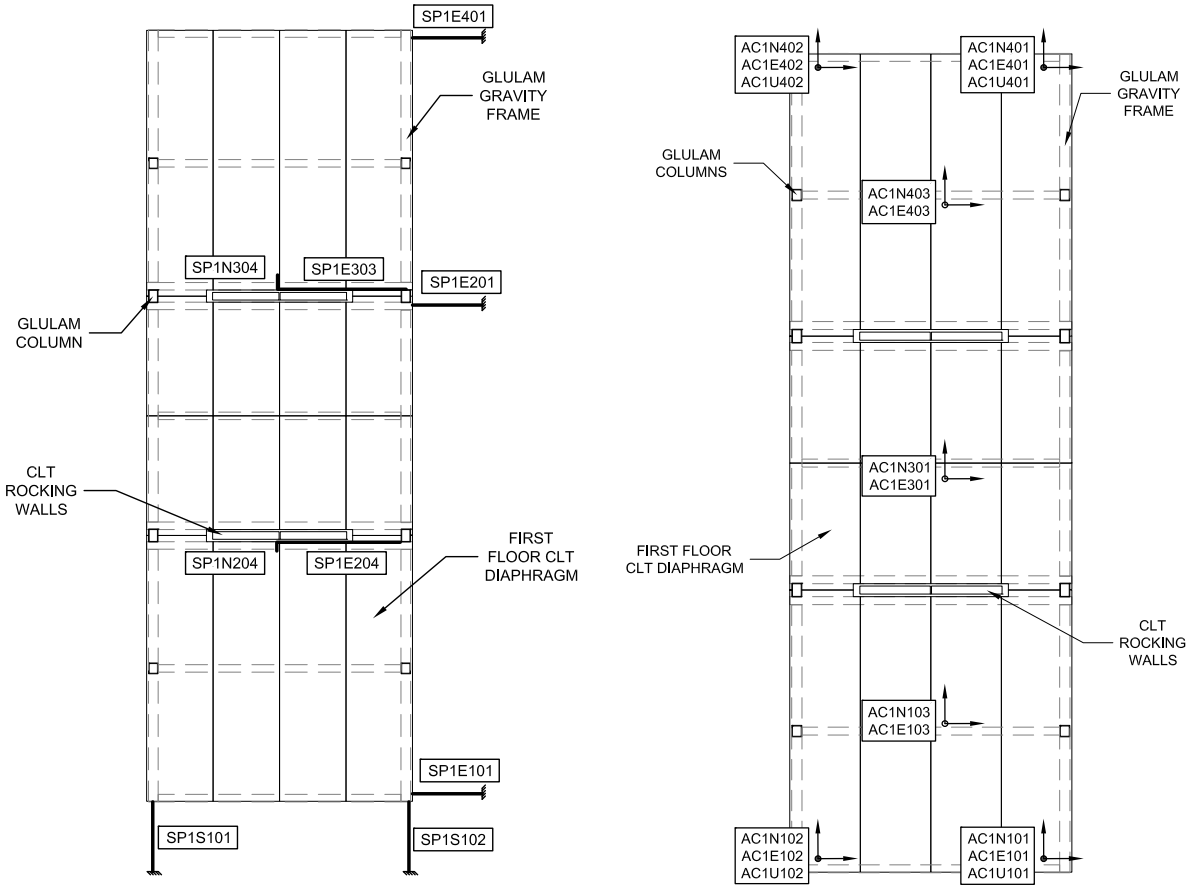

(a) String potentiometers (b) Accelerometers

Figure 4.25: Typical locations of sensors on the first floor

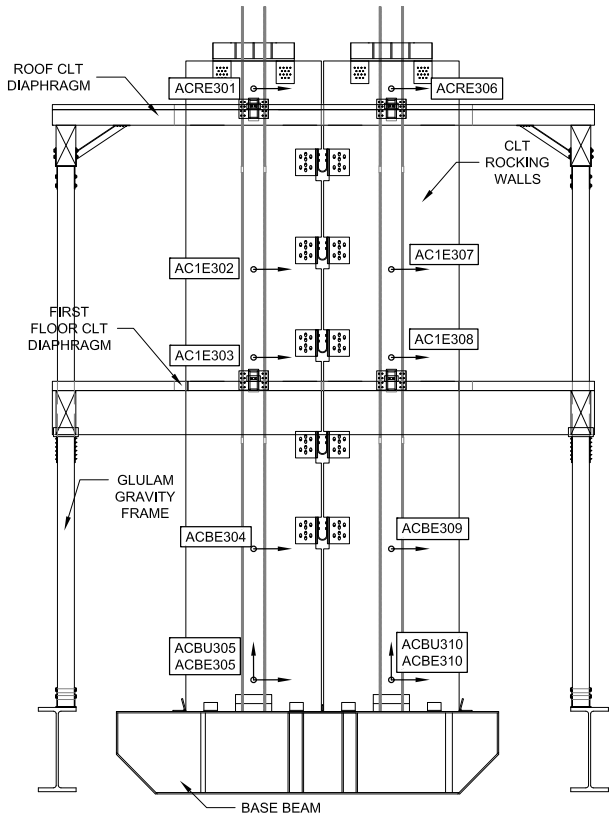

Figure 4.26: Typical location of accelerometers installed on the rocking walls

4.4.2 CLT Rocking Walls

Figure 4.27 shows the instrumentation layout for the load cells that were used to measure the force in the post-tensioning bars. The 6 inch tall load cells with outside diameters of 3.25 inches and an inside diameters of about 2.75 inches were placed between two Simpson Strong-Tie bearing plates that were 5 inches by 8.5 inches and $\frac{7}{8}$" thick. The load cells and bearing plates were then placed around each of the 16 post-tensioning bars at the top of the structure on the wall saddles and secured with a washer and nut. The bars were left un-tensioned until all instrumentation was complete and then the bars were tensioned after all the instruments were zeroed. Because the force in the post-tensioning bars was crucial to the test, back-up strain gauges were placed on the PT bars to measure the force in the bars if the load cells malfunctioned during the test. Because the load cells performed as expected, the strain gauges on the post-tension bars were not used.

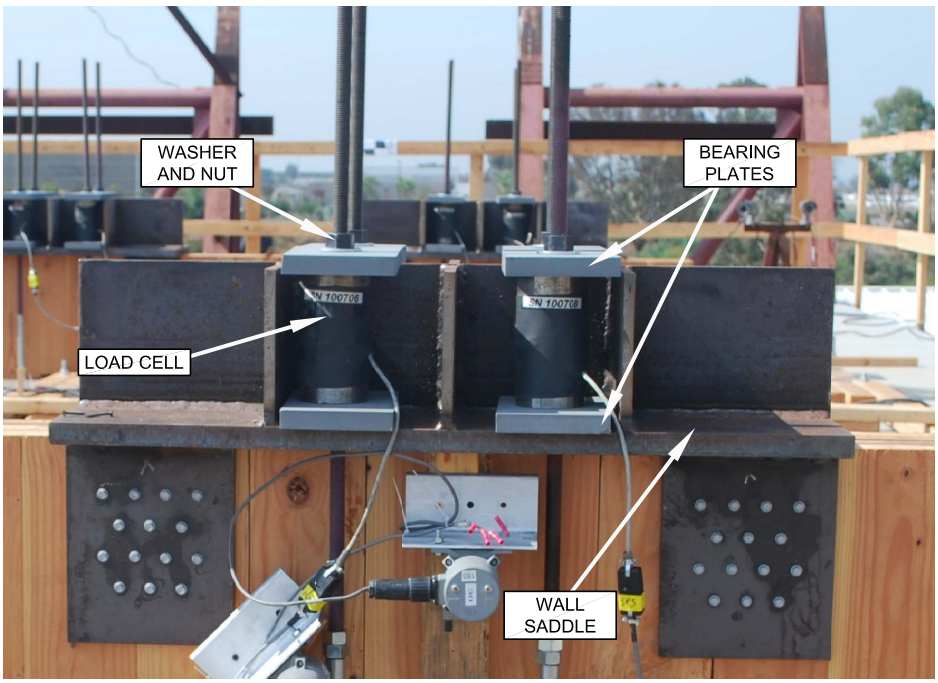

Figure 4.27: Typical load cells to measure force in PT bars

At the base of one face of two of the four wall panels, a series of six string potentiomenters

were installed as shown in Figure 4.28. The lower two string potentiometers were mounted about 17 inches vertically from the base beam and orientated diagonally to measure gap opening at the opposite corner. The four upper string potentiometers were placed higher up on the wall to measure deformations with in the panels. Two string potentiometers were mounted 35 inches vertically from the base beam and orientated vertically to measure axial deformation within the panels. Another two string potentiometers were mounted at the same location but orientated diagonally to measure shear deformations in the panel.

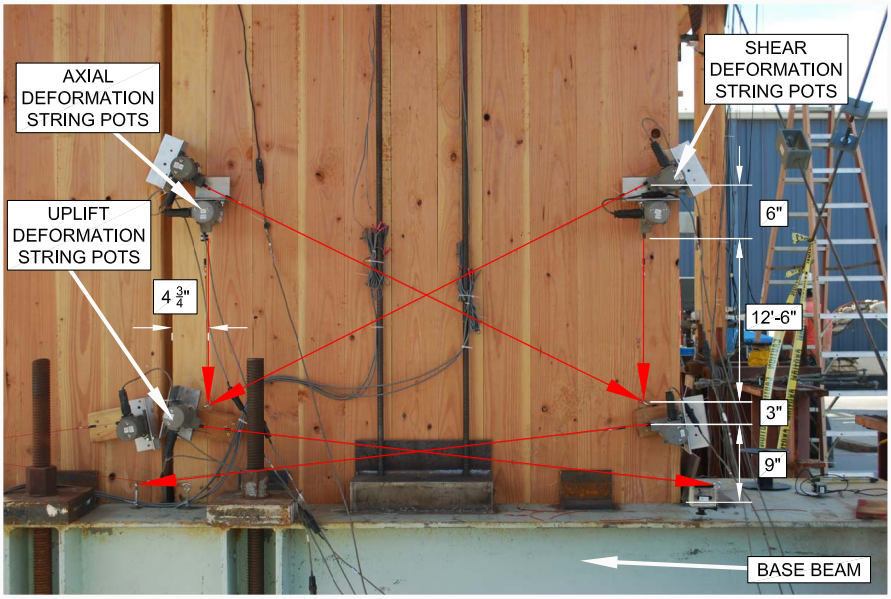

Figure 4.28: Typical layout of string pts to measure wall rocking and deformation

At the base of the other face of two of the four wall panels, Figure 4.29 shows how a series of eight linear potentiometers were mounted about 9 inches above the base beam and orientated vertically and connected to the base beam. They were placed at locations along the base of the wall that did not interfere with the welded wall supports or post-tensioning at the base. These instruments were intended to measure the uplift and any wall crushing along the base. On the other two walls that did not have this configuration, a modified set

up was installed using only two linear potentiometers. These two linear potentiometers were placed at each of the corners to measure the uplift.

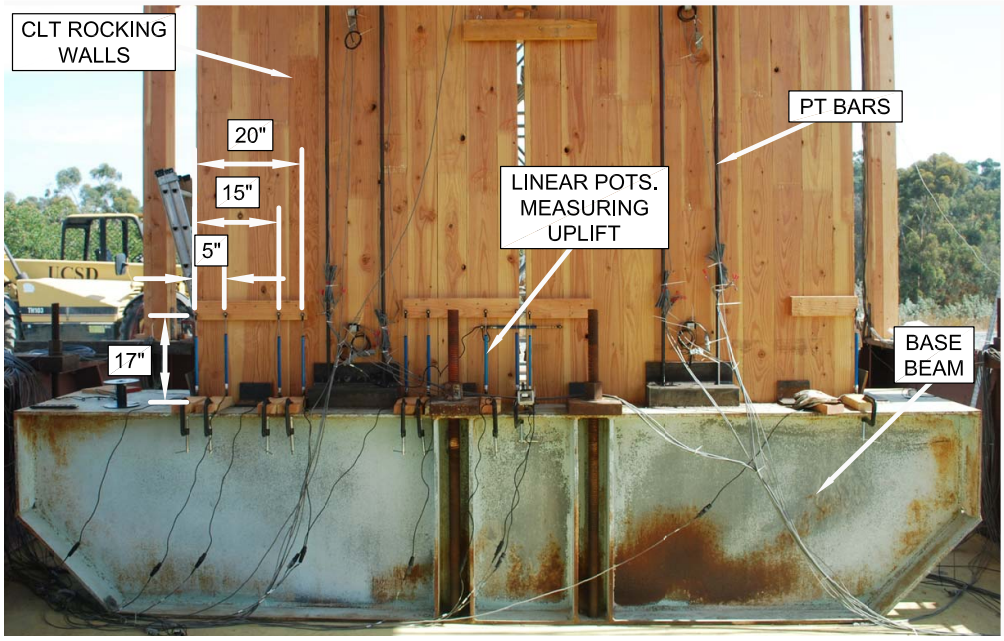

Figure 4.29: Typical layout of linear pots to measure wall rocking and uplift

The string potentiometers seen in Figure 4.30 were used to measure the relative movement between the shear key and the wall panels. Each shear key had a string potentiometer placed directly above it, mounted to the wall measuring vertical displacement of the shear key relative to the wall panels. On four of the eight shear keys, an additional string potentiometer was mounted to the wall panel and connected to the shear key at a 45° angle to capture any horizontal movement due to a small gap opening that may occur within the shear key slot in the wall panels. Strain gauges were used to measure the force transferred in each of the shear keys. A total of three strain gauges were applied to each shear key: one attached at a 45° angle on the top face of the key to measure shear strains, and one on each side of the key to measure normal strains. These three stain gauges were applied to the portion of the tongue spanning between the wall opening and the connection to the diaphragm to avoid

stress concentrations resulting from the bolt holes.

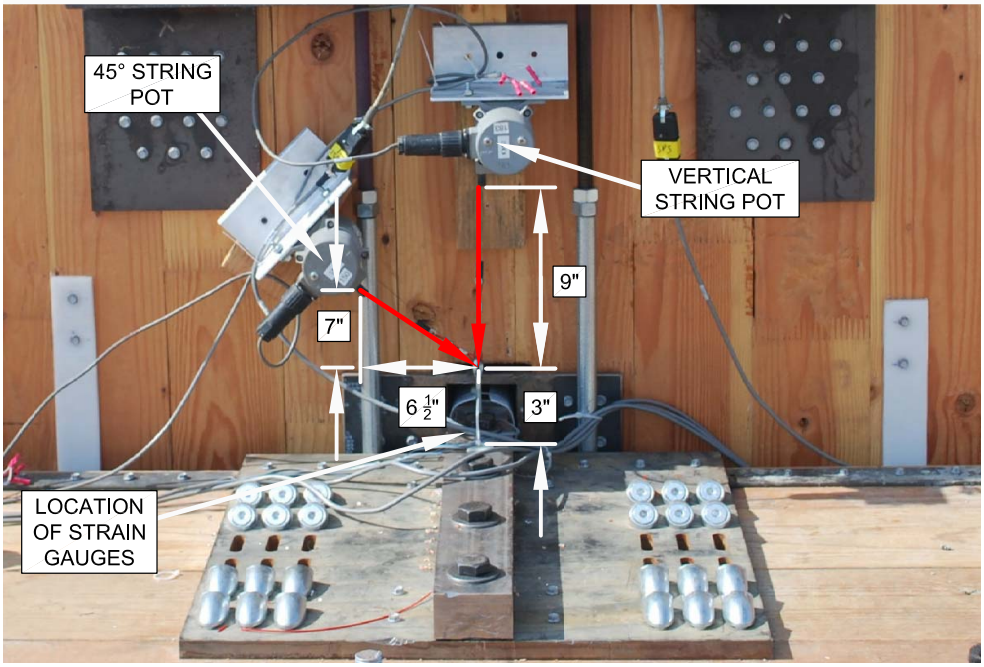

Figure 4.30: Typical layout of string pots and strain gauges measuring performance of the shera key

The final instruments on the walls were string potentiometers used to measure the shear displacement of the UFPs as seen in Figure 4.31 and linear potentiometers used to measure any variation in the panel spacing that could occur.

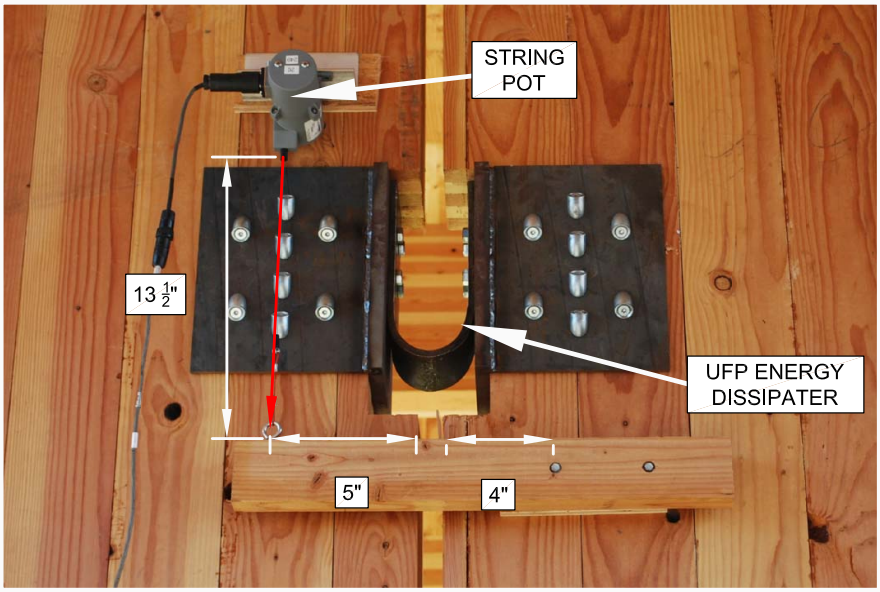

Figure 4.31: Typical layout of string pots measuring deformation of the UFPs

4.4.3 Columns

To measure the rocking of the pined columns, one of each type of column was instrumented with string potentiometers at the base and at both diaphragm levels. Figure 4.32 shows how two string potentiometers were used to measure the displacement changed between the diaphragm or base and the column face on both sides of the column.

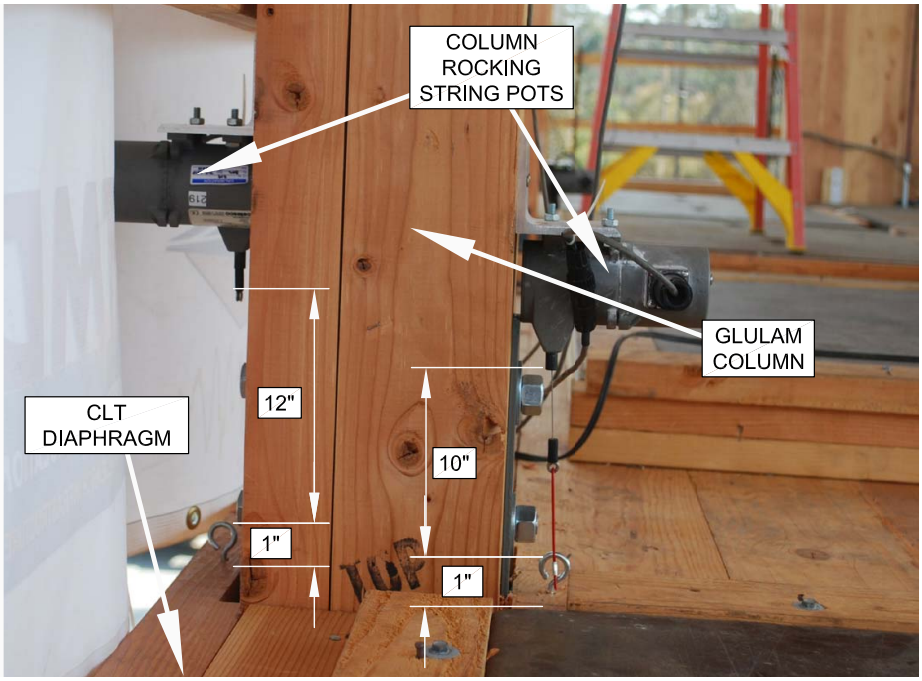

Figure 4.32: Typical layout of string pots measuring column rocking

4.4.4 Diaphragm

109 instruments were used to measure the relative movement of the diaphragm. They are included in Table 4.6 but will not be discussed in detail in this paper. More details about the diaphragm instrumentation can be found in DeMeza [2018].

4.5 Testing Plan and Ground Motion Records

In order to verify the performance of the design, the test specimen was subjected to fourteen total earthquake ground motions, chosen to represent three hazard levels from the modified performance objectives presented in 4.2.3. The main objective of the testing plan was to validate the performance of the CLT rocking walls at different levels of seismic intensity. The three different hazard levels were: (1) service level earthquake (SLE, i.e. 50% probability of exceedance in 30 years with a 43 year return period) defined by the USGS uniform hazard spectra; (2) design based earthquake (DBE, i.e. 10% probability of exceedance in 50 years

with a 475 year return period) defined by the uniform hazard spectra; and (3) maximum considered earthquake (MCE) defined by the USGS U.S. seismic design maps MCE spectra, referencing the 2015 NEHRP Provisions. The design curves were all generated for a site class B soil site in Oakland, CA at a latitude of 37.804° N and a longitude of -122.265° W. To generate the uniform hazard spectra, an average shear wave velocity of 2526 $\frac{ft}{sec}$ was used. An average shear wave velocity of 2526 $\frac{ft}{sec}$ is classified as site class B, however it should be noted that this is on the lower range of average shear wave velocities for a site class of B. Before and after each test, a two minute white noise excitation with a 0.03g PGA excitation was run. This white noise excitation was run to obtain the initial elastic natural period and to detect any potential building period changes is changes were made to the structure between tests, such as re-tensioning the PT after loss or adjustment of the wall to diaphragm connection.

The fourteen ground motions came from scaling four different ground motion recordings, three of which were selected from a suite of 22 bi-axial ground motions identified in FEMA P695 and one from the NGA West PEER ground motion database. The four original ground motions were: the 1979 Imperial Valley Earthquake - Delta (component 1 H-DLT262) from FEMA, the 1989 Loma Prieta Earthquake- Capitola (component 2 - CAP090) from FEMA, the 1987 Superstition Hills Earthquake Poe Road (component 2 - B-POE360) from FEMA, and the 1994 Northridge earthquake - Canoga Park (component 2 - NORTHR_CNP196) from PEER. Each ground motion was scaled to the three different hazard levels so the average of the spectra did not fall below the uniform hazard spectra for the SLE and DBE hazards and the response spectra for the MCE hazard at the 0.9 second approximate first mode fundamental period of the test building based on white noise excitation test results. Changes to the testing plan on site were made, so not all ground motions were run at all hazard levels. Table 4.7 shows the sequence of tests run. The table includes the target scale factor, the effective scale factor, the effective PGA and the spectral acceleration at the 0.9 second approximate first mode fundamental period. The target scale factor is the intended factor that should be applied to the raw FEMA or PEER ground motion files. Because

the execution of the shake table is not perfect there is some error between the input and output accelerations, so an effective scale factor was calculated. The effective scale factor was calculated by taking a ratio of the output response spectra to the raw FEMA or PEER response spectra between the periods of 0.4 seconds to 2 seconds. The effective PGA and the spectral acceleration at a period of 0.9 seconds were both taken from the output ground motion files. As shown, the scaling was more conservative for the SLE and DBE levels, primarily because of uncertainty in the building's period.

On the first two days of testing, four SLE ground motions were completed and one DBE level test that was the Northridge motion. Test 6 ran on the third day of testing and was open to the public. This test was the Northridge DBE ground motion repeated back-to-back. The objective repeating the motion back-to-back was to show the public the ability of the building to withstand multiple strong motions without the need for repair in between. On day four, the last day of testing, the first two tests were open to the public. The first test was Test 7 which was a SLE level earthquake to show how the building reacted in low, frequent earthquakes. The second test was Test 8, a repeat of Test 6. Once the table was closed to the public, two more DBE level tests were completed, followed by three MCE level tests. At the end of the MCE level tests, the PT bars had not yielded, so the Northridge MCE level earthquake was multiplied by a factor of 1.20 so the response of the building with yielded PT bars could be observed. Figure 4.33 and Figure 4.34 show the target uniform hazard curve for SLE and DBE hazard levels respectively and Figure 4.35 shows the MCE response spectra. Each figure has a plot with response spectra for the target ground motions and a plot with the response spectra for the effective ground motions. In addition, the average response spectra for the ground motions was also calculated and plotted. It should be noted test 6 and 8, shown as dashed lines in Figure 4.34, were not included in the calculation of the average for DBE because they were slightly above the DBE hazard level. Similarly, test 14 was not included in the average for the MCE hazard level. Also, each plot has a vertical dotted line plotted at the buildings estimated fundamental period of about 0.9 seconds to which the ground motions were scaled.

Table 4.7: Ground motion testing sequence

Day	Test	Event Name	Hazard Level	Target SF	Effective SF	Effective PGA (g)	Effective Sa @ 0.9 sec (g)
Day 1	1	Loma Prieta	SLE	0.42	0.36	0.16	0.15
Day 2	2	Loma Prieta	SLE	0.44	0.38	0.18	0.16
	3	Northridge	SLE	0.28	0.25	0.19	0.18
	4	Superstition Hills	SLE	0.40	0.37	0.13	0.12
	5	Northridge	DBE	1.0	0.99	0.53	0.69
Day 3	6	Northridge [a]	DBE	1.06	1.13	0.52	0.74
Day 4	7	Imperial Valley	SLE	0.50	0.42	0.13	0.21
	8	Northridge [a]	DBE	1.06	1.13	0.53	0.74
	9	Loma Prieta	DBE	1.21	1.16	0.52	0.49
	10	Superstition Hills	DBE	1.42	1.41	0.44	0.42
	11	Loma Prieta	MCE	1.37	1.32	0.62	0.57
	12	Northridge	MCE	1.32	1.31	0.73	0.91
	13	Superstition Hills	MCE	1.98	2.06	0.63	0.63
	14	Northridge	MCEx1.20	1.60	1.57	0.85	1.11

[a]Motion was run back to back without a break.

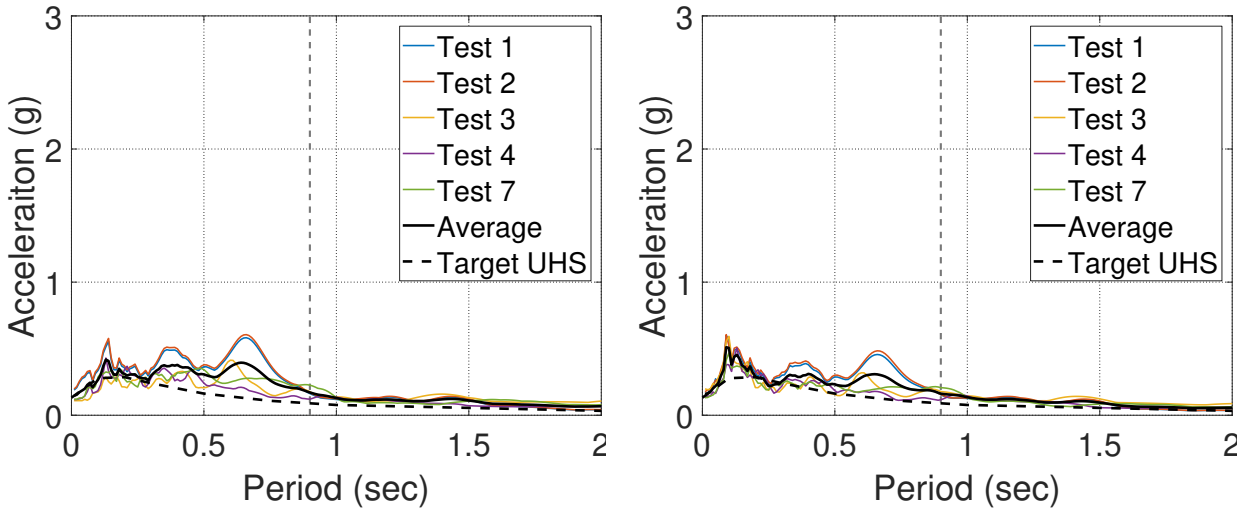

(a) Input ground motions

(b) Effective ground motions

Figure 4.33: Spectral acceleration response spectra of SLE level

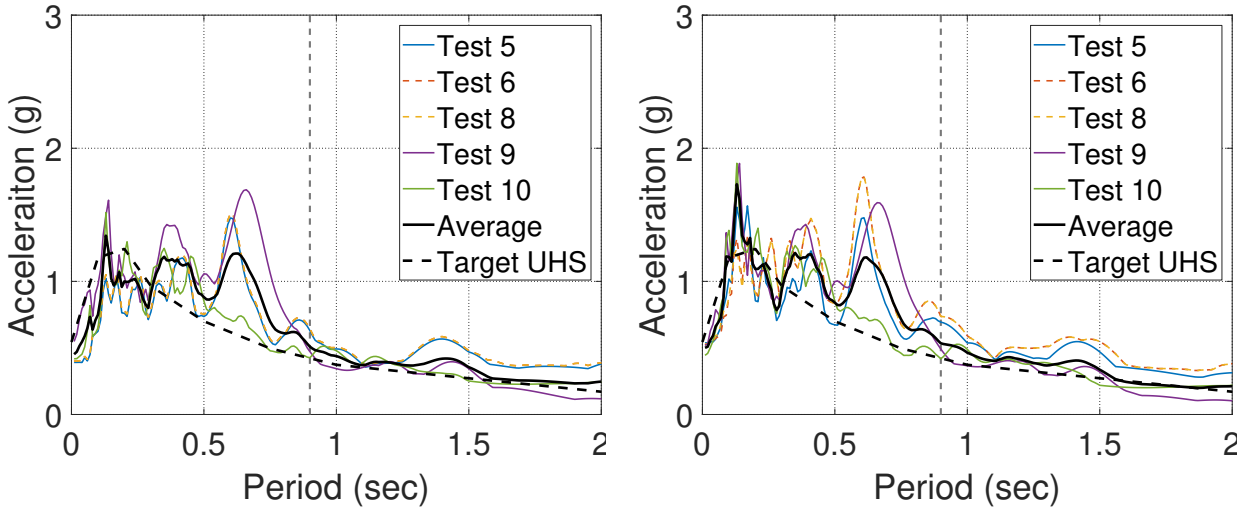

(a) Input ground motions

(b) Effective ground motions

Figure 4.34: Spectral acceleration response spectra of DBE level

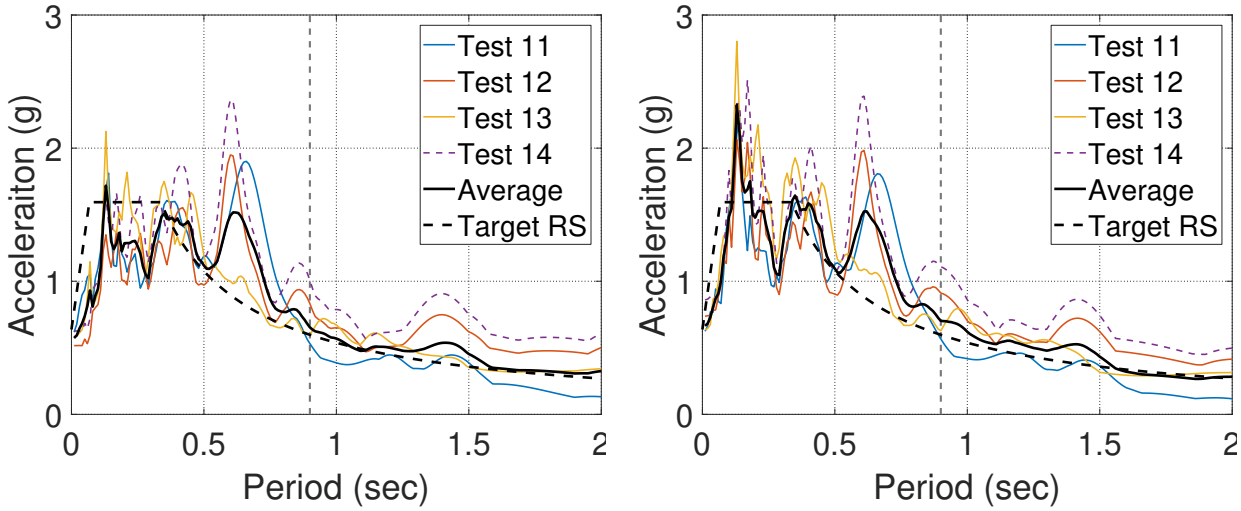

(a) Input ground motions

(b) Effective ground motions

Figure 4.35: Spectral acceleration response spectra of MCE level

Chapter 5

EXPERIMENTAL OBSERVATIONS

5.1 Overview

In this chapter, the experimental observations of the test specimen through the 14 ground motions will be discussed. During the testing sequence, some slight modifications to the specimen were changed to improve testing conditions. In the first section of this chapter these modifications will be presented. In the second section of this chapter, the observed damage to the test specimen during the total load history will be presented.

In order to observe damage throughout the test sequence, formal inspections were conducted by the research team. During these inspections, the building was visually scanned for damages and changes to the structure. Any observations were recorded and photographed. In addition, any modifications made on the specimen were made during the inspection times. White noise tests were always run before and after all formal inspections since the modifications or inspection process could change the natural frequency of the building. The inspection schedule is shown in Table 5.1

Table 5.1: White noise and inspsection schedule for the testing sequence

Day	Test	Motion
Day 1	1	WN 1 Loma Prieta SLE WN 2
Day 2	**INSPECTION 1**	
	2	WN 3 Loma Prieta SLE WN 4
	3	Northridge SLE WN 5
	4	Superstition Hills SLE WN 6
	5	Northridge DBE WN 7
Day 3	**INSPECTION 2**	
	6	WN 8 Northridge DBE WN 9
Day 4	7	Imperial Valley SLE WN 10
	8	Northridge DBE WN 11
	INSPECTION 3	
	9	WN 12 Loma Prieta DBE WN 13
	10	Superstition Hills DBE WN 14
	INSPECTION 4	
	11	WN 15 Loma Prieta MCE WN 16
	12	Northridge MCE WN 17
	INSPECTION 5	
	13	WN 18 Superstition Hills MCE WN 19
	INSPECTION 6	
	14	WN 20 Northridge MCEx1.2 WN 21

5.2 Modifications Made During Testing

During the 14 ground motions run on the test specimen, minor modifications were made to the specimen and test setup to improve the testing conditions. The changes made were not intended to alter the overall response of the structure, but to modify the components so they would perform more closely to how they were designed. The majority of these modifications were made during the first few ground motion runs when it was observed that the components were not performing as planned. However, some changes were made periodically through all 14 tests to represent repairs being made after earthquake events.

5.2.1 Rocking Wall Base Beam Modifications

As described in Section 4.2, the CLT rocking wall panels sat on top of large steel base beams which were then connected to the shake table as seen in Figure 5.1a. The base beams were not designed specifically for this test, they were reused from a previous project. As shown in Figure 5.1b, the cross section of the base beam was a double-web I-beam made entirely of $\frac{5}{8}$" steel plates. The two webs were spaced about 17" apart and the $6\frac{7}{8}$" CLT wall panels sat between the two webs. Plates were also welded on to the ends of the base beam so the inside of the base beam could not be accessed.

After the completion of the second day of testing, deformation in the top flange of the base beam was observed from videos recording the corner of the rocking wall. As the wall rocked, the top flange of the base beam deformed into a curved shape between the two flanges at the locations under the corners of the wall panels. As the portion of the flange between the two webs deflected downward, the portion of the upper flange outside of the two webs deflected upward. This happened because the top flange of the base beam was not stiff enough to support the compression forces at the wall panel corners.

Base beam flange deformation was observed during the first two days of testing when only four SLE and one DBE level earthquake motion was run. No significant permanent deformation was observed after the these tests, but the linear potentiometers located at the

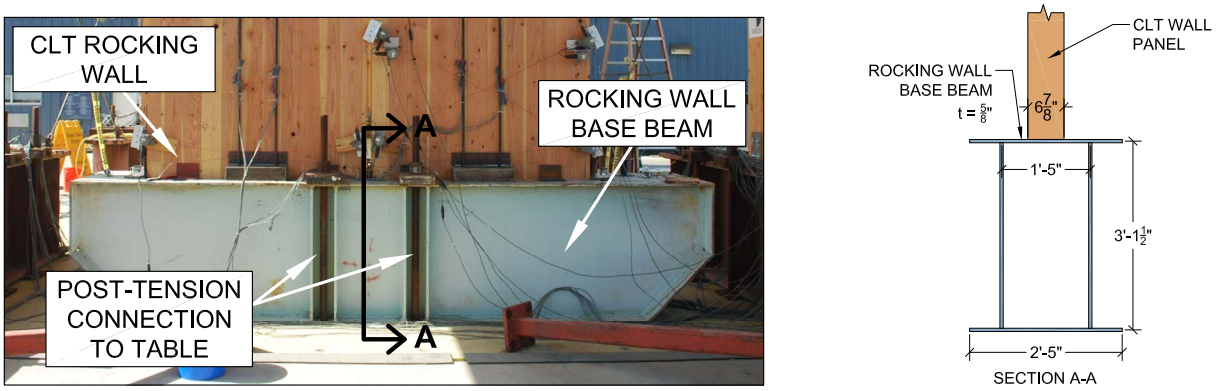

(a) Plan view of rocking wall base beam

(b) Cross section view

Figure 5.1: Rocking wall base beam

base of the wall (as seen in Figure 4.29) measured downward displacements as large as 0.08 inches during the SLE tests where the maximum upward displacement was only 0.27 inches. With this much downward deflection in the base beam from just the first SLE test, concern was raised for how much deformation would occur during the larger level earthquakes and if permanent deformation would occur.

In attempts to prevent excessive permanent deformation in the base beam, prior to the beginning the third day of testing (during inspection 2), stiffeners were added to the exterior of the beams as shown in Figure 5.2. The added stiffeners were pieces of scrap steel found on sight. One stiffener was added to each side of the base beam below the two exterior corners of the wall panels (four total stiffeners on each of the two base beams). Stiffeners were not added at the wall panel corners in the center of the wall because the base beam was already stiffened since it is where the table post-tensioning bars are located. Adding the additional stiffeners helped reduce base beam yielding and the movement of the flange portion located outside of the webs. However, as testing progressed, the portion of the flange between the two webs still deformed significantly and permanently, indicating yielding occurred. Because the inside of the beam could not be accessed, no other modifications were made to stiffen the beam. The permanent deformation of the base beam will be discussed in Section 5.3.2.

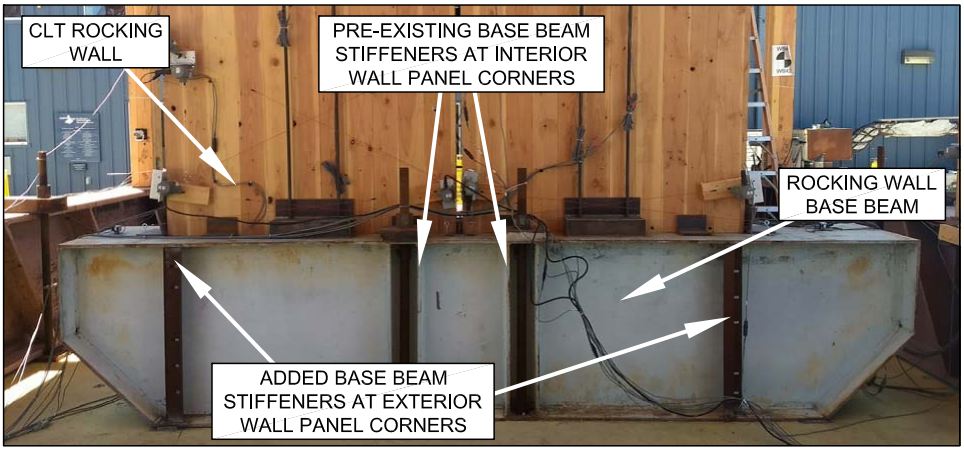

Figure 5.2: Location of added stiffners to rocking wall base beam

5.2.2 Wall to Diaphragm Connection Interface

In order for the wall to diaphragm connection to transfer shear force without transferring moment, the slotted pin connection interface was covered in a thin sheet of teflon to reduce the coefficient of friction. During the design of this connection, careful consideration was taken to insure the correct amount of space was available for the teflon and tongue plate to fit into the slotted hole in the wall. However, during installation, issues in fit-up were present at some of the connections, and modifications were made before testing and throughout testing.

At some locations, the steel tongue plate was wrapped with the thin teflon sheet, however, at other locations, there was extra space so the sides of the slotted hole were also covered in teflon. Part way through the testing sequence, the teflon became damaged at some of the locations and needed replacement. Figure 5.3 shows examples of damaged teflon from the shear transfer connection. In Figure 5.3 (a) the teflon which surrounded the tongue plate is laying next to the tongue plate and the connection shown also has the teflon lining the sides of the slotted hole. Figure 5.3 (b) shows a close-up of the damaged teflon covers. Each connection was slightly different because of small differences in fabrication and erection, but it is believed that they all performed relatively similarly and the periodic replacement of the

teflon did not have significant effects on the overall response of the structure. Majority of these changes occurred during Inspection 1.

(a) (b)

Figure 5.3: Damaged teflon on the wall to diaphragm shear trasfer connection

5.2.3 Re-Tensioning of PT Bars

Another modification made during testing was the re-tensioning of the PT bars between tests to account for prestress losses or gains. The forces in the bars were measured by load cells located at the top of the bars and all the post-tensioning was done by hand. The walls were designed to have an initial PT force of 12 kips per bar. When tensioning the bars, a tolerance of ± 0.3 kips was used. None of the bars yielded significantly until the final earthquake ground motion, however, during smaller ground motions in the testing sequence, the bars lost some initial stresses likely due to seating of the PT in the anchorage. To account for the changing of initial PT forces, the bars were re-tensioned between runs where significant stresses were lost. In general, if during the testing sequence the bars fell below or above their allowable initial force limit of 12 ± 0.3 kips, the bars were re-tensioned to be within limits. If bars

were re-tensioned between tests, a white noise test was run before and after the tensioning to insure any changes to the elastic period of the structure due to increased PT forces was known.

Table 5.2 shows the percentage of target initial PT force at the beginning and end of each test as well as the PT re-tensioning schedule. Some data was lost during test 5, including the forces in the PT bars which is why no data is presented there. Each percentage was calculated for the sum of all four bars on each CLT wall panel. In the table 100% signifies that the sum of the initial PT force at that panel equaled the target force of 48 kips (12 kips per each of the four bars). A number greater than 100% means on average, the PT bars were over stressed and a number less than 100% means on average, the PT bars were under-stressed from the target initial stress. The table also shows a schedule of when the bars were re-tensioned. From the table, it is clear that for the first three days of testing, when lower level motions were run, minimal fluctuation in the PT bar forces between the beginning and ends of tests occurred so re-tensioning was never required. During the last day of testing, when larger level motions were run, re-tensioning was done twice. Significant yielding was observed during the 14^{th} test, specifically in the east panel of the south wall. It should also be noted that fluctuating temperatures between morning and afternoon testing times changed the initial stresses in the bars. The temperature was cooler in the mornings which is why forces were typically greater during the first test of the day.

The re-tensinoing of the bars between earthquake ground motions is representative of repair after minor earthquakes in a real building using this technology or it could be representative of maintenance work completed on the building after a few years of operation. In addition, because the tests on this specimen were completed only a couple days after initial tensioning, prestress losses were not accounted for in calculations as they would be in a real structure.

Table 5.2: PT bar retensioning schedule with initial and final PT forces for each test

Day	Test	Time	North Wall		South Wall	
			West Panel	East Panel	West Panel	East Panel
Day 1	1	Initial	100%	101%	99%	102%
		Final	99%	101%	99%	100%
Day 2	**INSPECTION 1**					
	2	Initial	100%	101%	100%	100%
		Final	99%	101%	99%	100%
	3	Initial	99%	101%	99%	100%
		Final	99%	101%	99%	100%
	4	Initial	99%	101%	99%	100%
		Final	99%	101%	99%	100%
	5	Initial	-	-	-	-
		Final	-	-	-	-
Day 3	**INSPECTION 2**					
	6	Initial	101%	101%	100%	102%
		Final	99%	100%	99%	100%
Day 4	7	Initial	101%	102%	100%	103%
		Final	101%	102%	100%	103%
	8	Initial	101%	102%	100%	102%
		Final	100%	101%	100%	102%
	RE-TENSION & INSPECTION 3					
	9	Initial	100%	101%	100%	101%
		Final	100%	101%	99%	101%
	10	Initial	100%	101%	99%	101%
		Final	100%	101%	97%	101%
	INSPECTION 4					
	11	Initial	100%	101%	102%	101%
		Final	100%	101%	99%	100%
	12	Initial	100%	100%	98%	101%
		Final	97%	99%	96%	96%
	INSPECTION 5					
	13	Initial	99%	99%	99%	99%
		Final	97%	98%	97%	98%
	RE-TENSION & INSPECTION 6					
	14	Initial	101%	100%	101%	102%
		Final	83%	80%	82%	68%

5.3 Observed Damage

In general minimal damage was observed on the test specimen after the 14 ground motions. The building was not expected to perform as well as it did, but that could also be attributed to other factors such as the flexible base beams below the rocking walls which will be discussed in more detail in this section. The pictures and data presented in this section was mostly collected during the formal inspections discussed earlier.

Little to no damage was observed on the entire specimen during the SLE, DBE, and MCE level tests. After three MCE level ground motions that resulted in no significant damage, an amplified MCE level tests (1.2 MCE) was completed on the specimen to ensure PT yielding could be observed. After the PT yielded in the 1.2 MCE level test, no more tests were run on the specimen even through there was essentially no damage to the timber. This was primarily because the gravity frame had only been designed for drifts up to 5% and the structural integrity of gravity frame had to be maintained for future testing.

5.3.1 CLT Rocking Wall Panels

The CLT wall panels experienced no major structural damage or crushing at the rocking corners of the wall during any of the tests, however, there was some minor damage that wouldn't affect the wall structurally. After the first few tests, there was some minor splitting of the wood at the corners as seen in Figure 5.4 (a). This damage was most likely initially caused during transportation or installation of the wall panels. The rocking of the panels during the low level test then made the already existing damage more visible. In Figure 5.4 (b), the first laminate on the right panel is fairly small, about $\frac{3}{4}$ of an inch. Similar small laminations at the corners of the panels were present at a few of the corners. At these corners, a gap appeared between the small laminate and the one adjacent to it during testing, as seen in Figure 5.4 (b).

After the DBE level earthquakes, no additional damage was observed on the wall panels. After the MCE level tests and the 1.2 MCE level test there was some minor damage at the

Figure 5.4: Photo of rocking wall corner after SLE level ground motions with (a) minor cracking and (b) laminate spreading

corners of the walls as seen in Figure 5.5a. However, it appears that most of this damage did not impact the structural behavior. After testing, when the walls were removed from the test specimen, no visible signs of crushing or permanent deformation at the wall corners was present. Figure 5.5b shows a picture of one of the wall panel corners after the walls were removed. A square was put up against the corner and it can be seen that little to no crushing occurred. The permanent crushing measured on the walls at the wall corners ranged from 0.09 inches to 0.13 inches.

(a) Minimal damage at the corners

(b) Minimal permanent deformation to the corners after the walls were removed

Figure 5.5: Damage observed to corners of the rocking wall panels

5.3.2 Rocking Wall Base Beam

Although the permanent crushing deformation at the wall panel corners was almost zero, Figure 5.6 shows a relatively large gap between the base of the wall panel and the top of the base beam at the end of testing. Before the walls were removed, it was thought that this deformation was caused by permanent crushing or yielding of the CLT panels. However, as previously discussed with Figure 5.5b, this was not the case, the gap was actually formed because the rocking wall base beam deformed and yielded as the walls rocked on top of the beam. As mentioned earlier, stiffeners were added to reduce the deformations, but they did not completely prevent them.

The yielding of the base beam can be seen in plots of data collected by the linear potentiometers located at the base of the wall. The outside and inside linear potentiomenters shown in Figure 5.7a measured relatively large downward displacements. For example, during the 14^{th} ground motion, the two linear potentiomenters resulted in a maximum downward

Figure 5.6: Photo showing the gap between the base of the wall panel and the top of the base beam at the end of the testing sequence

displacement of 0.49 inches as seen in the plot in Figure 5.7b. The potentiometers were originally installed at the base to measure vertical uplift of the walls in the upward direction and measure panel crushing and elastic yielding in the downward direction. However, because the walls had such small permanent deformation, it was determined that this downward deformation was due to the base beam flange deflecting, not from wall panel deformation or crushing.

After deconstruction of the test specimen, the rocking wall base beams were inspected more closely. An exaggerated plan view showing the yielded shape of the rocking wall base beam can be seen in Figure 5.8 (a). The permanent yielded deformation at outside corners of the rocking wall, $d_{outside}$ ranged from 0.34 inches to 0.48 inches, and deformed over a length under the wall panel, $l_{outside}$, ranging from 10.5 inches to 14 inches. The permanent yielded deformation at the inside corners of the rocking wall, d_{inside} ranged from 0.31 inches to 0.27 inches, and deformed over a length under the wall panel, l_{inside}, ranged from 8 inches to 10.5 inches. The base beam yielded more at the locations under the outside corners of the wall because there were fewer stiffeners and because the compression forces under the

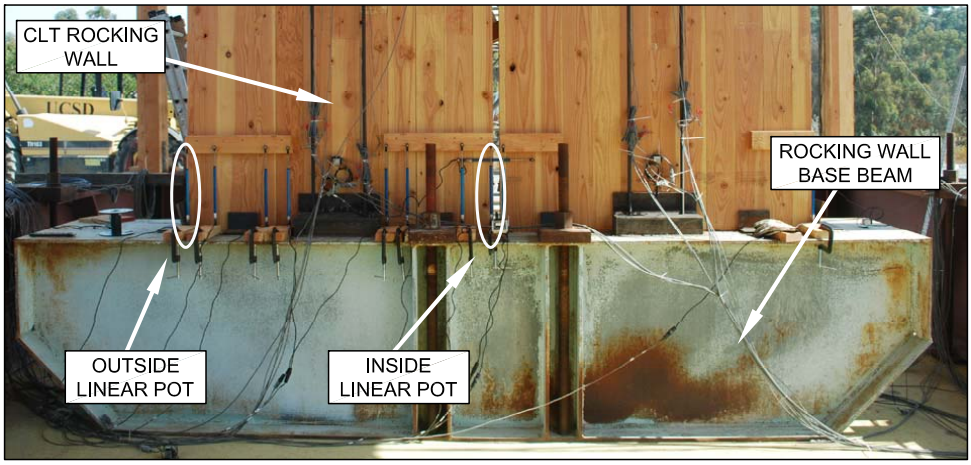

(a) Potentiomenter locations

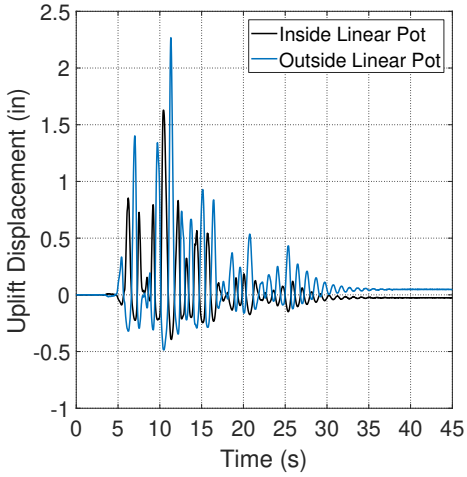

(b) Plot of measured displacements at the two ends of the southwest wall for the 14^{th} ground motion

Figure 5.7: Linear potentiometers measuring vertical displacement of rocking walls

inside corner are smaller due to the UFP shear forces, V_{UFP}, acting upward (see Figure 3.6). Figure 5.8 (b) shows a schematic of a cross section view of the base beam when the wall is rocking and pushing the center of the base beam top flange downward between the two webs.

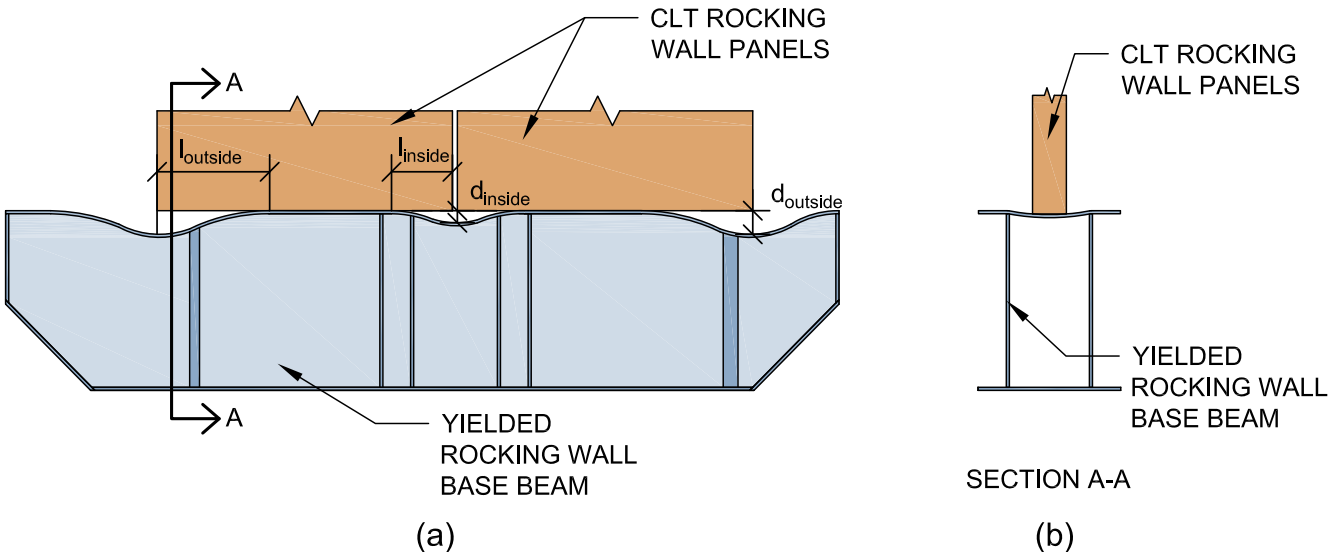

Figure 5.8: Yielded base beam shape at end of testing (a) plan view (b) cross section view

More damage of the CLT wall panels was predicted, prior to testing, than what was observed. It was predicted that CLT wall panel crushing would begin during the DBE hazard level earthquakes and excessive crushing would occur during the MCE hazard level earthquakes. However, significant crushing never occurred. This is because the base beam, which acted as the rocking wall foundation, was so flexible it protected the walls from damage. If a rigid foundation was used during the test, then CLT toe crushing may have been more extensive.

5.3.3 Gravity Frame and Diaphragm

Like with the CLT rocking walls, minimal damage was observed in the gravity frame. The gravity frame was designed to accommodate the large lateral drifts and performed very well.

Throughout the testing sequence, parts of the glulam gravity frame started to form longitudinal cracks, however, none of the cracks were concerning. Figure 5.9 shows an example of one of the cracks observed. This crack was located on one of the exterior beams on the roof, and the crack occurred close to one of the platform beam-column connections. Only four of these large cracks were observed across the entire specimen, although additional smaller, less prominent, cracks were present.

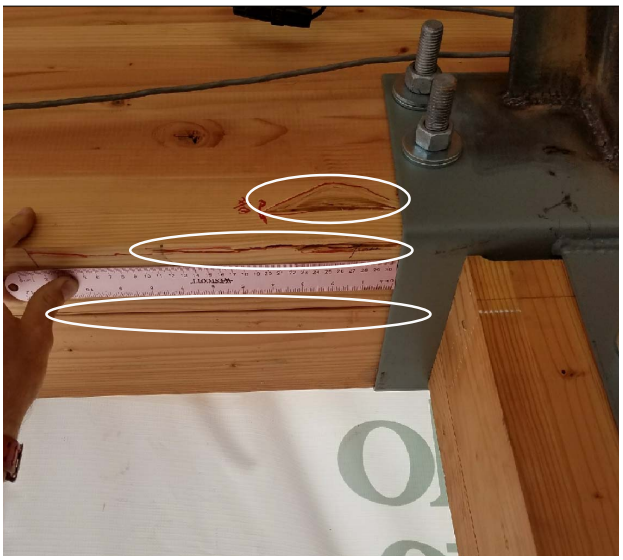

Figure 5.9: Longitudinal cracks in gravity frame beams

There was also minor damage in the gravity frame columns. The columns had slotted pin connections to allow for rocking at the base of the columns. Figure 5.10a shows how the corners of the columns were rounded and crushed slightly after the testing sequence. In this figure, the shaking and rocking of the column is out-of-plane. The laminations in the glumn columns also started to spread and form gaps throughout testing as shown in Figure 5.10b, although, none of these gaps were very significant at the end of testing.

No major damage was observed for the diaphragm. On the floor, the largest damage observed was at the interface between the plywood splines and the CLT diaphragm panels. There was some minor movement of the diaphragm relative to the splines. Figure 5.11 (a)

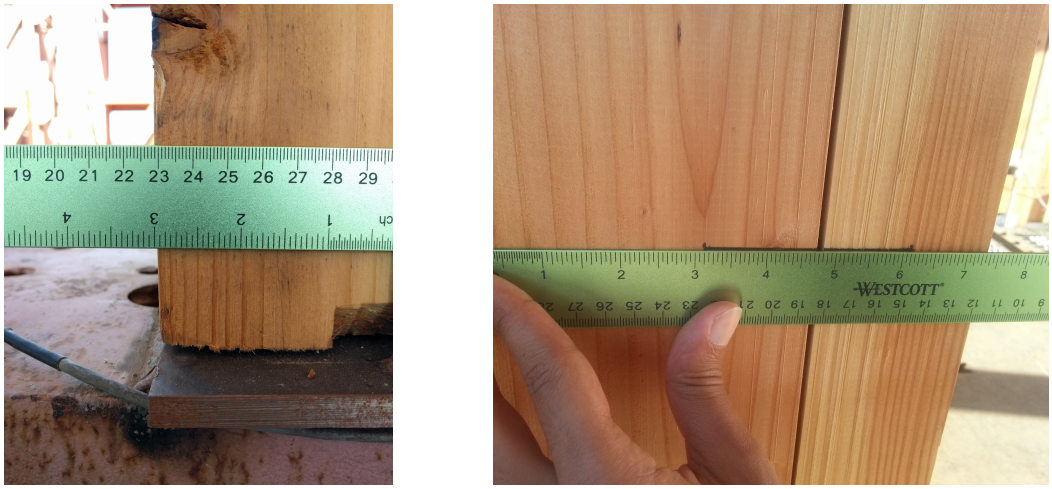

(a) Minor crushing at the column base (b) Spreading of the laminates

Figure 5.10: Damage obsered in the glulam gravity frames

shows a picture of the original diaphragm panel and spline interface and Figure 5.11 (b) shows the same connection after the testing sequence. The CLT roof diaphragm panels and splines could not be inspected due to the concrete cover. The concrete experienced cracking as seen in Figure 5.12. Most of the cracking occurred prior to shaking, and was typical concrete shrinkage cracks. Some additional cracking occurred throughout the testing sequence. More discussion on the damages on the diaphragm can be found in DeMeza [2018].

(a) Spline and diaphragm location before testing

(b) Spline and diaphragm location after testing

Figure 5.11: Damage observed in the CLT diaphragms

Figure 5.12: Concrete cracking on the roof diaphragm

Chapter 6

EXPERIMENTAL DATA ANALYSIS

6.1 Overview

This chapter documents the analysis of experimental data for the test specimen during the fourteen ground motion tests. Data was collected from the various instruments and this chapter explains how the data was processed and interpreted. First, data reduction and filtering, analysis of the white noise tests, and estimated damping will be discussed. Next, the data pertaining to the global response of the structure, such as drifts and base shear, will be presented, followed by the analysis of data for the PT bars, the wall panel base deformation, and the UFPs. At the end of this chapter, the experimental data will be summarized and compared to the design performance objectives and the predicted performance from design. It should be noted that a few sensors malfunctioned during the testing and data was lost. In addition, during test 5, one of the DAQ modules did not turn on leading to large amount of lost data. In this chapter, plots have been marked with "Lost Data" where appropriate and portions of tables are missing data where data was lost. It should also be noted that plots for only a selection of ground motions are included in this chapter, a full collection of the plots for all ground motions are found in Appendix B.

6.2 Data Reduction and Filtering

Raw data collected from the DAQ was corrected and filtered in various ways prior to data analysis. The DAQ collected data at a very high frequency of 240 Hz. To make data sizes more manageable while still maintaining the overall frequency response, the data was initially down sampled by a factor of two, for a sampling frequency of 120 Hz. In addition, all data except the white noise data was trimmed at the beginning and end to remove waiting

time between the start or end of instrument recording and testing. Also, initial offsets were removed from all instrumentation, except for the load cells. Finally, because of random noise in the data acquisition system, the recorded data from the accelerometers and strain gauges, were filtered using a band-pass butterworth filter with a lower cutoff frequency of 0.2 Hz and a higher cutoff frequency of 25 Hz. The other instruments did not pick up as much nose so they were not filtered. When accelerometer readings were used for displacement measurements, the data was filtered and then integrated twice to get displacement.

6.3 White Noise Analysis: Fundamental Period

White noise (WN) tests were run between every ground motion to obtain the natural elastic period of the building. Additional white noise tests were run before and after formal inspections to capture possible changes to the stiffness of the structure due to modifications. The white noise schedule can be found in Table 5.1. The elastic first mode period of the building was determined by analyzing each white noise test using a Fast Fourier Transform (FFT). Filtered acceleration data from the accelerometer located at the center of the roof was used to perform the FFT analysis because that was assumed to be the location closest to the center of mass. A simple one-dimensional median filter was also applied to the FFT data in order to achieve the smoother plots seen in Figure B.1 in the Appendix. The peak value from each FFT analysis plot was taken as the elastic first mode period.

Figure 6.1 summarizes the fundamental first mode elastic periods for each white noise test. In the figure, when a ground motion was run between two white noise tests, a solid line, with the labeled test number, connects the points which represent the white noise periods. If an inspection, with possible repairs, was performed a dashed line is used to connect the points. The different days are also called out on the plot. It can be seen that the building's period has an increasing trend, mostly due to increasing damage to the specimen throughout the testing sequence. The sharp increase in period during the first ground motion test (between WN 1 to WN 2) is most likely due to the initial "loosening" of the structure following construction. Majority of the modifications made to the wall-to-diaphragm connections were made after

the first ground motion, during inspection 1. The effect of improving the sliding ability of the wall to diaphragm connections, as discussed in Section 5.2.2, can be seen by the period increase between WN 2 and WN 3. Test 5 was the fist DBE motion run on the specimen, explaining the jump in period between WN 6 and WN 7. As discussed in Section 5.2.1, the rocking wall base beam was retrofitted with stiffeners before day 3 of testing (during the inspection 2). The stiffening of the base beam, would also stiffen the entire specimen, which explains the large decrease in period during inspection 2 (between WN 7 and WN 8). Small fluctuations in the periods are seen between WN 8 and WN 15. After WN 15, MCE level tests began which resulted in slightly more damage to the specimen, which can be seen by the general increase in period between WN 15 and WN 21.

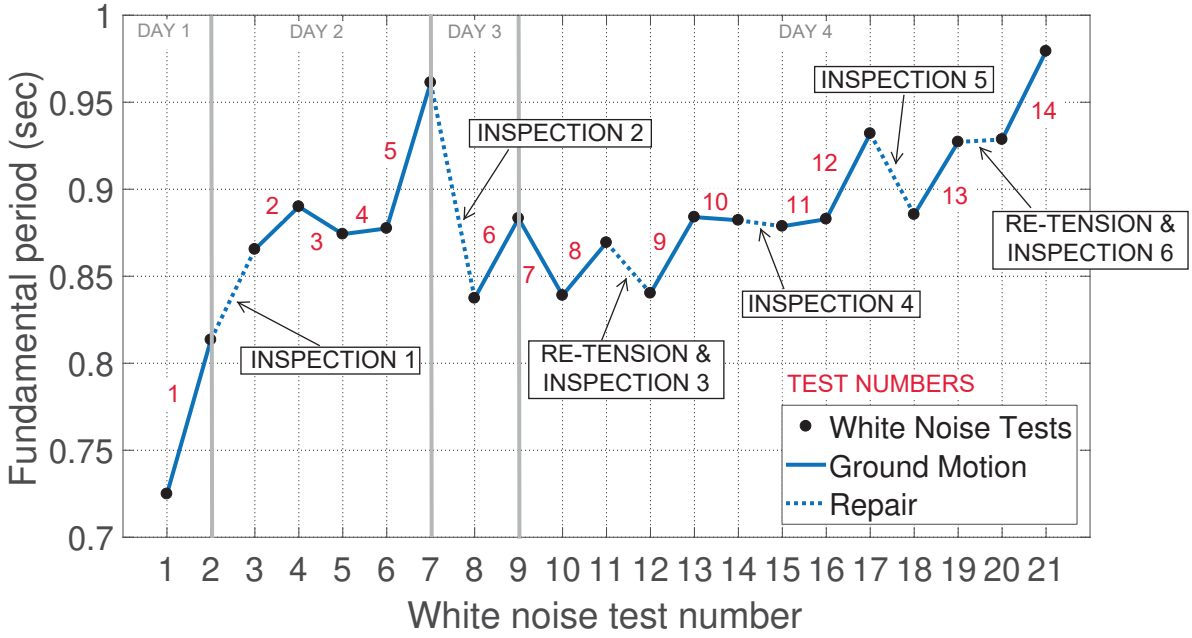

Figure 6.1: Fundamental first mode elastic period of building from white noise tests

As shown in Figure 6.1, the natural elastic period of the specimen is between 0.73 seconds and 0.98 seconds for all the tests, which is relatively long for a two-story building. Before the rocking wall base beam was stiffened (before WN 8), the elastic period appears to change

significantly, ranging from 0.73 seconds to 0.96 seconds. However, after stiffening of the base beam, the period of the building stays fairly stagnant, bouncing between 0.84 seconds and 0.88 seconds, until the MCE level tests. After starting the MCE level tests, the elastic period increased and bounced between 0.88 seconds and 0.98 seconds. For the remainder of the data analysis, a building period of 0.9 seconds was used to analyze the structure.

6.4 Estimated Damping Coefficient

At the beginning of the forth day of testing, a free vibration test was performed to determine an estimated damping coefficient by analyzing the decay of motion. With the instruments recording, the roof of the specimen was struck three times by a mass suspended from a crane that applied point loading in the direction of table shaking to excite the first mode of vibration. Between each excitation by the mass sufficient time was left to measure the free vibration response. The accelerometer located at the center of the roof was used to determine the displacement of the roof during free vibration. A plot showing the free vibration readings from this accelerometer are shown in Figure 6.2.

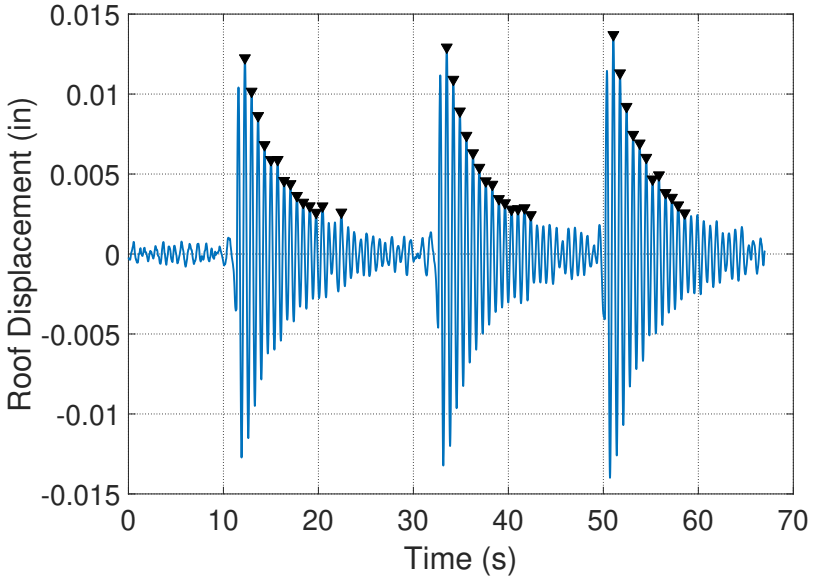

Figure 6.2: Free vibration displacement of the roof when the structure was excited

To determine the damping coefficient, free vibration of a single degree of freedom, linear spring mass system was assumed. Each of the three excitations were analyzed separately and the results were averaged. For each excitation, local maxima were identified during the free vibration range as shown by the marked peaks in Figure 6.2. For each excitation, the period of oscillation,T, was first determined by subtracting the time of the first prominent peak, t_o, from the last prominent peak, t_n, and dividing by the number of peaks, n (Equation 6.1). The logarithmic decrement, δ, can be calculated by taking the natural log of the displacement at one of the peaks, $x(t_n)$, divided by the displacement at the adjacent peak, $x(t_{n+1})$. The same value for δ should result from using any two adjacent points, but the averaged formula was used in this case for more accurate results (Equation 6.2). The damping coefficient ξ was then determined using Equation 6.3 [Chopra, 2007]. The calculated periods, logarithmic decrement, and damping coefficient from each excitation and the averages are shown in Table 6.1. An averaged damping coefficient of 1.92% was estimated for the specimen.

$$T = \frac{t_n - t_o}{n} \tag{6.1}$$

$$\delta = ln\left(\frac{x(t_n)}{x(t_{n+1})}\right) = \frac{1}{n}\left(\frac{x(t_o)}{x(t_n)}\right) \tag{6.2}$$

$$\xi = \frac{\delta}{\sqrt{4\pi^2 + \delta^2}} \tag{6.3}$$

Table 6.1: PT bar retensioning schedule with initial and final PT forces for each test

	Excite 1	Excite 2	Excite 3	Average
Period (sec)	0.629	0.632	0.619	0.627
Log. Decrement δ	0.108	0.119	0.135	0.121
Damping Cof. ξ	1.72%	1.89%	2.15%	**1.92%**

6.5 Global Response

Story drifts are a good way to quantify the global response of the building. Both string potentiometers and acceleromenters were installed on the structure to measure these drifts. Three string pots, measuring displacement in the direction of shaking, and seven accelerometers measuring acceleration in the direction of shaking, were installed on each level of the structure. In addition, five accelerometers were spaced along the height of each wall to measure their movement. All three of these were used to determine drifts of the structure. To compare the results from each source, the data from the three string potentiometers on each level were averaged, the integrated data from the seven accelerometers on each level were averaged, and the integrated accelerometer data from the wall accelerometers located closest to each level were averaged. Drift time histories were calculated from each of the three averaged displacements and plotted against each other. Plots for an SLE, DBE, and the MCEx1.2 level test are shown in Figure 6.3 and the plots for all tests can be found in Figure B.2 in the Appendix. All readings produced very similar results, so it was determined that any of the three options would be representative of the overall building drift. Because the accelerometers were spaced over the whole diaphragm and could give a good representation of the whole movement, they were used for the remainder of the data analysis. In addition, none of the accelerometer data was lost for any of the tests. Because the drift calculations from the wall accelerometers matched well with the other drift calculations, it is clear that there was minimal slip or relative movement at the wall to diaphragm connection.

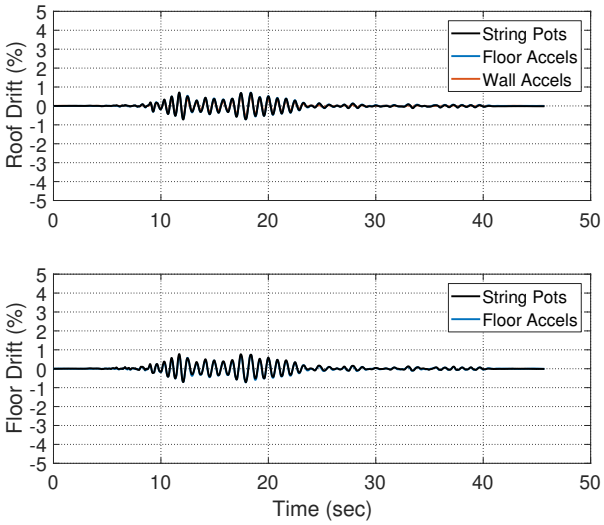

(a) Test 1 Loma Prieta SLE

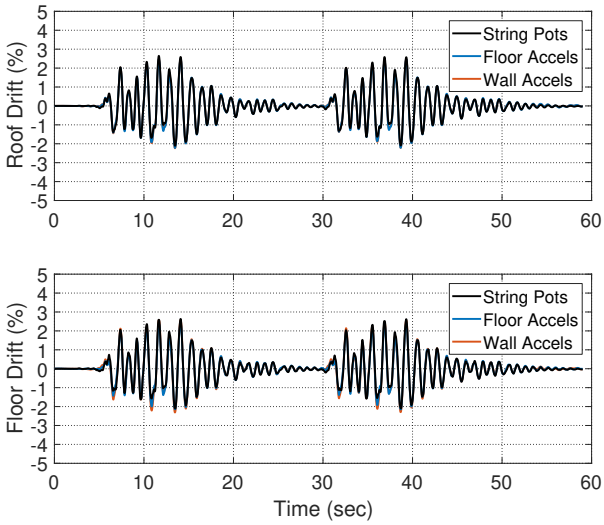

(b) Test 8 Northridge DBE

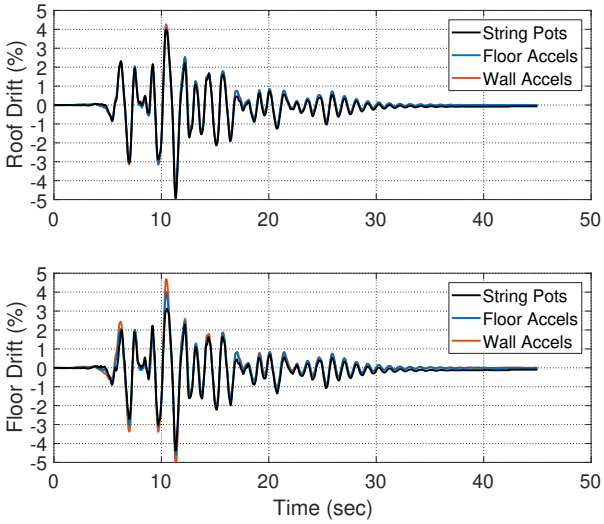

(c) Test 14 Northridge MCEx1.2

Figure 6.3: Drift time histories

6.5.1 Peak Roof and Floor Drifts

The maximum absolute displacement of each story was obtained from the drift time histories of the averaged floor accelerometers on each level of the specimen. The absolute maximum roof drift and floor drift for each test is shown in Table 6.2. The last column in the table is the ratio of roof drift to floor drift. This ratio is very close to 1.0 for all tests, meaning the behavior of the specimen is controlled by first mode response. This can also be seen in Figure 6.4, which plots the spectral acceleration at the building's approximate period of 0.9 seconds verses the roof drift and floor drift. The peak drifts are similar for both stores, also indicating primarily first mode response. The spectral acceleration at the building's period is representative of the earthquake intensity. There is a clear positive trend between the increasing spectral acceleration and the drift ratios. Note that in Figure 6.4, the hazard levels for each test are called out by color on the plot.

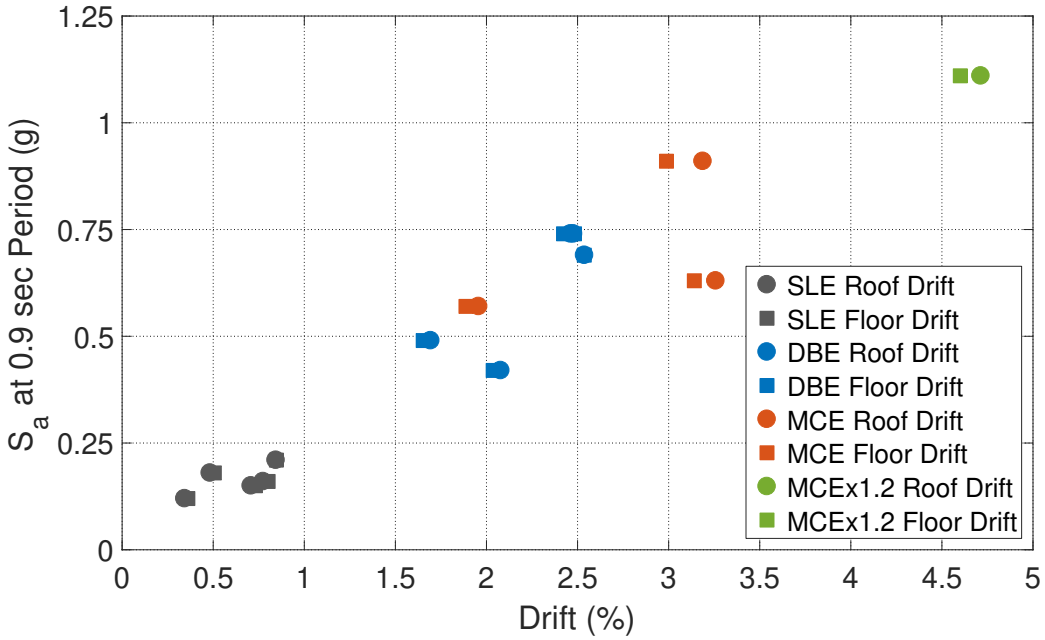

Figure 6.4: Peak drifts

Looking at the peak drifts in Figure 6.4, the SLE tests all experienced drifts ranging from

Table 6.2: Peak drifts

Test	**Hazard Level**	S_a **at 0.9 sec (g)**	**Floor Drift**	**Roof Drift**	$\frac{RoofDrift}{FloorDrift}$
1	SLE	0.15	0.73%	0.71%	0.97
2	SLE	0.16	0.80%	0.77%	0.97
3	SLE	0.18	0.51%	0.48%	0.95
4	SLE	0.12	0.36%	0.34%	0.95
5	DBE	0.69	2.54%	2.54%	1.00
6	DBE	0.74	2.48%	2.46%	0.99
7	SLE	0.21	0.85%	0.84%	1.00
8	DBE	0.74	2.42%	2.48%	1.02
9	DBE	0.49	1.65%	1.69%	1.02
10	DBE	0.42	2.04%	2.08%	1.02
11	MCE	0.57	1.89%	1.96%	1.04
12	MCE	0.91	2.99%	3.19%	1.07
13	MCE	0.63	3.14%	3.26%	1.04
14	MCEx1.2	1.11	4.60%	4.71%	1.02

0.36% to 0.85% and DBE tests experienced drifts between 1.65% and 2.54%. Two of the three MCE hazard level tests, test 12 and test 13, experienced very similar drifts, ranging between 3.0% and 3.26%, however, the third MCE level test,(test 11 Loma Prieta MCE) only experienced a drift of 1.96% due to the relatively low spectral acceleration at the 0.9 sec period. Finally, as expected test 14, Northridge MCEx1.2 experienced the highest drift of 4.71%. It should be noted that the drifts for SLE and MCE motions were lower than the predicted design values and are lower than what is allowed by performance objectives.

6.5.2 Residual Drifts

Because the wall panels experienced no CLT crushing, PT bars did not experience significant yielding until the last test, and minimal damage to the overall structure occurred, residual

drifts between tests and at the completion of testing were very small and almost negligible. Residual drifts were calculated using the average of the string potentiometers measuring global displacement in the direction of shaking. Results can be seen in Table 6.3. As seen in the table, residual drifts stayed below 0.06% for all tests before the 14^{th} test where the PT bars yielded. During the the 14^{th} test, residual drifts for the roof and floor were 0.07% and 0.10% respectively, which is still well within the 0.2% code based residual drift limit at DBE hazard level earthquakes [ASCE, 2010].

Table 6.3: Residual drifts after each test

Test	**Hazard**	**Residual Drifts**	
	Level	**Roof**	**Floor**
1	SLE	-0.02%	-0.01%
2	SLE	0.00%	0.00%
3	SLE	0.01%	0.00%
4	SLE	0.00%	-0.01%
5	DBE	0.06%	-
6	DBE	-0.01%	0.00%
7	SLE	0.01%	0.02%
8	DBE	-0.02%	-0.03%
9	DBE	0.03%	0.04%
10	DBE	-0.02%	-0.03%
11	MCE	0.00%	0.00%
12	MCE	-0.01%	-0.01%
13	MCE	-0.03%	-0.02%
14	MCEx1.2	-0.07%	-0.10%

6.5.3 Base Shear and Global Hysteresis

The performance of the specimen was also investigated by looking into the story shears. The story shears were calculated using two methods: 1) calculating the inertial force at each

story by applying Newton's second law, and 2) using the strain gauge readings from the wall-to-diaphragm shear connections to calculate the transferred shear force at each floor.

For method one a rigid diaphragm was assumed and Newton's second law was applied by multiplying the average of the accelerometer readings on each story by the mass associated with each story. The mass used for this calculation was slightly different than the design mass. This mass was calculated after the completion of the test by adding up the mass of everything that was actually installed on the structure. A factor of 1.025 was then then applied to the weight to account for the weight of instrumentation, hardware, and other pieces not accounted for. This resulted in a seismic mass for the roof and floor of 94.50 kips and 91.81 kips respectively (slightly different than the design mass of 91.64 kips for the roof and 74.24 kips for the floor).

The strain gauges installed on the tongue plate of the wall-to-diaphragm shear connections were used for the second method of calculating story shears. At each connection a strain gauge at 45° was installed on the steel tongue plate connecting the wall to the diaphragm. Assuming plane strain conditions, the max shear strain, γ_{max}, in each connection was calculated by multiplying the 45° strain gauge reading, ϵ_{45} by 2 as seen in Equation 6.4. The shear stress was found by multiplying the shear strain by the shear modulus, G as seen in Equation 6.5. To convert from shear stress to shear force, the equation for shear stress $\tau = \frac{VQ}{It}$, where V is the shear force, Q is the first moment area, I is the moment of inertia, and t is the thickness of the cross section at the point of interest, can be used. This equation quantifies the shear stress through a cross section. Knowing the maximum shear stress occurs at the centroid of a cross-section, the shear stress equation was used to solve for the maximum shear stress at the centroid of a rectangular cross-section. This was then rearranged to solve for the maximum shear force in the rectangular shear transfer connection, as seen in Equation 6.6, where A_{plate} is the cross sectional area of the tongue plate in the connection.

$$\gamma_{max} = 2\epsilon_{45} \tag{6.4}$$

$$\tau_{max} = \gamma_{max} G \tag{6.5}$$

$$V_{max} = \frac{2}{3} A_{plate} \tau_{max} \tag{6.6}$$

To calculate the shear force with the second method, Equations 6.4, 6.5, and 6.6 were rearranged to get the final equation used to convert the 45° strain gauge reading to shear force (Equation 6.7). For this derivation, a rectangular tongue plate cross-section was assumed. The plate actually had slightly rounded edges, but a rectangular cross-section was assumed for simplicity. For these calculations a shear modulus, G, of 11500 ksi was used for the structural steel and cross sectional areas of the tongue plates for the roof and the floor, A_{plate}, of 4.83 in^2 and 2.53 in^2, respectively, were used. To calculate the total story shear the sum of the shear forces from each of the four connections were summed together. The base shear was then calculated as the sum of both story shears. It should be noted that the strain gauges on the steel tongue plates were elastic.

$$V_{max} = \frac{2}{3} \left(2G\epsilon_{45}\right) \tag{6.7}$$

The results of both methods used to calculate the base shear were plotted against roof drift to produce the global hysteresis seen in Figure 6.5. The values in these plots are representative of the shear forces in one wall (half of the total structure). From the plots, it is clear that the base shear calculated from the accelerometer data produces larger values than the data from the strain gauges for all tests, which could be a result of a few sources of error. First, the mass of the building could have been smaller than what was estimated. Also, incorrect assumptions could have been made in the calculation of the force. The tongue plate may not have been acting in plane strain or the assumed modulus of elasticity could be

off. A big source of error could be attriubted to the instalation of the strain gauges. They were placed at roughly a 45° angle, but the placements could be slightly off, violating our assumptions made during calculations. In addition, there could be errors in the strain gauge readings causing these differences. Despite these differences and the resulting uncertainty in base shear, the two methods do show similar trends in the base shear versus drift response.

From the plots in Figure 6.5 the expected responses of the specimen at the different hazard levels is evident. Looking at the SLE tests (Figures 6.5a, 6.5b, 6.5c, 6.5d, and 6.5g), a relatively linear base shear verses drift response is present. Some slight nonlinear response is present due to minor yielding of the UFPs and slight panel rocking. In the DBE hazard level tests (Figures 6.5e, 6.5f, 6.5h, 6.5i, and 6.5j), definite nonlinear response and damping are visible in the hysteretic response. Test 11 (Figure 6.5k) also appears to have a similar amount of non-linearity and damping to the DBE hazard level tests even though it is an MCE scaled motion. As mentioned before, test 11 has a relatively low spectral acceleration at the buildings approximate period, explaining this lower response. The other MCE level tests (Figures 6.5l and 6.5m), show significant damping and nonlinear behavior as expected. Finally, the MCEx1.2 level ground motion (Figure 6.5n) shows considerable damping and non-linearity. This motion was also the only test that saw PT yielding. The PT yielding behavior is seen at the maximum negative drifts in the figure.

The peak base shear per wall and the drift at which they occur are summarized in Table 6.4. Included in the table are values of the story shears normalized to the total base shear. Based on the equivalent lateral force procedure in ASCE 7-10, the vertical distribution of seismic forces for the roof and the floor should be 0.69 and 0.31, respectively (see Appendix A). Examining the values in the table shows the vertical distribution appears to be about even between the two stories. For some of the tests, the vertical distribution is opposite of what we would expect in design, the floor is experiencing a higher proportion of the total seismic force than the roof. This could be the result of higher mode effects on the structure. The ratios are also relatively consistent between the accelerometer and strain gauge data, however, these peak values are just looking at a specific instant in time, so it may not

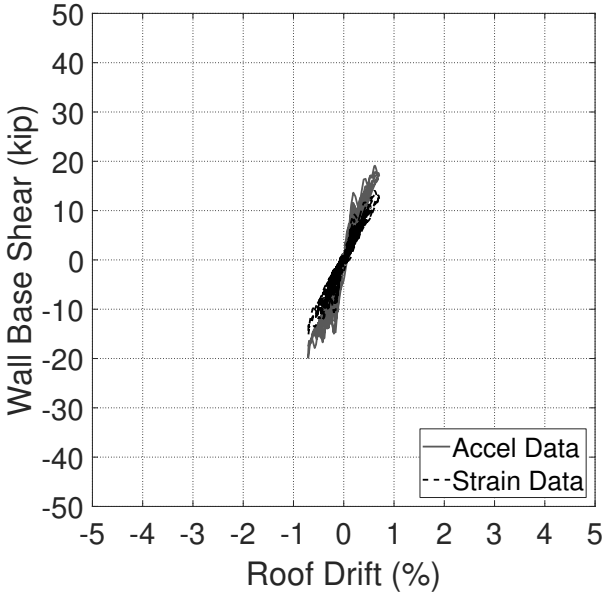

(a) Test 1 Loma Prieta SLE

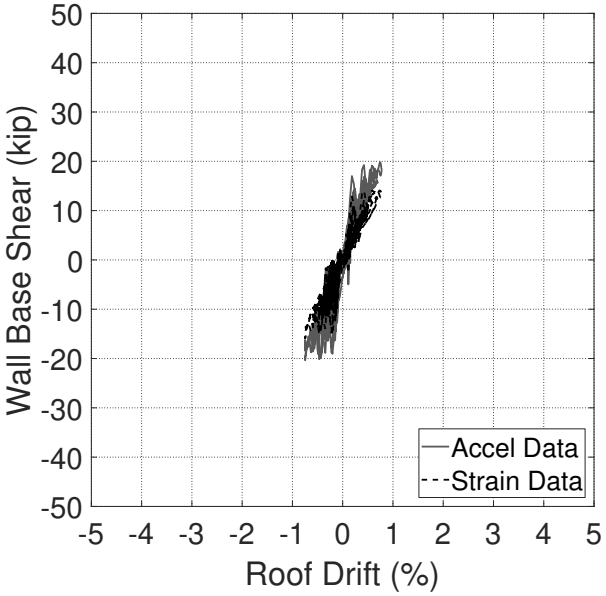

(b) Test 2 Loma Prieta SLE

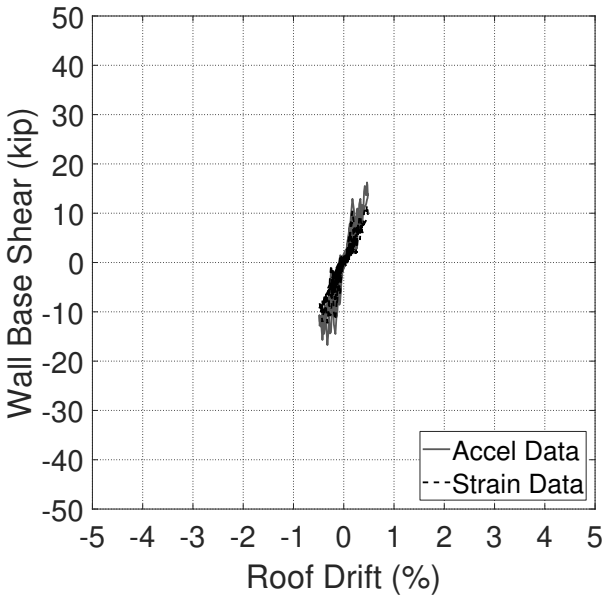

(c) Test 3 Northridge SLE

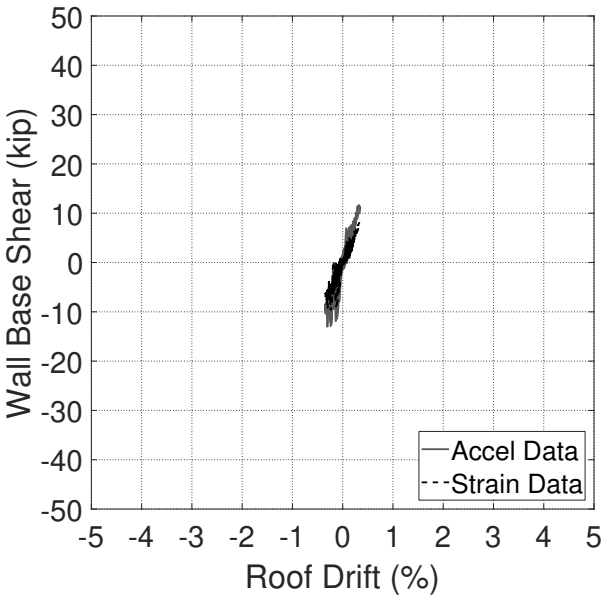

(d) Test 4 Superstition Hills SLE

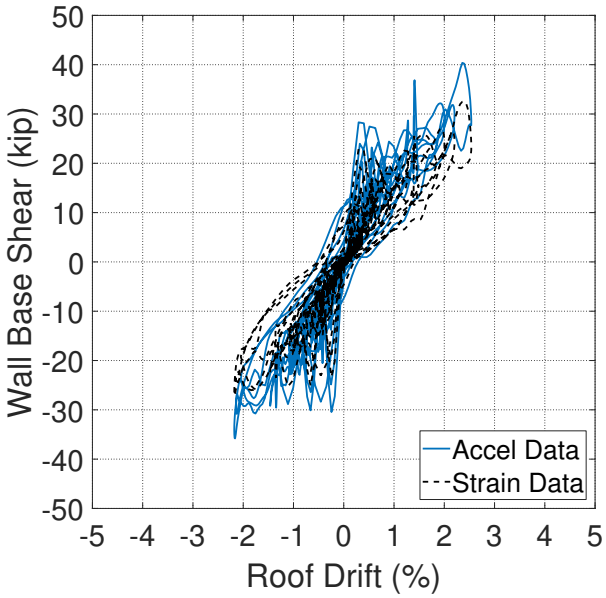

(e) Test 5 Northridge DBE

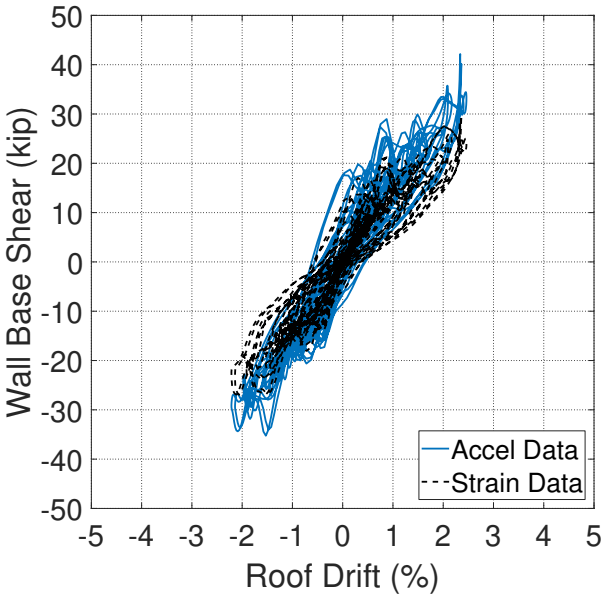

(f) Test 6 Northridge DBE

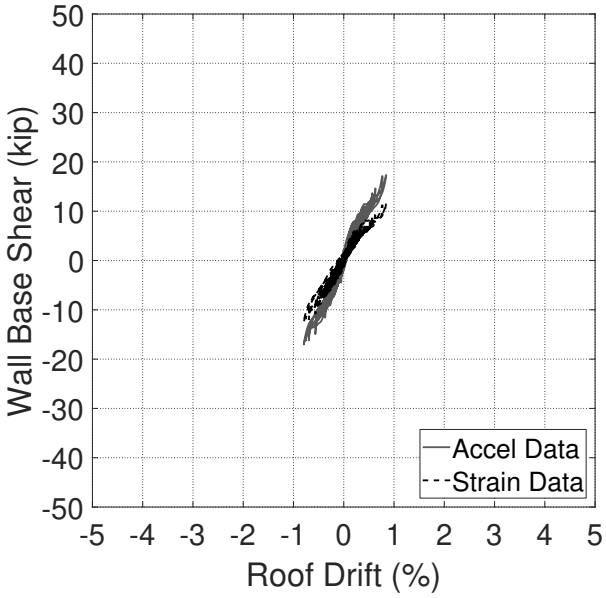

(g) Test 7 Imperial Valley SLE

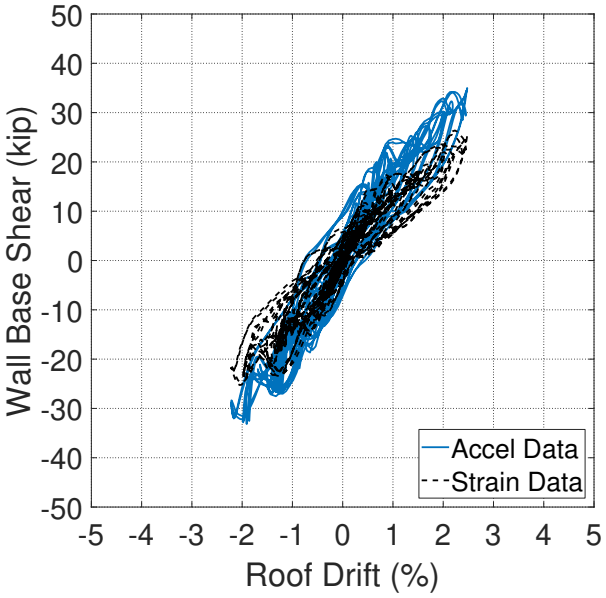

(h) Test 8 Northridge DBE

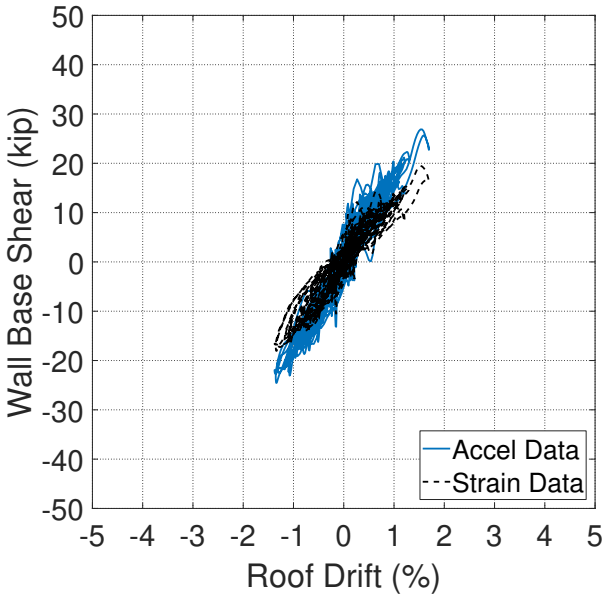

(i) Test 9 Loma Prieta DBE

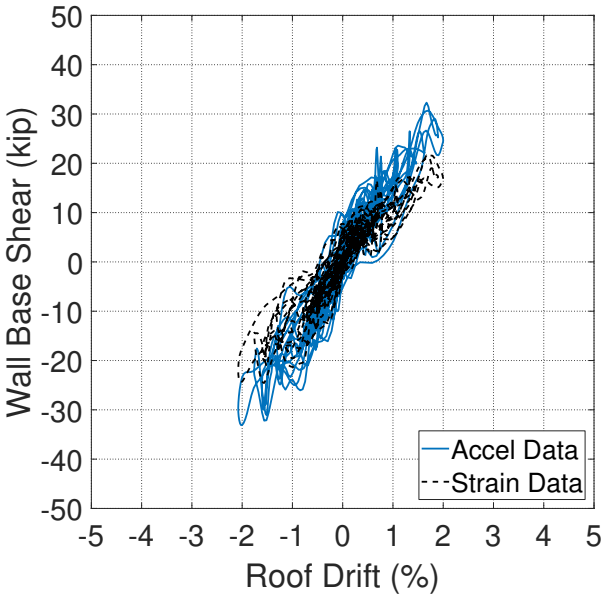

(j) Test 10 Superstition Hills DBE

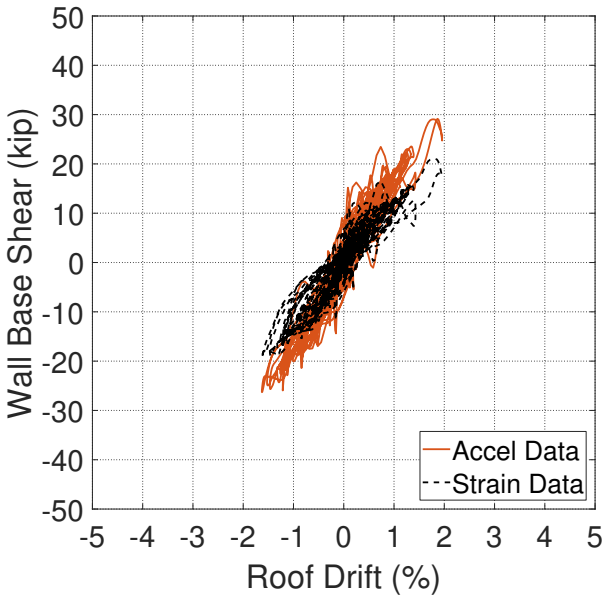

(k) Test 11 Loma Prieta MCE

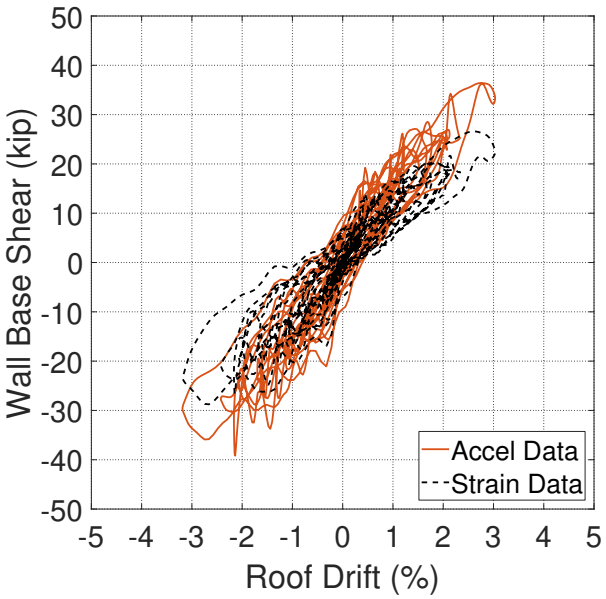

(l) Test 12 Northridge MCE

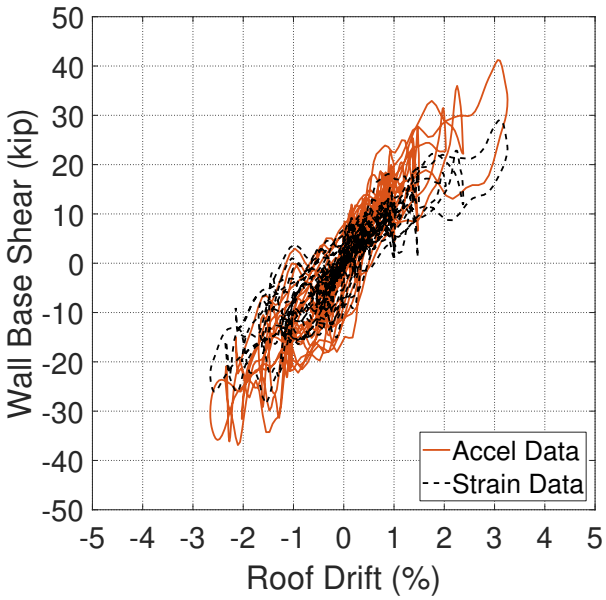

(m) Test 13 Superstition Hills MCE

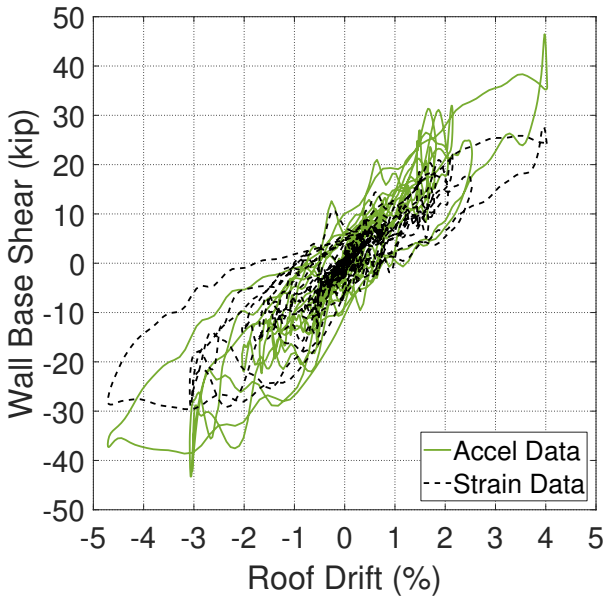

(n) Test 14 Northridge MCEx1.2

Figure 6.5: Base shear vs. roof drift hysteresis

accurately represent the response at all points in time. It should be noted that the exact base shear of the system is unknown, because assumptions are made in both cases, however, there is more confidence in the base shear calculations from the accelerometers because the accelerometers have proven to provide data that matches up with the other instruments on the specimen and because more assumptions are needed for the strain gauge base shear calculations.

Figure 6.6 plots peak base shear for both methods of calculation verses the spectral acceleration of the ground motion at the 0.9 second building period. All the SLE tests show similar base shear results and there is a clear jump in base shear values from SLE to DBE. The base shear values of the DBE, MCE, and MCEx1.2 hazard level motions show a general positive trend, but they start to level off as the specimen yields more.

Table 6.4: Peak story and base shears for each ground motion

Test	Sa at 0.9 sec (g)	From Accelerometer Data				From Strain Gauge Data			
		Drift at Peak V_{base}	$\frac{V_{roof}}{V_{base}}$	$\frac{V_{floor}}{V_{base}}$	Peak V_{base} (kips)	Drift at Peak V_{base}	$\frac{V_{roof}}{V_{base}}$	$\frac{V_{floor}}{V_{base}}$	Peak V_{base} (kips)
1	0.15	-0.71%	0.51	0.49	19.86	-0.71%	0.50	0.50	15.29
2	0.16	-0.75%	0.53	0.47	20.35	-0.75%	0.54	0.46	15.95
3	0.18	-0.33%	0.54	0.46	16.74	-0.33%	0.54	0.46	12.32
4	0.12	-0.30%	0.61	0.39	13.03	-0.24%	0.54	0.46	9.67
5	0.69	2.36%	0.32	0.68	40.38	2.40%	0.30	0.70	32.56
6	0.74	2.34%	0.21	0.79	42.16	2.36%	0.29	0.71	29.74
7	0.21	0.84%	0.57	0.43	17.35	-0.79%	0.62	0.38	12.60
8	0.74	2.48%	0.57	0.43	34.99	2.23%	0.45	0.55	26.38
9	0.49	1.56%	0.45	0.55	26.88	1.53%	0.43	0.57	19.49
10	0.42	-2.02%	0.47	0.53	33.12	-1.56%	0.21	0.79	24.60
11	0.57	1.86%	0.46	0.54	29.15	1.82%	0.48	0.52	21.01
12	0.91	-2.14%	0.20	0.80	39.18	-2.66%	0.49	0.51	28.77
13	0.63	3.07%	0.44	0.56	41.22	3.11%	0.42	0.58	29.13
14	1.11	3.98%	0.35	0.65	46.44	-3.02%	0.60	0.40	29.63

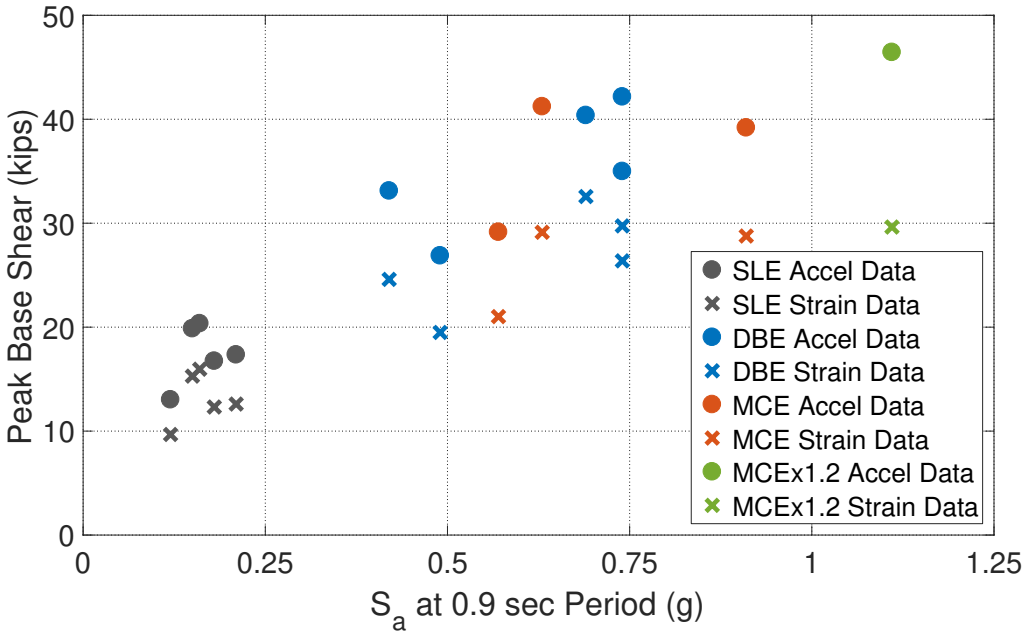

Figure 6.6: Peak base shear forces for each ground motion

6.5.4 Torsional Response

The specimen was built and designed to be symmetric with the center of mass and center of stiffness in the same location to eliminate any torsional response of the building. Rotation angles of the diaphragm were calculated, base on a procedure from Bahmani [2015], to insure no significant accidental torsion was present during testing. It should be noted that this calculation assumes a rigid diaphragm. Figure 6.7 shows the translation and torsional displacements of a rigid diaphragm. The rotation angles (θ_1, θ_2, θ_3, and θ_4) were calculated by finding the difference in displacements at two adjacent corners and dividing by the length of the diaphragm perpendicular to the displacements (Equation 6.8). Accelerometers at the corners of the diaphragms, measuring parallel and perpendicular to the direction of shaking were used to obtain the displacements. The average rotation angle was then calculated (Equation 6.9) for the floor and roof level.

$$\theta_1 = \frac{\Delta X_4 - \Delta X_1}{L_y}; \theta_2 = \frac{\Delta Y_2 + \Delta Y_1}{L_x}; \theta_3 = \frac{\Delta X_3 - \Delta X_2}{L_y}; \theta_4 = \frac{\Delta Y_3 + \Delta Y_4}{L_x}; \tag{6.8}$$

$$\theta_{Avg} = \frac{\theta_1 + \theta_2 + \theta_3 + \theta_4}{4} \tag{6.9}$$

Figure 6.8 shows the time history torsional response plots of the test specimen for an SLE, DBE, and the MCEx1.2 ground motion, plots for all the tests can be found in Figure B.3 in the Appendix. The plots show the torsional response for the floor and roof with respect to the ground. The floor rotations are about half for all the tests, showing that the rotation increases linearly up the height of the structure. The average floor rotation angle ranged from 0.0003 radians (0.02°) to 0.0014 radians (0.08°). The average roof rotation angle ranged from 0.0006 radians (0.03°) to 0.0026 radians (0.15°). Because the rotation angles are so small, it is assumed that the center of mass and center of stiffness coincide as designed and that torsional effects were negligible during tests and will therefore be ignored during analysis.

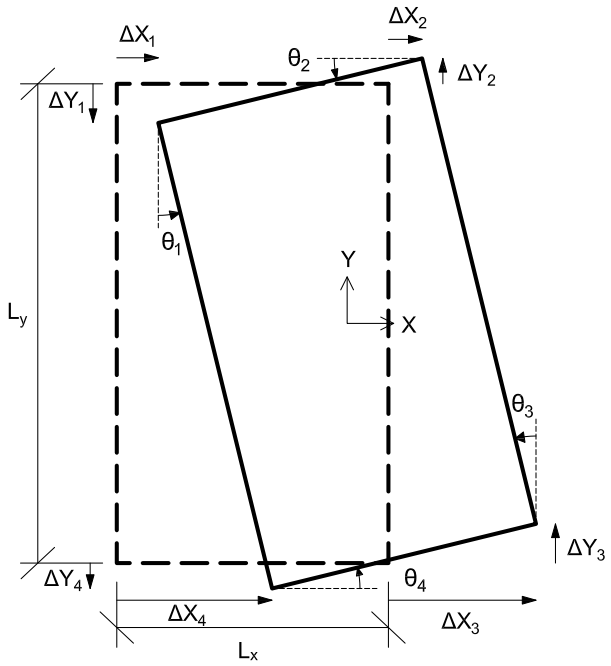

Figure 6.7: In-plane translational and torsional diaplacements of a rigid diaphragm

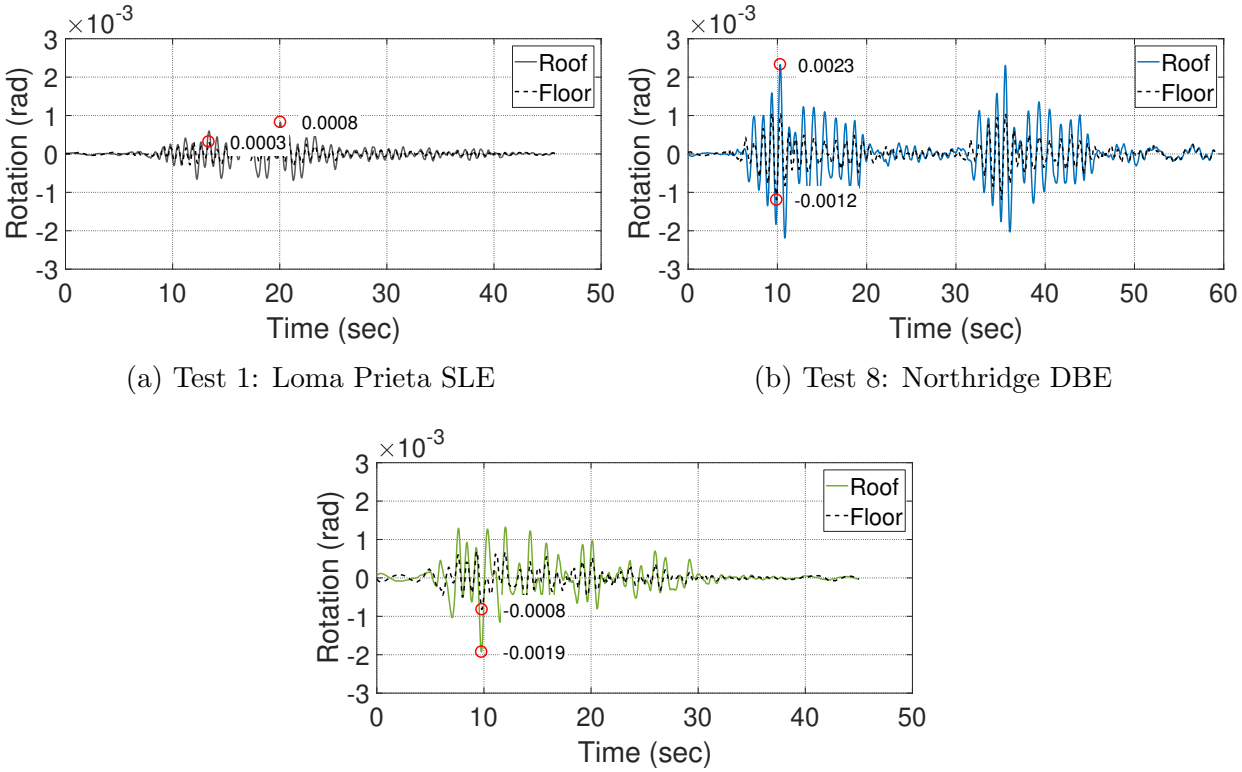

(a) Test 1: Loma Prieta SLE

(b) Test 8: Northridge DBE

(c) Test 14: Northridge MCEx1.2

Figure 6.8: Time history rotation response of test specimen

6.6 PT Bar Forces

An important characteristic of the system is the change in PT force throughout testing. PT bar forces were recorded using load cells, and as discussed earlier, the bars were periodically re-tensioned throughout the testing sequence, but significant bar forces were not lost until the last test when the PT bars yielded. Figure 6.9 shows plots of the PT force versus drift for an SLE, DBE, and the MCEx1.2 hazard level ground motion, plots for all the tests can be found in Figure B.4 in the Appendix. For each test, four plots are shown, each with plots for the north and south wall forces. Each of the four plots shows the sum of forces in the two bars located at the same location along the width of the wall, as denoted by the graphic on the figure. The expected yield force of 61.5 kips is also shown on the plot. This yield force is for both bars at the locations and was calculated based on the manufactures specified yield stress of 92 ksi.

From the plots in Figure 6.9, it is clear that the north and south walls behave similarly since there was very little torsion observed during testing. Small differences in the behavior of the north and south walls could be attributed to minor differences in the material properties between each bar or due to differences in installation and construction of the two walls. The idealized response of a fully rigid rocking wall with PT bars located at the center of the wall width is shown in Figure 6.10. The response of the PT bars in the test specimen differed for a few reasons. First, bars were not located at the center of the wall width, they were spaced 10 inches apart, so bars further from the rocking toe will experience higher forces. For example in Figure 6.9, PT bars 1 and 3 saw higher forces than bars 2 and 4 at positive drifts. The second reason why the plots differ from the idealized case is because the wall is not rigid. Because the CLT wall panels are elastic, they deform at the rocking corners which can cause the flattened portion of the plots around 0% drift. This flattened portion of the plot is also a result of the elastic shear and flexural deformations in the panel. The wall panels actually deform prior to rocking because of these deformations. In the tests, the flattening of the plots at 0% drift (i.e., the regions were the PT force is constant despite

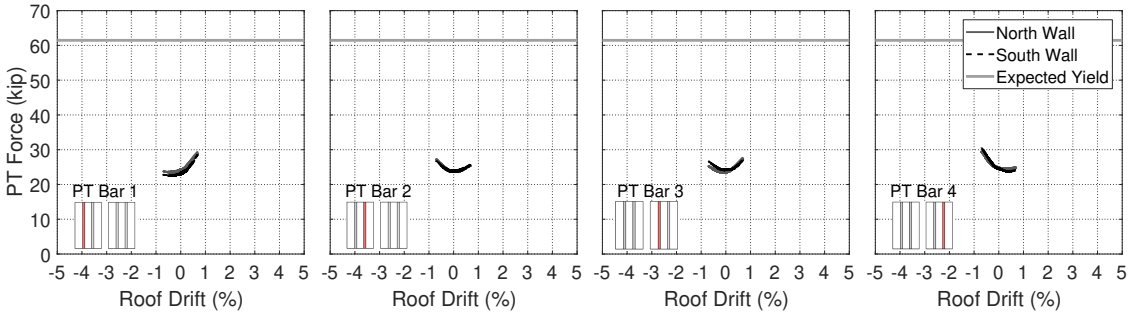

(a) Test 1 Loma Prieta SLE

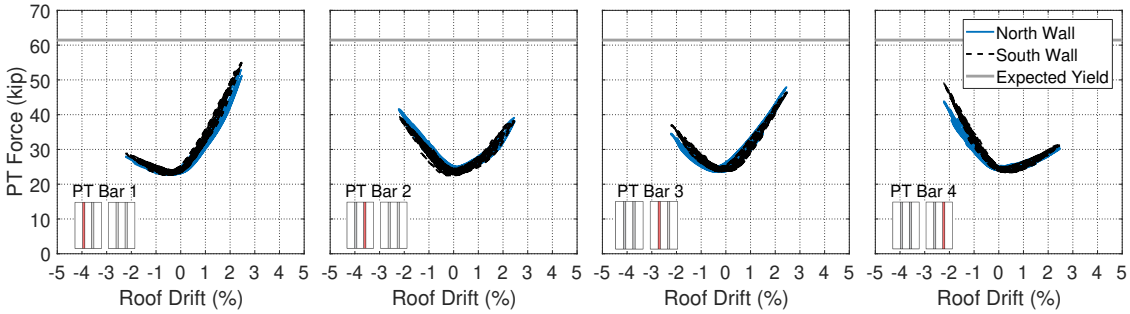

(b) Test 8 Northridge DBE

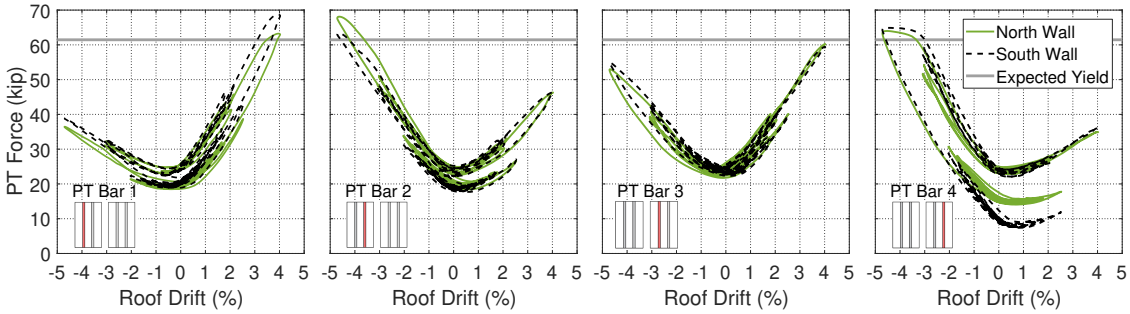

(c) Test 14 Northridge MCEx1.2

Figure 6.9: Base shear vs. roof drift hysteresis

increasing drift) are also a result of yielding of the base beam.

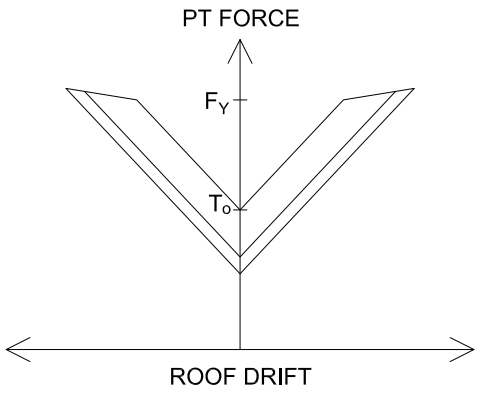

Figure 6.10: Idealized PT force verces drift response for a rigid rocking wall system

The overall peak PT forces and yield force ratios for each test are listed in Table 6.5. A plot of the Peak PT forces for each test verses the ground motion's spectral accelerations at the building's period are plotted in Figure 6.11. The PT bars were initially stressed to about 40% of their yield force. SLE level tests lead to PT fores that were about 50% of their yield force while DBE tests lead to peak to yield force ratios between 70% to 90%. The two larger MCE hazard level tests (test 12 and 13) lead to PT force right above the expected yield force, however, as discussed earlier these tests did not actually cause much yielding in the bars, meaning the actual yield stress was probably slightly higher than the specified yield force. In the MCEx1.2 hazard level testthe PT bar forces were 12% above the expected yield force, which lead to significant yielding as seen in Figure 6.9c. It should be noted that these PT forces are well within the performance objective limits used for design of the specimen.

Table 6.5: Peak PT Forces for each ground motion

Test	Hazard Level	S_a at 0.9 sec (g)	Drift at Peak PT Force	Peak PT Force (kips)	$\frac{Peak\ PT\ Force}{PT\ Yield\ Force}$
1	SLE	0.15	-0.71%	30.83	0.50
2	SLE	0.16	-0.75%	30.75	0.50
3	SLE	0.18	-0.48%	27.36	0.45
4	SLE	0.12	-0.34%	26.07	0.42
5	DBE	0.69	-	-	-
6	DBE	0.74	2.46%	54.02	0.88
7	SLE	0.21	0.84%	31.84	0.52
8	DBE	0.74	2.48%	55.00	0.89
9	DBE	0.49	1.69%	42.57	0.69
10	DBE	0.42	-2.08%	48.28	0.79
11	MCE	0.57	1.95%	46.47	0.76
12	MCE	0.91	3.01%	62.48	1.02
13	MCE	0.63	3.24%	63.68	1.04
14	MCEx1.2	1.11	3.96%	68.68	1.12

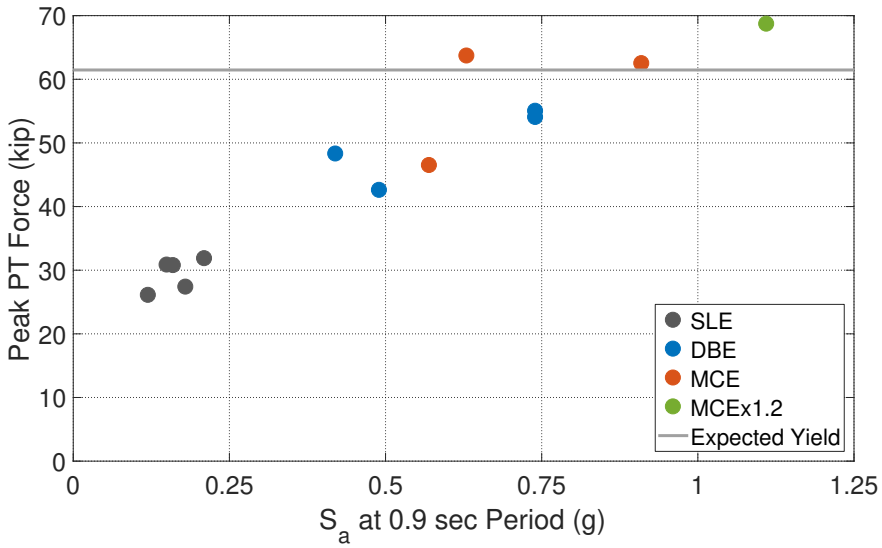

Figure 6.11: Peak PT forces for each ground motion

6.7 Wall Panel Base Deformation

The linear potentiometers installed at the base of the rocking wall panels were used to investigate the deformations at the base of the wall throughout testing. This was also important to look at because the base beam that the walls sat on experienced unexpected deformations. As seen in Figure 6.12, eight linear potentiometers were placed on the south face of the North-West (linear pots. 1-8) and South-East (linear pots. 9-16) wall panels, and two linear potentiometers were placed on the south face of the North-East and South-West wall panels. As mentioned earlier, these potentiometers were intended to measure the uplift at the base of the wall in the positive direction, as well as the elastic deformations and crushing of the wall panels in compression in the negative direction. However, because the base beams were not stiff enough, when the wall panels went into compression the base beam deformed so the linear potentiometers measured both the base beam deformation and the deformations in the wall panels. Plots of the measured time history data from these linear potentiometers can be found in Figure B.5 in the Appendix.

To get a better idea of how the base beam deformed during testing, the deformation from linear pots. 1-8 on the north wall, and linear pots. 9-16 on the south wall were plotted at the point of peak positive drift and peak negative drift. Figure 6.13 shows these wall panel base deformations for an SLE, DBE, and the MCEx1.2 hazard level tests and the plots for all ground motion tests can be found in Figure B.6 in the Appendix. In each figure, the top two plots show the base deformation for the North-West panel and the South-East panel at peak positive drift and the bottom plots shown the deformation at peak negative drifts. For most tests the uplift and downward deformation is greater at the exterior wall corners (exterior corners are located at a panel width of 0 inches for the North-West wall panel and 60 inches for the South-East wall panel). These deformations are greater at the exterior corners because the shear force from the UFPs decrease the compression force at the interior corners (see free body diagram in Figure 3.7). The downward deformations from the base beam are also smaller because the base beams were stiffened more heavily at these locations.

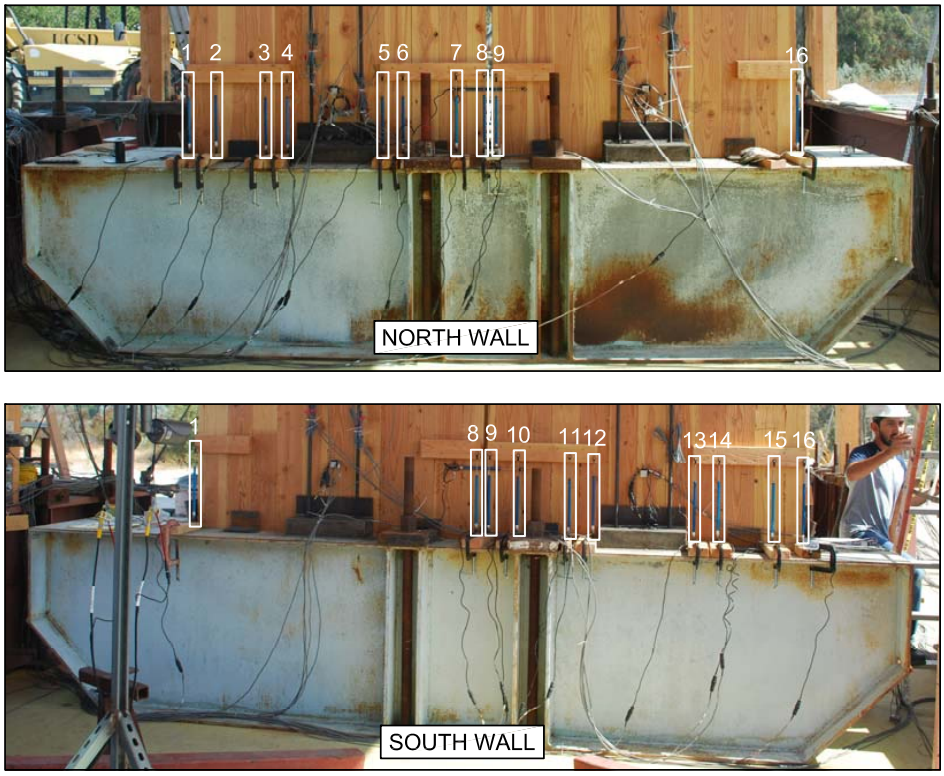

Figure 6.12: Linear potentiometer locations used to measure uplift and downward deformations of the rocking wall panels during testing

From these plots the deformation distribution across the base of the wall panel is relatively linear, showing very little deformation was a result of deformations in the panel, and most of the deformations were due to the base beam deforming and yielding. On the plots, a line showing $\theta_{drift} b_w$ is also plotted. This line represents the peak base beam deformation that would have occurred if the wall panels were completely rigid and rocked on top of a rigid foundation. For every ground motion, the actual measured uplift is below the $\theta_{drift} b_w$ line.

Table 6.6 summarizes the peak uplift and peak downward deformations experienced for each ground motion as well as the drift at which it occurred. Figure 6.14 peak uplift values verses the spectral acceleration at the building's period (Figure 6.14a) and peak downward displacements (Figure 6.14b) for each ground motion. A clear positive trend is visible for both plots. The wall panels experienced uplift deformations as large as 2.24 inches and downward deformations as large as 0.68 inches.

Table 6.6: Peak displacements at wall base

Test	**Hazard Level**	S_a **at 0.9 sec** (g)	**Peak Uplift**		**Peak Downward Def.**	
			drift	**deformation (in)**	**drift**	**deformation (in)**
1	SLE	0.15	-0.71%	0.25	0.70%	-0.09
2	SLE	0.16	-0.75%	0.26	0.77%	-0.09
3	SLE	0.18	0.48%	0.15	0.48%	-0.07
4	SLE	0.12	0.34%	0.08	0.34%	-0.05
5	DBE	0.69	-	-	-	-
6	DBE	0.74	2.46%	1.08	2.46%	-0.33
7	SLE	0.21	0.84%	0.32	0.84%	-0.18
8	DBE	0.74	2.48%	1.10	2.48%	-0.34
9	DBE	0.49	1.69%	0.72	1.69%	-0.27
10	DBE	0.42	-2.08%	0.93	2.00%	-0.29
11	MCE	0.57	1.96%	0.85	1.96%	-0.29
12	MCE	0.91	-3.19%	1.38	-3.19%	-0.44
13	MCE	0.63	3.26%	1.47	3.26%	-0.44
14	MCEx1.2	1.11	-4.71%	2.24	-4.71%	-0.68

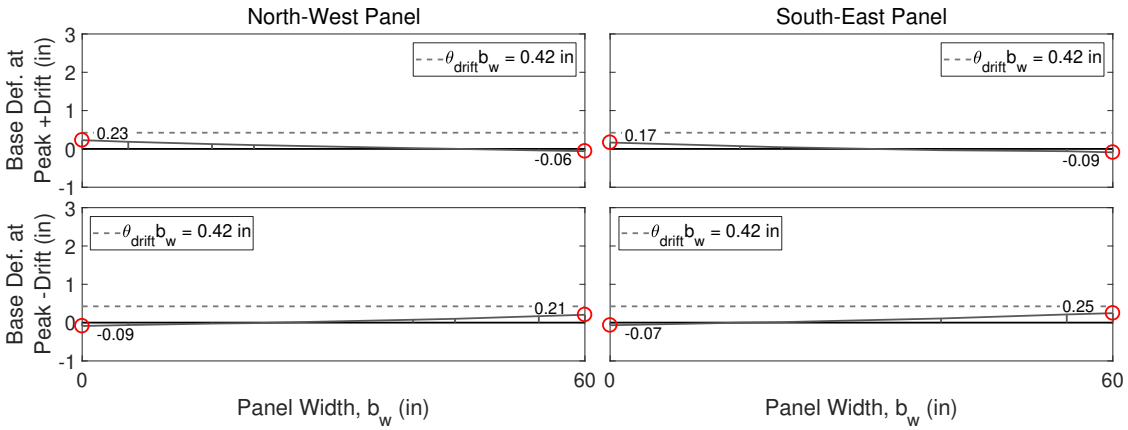

(a) Test 1 Loma Prieta SLE

(b) Test 8 Northridge DBE

(c) Test 14 Northridge MCEx1.2

Figure 6.13: Wall panel base deformation

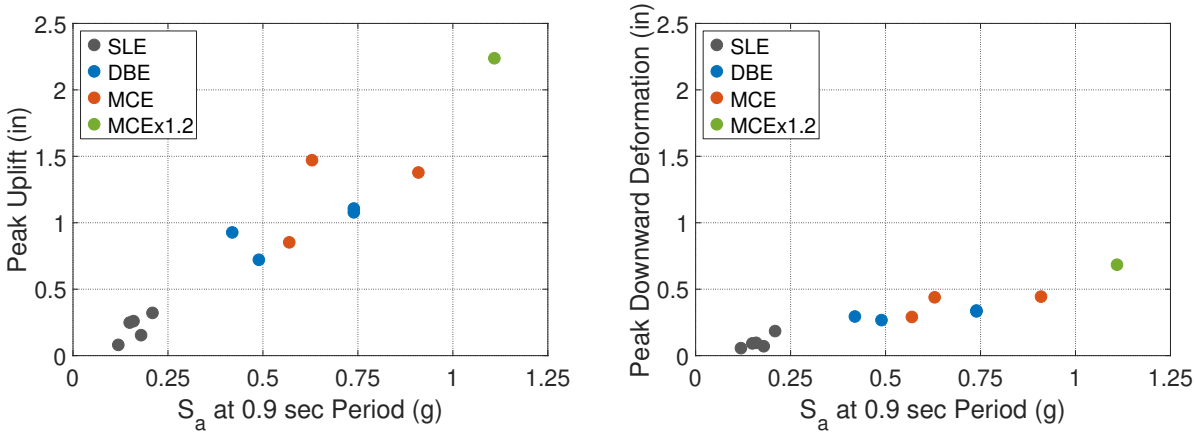

(a) Peak uplift deformation

(b) Peak downward deformation

Figure 6.14: Peak deformations at the wall panel bases for each ground motion

6.8 UFP Energy Dissipaters

String potentiometers were used to measure the deformation of the two UFP ends relative to each other. To obtain the UFP forces, the measured displacements from the string potentiometers were inputted into a Menegotto-Pinto material model (Steel02 material) from OpenSees [Mazzoni et al., 2009]. The model was originally calibrated using material test results by Ganey [2015]. Figure 6.15 shows the resulting UFP force verses the ratio of displacement to yield displacement for UFPs in an SLE, DBE, and the MCEx1.2 hazard level tests. The yield displacement was determined by dividing the initial stiffness calculated with equation 3.3 by the plastic force calculated with Equation 3.2. Plots for all the tests can be found in Figure B.7 of the Appendix. A ratio of displacement over the yield displacement was used to quantify a measure of ductility. Each coupled wall had five UFPs spaced up the height of the wall. The top, middle, and bottom UFPs were instrumentated with the string potentiometers. However, the string potentiometers measuring the top and bottom UFP displacements failed during many of the tests, so only the measurements for the middle UFP are shown in the plots. The plots also include a line showing the estimated plastic force

of the UFP which was 5.24 kips, calculated per Equation 3.2.

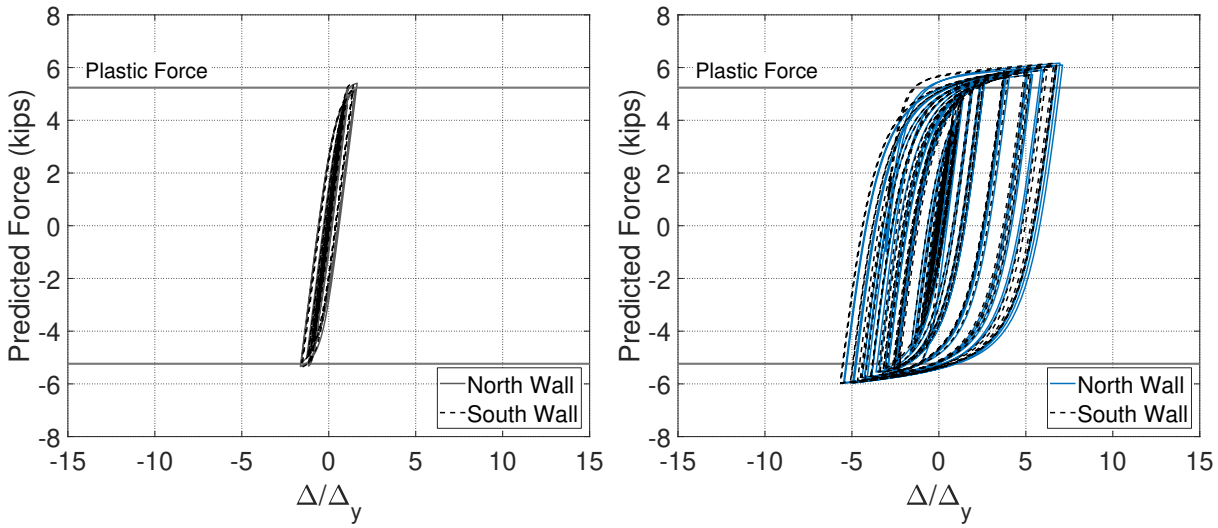

(a) Test 1 Loma Prieta SLE

(b) Test 8 Northridge DBE

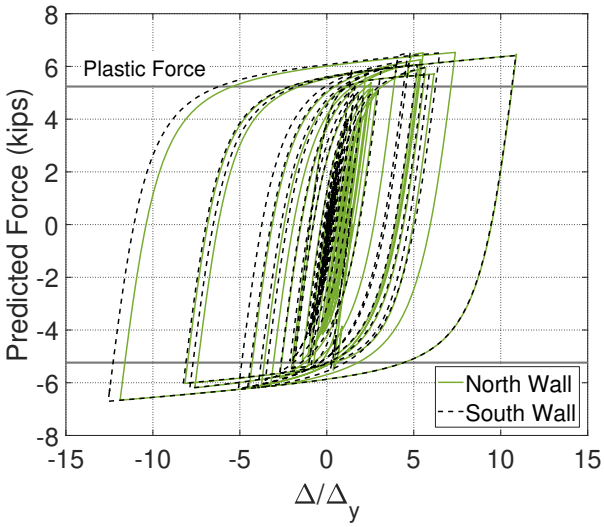

(c) Test 14 Northridge MCEx1.2

Figure 6.15: Predicted UFP hysteresis

Table 6.7 summarizes the peak UFP forces for each ground motion and the drift at which they occur. The table also includes the ratio of peak UFP force to the expected yield force of the UFP.In addition, a column showing the ratio of peak UFP displacement

to the estimated yield displacement is also shown to represent the ductility demands. These results are also summarized in Figure 6.16 which plots the ratio of peak UFP displacement to the yield displacement verses the spectral acceleration at the buildings period for each test. From the plots and table, it is clear that the UFPs reach their yielding force at very small deformations. The UFPs reached their yield force in all tests except test 4, an SLE hazard level earthquake. For all the SLE hazard level tests, the UFPs are behaving mostly linearly. At DBE, MCE, and MCEx1.2 hazard levels, the UFPs behave non-linearly and show significant energy dissipation. Also, from Figure 6.16, an increase in energy dissipation with hazard level is also seen. It should be noted that the values in the plots and in the table are for a single UFP on one wall. Because there were five UFPs spaced evenly up the height of the wall, the total expected force per wall from the UFPs would be five times the values shown in the table and plots. In should also be noted that the force per UFP is much smaller than the forces seen in the PT bars, so they will not dramatically affect the total moment in the wall. Because only minor UFP yielding occurred during SLE tests, the observed behavior of the UFPs met design performance objectives.

Table 6.7: Peak UFP Forces

Test	Hazard Level	S_a at 0.9 sec (g)	Drift at Peak PT Force	Peak UFP Force (kips)	$\frac{Peak\ UFP\ Force}{UFP\ Yield\ Force}$	$\frac{\Delta_{max}}{\Delta_y}$
1	SLE	0.15	0.68%	5.41	1.03	1.63
2	SLE	0.16	-0.75%	5.50	1.05	1.60
3	SLE	0.18	0.48%	5.39	1.03	1.06
4	SLE	0.12	0.34%	3.54	0.68	0.68
5	DBE	0.69	2.53%	5.99	1.14	6.76
6	DBE	0.74	2.34%	6.12	1.17	6.59
7	SLE	0.21	-0.76%	5.44	1.04	1.84
8	DBE	0.74	2.39%	6.17	1.18	6.96
9	DBE	0.49	1.69%	5.71	1.09	4.67
10	DBE	0.42	1.98%	5.88	1.12	5.32
11	MCE	0.57	1.95%	5.81	1.11	5.35
12	MCE	0.91	-3.17%	6.27	1.20	8.66
13	MCE	0.63	3.24%	6.28	1.20	9.21
14	MCEx1.2	1.11	-4.17%	6.70	1.28	11.68

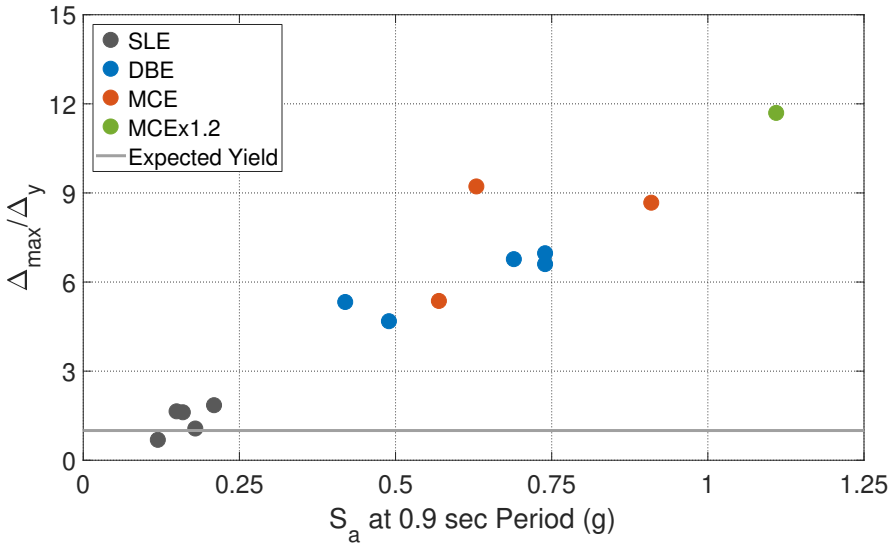

Figure 6.16: Ratio of peak UFP displacement to expected yield displacement for each ground motion

6.9 Comparison of Results to Performance Objectives and Predicted Behavior

Overall, the test specimen performed very well through the fourteen ground motion tests and met all design performance objectives for CLT base crushing, PT bar yielding, and UFP yielding. However, the specimen experienced relatively low forces compared to what was predicted in design. Drift limits for the performance objectives for the SLE and MCE tests were achieved and the 2% drift limit for the DBE motions was only slightly exceed. This section will discuss how well the specimen performed in terms of the performance objectives and the analyzed results will be compared to the predicted design.

6.9.1 Comparison of Results to Performance Objectives

As mentioned, all performance objectives for CLT crushing at the base, PT bar yielding, and UFP yielding were met. Figure 6.17 summarizes the modified performance objectives used for design (from Section 4.2.3) and shows the observed performance of the specimen with corrections made in green. Based on the performance objectives, CLT crushing could have occurred during DBE ground motions, however CLT crushing was not observed for any of the tests. In addition, PT yielding did not occur until the MCEx1.2 ground motion was run, which meets performance objectives, but PT yielding could have occurred during MCE level tests and performance objectives still would have been met. UFP yielding also met all performance objectives. Minor yielding was observed during SLE ground motions and major yielding was observed during DBE and MCE level ground motions. Observed drifts for the SLE and MCE level tests stayed below the specified drift limits, and the DBE level ground motions mostly stayed close to the specified 2% drift limit. Four out of the five DBE tests exceeded the drift limit, but the average of all the DBE tests was only 2.24% which just exceeds the performance objectives slightly. High drifts during the DBE tests were most likely a result of the flexible base beam that increased the specimens period and in turn increased building drifts. Also, if a rigid foundation was used during testing, then more damage would have probably occurred, especially with crushing of the CLT wall base.

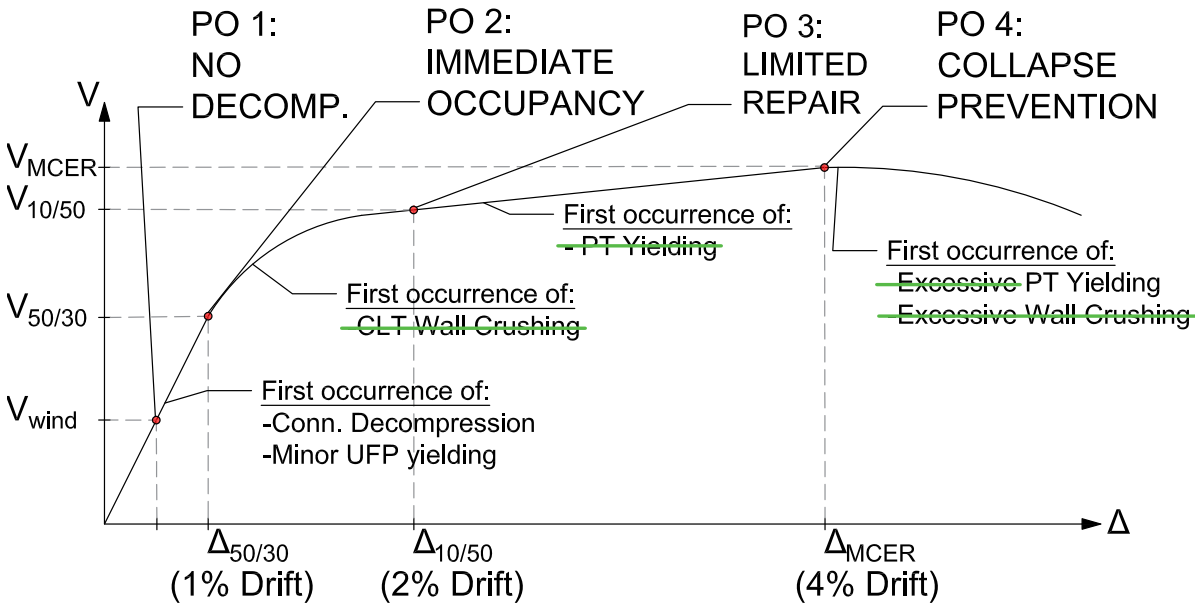

Figure 6.17: Summary of achieved performance objectives

However, because no crushing was observed in any of the tests, the CLT crushing performance objectives would have likely still been achieved with the rigid foundation base beam.

6.9.2 Comparison of Results to Predicted Behavior

As discussed in Section 4.2.3, the performance of the CLT rocking walls were predicted using the design procedure presented in Chapter 3. To compare the predicted design performance to the observed and instrumented response, base shear force per wall was used. The Figure 6.18 plots the measured base shear per wall at peak drift verses the peak drift for each test. Measured base shear forces calculated from both accelerometer data and strain gauge data is provided in the figure. The predicted design performance from 4.2.3 is also plotted on 6.18. Calculated test results show similar trends to the predicted design performance, but for almost all tests the observed base shear force is lower than the design values. Again, this is most likely due to flexible foundation base beam that decreased the stiffness of the structure. It should be noted that in Figure 6.18, observed response calculated from the

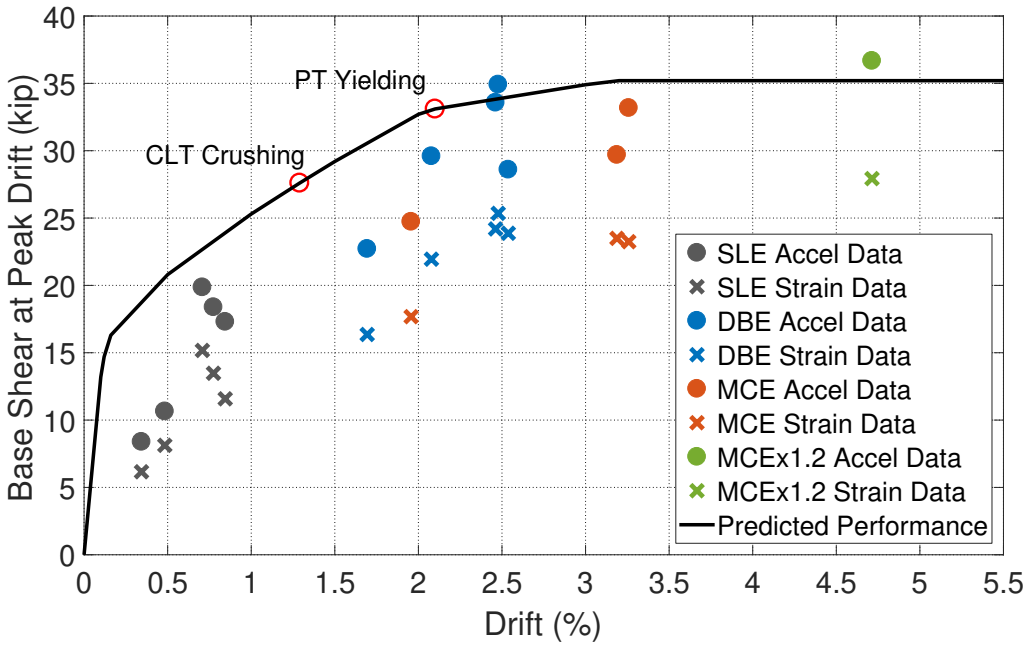

Figure 6.18: Summary of achieved performance objectives

accelerometer data and the strain gauge data is shown. However, there is more confidence in the measurements calculated from accelerometer data (as discussed in Section 6.5.3), which are closer to the predicted response than the forces calculated from the strain gauge data.

Chapter 7
SUMMARY AND CONCLUSIONS

7.1 Overview

The purpose of this research was to perform dynamic tests on a large-scale building with coupled post-tensioned rocking CLT shear walls as the lateral system and to study how the response and behavior compared to the behavior predicted by the performance-based design procedure. The rocking CLT shear walls utilized unbonded post-tensioned bar connections, UFP energy dissipation devices, and a slotted pin connection to transfer force between the rocking CLT walls and the CLT diaphragm. This chapter contains a brief summary of the work completed, the conclusions drawn from the tests and data analysis, and suggestions for future work to be completed.

7.2 Summary

A summary of the work completed in this thesis is presented here:

7.2.1 Rocking CLT Wall Behavior

Building on prior research, the rocking behavior of CLT walls is summarized as follows: under small lateral loads before rocking, the walls behave elastically until the decompression moment, M_{dec} is reached. After the decompression moment, the stiffness of the system is reduced and the panels begin to rotate as a gap, θ_{gap} forms at the base of the wall. As θ_{gap} opens, the PT bars elongate providing the recentering moment necessary for the wall system. As the coupled wall panels move relative to each other, the UFPs coupling the walls deform. The yielding of the UFPs occur at relatively low drifts and once they yield they dissipate energy in the system, decreasing accelerations. However, the forces from the UFPs

are small relative to the forces from the PT bars, so their contribution to the overall base moment is not large. During this process, the CLT wall panels compress on the rocking corner over a compression zone. From prior research, the CLT is assumed to have an elastic, perfectly-plastic behavior and the equivalent compression force acts at the centroid of this compression zone.

To achieve the desired performance objectives for the CLT rocking wall systems, a connection between the wall and diaphragm that transfers shear force while accommodating the displacements is necessary. It is also necessary to design a gravity frame that can also accommodate these displacements.

7.2.2 Performance-Based Design Procedure for CLT Rocking Walls

A performance-based design procedure based on previous research on CLT rocking walls was adapted for this project. The suggested performance objectives for a rocking CLT wall lateral system are as follows:

- **PO 1: Wind Loading** No wall decompression under design wind loading
- **PO 2: Immediate Occupancy** No repair of the system is required after a 50% in 50 year hazard level earthquake event
- **PO 3: Limited Repair** Only minimal repairs such as UFP replacement are required after a 10% in 50 year hazard level earthquake event and the system fully re-centers
- **PO 4: Collapse Prevention** Damage to the system is limited to prevent building collapse during a 2% in 50 year hazard level earthquake event

The design procedure utilized for this research is summarized in the following steps:

1. Determine seismic demands

2. Determine system parameters and dimensions including the CLT wall dimensions and the PT bar properties

3. Calculate the decompression moment

4. Select UFP dimensions for the desired dissipation ratio

5. Check that the elastic seismic moment demands from the step 1 are smaller than the elastic moment capacity (the decompression moment) from the step 3

6. Determine the full moment-drift response using the cross-section analysis procedure

7. Check if design meets performance objectives

7.2.3 Design of Test Specimen with Modified Performance Objectives

The test specimen presented in this thesis was designed using the performance-based design procedure outlined above. The specimen was two stories with a first floor story height of 12 feet and a second floor story height of 10 feet. The specimen had a full glulam gravity frame with CLT diaphragms. The lateral system consisted of two CLT rocking walls that each had two 24'x5'x6$\frac{7}{8}$" CLT wall panels coupled together with five UFP energy dissipating devices designed for an energy dissipation ratio of 40%. Each wall panel was post-tensioned with four high-strength steel rods with an initial PT force equal to 40% of it's yield force. The wall panels were connected to the diaphragm using low friction slotted pin connections and the glulam gravity frame was designed to accommodate the relatively large drifts.

The performance objectives outline above are intended for larger buildings than the test specimen in this thesis, so modified performance objectives were created for design. For the modified performance objectives, hazard levels were first modified to agree with the recently released document from the Los Angeles Tall Buildings Structural Design Council. In addition, because the the test specimen was shorter than the what was intended in the design procedure, drift limits for CLT crushing at the base and PT bar yielding were decreased.

A test sequence of fourteen ground motions was used, consisting of five service level earthquakes, five design based earthquakes, three maximum considered earthquakes, and one earthquake that was 20% larger than a maximum considered earthquake.

7.2.4 Results of of the Dynamic Tests and Evaluation of Performance Objectives

Extensive data analysis was performed on the test specimen. The main results of the tests are summarized below:

- The fundamental period of the building, determined from white noise tests, was around 0.9 seconds which is relatively long for a two-story structure, however this increase in period can be attributed to the flexible rocking wall base beam that acted as the foundation for the lateral system.

- Using decay of motion calculations on accelerations from free vibration tests, the damping coefficient was calculated as 1.92%.

- Peak roof and floor drifts ranged between 0.5% and 0.9% for SLE level tests, 1.7% and 2.5% for DBE level tests, 1.9% to 3.3% for MCE level tests, and reached 4.7% drift in the MCEx1.2 level test. Also, roof drifts and floor drifts were very similar for all tests showing the response was controlled by the first mode.

- All tests before the MCEx1.2 level test had residual drifts under 0.06% and for the MCEx1.2 level test the residual drift was 0.10%, which is still well within the 0.2% performance objective limit for residual drifts.

- Base shear forces calculated from strain gauges differed from those calculated from accelerometer data, however both produced similar trends and there was more confidence in the measurements from the accelerometers. SLE level tests remained mostly linear, non-linearity was present in DBE level test with some damping, and MCE level tests showed considerable non-linearity and damping.

- Torsional response was so small that it was considered negligible for analysis purposes.
- The PT bars did not yield until the MCEx1.2 level test.
- No CLT crushing at the base of the wall panels was observed at the base of the wall panels, but the rocking wall base beam saw significant permanent deformation at the end of testing.
- UFPs yielded at very low drifts. They experienced significant non-linearity and damping starting in DBE level tests.

Overall, the test specimen performed very well through the fourteen ground motion tests and the observed and instrumented response of the test specimen met all performance objectives for PT bar yielding, CLT crushing at the base, and UFP yielding. In terms of building drift response, the 1% drift limit for SLE hazard level tests were met, as well as the 4% drift limit for MCE hazard level tests. The DBE hazard level tests had a drift limit of 2% which was exceeded for four of the five DBE tests, but only had an average drift of 2.24% for all the DBE tests which only exceeds the performance objective slightly.

The predicted base shear response calculated from the design procedure was slightly higher than the measured base shear forces. The lower measured values were most likely a result of the flexible foundation decreasing the overall stiffness of the structure and in turn, decreasing the base shear forces.

7.3 Conclusions

A full-scale test of a two-story timber building with a glulam gravity frame and a lateral system made of coupled post-tensioned rocking CLT walls with UFP energy dissipating devices was completed and showed promising results for the future 10-story shake table test and for the future of tall CLT construction. In the test, the CLT rocking walls provided the system with the strength, energy dissipation, and recentering necessary to achieve the design

performance objectives. In addition, other details in the design such as the gravity frame design, the diaphragm design, and the connection details (specifically wall to diaphragm slotted pin connection and the slotted gravity frame connections) also performed successfully and were able to accommodate the large deformations, showing that a system like this shows great potential for implementation.

The walls were designed using the proposed procedure and the specimen responded very closely to the predicted response from that procedure. Base shear forces were slightly smaller than what was predicted, however this is due to the flexible rocking wall base beam that decreased the stiffness of the whole specimen. The proposed procedure also specified performance objectives at three different seismic hazard levels for PT bar yielding, CLT crushing at the base, and UFP yielding which were all achieved. Included in the performance objectives were target drift limits which were met for the service level earthquakes and the maximum considered earthquakes. The 2% drift limit for the design based earthquakes was slightly exceeded.

Overall the system showed a very ductile response. Drift controlled the design at the design based earthquake level and the system was able to fully re-center at all hazard levels. It is believed the base beam, that acted as the foundation for the rocking walls, protected the base of the CLT walls from crushing during testing and increased the period of the whole structure. A rigid foundation would have resulted in a stiffer system with lower drifts that would have more closely met the performance objectives for drift limits. In addition, this would have led to increased CLT panel crushing at the base, but because no crushing was observed in any of the tests, the CLT crushing performance objectives would likely have still been achieved with a more rigid foundation.

7.4 Future Work

Additional work is needed for rocking CLT walls to be implemented in tall mass timber construction. The following recommendations are made for future work based upon the limitations of the research presented in this thesis. Recommendations are made for research

needs for experimental research, numerical modeling, and the design procedure.

7.4.1 Experimental Research

- The design procedure and performance objectives are intended for buildings taller than two stores. Additional testing is needed on larger specimens to validate the design procedure and to test the response with a fully rigid foundation.

- Multi-directional testing is needed to observe the behavior of the walls with torsional effects on the building and to observe the effect of forces causing the walls to rocking in directions other than the principle in-plane direction.

- Non-structural elements need to be included in testing to see their effect on the stiffness and strength of the overall system and to observe how they will respond to the larger deformations in the rocking system and how much damage they will see.

- Additional material tests are needed on CLT to have a better understanding of its response in shear, flexure, and compression.

7.4.2 Numerical Modeling

Preliminary 2D numerical models have been created for the CLT rocking walls in the test specimen, however they are not complete and have not been included in this thesis. Numerical modeling needs for this project along with modeling needed for future work is presented here:

- Complete numerical models of the CLT rocking wall lateral system in the test specimen presented in this research is needed, including a representative model for the nonlinear behavior of the rocking wall foundation base beam. A full 3D model with torsional effects and the response of the diaphragm is also needed.

- Additional 3D modeling on CLT rocking wall structures is needed to understand the response in multiple directions and to understand the response of the walls to induced torsion.

- The effect of a rigid diaphragm verses a flexible diaphragm should be investigated.

- Modeling of non-structural elements is needed to account for the strength and stiffness effects of these elements on the overall structure.

7.4.3 Design Procedure

- Losses from damaged non-structural elements were not accounted for in the design procedure or in the performance objectives. These losses could be significant and need to be accounted for in the performance based design procedure. More research is needed here to investigate this effect.

REFERENCES

Akbas, T., Sause, R., Ricles, J. M., Ganey, R., Berman, J., Loftus, S., Dolan, J. D., Pei, S., van de Lindt, J. W., and Blomgren, H.-E. (2017). "Analytical and experimental lateral-load response of self-centering posttensioned clt walls." *Journal of Structural Engineering*, 143(6), 04017019.

APA (2017). *Standard for Performance Rated Cross-Laminated Timber, ANSI/APA PRG 320-2017*. APA - The Engineered Wood Association.

ASCE (2010). *Minimum Design Loads for Buildings and Other Structures. ASCE 7-10*. American Society of Civil Engineering.

ATC (2009). "Qualification of building seismic performance factors." *Report No. FEMA P-695*, Prepared by the Applied Technology Council for the Federal Emergency Management Agency.

AWC (2015). *National Design Specification for Wood Construction*. American Wood Council.

Bahmani, P. (2015). "Performance-based seismic retrofit (pbsr) methodology for multi-story buildings with full-scale experimental validation." Ph.D. thesis, Colorado State University. Libraries, Fort Collins, CO.

Baird, A., Smith, T., Palermo, A., and Pampanin, S. (2014). "Experimental and numerical study of u-shaped flexural plate (ufp) dissipators." *NZSEE Conference*.

Barbosa, A. R., Sinha, A., Higgins, C., and Soti, R. (2018). "Structural testing for the dr johnson's clt panels." *Report No. 17-03*, Oregon State University.

Buchanan, A. H. (1990). "Bending strength of lumber." *Journal of Structural Engineering*, 116(5), 1213–1229.

Ceccotti, A., Sandhass, C., Okabe, M., Yasumura, M., Minowa, C., and Kawai, N. (2013). "Sofie project - 3d shaking table test on a seven-storey full-scale cross-laminated timber building." *Earthquake Engineering and Structural Dynamics*, 42, 2003–2021.

Chopra, A. K. (2007). *Earthquake Dynamics of Structures: Theory and Applications to Earthquake Engineering*. Prentice Hall, Upper Saddle River, New Jersey, 3rd edition.

DeMeza, B. (2018). "Design and testing of shake-table specimen of cross-laminated timber and cross-laminated timber-concrete composite diaphragms." M.S. thesis, Oregon State University, Corvallis, OR.

Dujic, B., Pucelj, J., and Zarnic, R. (2004). "Testing of racking behavior of massive wooden wall panels." *Proceedings of the International Council for Research and Innovation in Building and Construction*, Edinburgh, Scotland, Working Commission W18 - Timber Structures, Meeting 37, 37–15–2.

Dujic, B., Strus, K., Zarnic, R., and Ceccotti, A. (2010). "Prediction of dynamic response of a 7-storey massive xlam wooden building tested on a shaking table." *11th World Conference on Timber Engineering*, Trentino, Italy.

Dujic, B. and Zarnic, R. (2006). "Study of lateral resistance of massive x-lam wooden wall system subjected to horizontal loads." *International Workshop on Earthquake Engineering on Timber Structures*.

Filiatrault, A. and Folz, B. (2002). "Performance-based seismic design of wood framed buildings." *Journal of Structural Engineering*, 128(1), 39–47.

Flaig, M. and Bla, H. J. (2013). "Shear strength and shear stiffness of clt-beams loaded in plane." *Proceedings of the International Council for Research and Innovation in Building*

and Construction, Vancouver, Canada, Working Commission W18 - Timber Structures, Meeting 46, 46–12–3.

Ganey, G. S. (2015). "Seismic design and testing of rocking cross laminated timber walls." M.S. thesis, University of Washington, Seattle, WA.

Ganey, R., Berman, J., Akbas, T., Loftus, S., Dolan, J. D., Sause, R., Ricles, J., Pei, S., van de Lindt, J., and Blomgren, H. (2017). "Experimental investigation of self-centering cross-laminated timber walls." *Journal of Structural Engineering*, 143(10).

Gavric, I., Fragiacoma, M., and Ceccotti, A. (2012). "Strength and deformation characteristics of typical x-lam connections." *12th World Conference on Timber Engineering*.

Green, M. C. and Karsh, E. J. (2012). "The case for tall wood buildings." *Report No. 1*, MGB Architecture and Design.

He, M., Sun, X., and Li, Z. (2018). "Bending and compressive properties of corss-laminated timber (clt) panels made from canadian hemlock." *Construction and Building Materials*, 185, 175–183.

Higgins, C., Barbosa, A. R., and Blank, C. (2017). "Structural tests of composite concrete-cross-laminated timber floors." *Report no.*, Oregon State University, Corvallis, OR.

Iqbal, A., Pampanin, S., Palermo, A., and Buchanan, A. H. (2015). "Performance and design of lvl walls coupled with ufp dissipaters." *Journal of Earthquake Engineering*, 19(3), 383–409.

Karacabeyli, E. and Douglas, B. (2013). *CLT Handbook: Cross-laminated timber*. U.S. Ed. Special Publication-SP-529E. FPInnovations.

Kelly, J. M., Skiner, R. I., and Heine, A. J. (1972). "Mechanisms of energy absorption in special devices for use in earthquake resistant structures." *Bulletin of N. Z. Society for Earthquake Engineering*, 5(3), 63–88.

Kretschmann, D. E. (2013). "Mechanical properties of wood. chapter 5 in wood handbook." *Report No. FPL-GTR-190*, Forest Products Laboratory and U.S. Department of Agriculture.

Kurama, Y., Pessiki, S., Sause, R., and Lu, L. (1999). "Seismic behavior and design of unbonded post-tensioned precast concrete walls." *PCI Journal*, 44(3), 72–89.

LATBSDC (2018). *An Alternative Procedure FOr Seismic Analysis and Design of Tall Building Located in the Los Angeles Region*. Los Angeles Tall Building Structural Design Council.

Lauriola, M. and Sandhaas, C. (2006). "Quasi-static and pseudo-dynamic tests on xlam walls and buildings." *International Workshop on Earthquake Engineering on Timber Structures*.

Mazzoni, S., McKenna, F., Scott, M., and Fenves, G. (2009). *Open Systems for Earthquake Engineering Simulation User Command-Language Manual - OpenSees version-2.0*. Pacific Earthquake Engineering Research Center, University of California, Berkeley, Berkely, CA.

Moroder, D., Pampanin, S., Palermo, A., Smith, T., Sarti, F., and Buchanan, A. (2017). "Diaphragm connections in structures with rocking timber walls." 27, 165–174.

Naturally:wood (2018). "Brock commons tallwood house.

Newcombe, M. P., Pampanin, S., Buchanan, A., and Palermo, A. (2008). "Section analysis and cyclic behavior of post-tensioned jointed ductile connections for multi-story timber buildings." *Journal of Earthquake Engineering*, 12(sup1), 83–110.

Palermo, A., Pampanin, S., and Buchanan, A. (2006). "Experimental investigation on lvl seismic resistant wall and frame subassemblies." *First European Conference on Earthquake Engineering and Seismology*, Geneva, Switzerland.

Pampanin, S., Priestley, M. J. N., and Sritharan, S. (2001). "Analytical modeling of the

seismic behavior of precast concrete frames designed with ductile connections." *Journal of Earthquake Engineering*, 5(3), 329–367.

Pang, W., Rosowsky, D., Pei, S., and van de Lindt, J. W. (2010). "Simplified direct displacement design of six-story woodframe building and pretest seismic performance assessment." *Journal of Structural Engineering*, 136(7), 813–825.

Pei, S., Barbosa, A. R., McDonnel, E., Blomgren, H., Dolan, J. D., Berman, J. W., van de Lindt, J. W., and Zimmerman, R. B. (2018). "Full-scale shake table testing of a two-story mass-timber rocking wall building." *Proceedings of the 11th National Conference in Earthquake Engineering*, Los Angeles, CA, Earthquake Engineering Research Institue.

Pei, S., van de Lindt, J. W., and Popovski, M. (2013). "Approximate r-factor for cross-laminated timber walls in multistory buildings." *Journal of Architectural Engineering*, 19(4), 245–255.

Popovski, M., Schneider, J., and Schweinsteiger, M. (2010). "Lateral load resistance of cross-laminated wood panels." *11th World Conference on Timber Engineering*, Trentino, Italy.

Priestley, N. (1991). "Overviw of presss research program." *PCI Journal*, 36(4), 50–57.

Sarti, F., Palermo, A., and Pampanin, S. (2016). "Development and testing of an alternative dissipative posttensioned rocking timber wall with boundary columns." *Journal of Structural Engineering*, 142(4).

Seo, C. Y. and Sause, R. (2005). "Ductility demands on self-centering systems under earthquake loading." *ACI Structural Journal*, 102(2), 275–285.

Serrano, E. and Enquist, B. (2010). "Compression strength perpendicular to grain in cross-laminated timber (clt)." *11th World Conference on Timber Engineering 2010, WCTE 2010*, Vol. 1 (01).

Smith, T., Pampanin, S., Buchanan, A., and Fragiacomo, M. (2008). "Feasibility and detailing of post-tensioned timber buildings for seismic areas." *2008 NZSEE Conference*.

SOM (2013). "Timber tower research project: Final report." *Skidmore, Owings and Merrill Final Report*.

Stanton, J., Stone, W., and Cheok, G. S. (1997). "A hybrid reinforced precast frame for seismic regions." *PCI Journal*, 42(2), 20–32.

USGS (2018). "Earthquake Hazards Program, <http://earthquake.usgs.gov/hazards/>.

van de Lindt, J. W., Pei, S., Pryor, S. E., Shimizu, H., and Isoda, H. (2010). "Experimental seismic response of a full-scale six-story light-frame wood building." *Journal of Structural Engineering*, 136(10), 1262–1272.

Zimmerman, R. and McDonnell, E. (2018). "Framework - innovation in re-centering mass timber wall buildings." *Proceedings of the 11th National Conference in Earthquake Engineering*, Los Angeles, CA, Earthquake Engineering Research Institue.

Appendix A

SPECIMEN DESIGN CALCULATIONS

A.1 Overview

This section summarizes the design calculations completed for the design of the CLT rocking walls in the full-scale two-story shake table specimen.

A.2 Calculate Seismic Demands

As explained in section 4.2.3, the design values were calculated based on ASCE 7-10 design procedures [ASCE, 2010]. Figure 4.13 also shows the design spectra used. Using the building's approximate fundamental period, T_a of $0.20s$, the seismic response coefficient can be calculated as:

$$C_s = \frac{S_{DS}}{\frac{R}{I_e}} = \frac{1.06}{\frac{6}{1}} = 0.18$$

The seismic base shear was then calculated by multiplying the seismic response coefficient by the total design seismic weight of the building as shown:

$$V_{base} = C_s W = (0.18)(166\ kips) = 29.4\ kips$$

The seismic story shear were then determined with the equivalent lateral force method from ASCE 7-10 [ASCE, 2010], which resulted in the following story shears and overturning moment demands for each wall in the structure:

$$F_1 = 4.52\ kips$$

$$F_2 = 10.17\ kips$$

$$M_{demand} = 3365\ kip\text{-}in$$

where the F_1 is the story shear for the floor and F_2 is the story shear for the roof. These are the forces and moments acting on each of the two walls in the structure (the total story shears and overturning moment would be double the above values).

A.3 Determine System Parameters and Dimensions

The following design parameters and dimensions were chosen for the test specimen:

$$L_w = 60\ in$$

$$b_w = 6.875\ in$$

$$h_w = 288\ in$$

$$A_p = 0.334\ in^2$$

$$L_p = 288\ in$$

$$T_o = 12\ kips$$

A.4 Calculate Decompression Moment

A total of 4 PT bars were used in each of the wall panels, each with an initial post-tensioning force of, T_o. The rocking walls were assumed to hold no gravity load, W. With these forces, the decompression moment for each wall panel was calculated as:

$$
\begin{aligned}
M_{dec} &= (W + \Sigma T_o)d \\
&= (0\ kips + 4(12\ kips)) \left(\frac{60\ in}{2} - \left(\frac{1}{3}\right)\left(\frac{3}{8}\right) 60\ in \right) = 1080\ kip\text{-}in
\end{aligned}
$$

Because the specimen has two floors, the lateral forces acted at two locations. However, to simplify the calculations, an equivalent lateral force and location were determined. The height of the first floor, h_1, and the second floor, h_2, were 12 ft and 10 ft respectively. The effective height was calculated as follows:

$$
\begin{aligned}
h_{eff} &= \frac{F_1 h_1 + F_2(h_1 + h_2)}{F_1 + F_2} \\
&= \frac{4.52\ kips(12\ ft) + 10.17\ kips(12\ ft + 10\ ft)}{4.52\ kips + 10.17\ kips} = 229\ in
\end{aligned}
$$

With the effective height, the flexural and shear stiffness were calculated and used to determine the total elastic stiffness of the wall panels as follows:

$$
\begin{aligned}
k_{flex} &= \frac{2E_w I_w}{h_{eff}^2 \left(h_w - \frac{h_{eff}}{3}\right)} \\
&= \frac{2(1238\ ksi)(123750\ in^4)}{(229\ in)^2 \left(288\ in - \frac{229\ in}{3}\right)} = 30.8\ \frac{kip}{in} \\
k_{shear} &= \frac{G_w A_w}{h_{eff}} \\
&= \frac{(80\ ksi)(412.5\ in^2)}{229\ in} = 144\ \frac{kip}{in} \\
k_w &= \left(\frac{1}{k_{flex}} + \frac{1}{k_{shear}} \right)^{-1} \\
&= \left(\frac{1}{30.8\ \frac{kip}{in}} + \frac{1}{144\ \frac{kip}{in}} \right)^{-1} = 25.4\ \frac{kip}{in}
\end{aligned}
$$

A.5 Select UFP Dimensions and Desired Dissipation Ratio

The following dimensions were chosen for the UFPs:

$$D_u = 3.625\ in$$
$$b_u = 4.5\ in$$
$$t_u = 0.375\ in$$

The UFP plastic force was:

$$F_p = \frac{f_y b_u t_u^2}{2D_u}$$
$$= \frac{(50\ ksi)(4.5\ in)(0.375\ in)^2}{2(3.625\ in)} = 5.237\ kips$$

The moment due to the UFP was:

$$M_{UFP} = F_p L_w$$
$$= (5.237\ kips)(60\ in) = 314\ kip\text{-}in$$

A desired energy dissipation ratio of 0.30 was desired for the design. The number of UFPs required to achieve a ratio of at least 0.30 between the two wall was calculated as:

$$n_{UFPs} = \frac{2\beta M_{dec}}{M_{UFP}}$$
$$= \frac{2(0.30)(2)(1080 kip\text{-}in)}{314\ kip\text{-}in} = 5\ UFPs$$

A.6 Check that Capacity is Greater than Demand

The decompression moment above is for just one of the wall panels. Because the seismic demand moment was calculated for an entire wall (which is made up of two coupled wall panels), the decompression moment was also needed for the whole wall. This was done by multiplying the decompression moment for one panel by 2 and adding in the moment from the UFPs. In the design, the forces in the UFPs were included in the decompression moment because the structure was relatively small so the UFPs would yield earlier, making the point at which the wall reaches decompression moment and the point at which the UFPs yield, almost the same. The decompression moment for the whole wall was calculated as:

$$\begin{aligned} M_{dec(wall)} &= M_{dec} + n_{UFPs} M_{UFP} \\ &= (2)(1080\ kip\text{-}in) + (5)(314\ kip\text{-}in) = 3731\ kip\text{-}in \end{aligned}$$

The elastic deformation at the decompression point is:

$$\begin{aligned} \Delta_e &= \frac{M_{dec(wall)}}{k_w h_{eff}} \\ &= \frac{3731\ kip\text{-}in}{(25.4\ \frac{kip}{in})(229\ in)} = 0.186\ in \end{aligned}$$

The capacity of the wall is equal to the decompression moment. This must be greater than the demand moment to satisfy design requirements. The demand to capacity ratio was:

$$\frac{M_{demand}}{M_{dec(wall)}} = 0.9$$

This satisfies the design requirements.

A.7 Perform Cross Section Analysis Procedure for a Full Moment-Drift Response

The cross section analysis procedure was performed for a range of drifts to determine the moment-drift response of the structure. An example calculation for 1% drift is shown here.

Impose Gap Rotation

For this design a drift of 1% was imposed on the structure, and the resulting gap rotation at the base was estimated as shown:

$$\theta_{gap} = \theta_{gap} - \frac{\Delta_e}{h_{eff}}$$
$$= 0.10 - \frac{0.186\ in}{229\ in} = 0.009$$

Estimate Neutral Axis Depth

A neutral axis depth was iterated on to get the length that would satisfy equilibrium:

$$c = 6.27\ in$$

Solve for PT Tension Force

The specimen had four total PT bars, two on each side of the wall, centered about the center line of the wall and spaced 10 inches apart. With the imposed gap rotation, the change in length of each set of PT bars was determined as follows:

$$\Delta_{PT1} = \theta_{gap}\left(\frac{1}{2}(L_w - s) - c\right)$$
$$= 0.009\left(\frac{1}{2}(60\ in - 10\ in) - 6.27\ in\right) = 0.17\ in$$
$$\Delta_{PT2} = \theta_{gap}\left(\frac{1}{2}(L_w + s) - c\right)$$
$$= 0.009\left(\frac{1}{2}(60\ in + 10\ in) - 6.27\ in\right) = 0.26\ in$$

The stiffness of the each PT bar was calculated as follows:

$$k_{PT} = \frac{A_{PT}E_{PT}}{L_{PT}}$$
$$= \frac{(0.334\ in^2)(29000\ ksi)}{288\ in} = 33.63\ kip\text{-}in$$

The change in force due to the change in length of each PT bar was determined as follows:

$$\Delta T_1 = k_{PT}\Delta_{PT1}$$
$$= (33.63\ kip\text{-}in)(0.17\ in) = 5.79\ kip$$
$$\Delta T_2 = k_{PT}\Delta_{PT2}$$
$$= (33.63\ kip\text{-}in)(0.26\ in) = 8.88\ kip$$

The resulting total force of each bar at each location was calculated as follows:

$$
\begin{aligned}
T_1 &= T_o + \Delta T_1 \\
&= 12\ kips + 5.79\ kips = 17.79\ kips \\
T_2 &= T_o + \Delta T_2 \\
&= 12\ kips + 8.88\ kips = 20.88\ kips
\end{aligned}
$$

At each location there were two PT bars, so the total force from the PT bars was calculated as:

$$
\begin{aligned}
\Sigma T &= 2(T_1) + 2(T_2) \\
&= 2(17.79\ kips) + 2(20.88\ kips) = 77.3 kips
\end{aligned}
$$

Solve for CLT Compression Force

Next,the maximum compression strain at the base of the wall was calculated as follows:

$$
\begin{aligned}
\epsilon_c &= \left(\frac{\theta_{gap} h_w}{l_p(h_w - \frac{l_p}{2})} + \frac{M_{dec}}{E_w I_w} \right) \\
&= \left(\frac{(0.009)(288\ in)}{13.75\ in(288\ in - \frac{13.75\ in}{2})} + \frac{1080\ kip\text{-}in}{(1238\ ksi)(123750\ in^4)} \right) = 0.004\ \frac{in}{in}
\end{aligned}
$$

The constitutive relationship was used to determine the stress distribution along the neutral axis depth c. For the constitutive relationship, a yield stress, f_y, of 3.627 psi was used. Integrating the stress distribution, f_c, over the compression area of the neutral axis depth, multiplied by the wall thickness, resulted in the total compression force at the base of the wall panel:

$$C = \int_0^c f_c(c) b_w dx$$
$$= 103.5 \; kips$$

Satisfy Equilibrium

To complete the cross section analysis procedure, equilibrium needs to be checked. Because the walls are coupled together, the plastic force from each UFP should also be considered in the equilibrium equation. For the case of 2.0% drift, equilibrium was check with the equation:

$$\Sigma T + W + n_{UFPs} F_P = C$$
$$77.3 \; kips + 0 \; kips + 5(5.237 \; kips) = 103.5 \; kips$$
$$103.5 \; kips = 103.5 \; kips$$

Determine Overturning Moment

The total overturning moment at the base of one wall panel was calculated as follows:

$$M_{panel} = 2T_1 \left(\frac{L_w}{2} - \frac{s}{2} \right) + 2T_2 \left(\frac{L_w}{2} + \frac{s}{2} \right) - C\overline{c}$$
$$= 2(17.79 \; kips) \left(\frac{60 \; in}{2} - \frac{10 \; in}{2} \right) + 2(20.88 \; kips) \left(\frac{60 \; in}{2} + \frac{10 \; in}{2} \right) - (103.5 \; kips)(2.26 \; in)$$
$$= 2117 \; kip\text{-}in$$

To calculate the total overturning moment at the base of the wall, the forces from both panels should be considered, as well as the forces from the UFPs. This moment was calculated as

follows:

$$\begin{aligned} M_{total} &= 2(M_{panel}) + n_{UFPs} F_p L_w \\ &= 2(2117\ kip\text{-}in) + 5(5.237\ kips)(60\ in) = 5805\ kip\text{-}in \end{aligned}$$

The approximate base shear per wall can be calculated as follows:

$$\begin{aligned} V_{base} &= \frac{M_{total}}{h_{eff}} \\ &= \frac{5805\ kip\text{-}in}{229\ in} = 25.35\ kips \end{aligned}$$

A.8 Check if Performance Objectives are Met

The wall needed to be checked if performance objectives are met. At 1% drift, the modified performance objectives state that there should be no PT yielding or panel crushing:

$$\begin{aligned} T_1 &= 17.79\ kips < T_y = 30.73\ kips \\ T_2 &= 20.88\ kips > T_y = 30.73\ kips \\ \epsilon_c &= 0.004\ \frac{in}{in} < \epsilon_{crush} = 0.0056\ \frac{in}{in} \end{aligned}$$

Performance objectives are met for 1% drift. This process was repeated for the full range of drifts. Once all performance objectives were met, design was complete.

Appendix B

ADDITIONAL EXPERIMENTAL DATA ANALYSIS FIGURES

B.1 Overview

Chapter 6 described how the experimental test data was processed and interpreted and presented the results. In Chapter 6, plots for only a few ground motion tests were presented. A full collection of the plots will be presented in this chapter.

B.2 White Noise Analysis: Fundamental Period

Figure B.1 shows the FFT plots for the while noise tests discussed in Section 6.3. FFT analyses were performed on the acceleration data from the accelerometer located at the center of the roof.

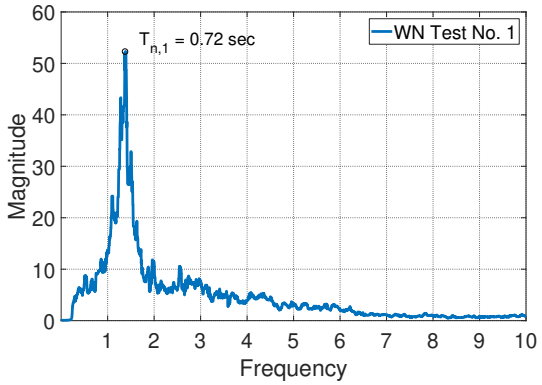

(a) Test 1 Loma Prieta SLE

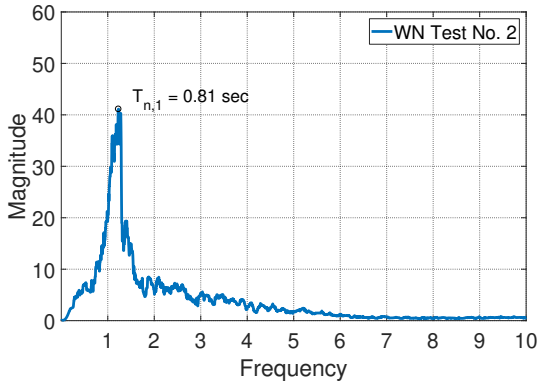

(b) Test 2 Loma Prieta SLE

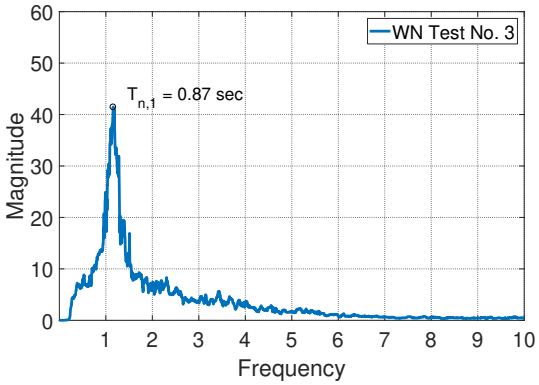

(c) Test 3 Northridge SLE

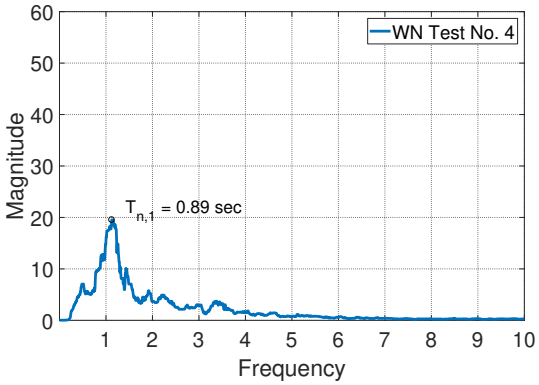

(d) Test 4 Superstition Hills SLE

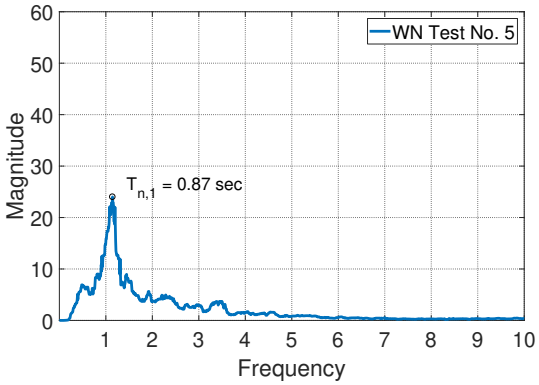

(e) Test 5 Northridge DBE

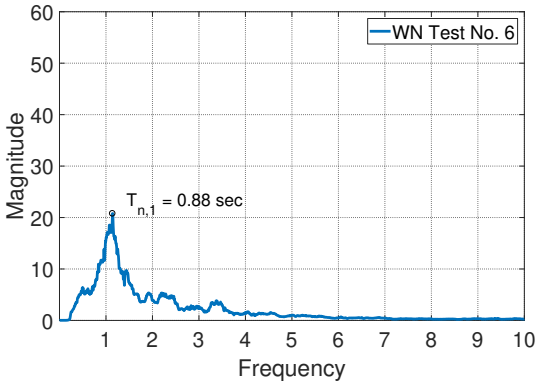

(f) Test 6 Northridge DBE

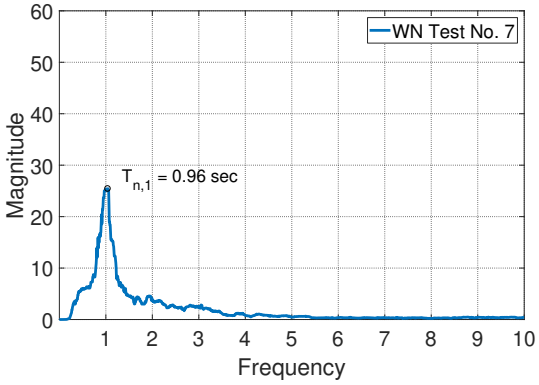

(g) Test 7 Imperial Valley SLE

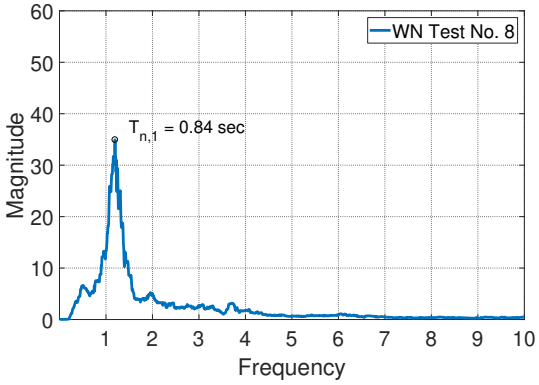

(h) Test 8 Northridge DBE

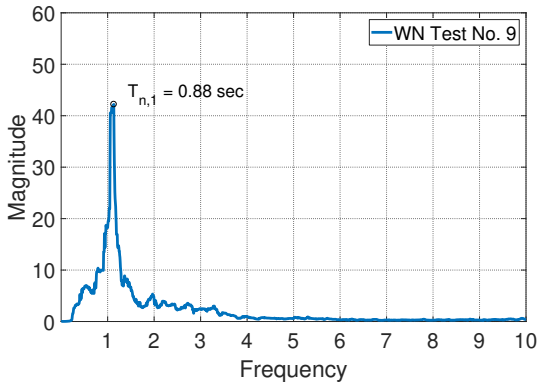

(i) Test 9 Loma Prieta DBE

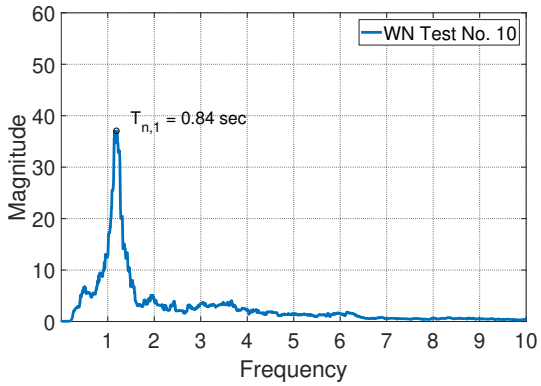

(j) Test 10 Superstition Hills DBE

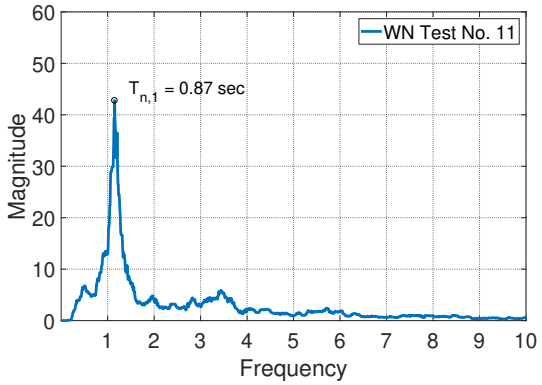

(k) Test 11 Loma Prieta MCE

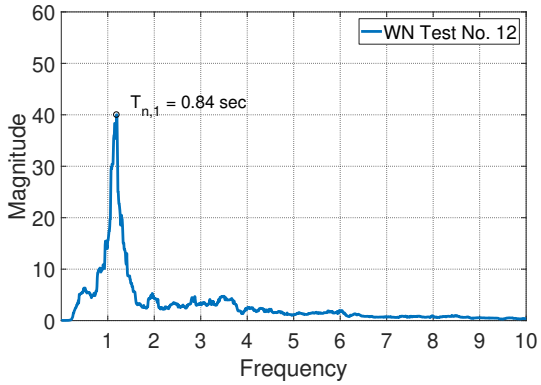

(l) Test 12 Northridge MCE

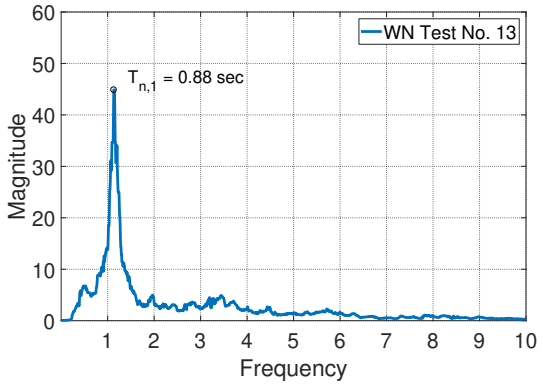

(m) Test 13 Superstition Hills MCE

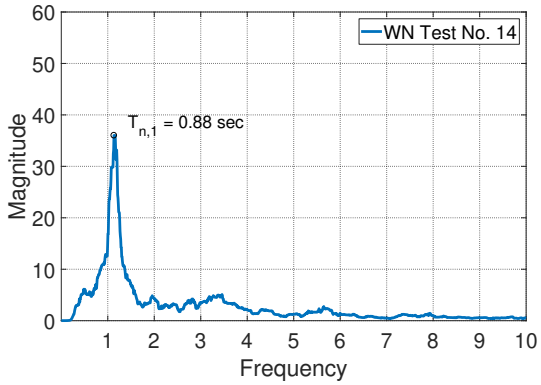

(n) Test 14 Northridge MCEx1.2

Figure B.1: Drift time histories

B.3 Global Response: Roof and Floor Drifts

Figure B.2 shows the drift time histories for each of the ground motions as discussed in Section 6.5. For each test, the drifts calculated from the string potentiometers located on each floor level, the accelerometers on the floors, and the accelerometers on the walls were all compared and showed similar results. Ultimately, the drifts calculated from the accelerometers on the floors were used for the remainder of the data analysis.

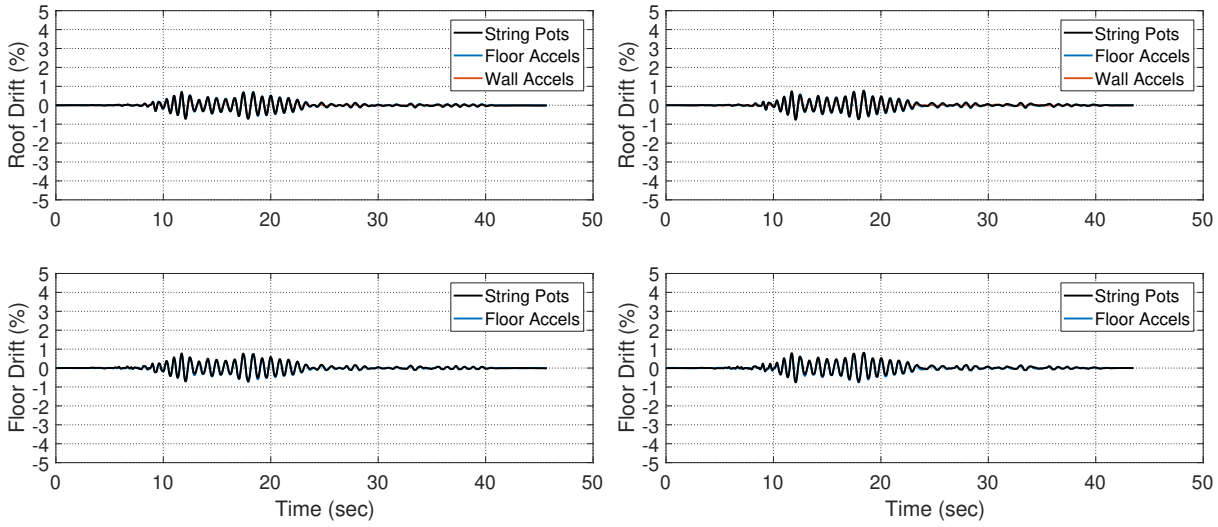

(a) Test 1 Loma Prieta SLE

(b) Test 2 Loma Prieta SLE

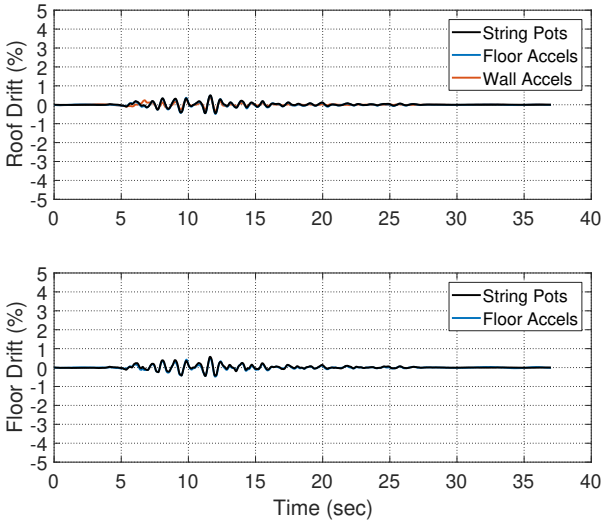

(c) Test 3 Northridge SLE

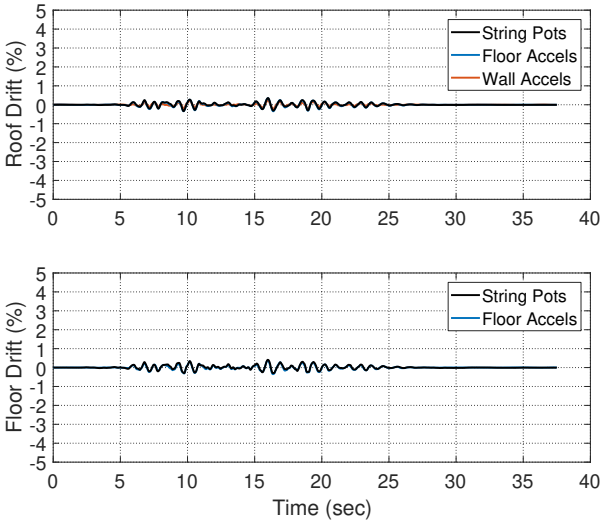

(d) Test 4 Superstition Hills SLE

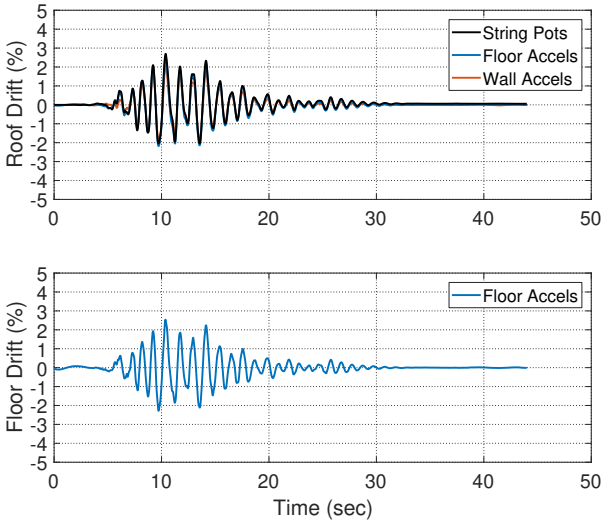

(e) Test 5 Northridge DBE

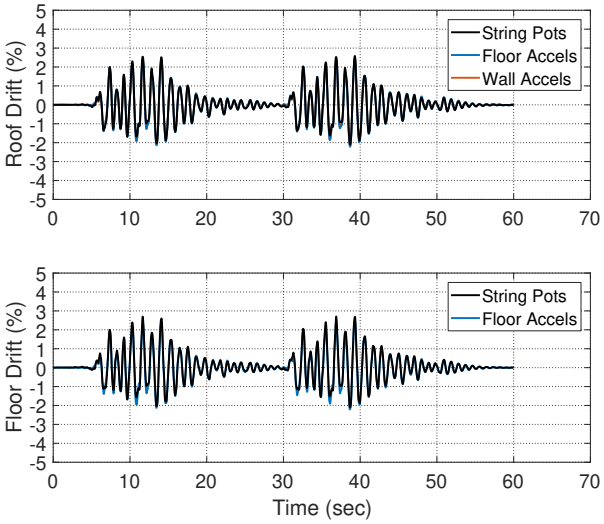

(f) Test 6 Northridge DBE

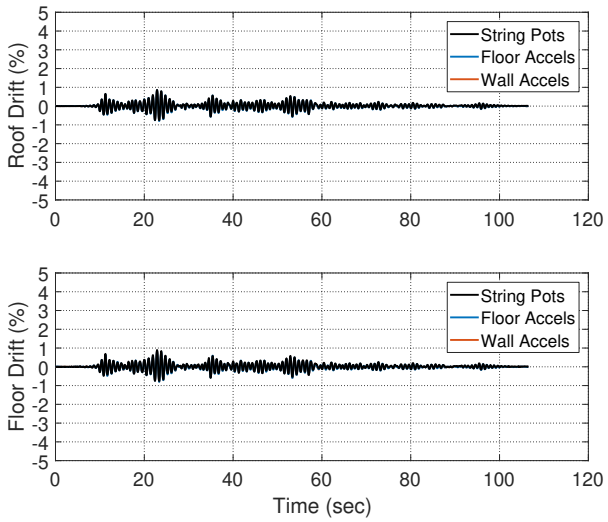

(g) Test 7 Imperial Valley SLE

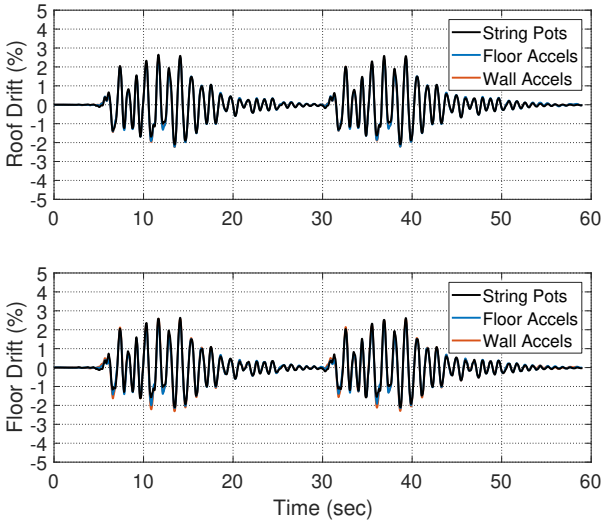

(h) Test 8 Northridge DBE

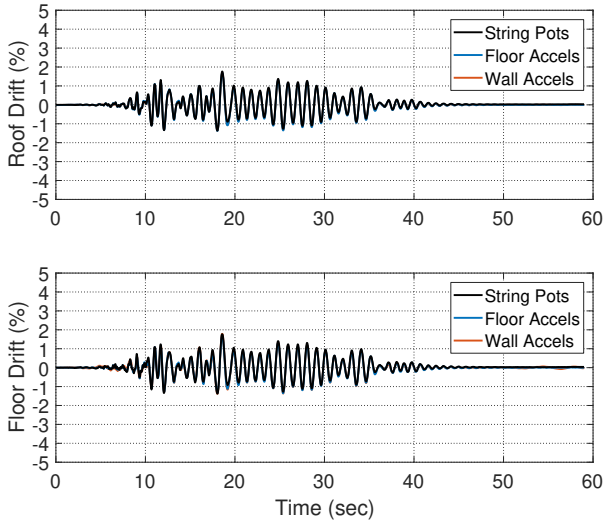

(i) Test 9 Loma Prieta DBE

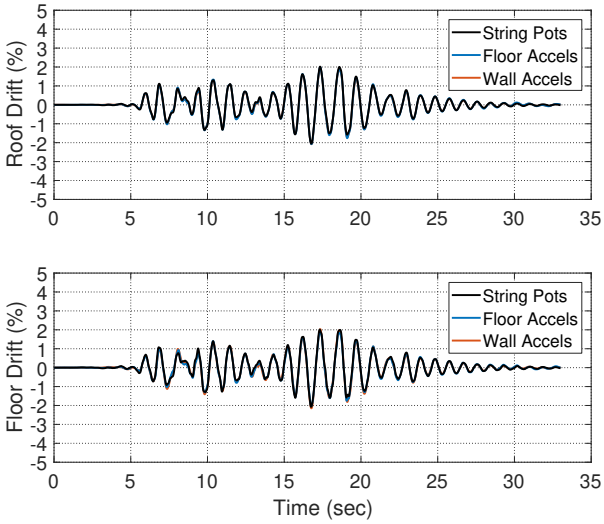

(j) Test 10 Superstition Hills DBE

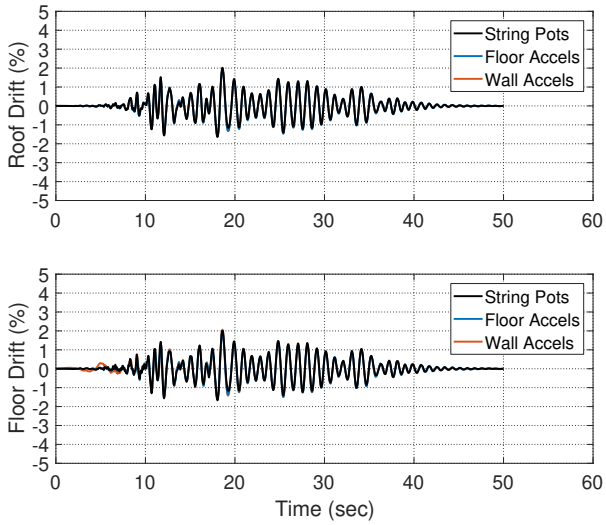

(k) Test 11 Loma Prieta MCE

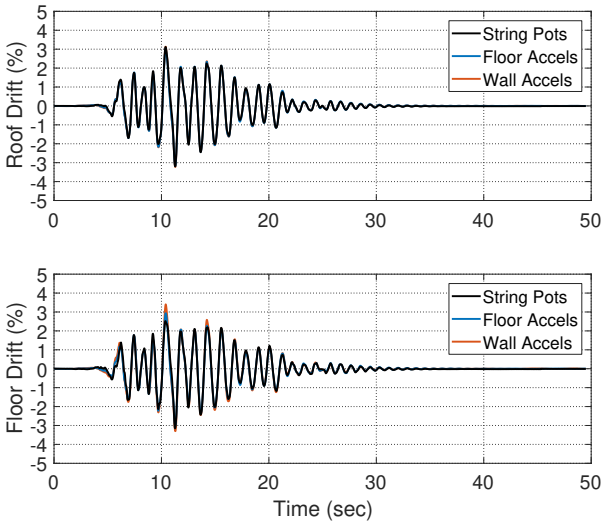

(l) Test 12 Northridge MCE

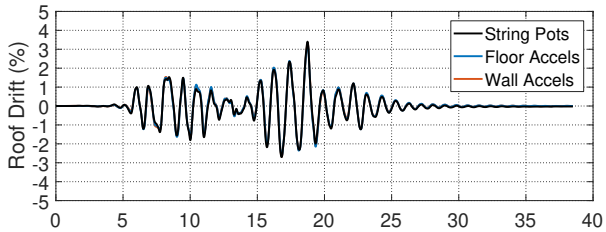

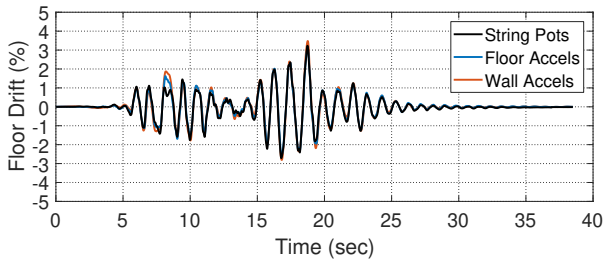

(m) Test 13 Superstition Hills MCE

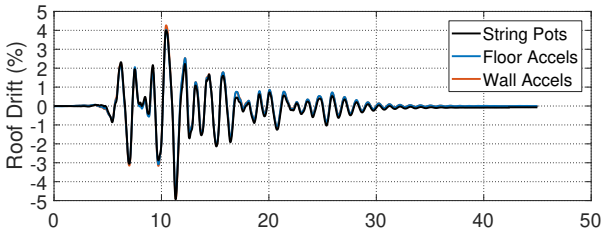

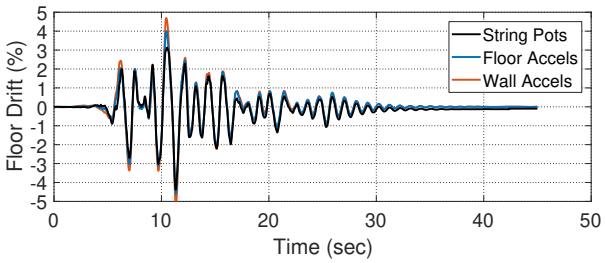

(n) Test 14 Northridge MCEx1.2

Figure B.2: Drift time histories

B.3.1 Global Response: Torsion

Figure B.3 shows plots of the time histories for torsional rotation angles calculated in Section 6.5.4. Both roof rotation angles and floor rotation angles are shown. Both show very small rotation angles verifying the assumption that torsional response can be ignored.

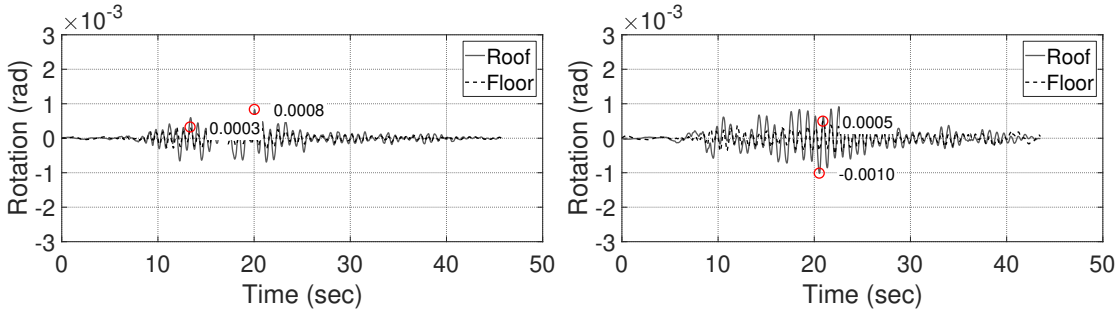

(a) Test 1 Loma Prieta SLE

(b) Test 2 Loma Prieta SLE

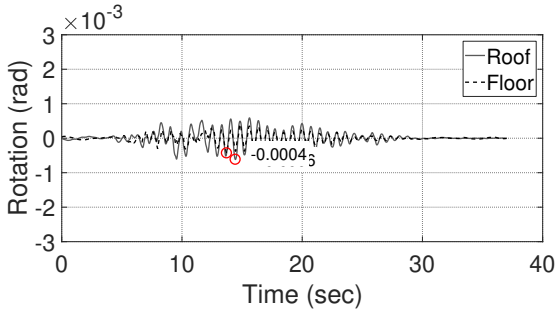

(c) Test 3 Northridge SLE

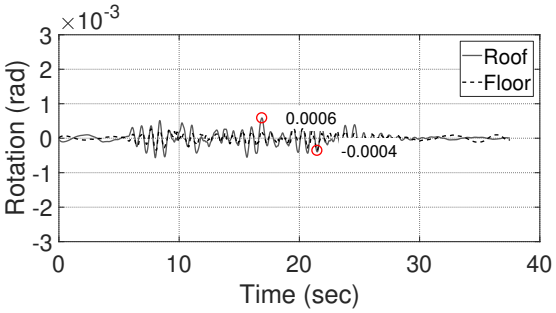

(d) Test 4 Superstition Hills SLE

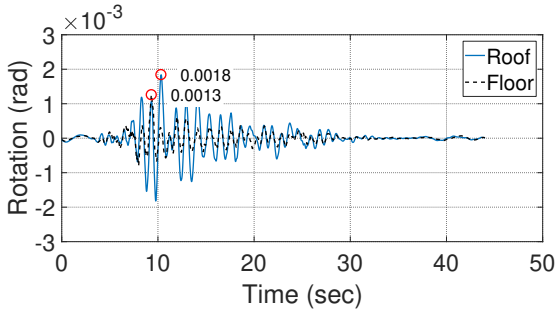

(e) Test 5 Northridge DBE

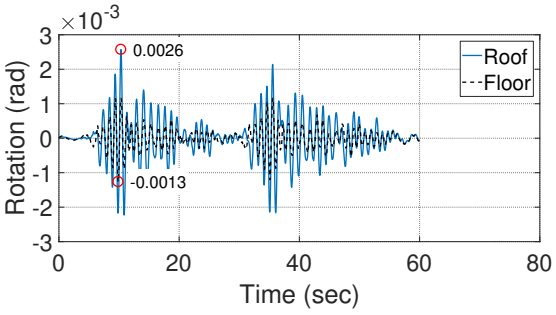

(f) Test 6 Northridge DBE

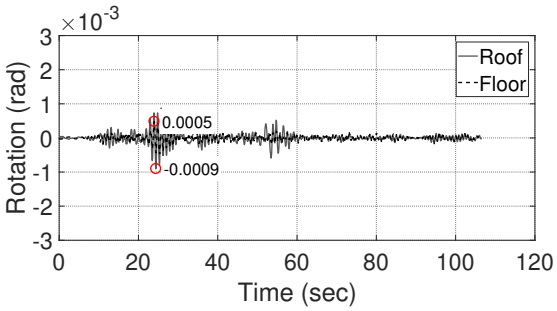

(g) Test 7 Imperial Valley SLE

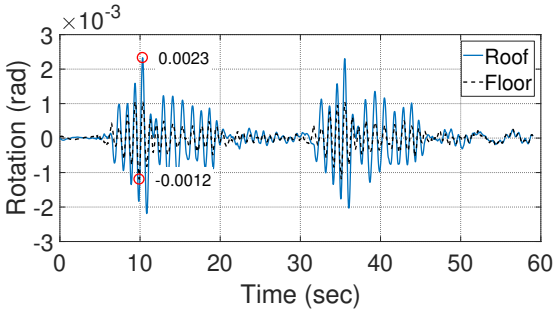

(h) Test 8 Northridge DBE

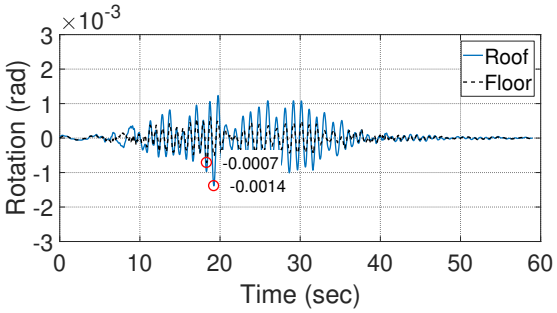

(i) Test 9 Loma Prieta DBE

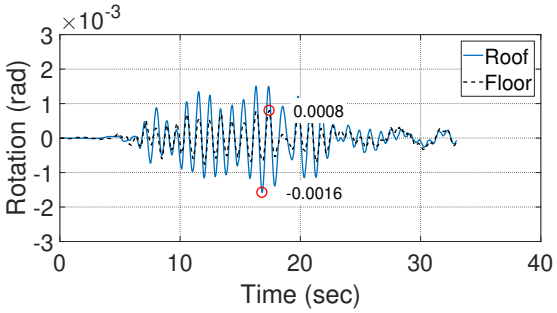

(j) Test 10 Superstition Hills DBE

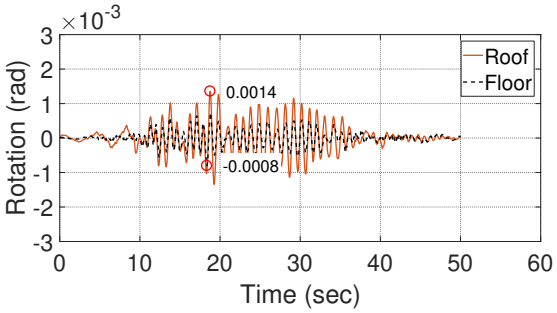

(k) Test 11 Loma Prieta MCE

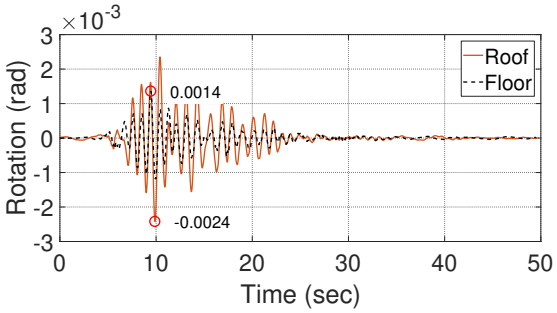

(l) Test 12 Northridge MCE

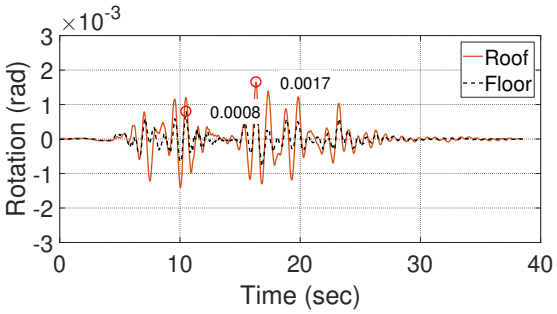

(m) Test 13 Superstition Hills MCE

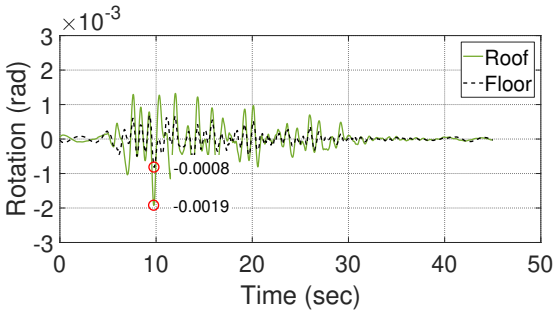

(n) Test 14 Northridge MCEx1.2

Figure B.3: Drift time histories

B.4 PT Bars

Figure B.4 shows plots of the PT forces verses drift for each ground motion test as discussed in Section 6.6. Graphics are shown on each subplot, denoting which PT bar force is being plotted. The forces are the sum are the two bars located at the shown location. The expected yield force is also shown on each figure.

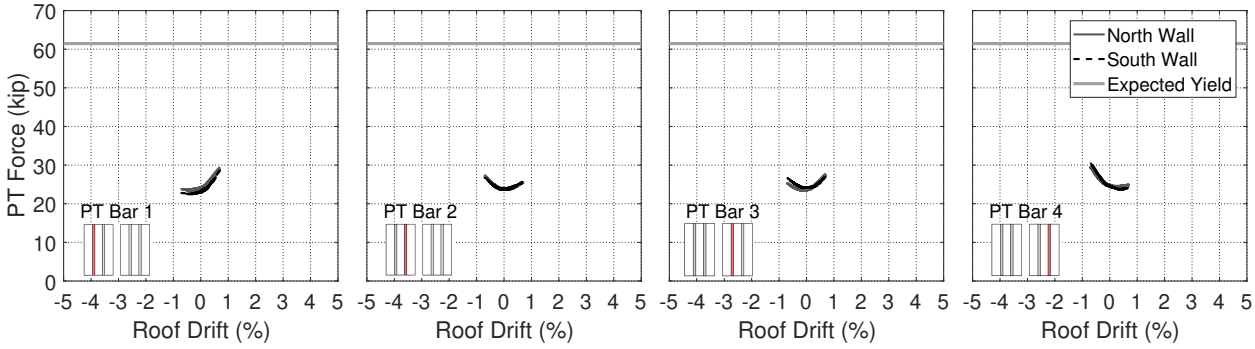

(a) Test 1 Loma Prieta SLE

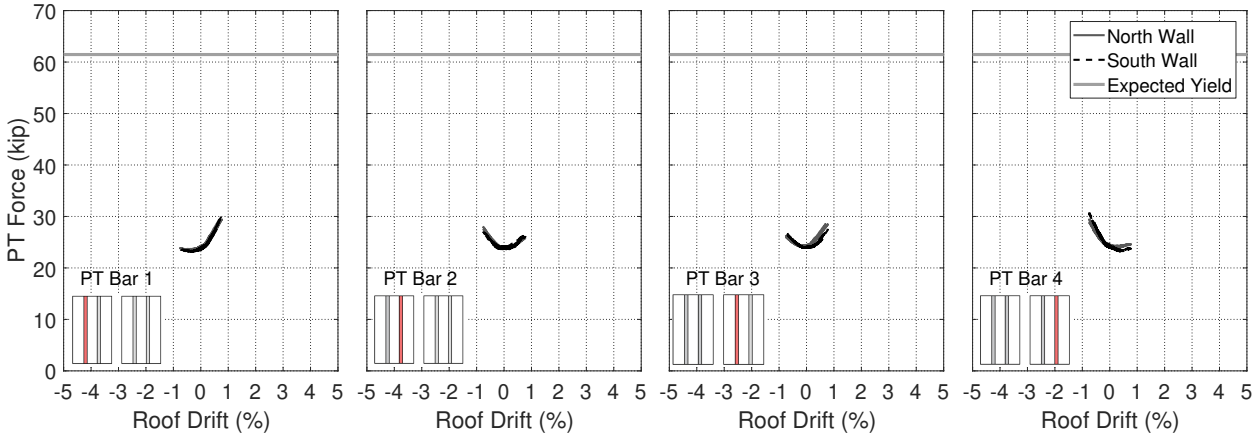

(b) Test 2 Loma Prieta SLE

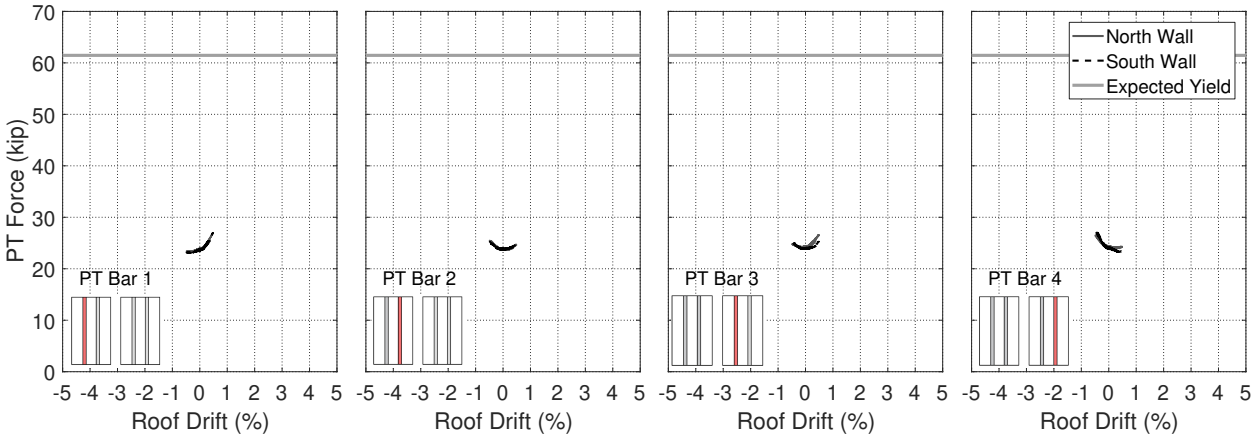

(c) Test 3 Northridge SLE

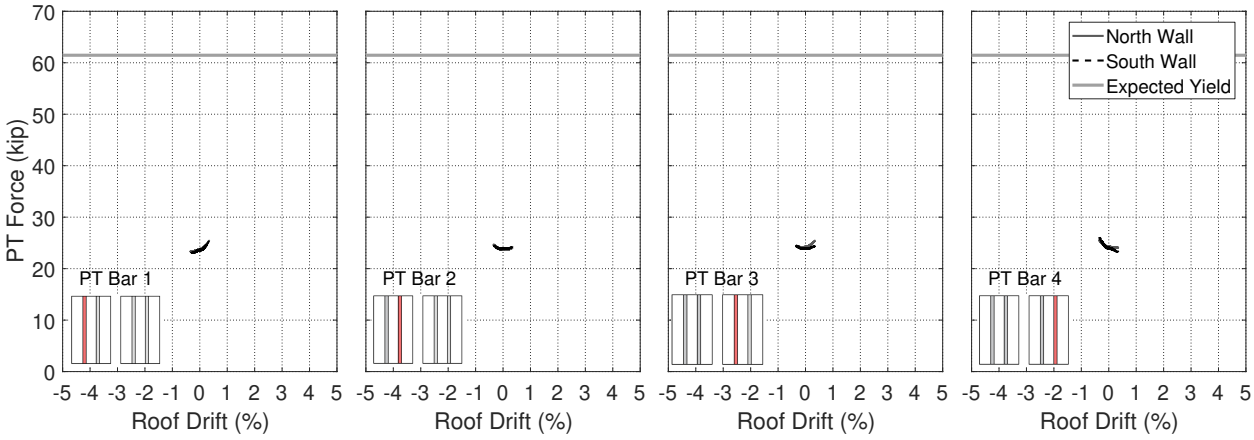

(d) Test 4 Superstition Hills SLE

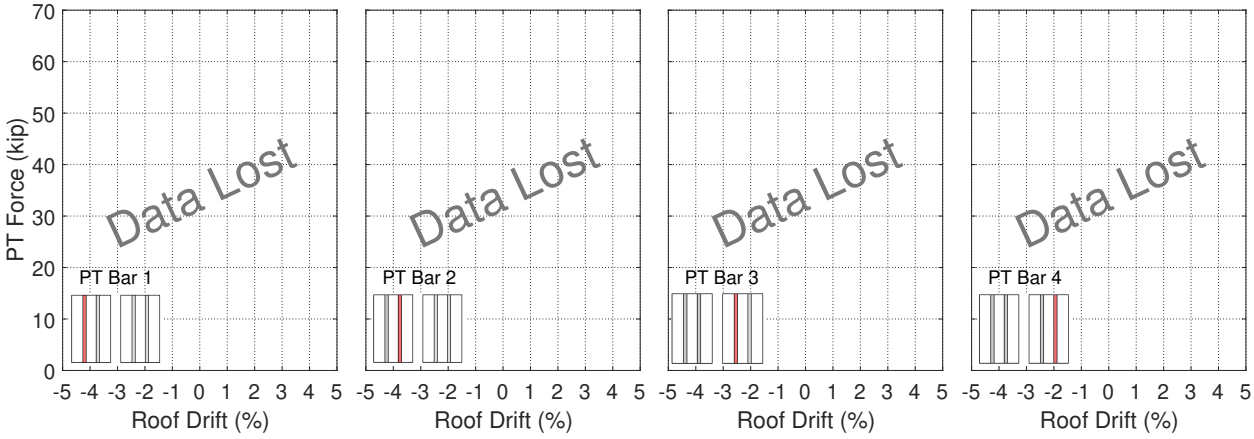

(e) Test 5 Northridge DBE

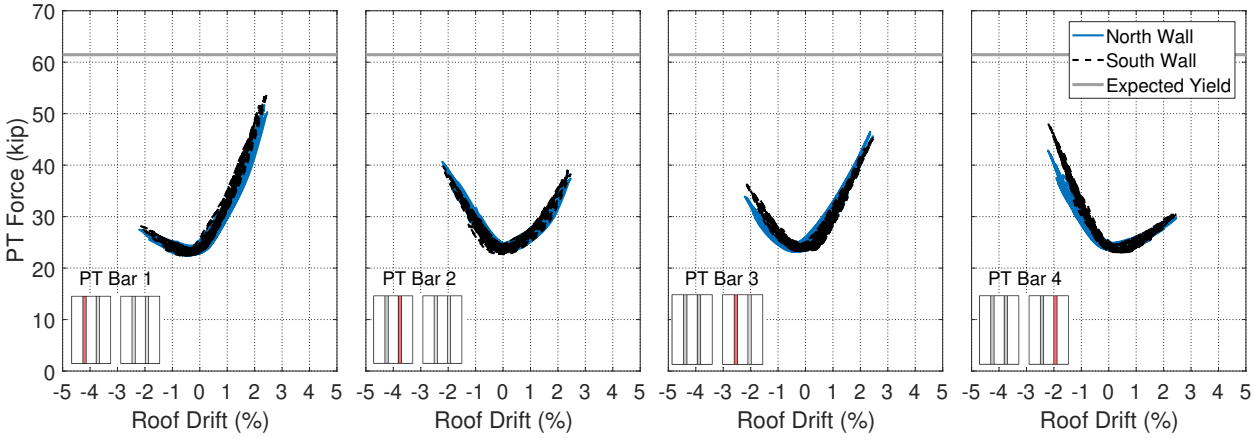

(f) Test 6 Northridge DBE

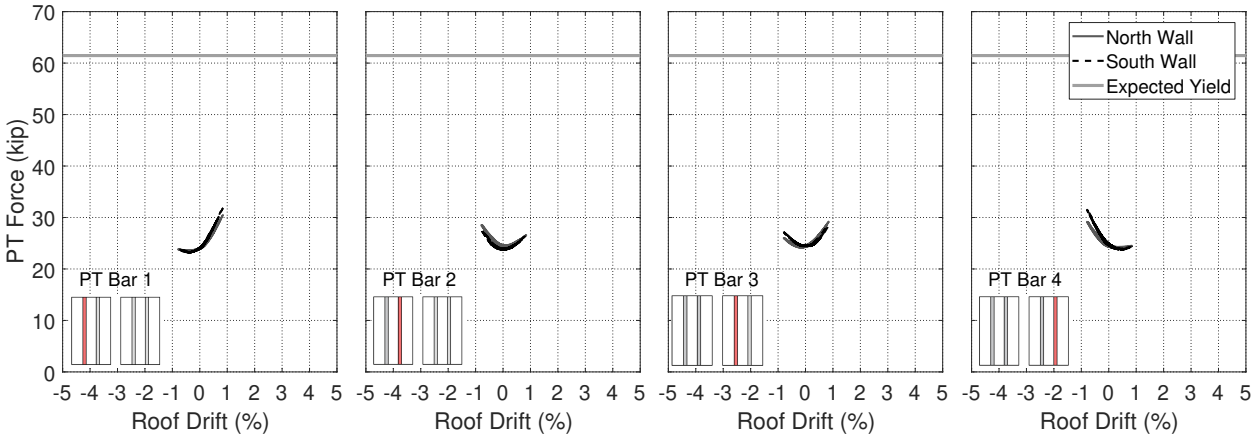

(g) Test 7 Imperial Valley SLE

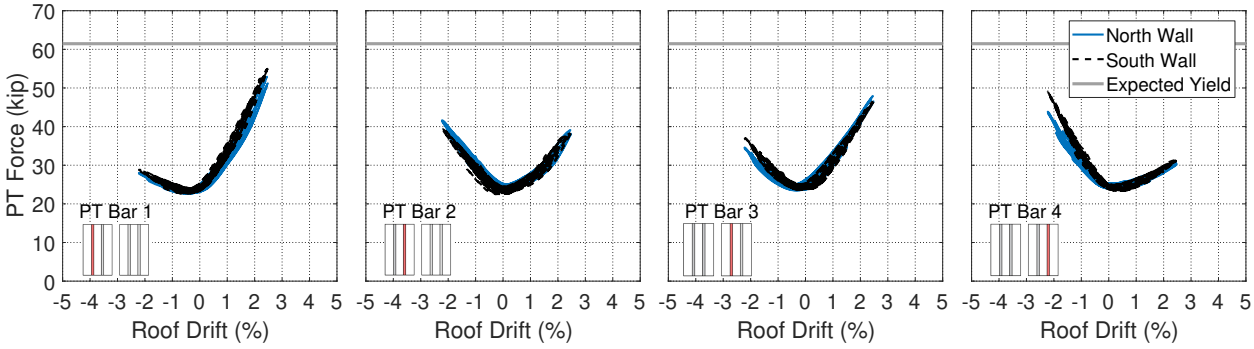

(h) Test 8 Northridge DBE

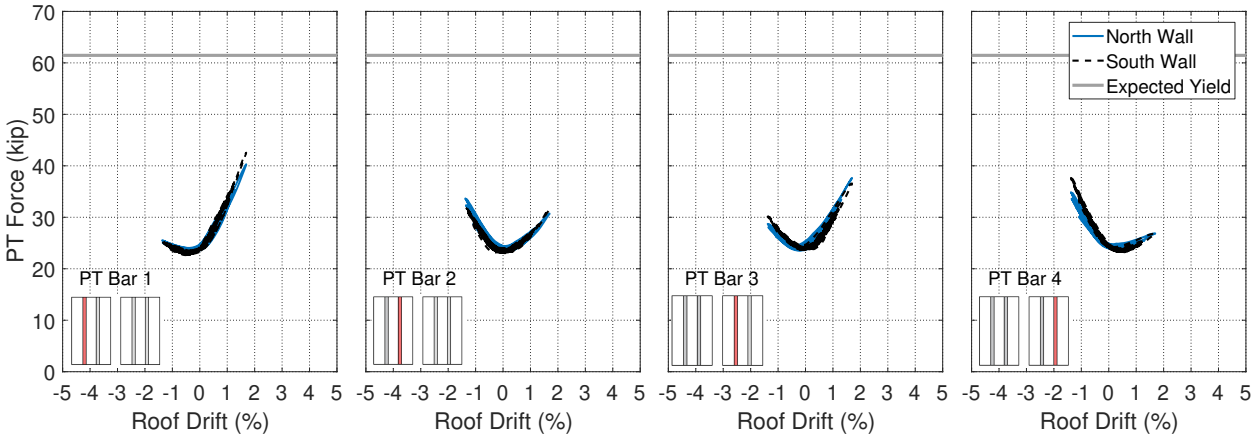

(i) Test 9 Loma Prieta DBE

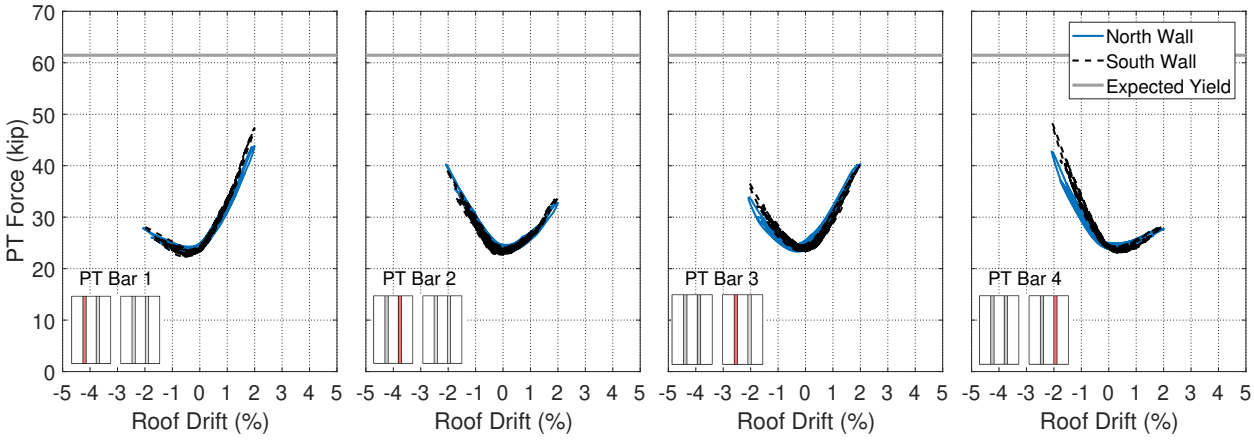

(j) Test 10 Superstition Hills DBE

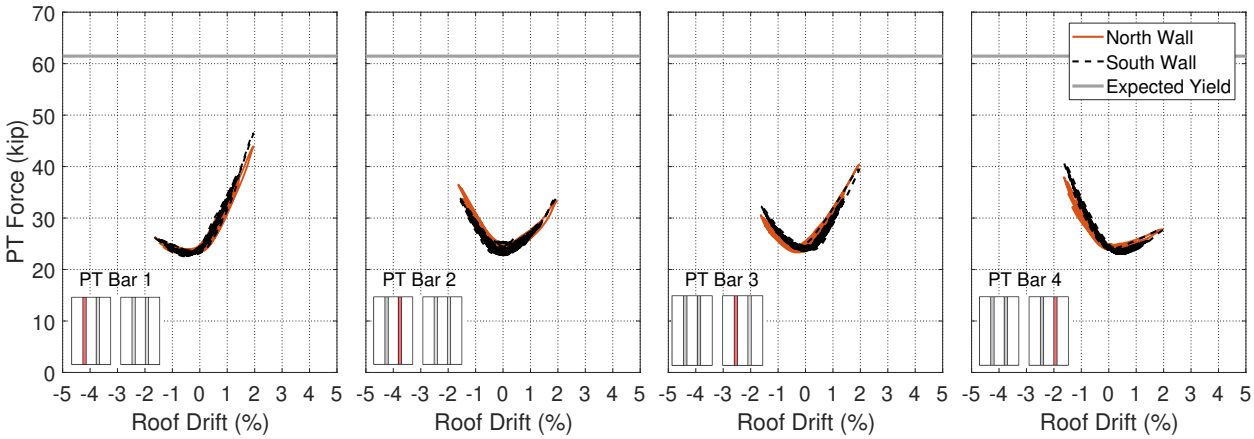

(k) Test 11 Loma Prieta MCE

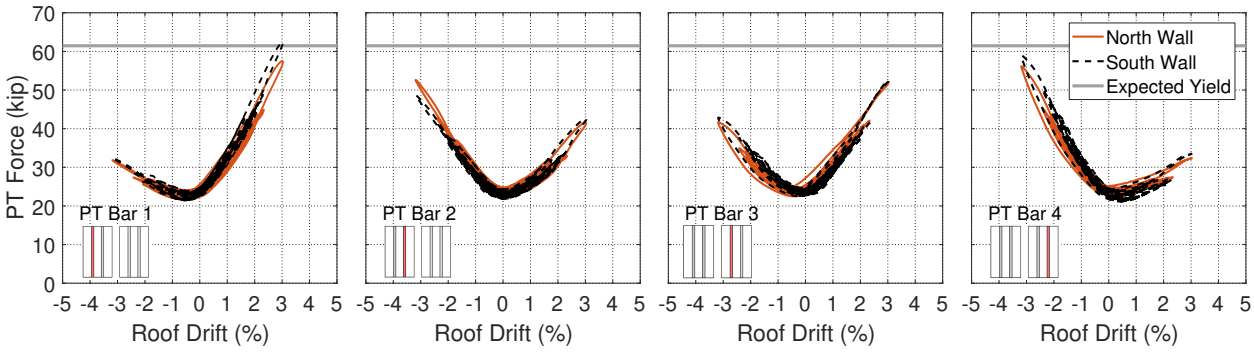

(l) Test 12 Northridge MCE

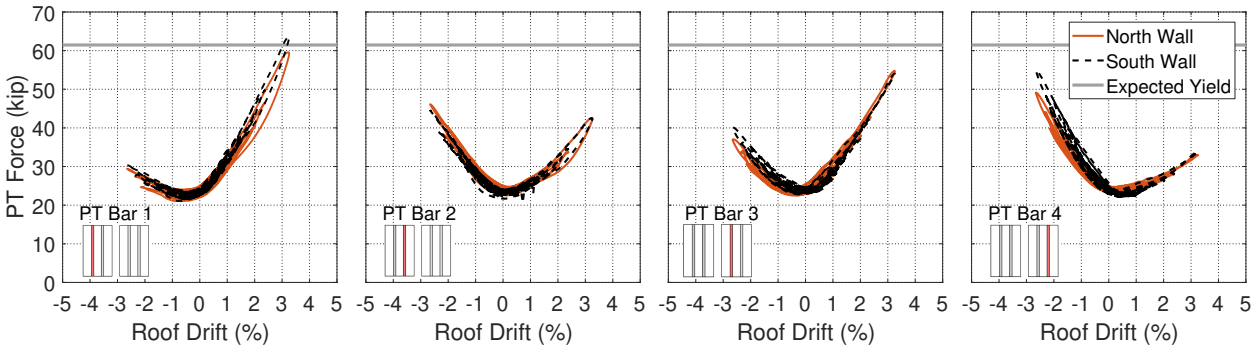

(m) Test 13 Superstition Hills MCE

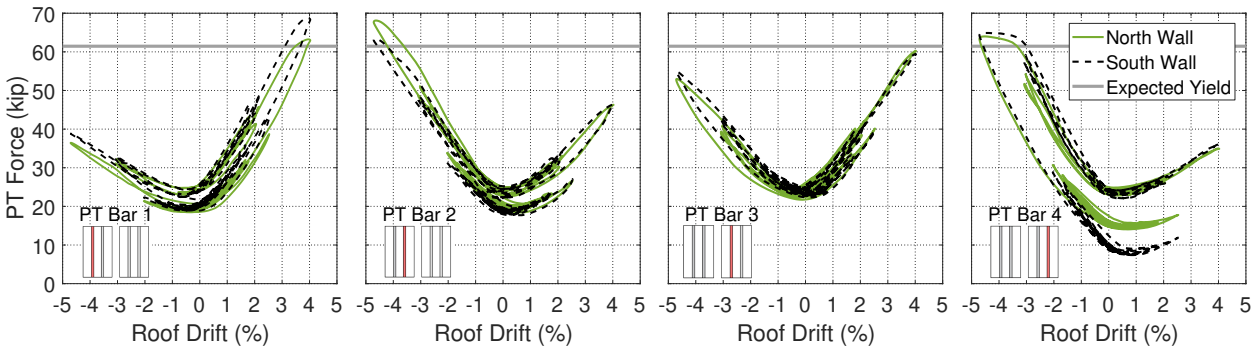

(n) Test 14 Northridge MCEx1.2

Figure B.4: Base shear vs. roof drift hysteresis

B.5 Wall Panel Base Deformation: Time Histories

Figure B.5 show the time histories from the linear potentiometers at the base of the rocking wall panels as discussed in Section 6.7. Each page shows the plots for one ground motion test. The upper set of plots show the time histories for the linear potentiometers on the west walls and the lower set of plots show the time histories for the linear potentiometers on the east walls. At the bottom is a key showing which linear potentiometer is plotted on each subplot.

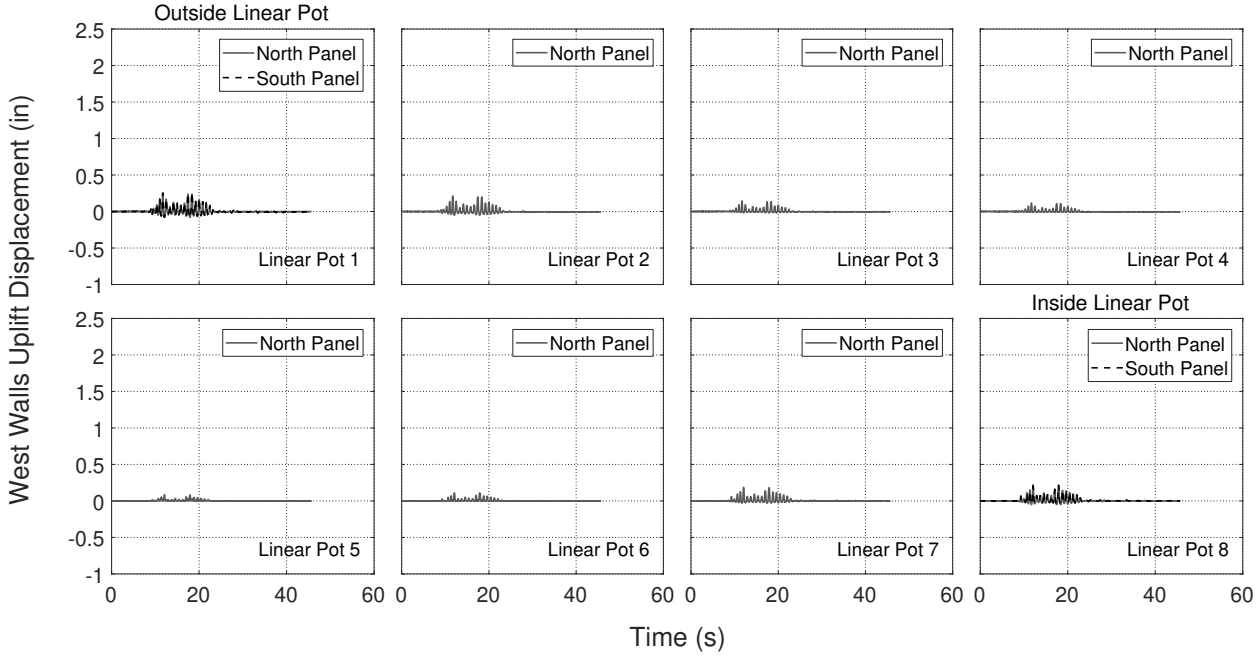

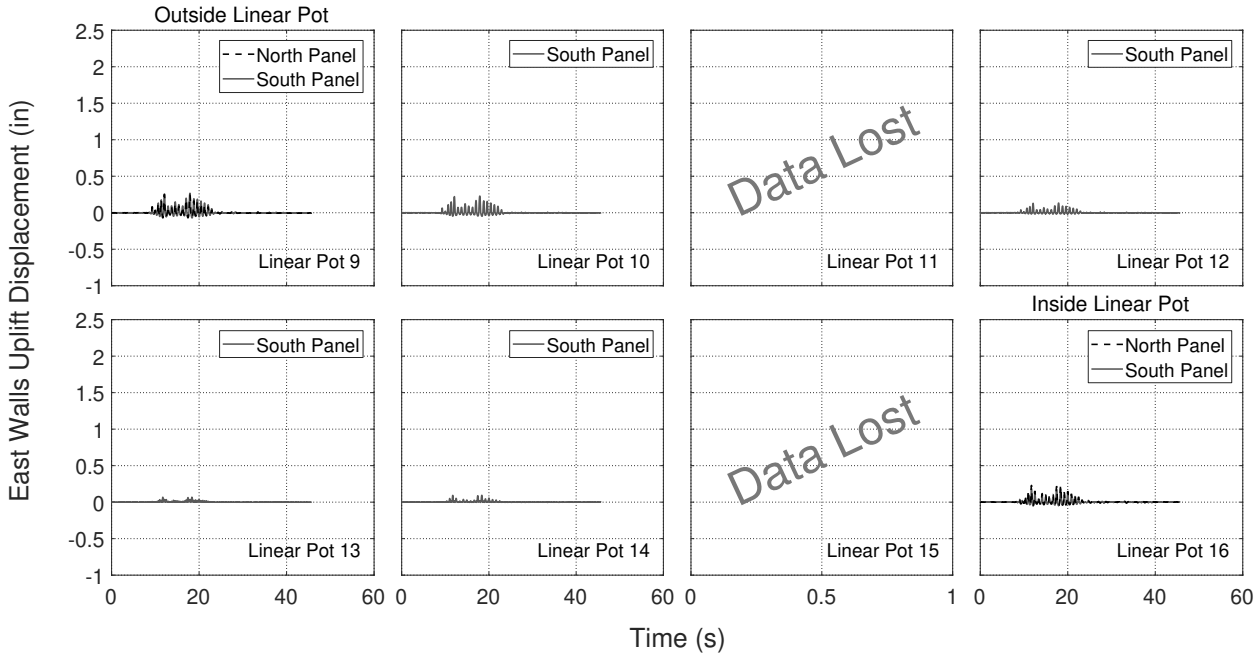

(a) East Walls - Test 1: Loma Prieta SLE

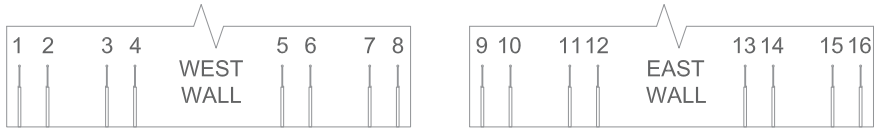

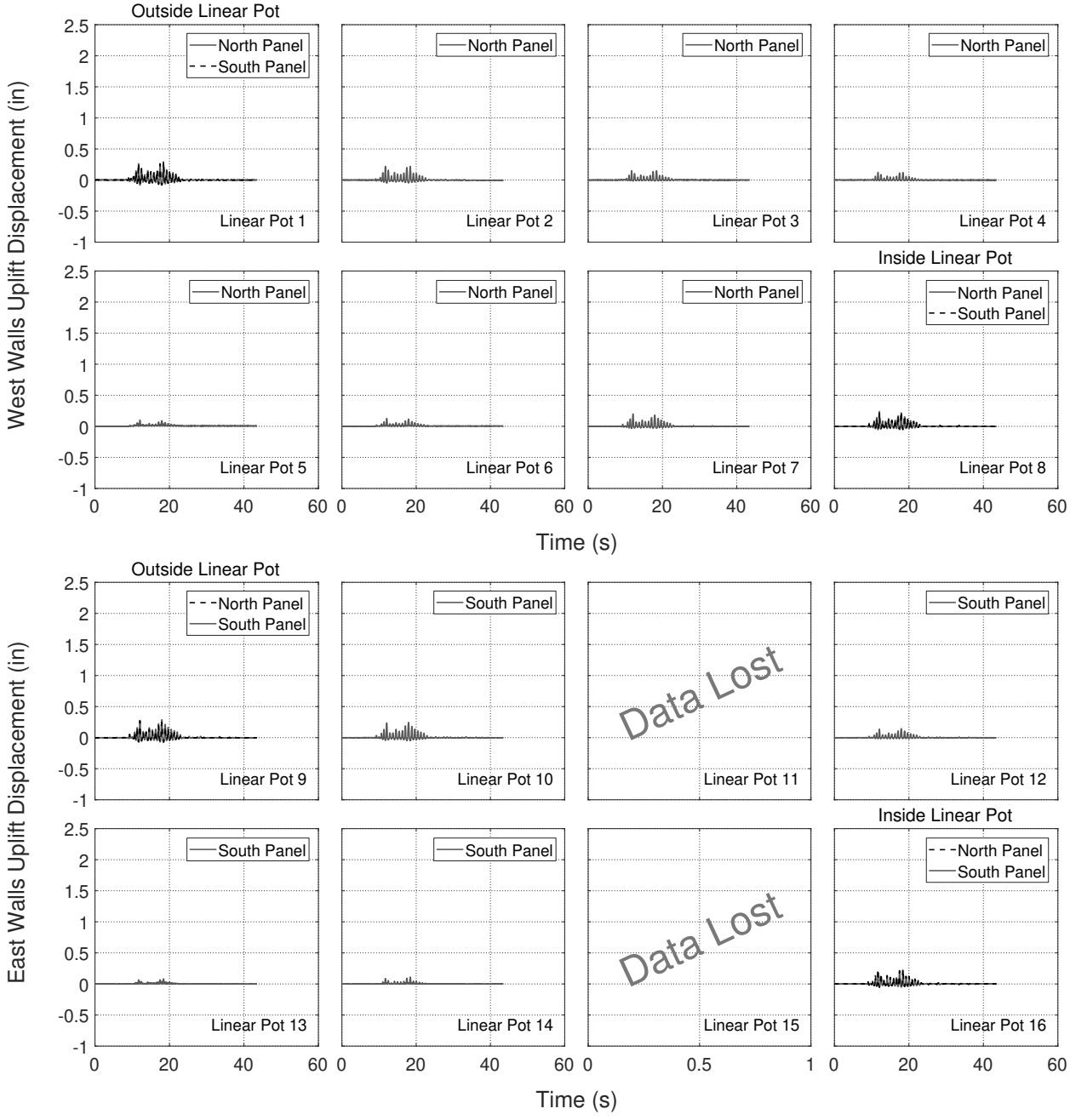

(b) East Walls - Test 2: Loma Prieta SLE

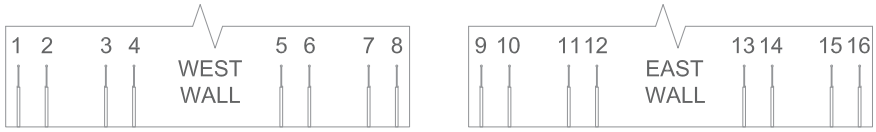

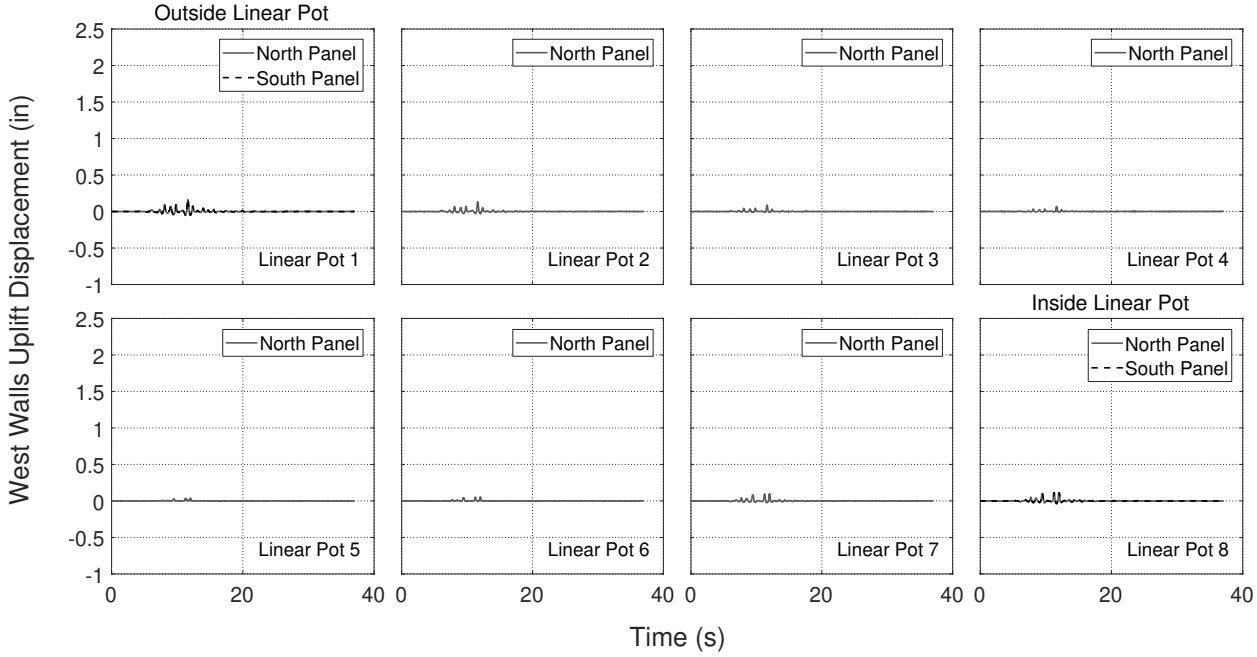

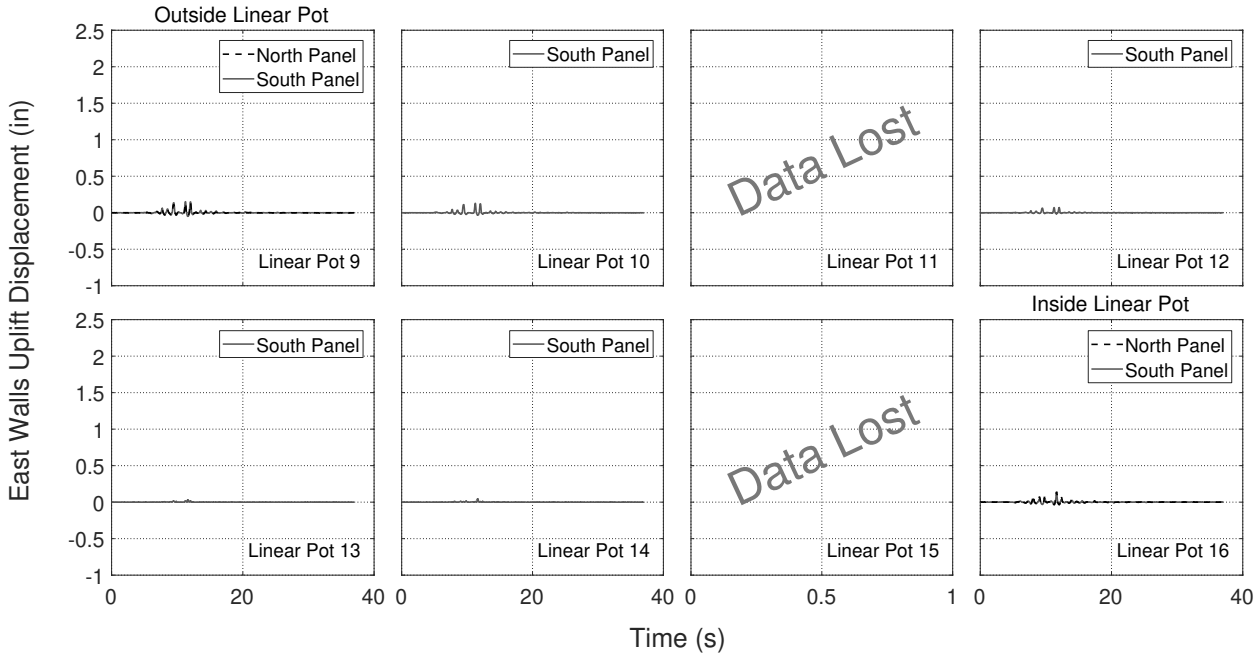

(c) East Walls - Test 3: Northridge SLE

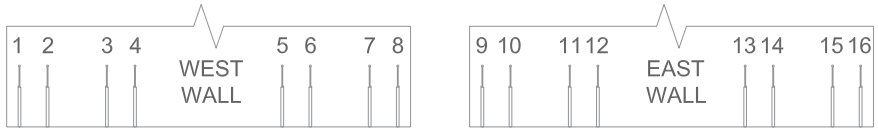

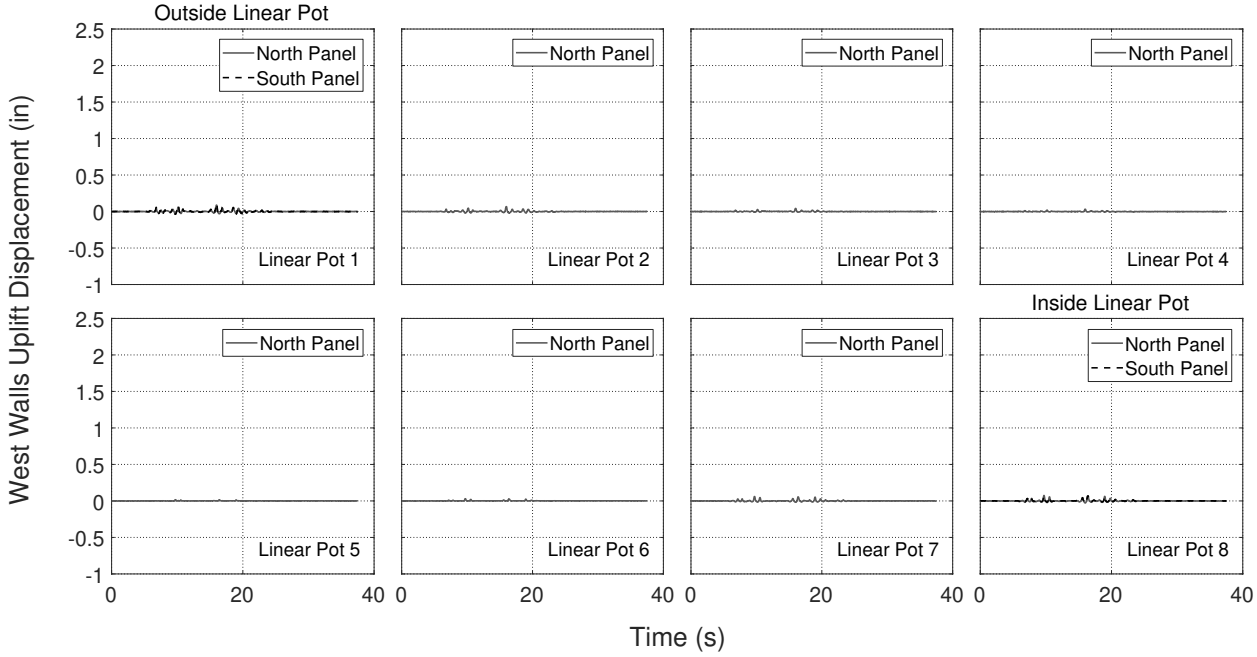

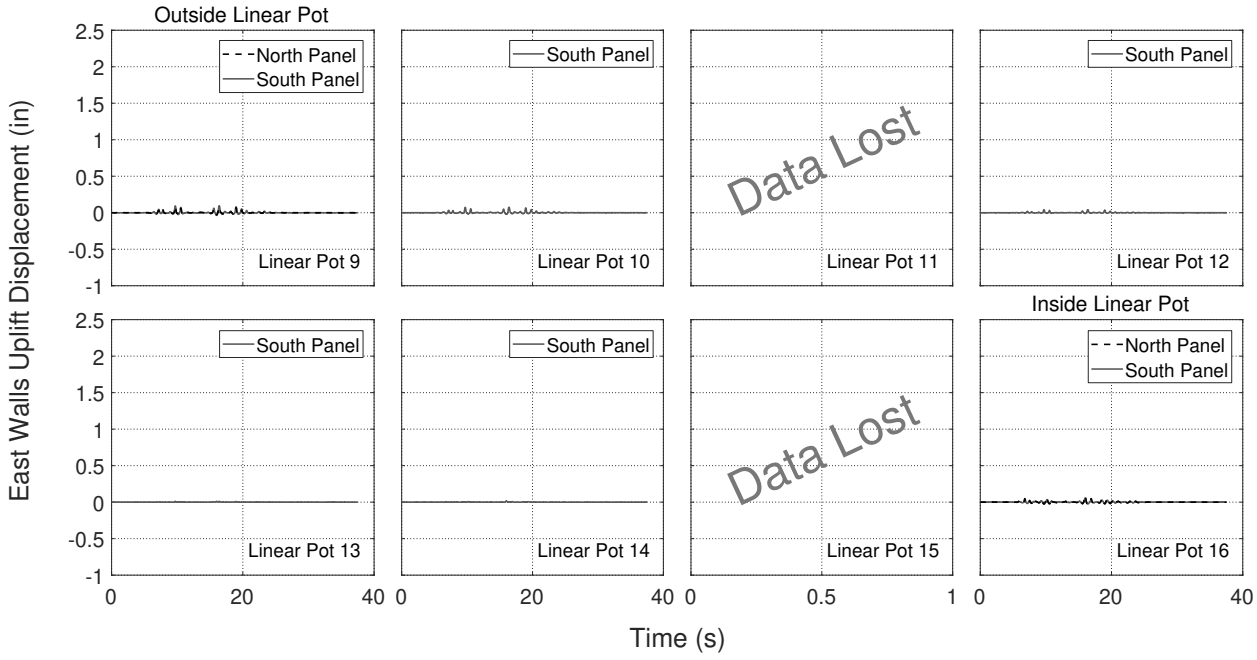

(d) East Walls - Test 4: Superstition Hills SLE

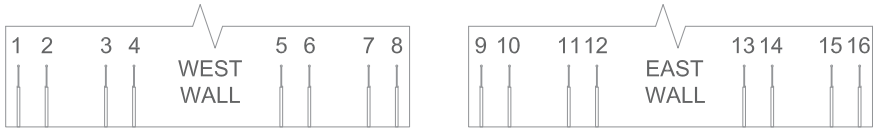

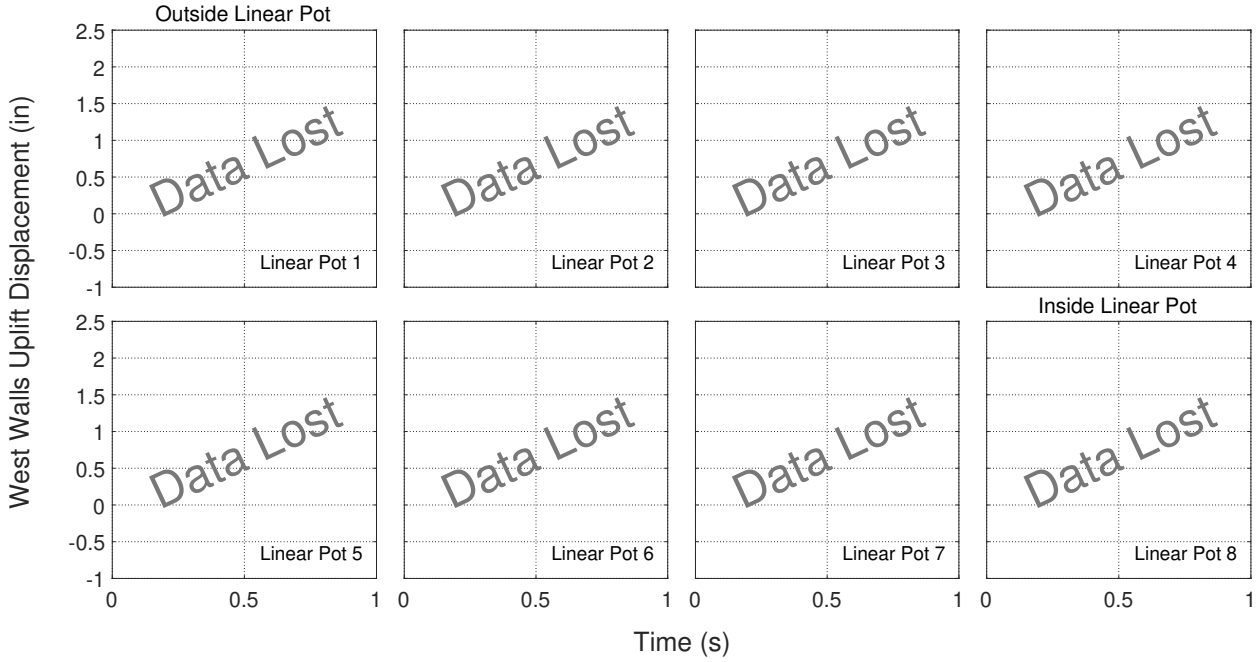

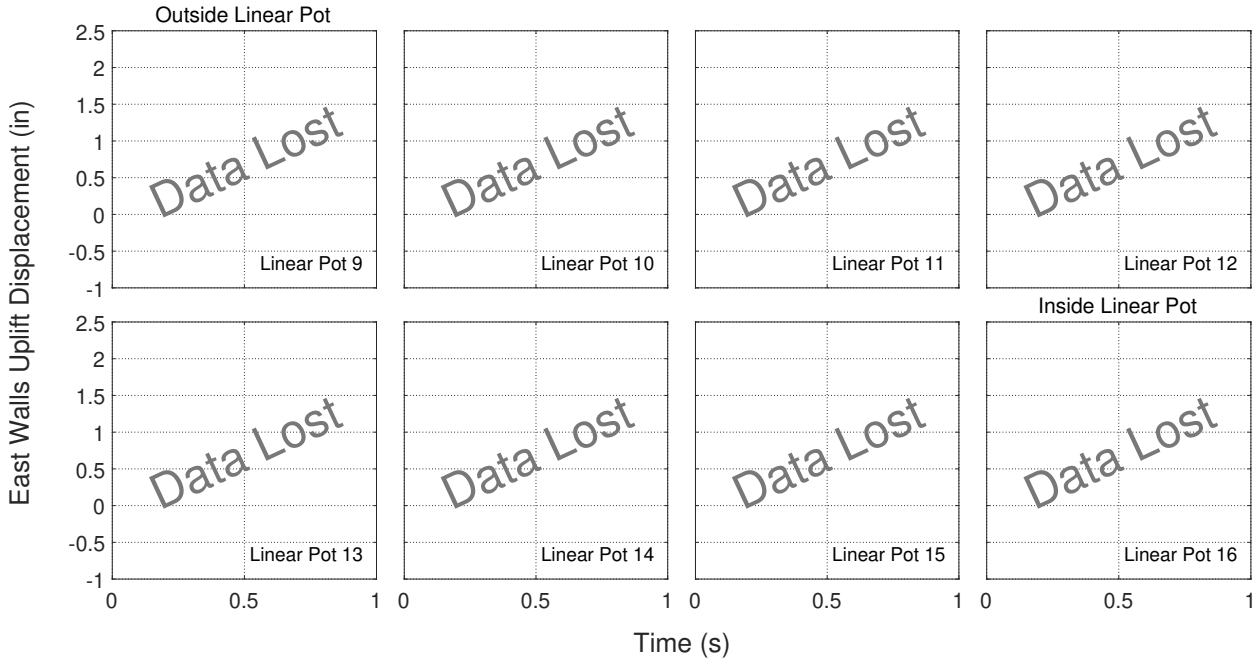

(e) East Walls - Test 5: Northridge DBE

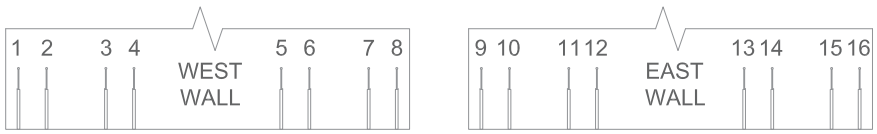

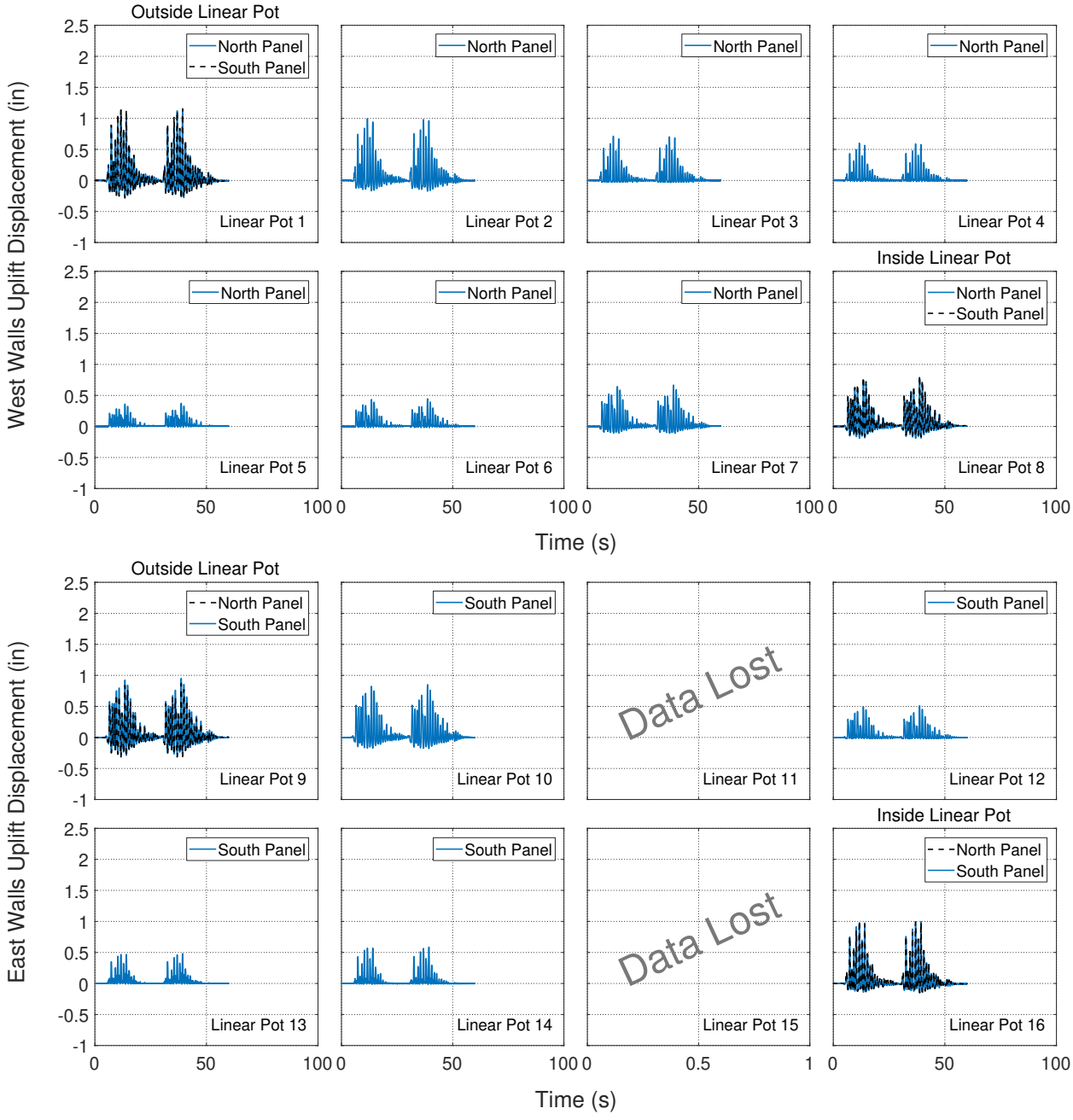

(f) East Walls - Test 6: Northridge DBE

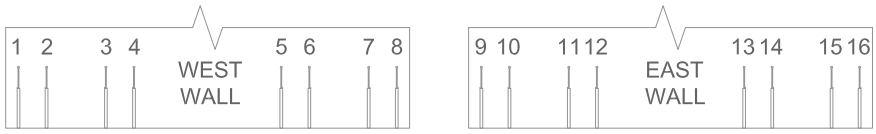

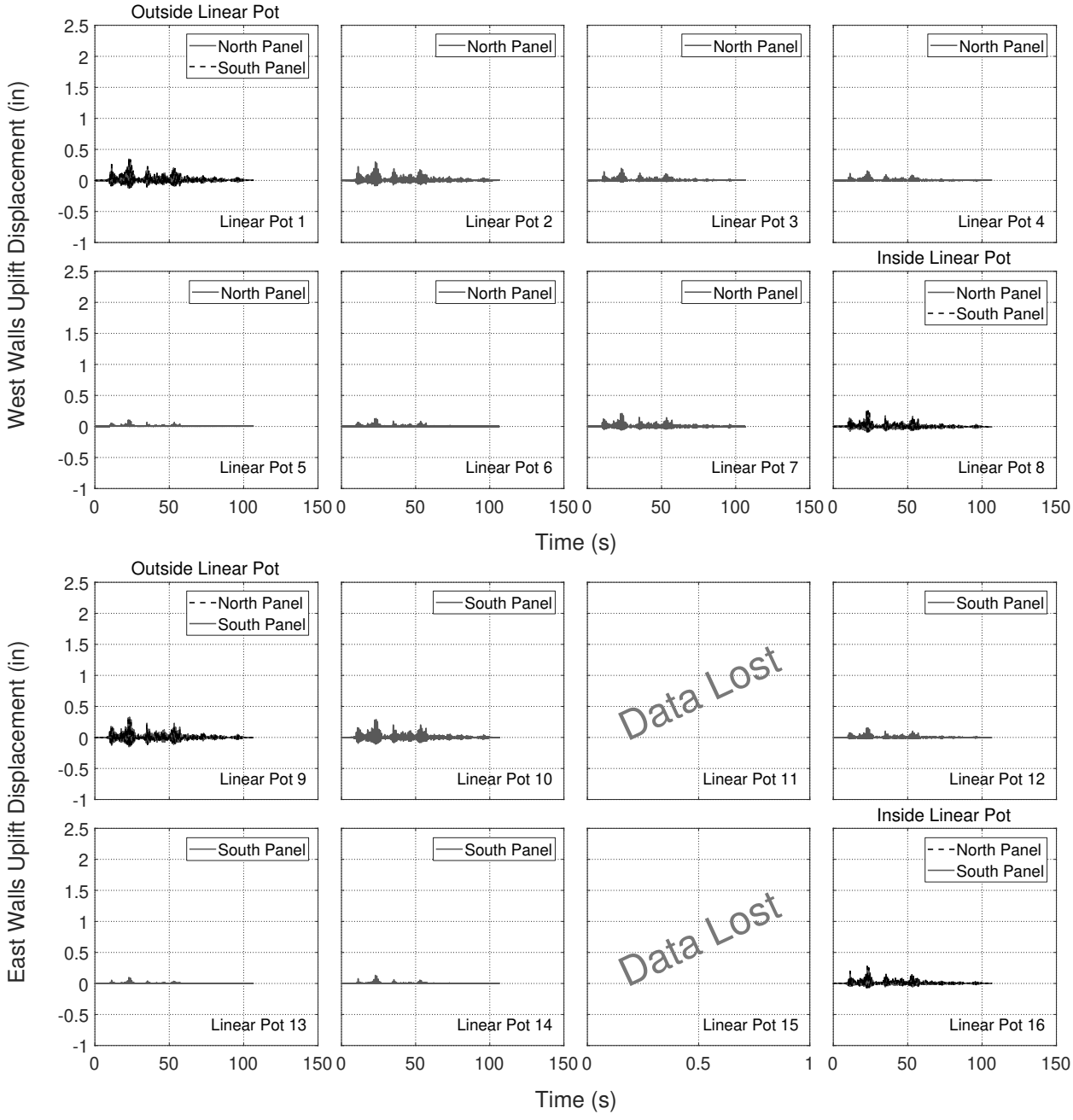

(g) East Walls - Test 7: Imperial Valley SLE

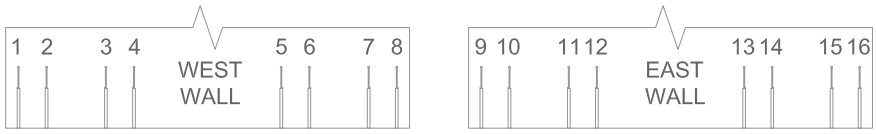

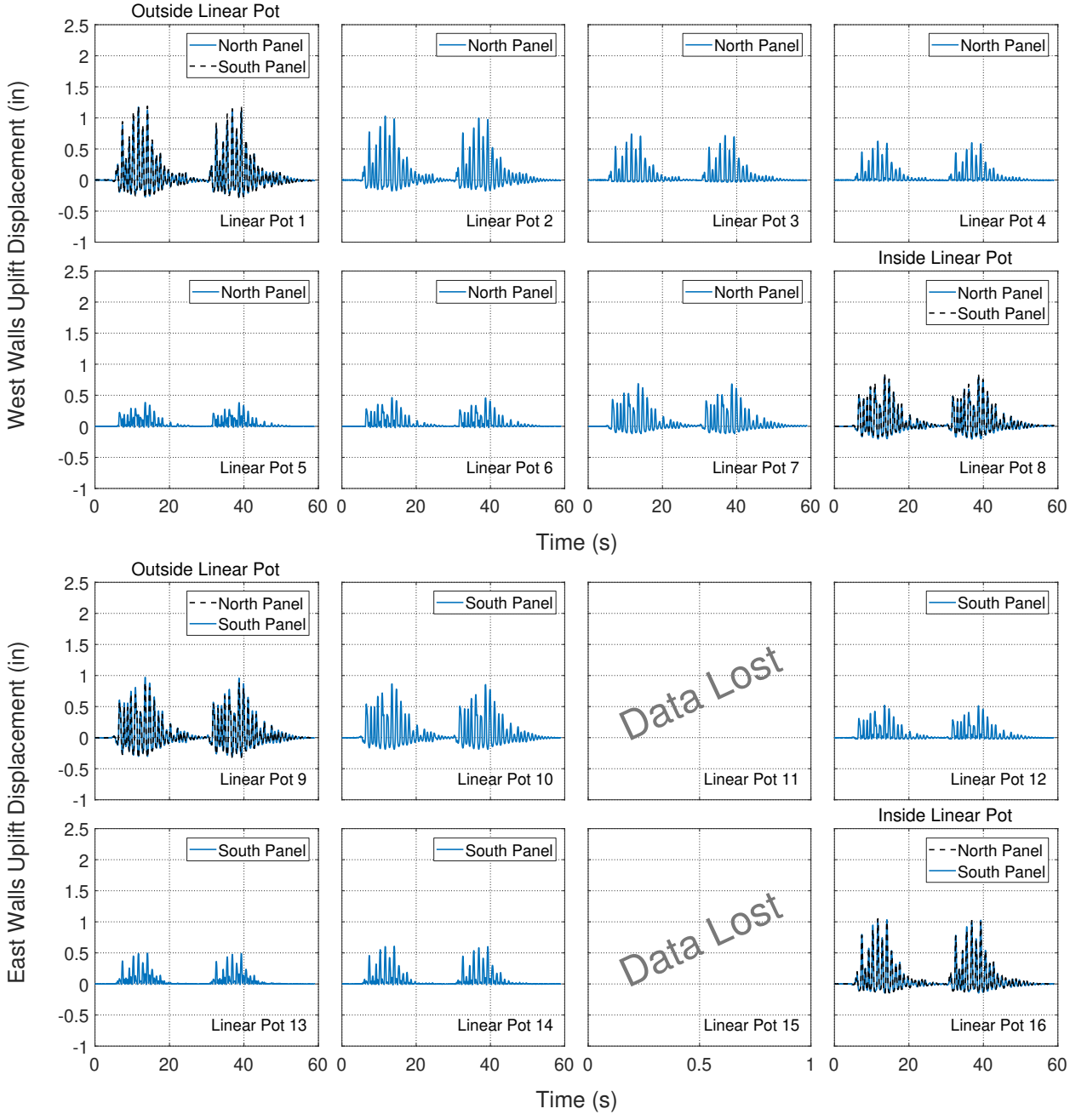

(h) East Walls - Test 8: Northridge DBE

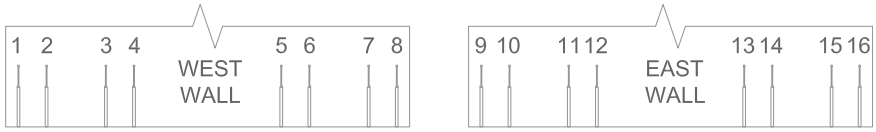

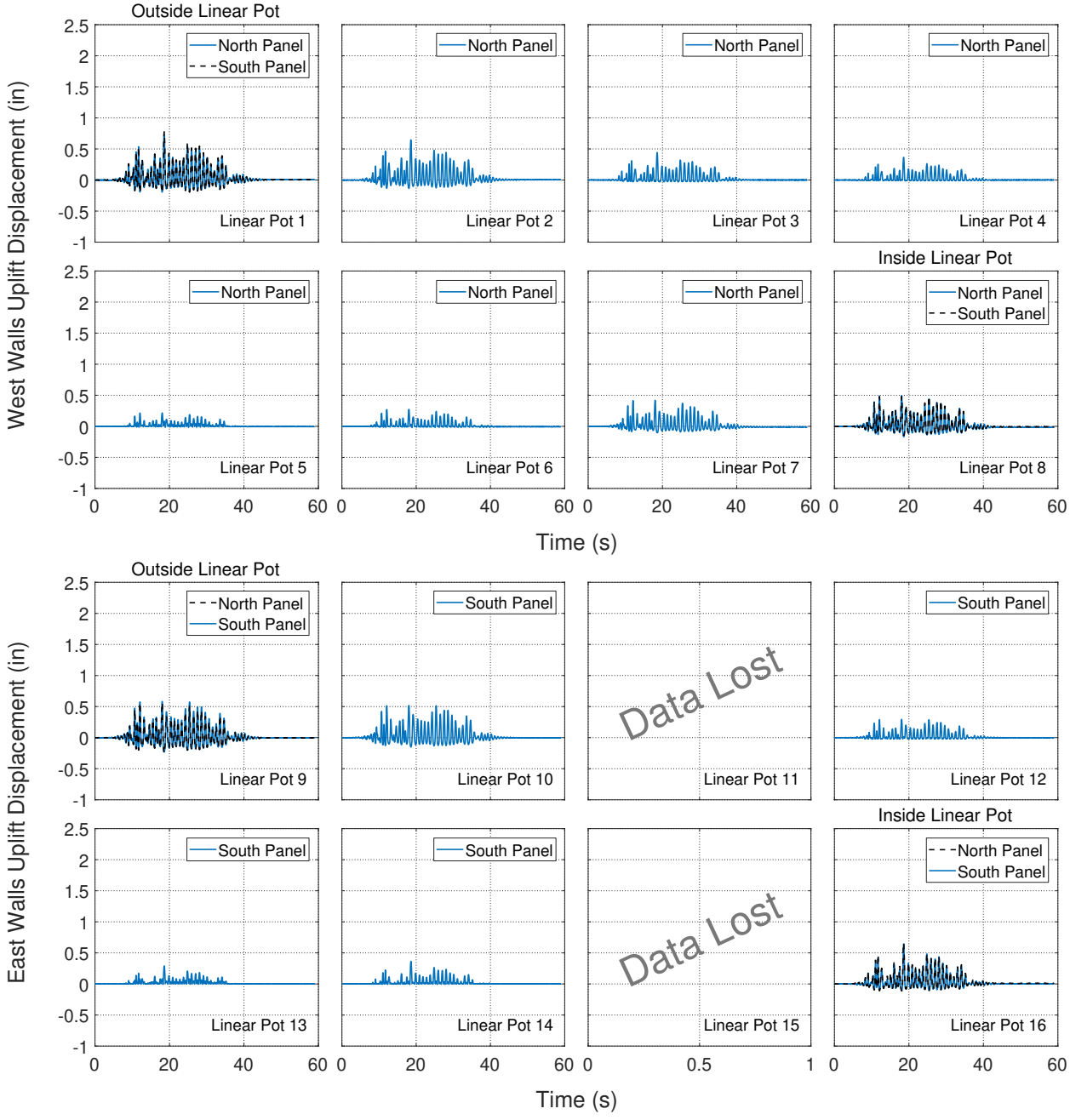

(i) East Walls - Test 9: Loma Prieta DBE

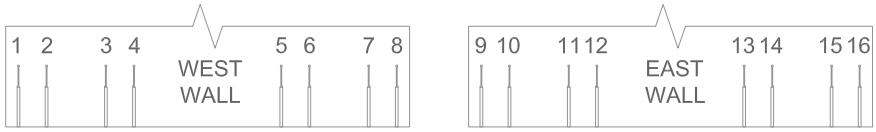

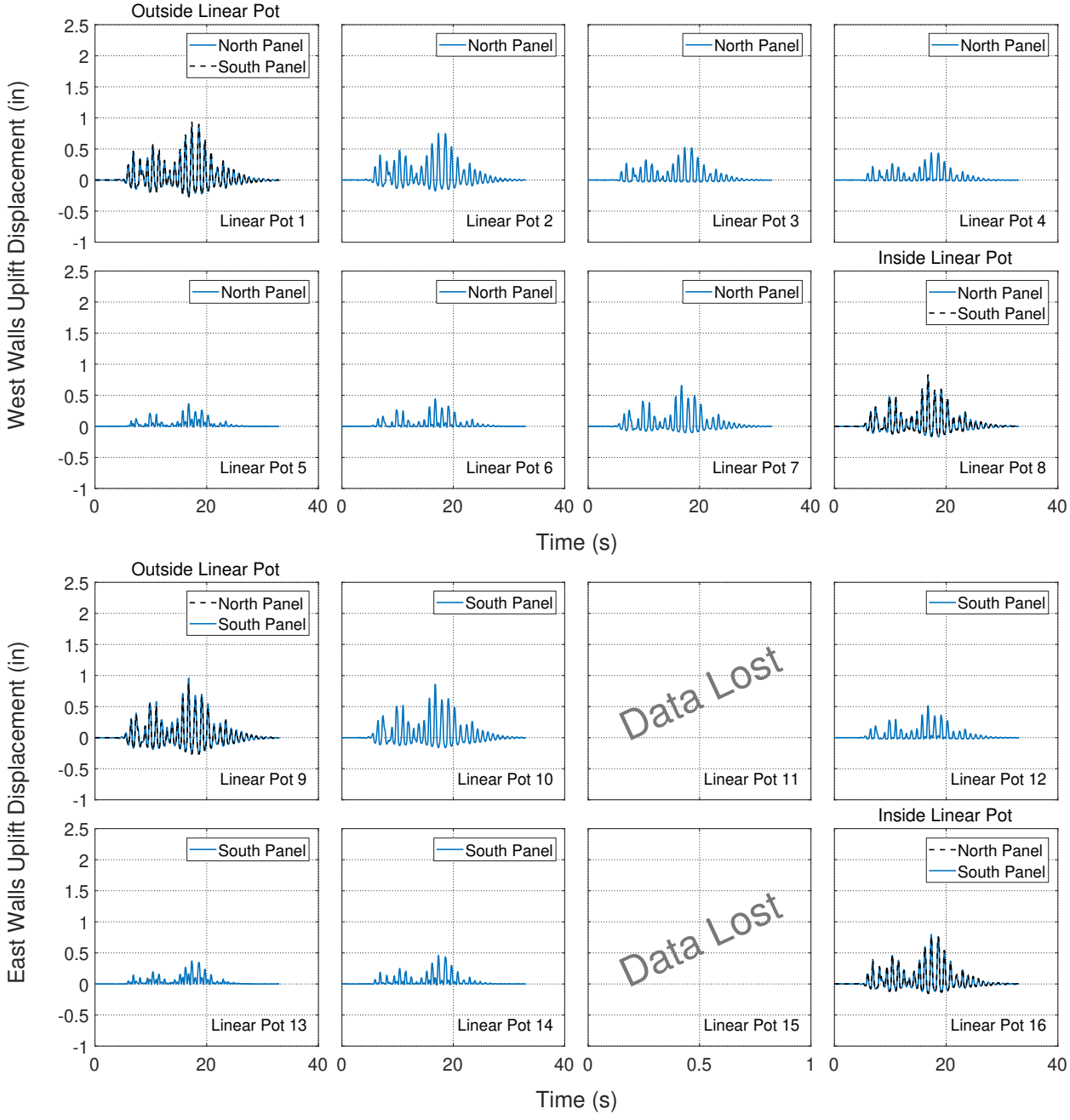

(j) East Walls - Test 10: Superstition Hills DBE

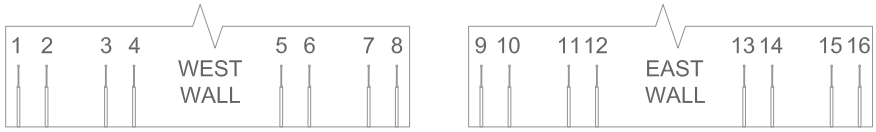

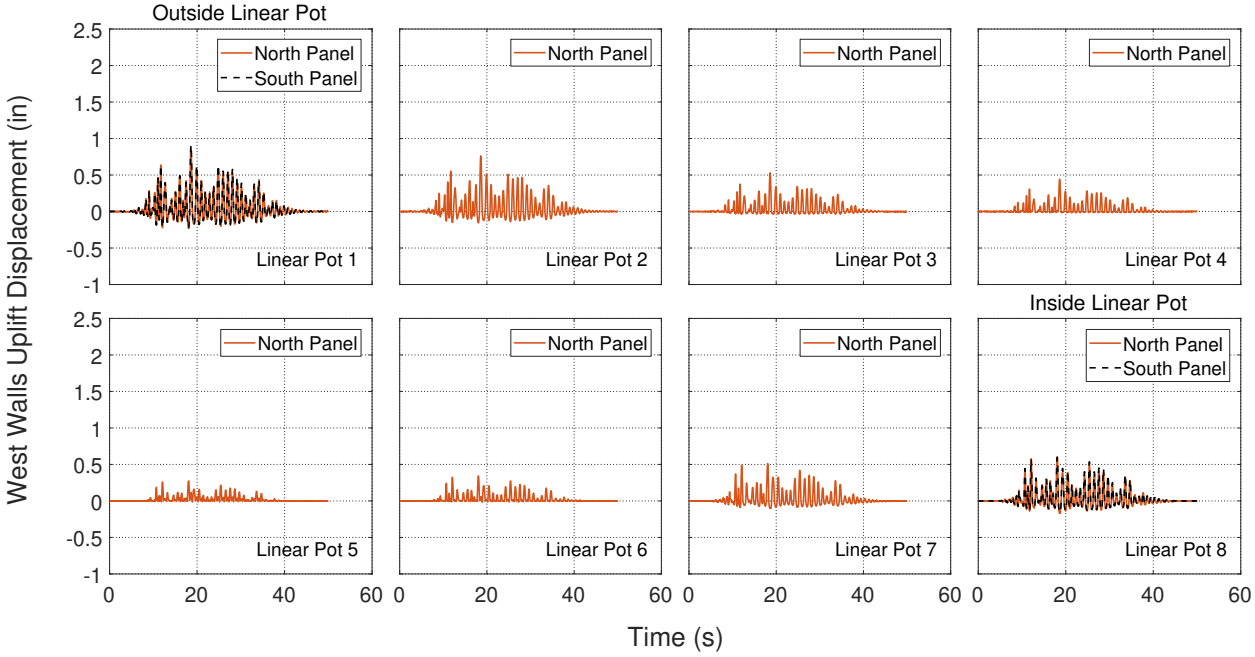

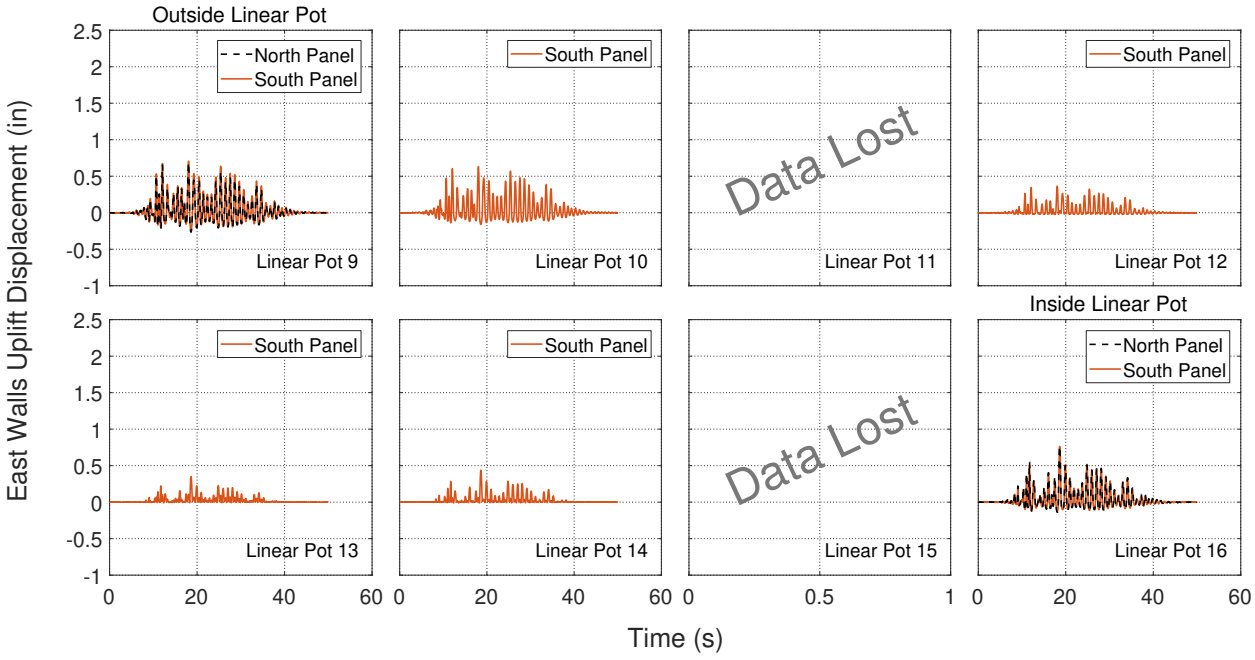

(k) East Walls - Test 11: Loma Prieta MCE

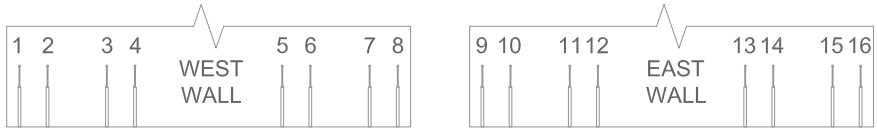

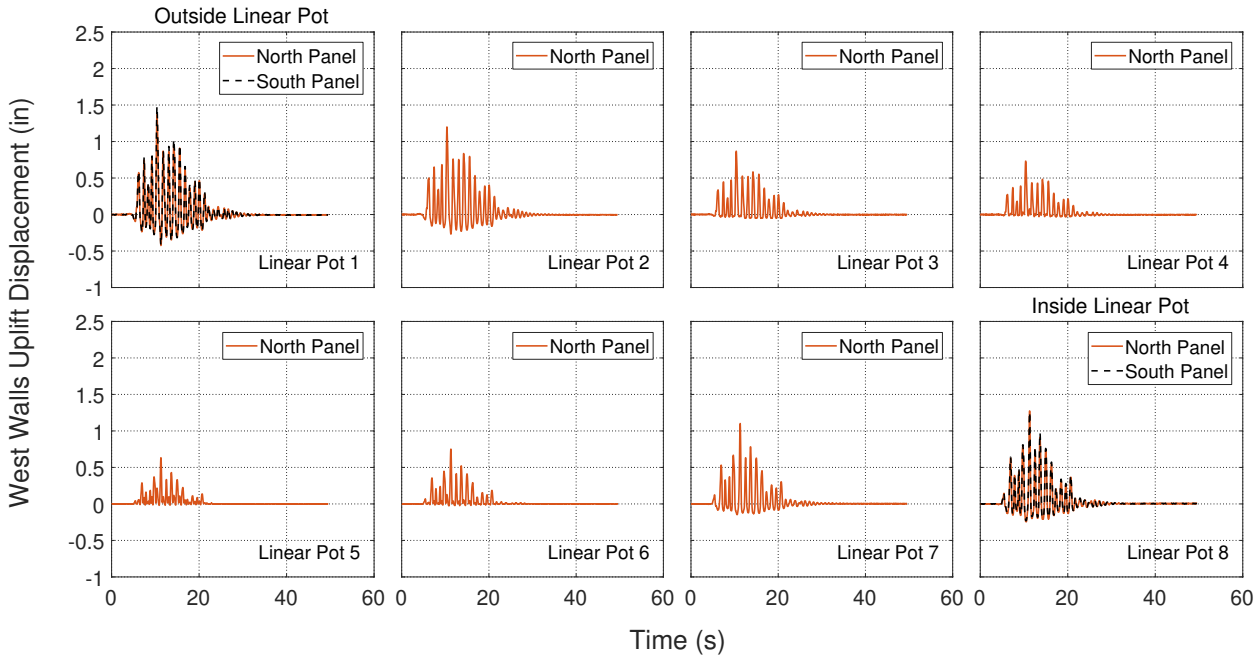

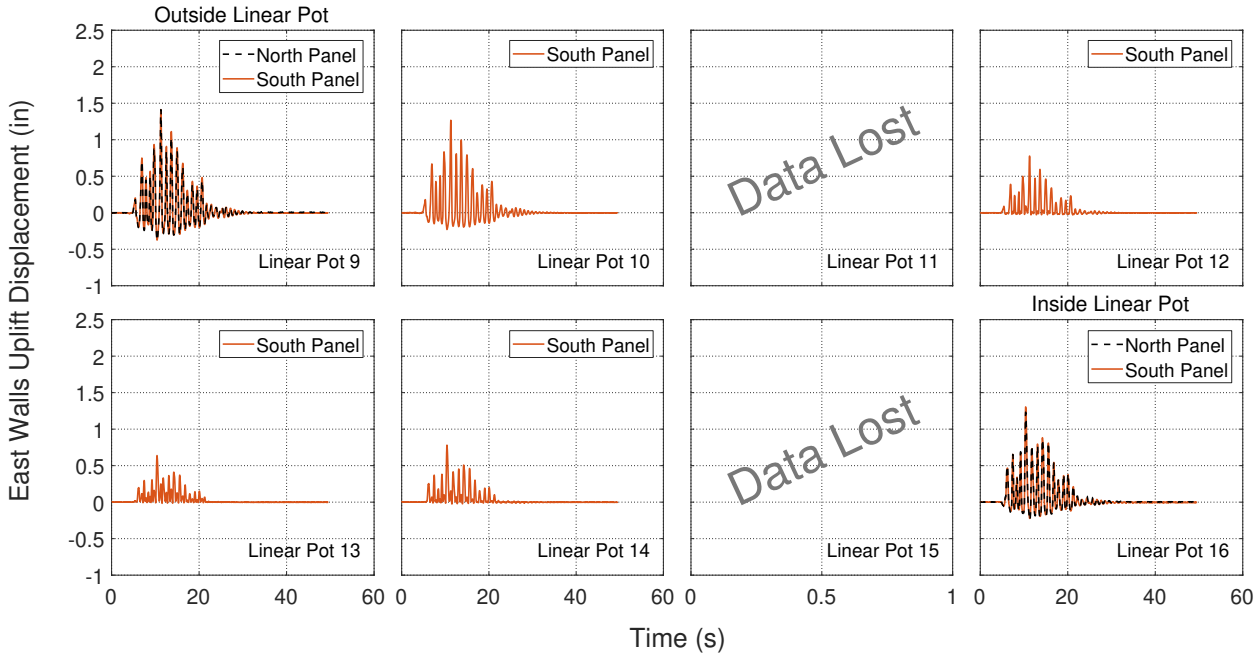

(l) East Walls - Test 12: Northridge MCE

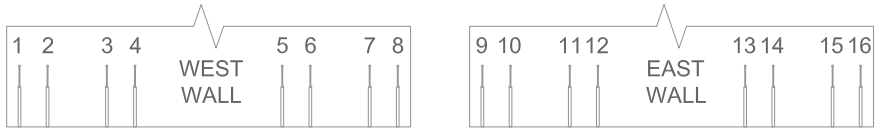

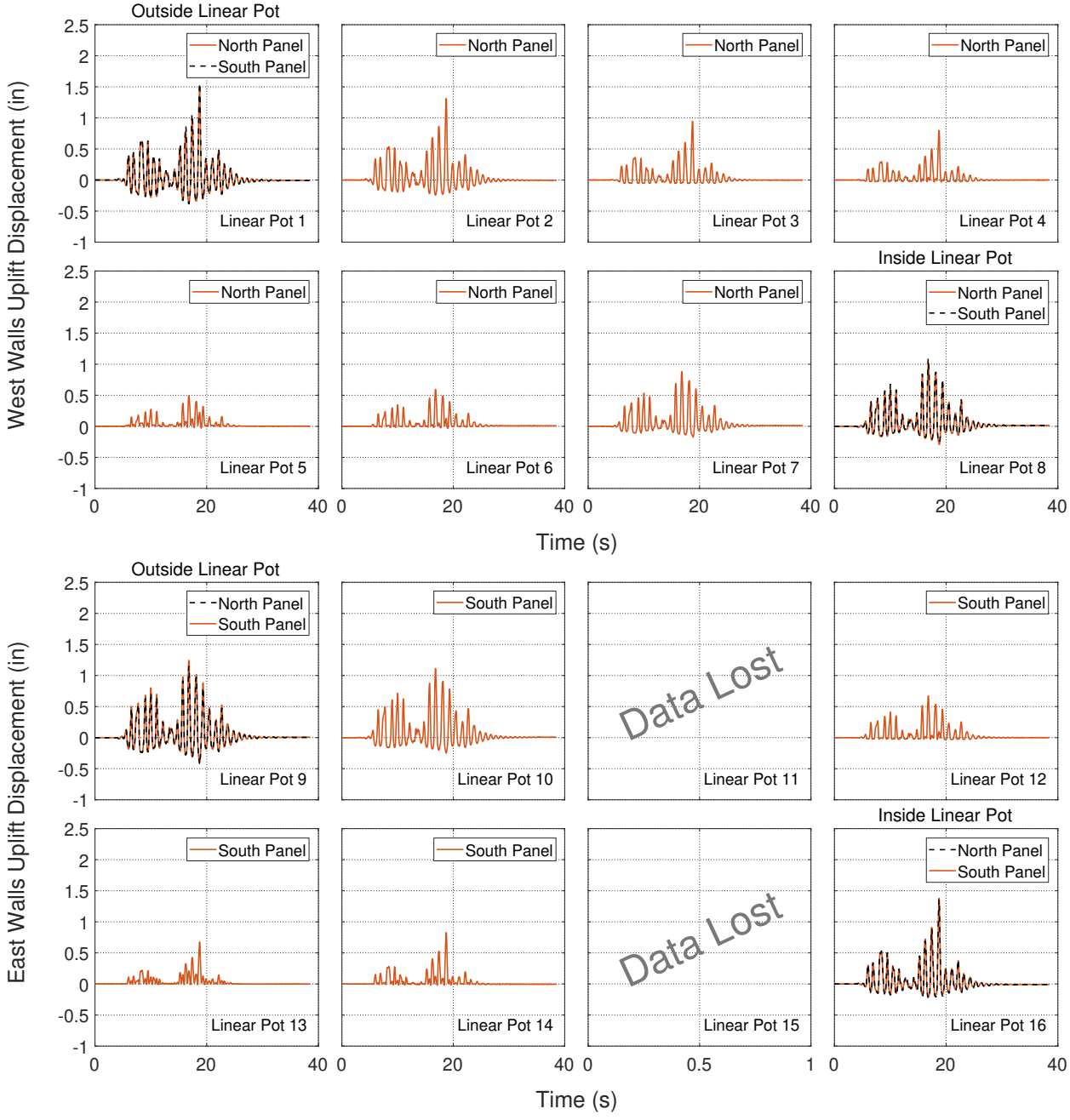

(m) East Walls - Test 13: Superstition Hills MCE

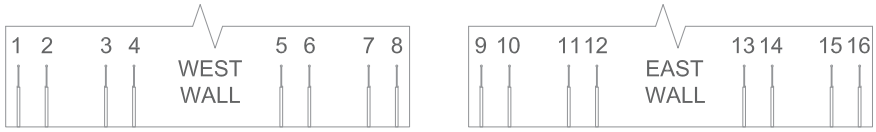

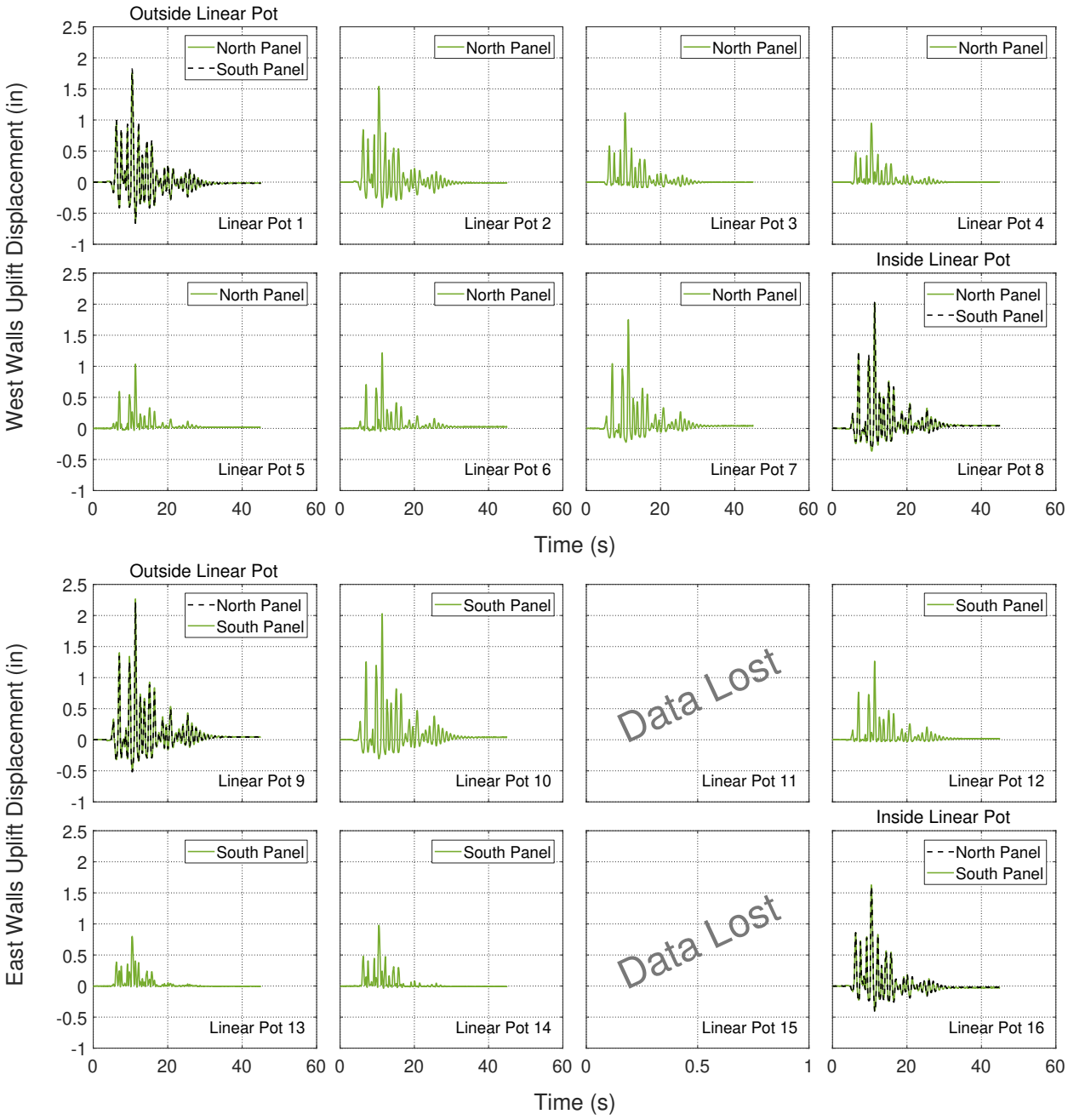

(n) East Walls - Test 14: Northridge MCEx1.2

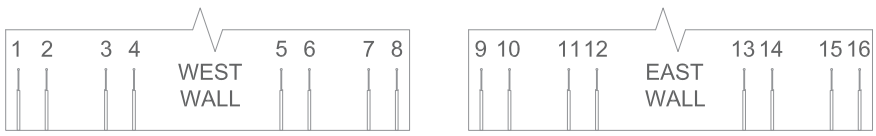

Figure B.5: Linear pot measurements

B.6 Wall Panel Base Deformation: Peak Deformations

Figure B.6 show deformation of the base beam across the width of the wall as discussed in Section 6.7. The values shown in these plots come from the linear potentiometer data at the points of peak positive and negative drift. In addition, a line of $\theta_{drift} b_w$ is also plotted. This line represents the peak uplift that would occur if the wall were completely rigid on a rigid foundation.

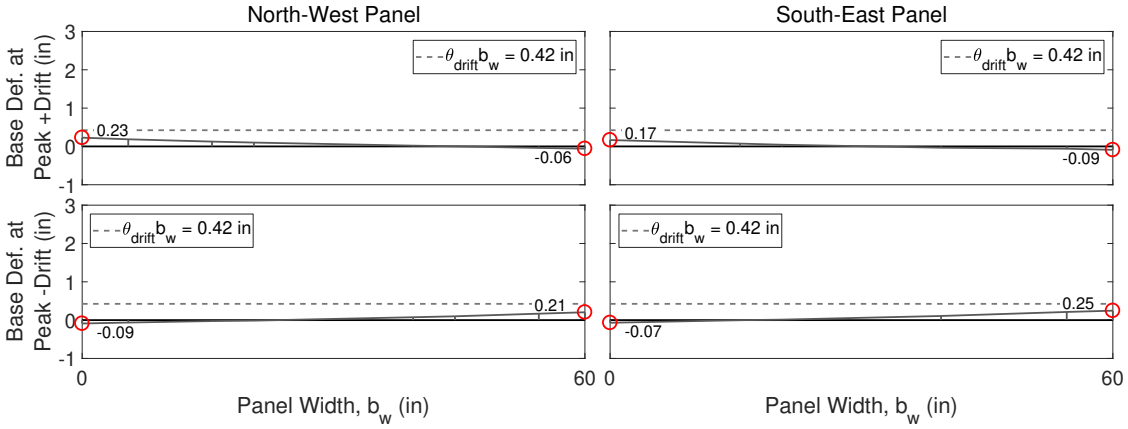

(a) Test 1 Loma Prieta SLE

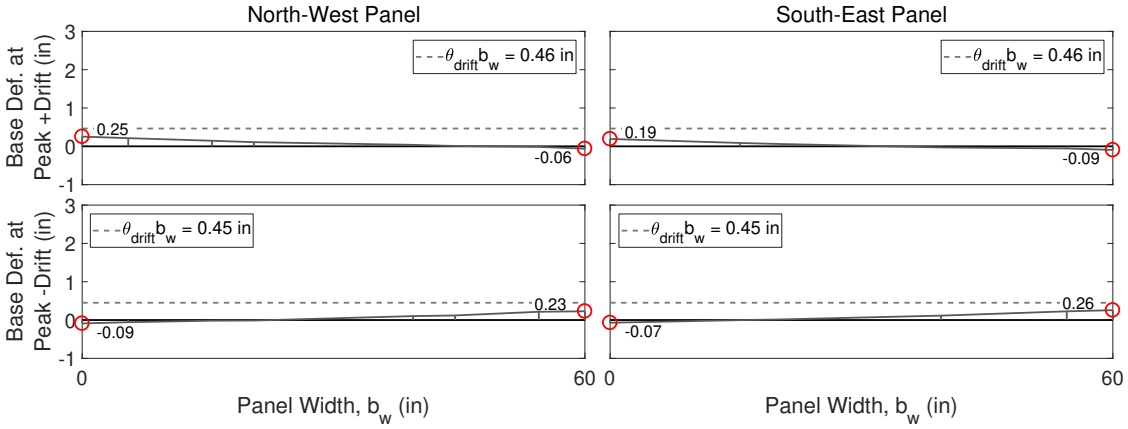

(b) Test 2 Loma Prieta SLE

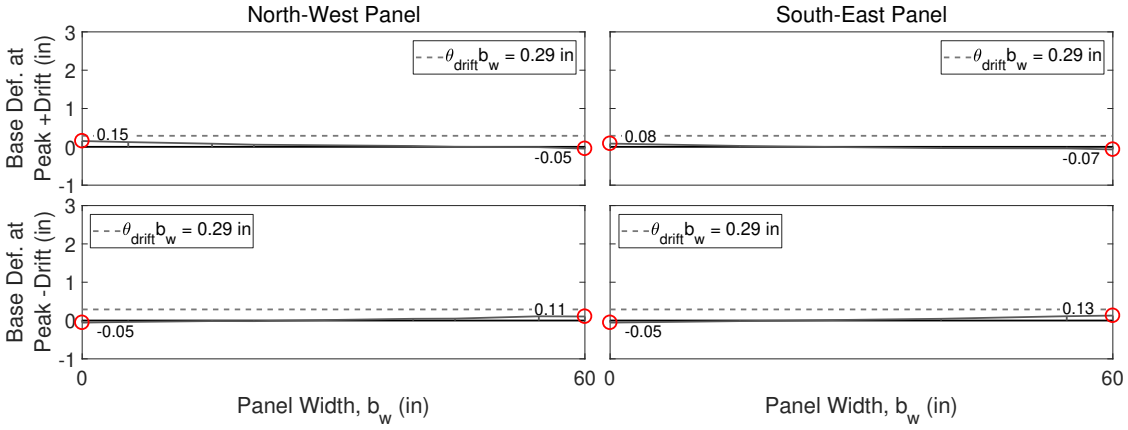

(c) Test 3 Northridge SLE

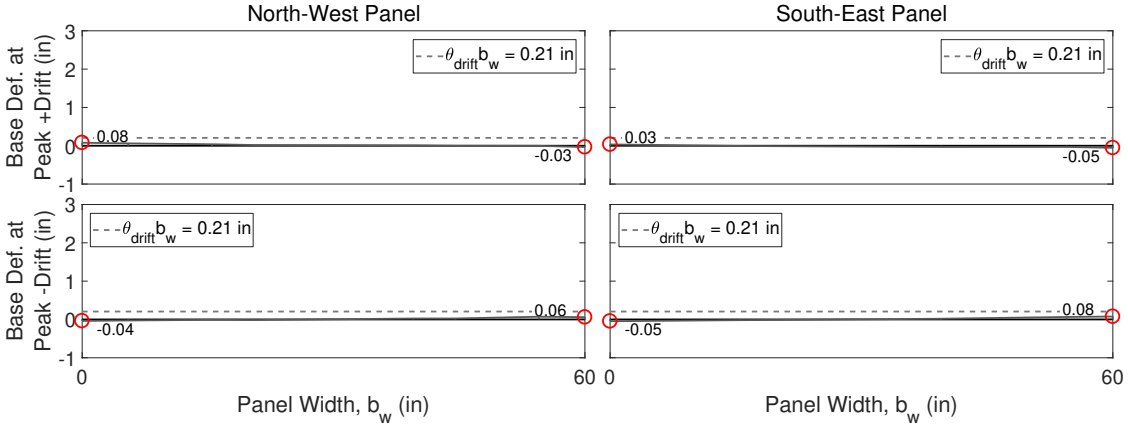

(d) Test 4 Superstition Hills SLE

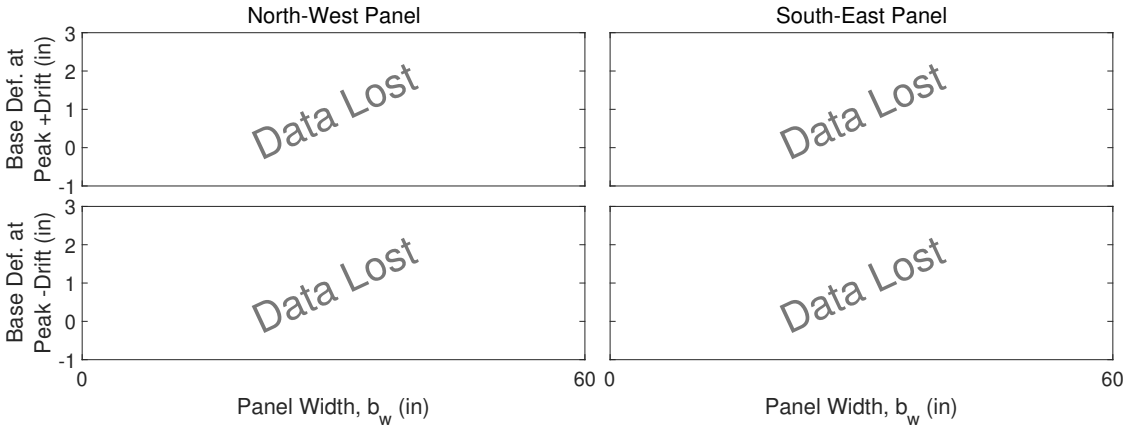

(e) Test 5 Northridge DBE

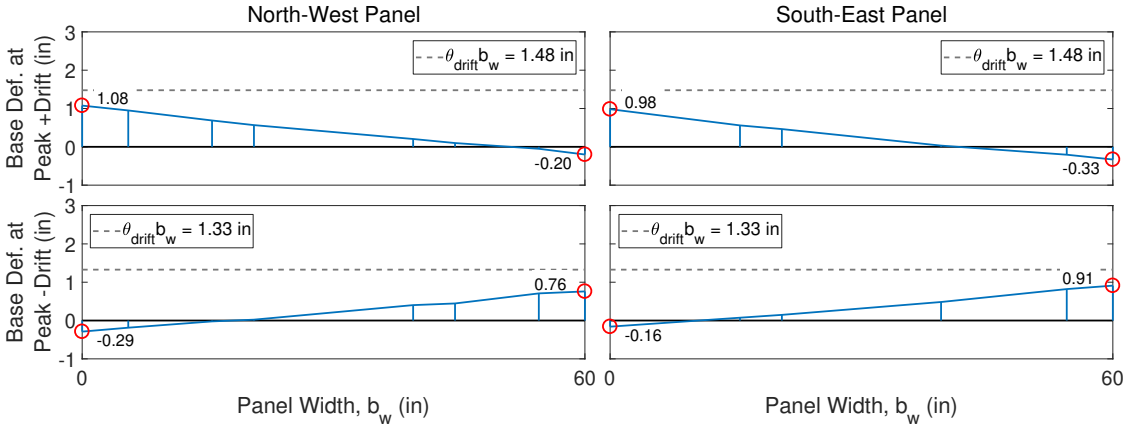

(f) Test 6 Northridge DBE

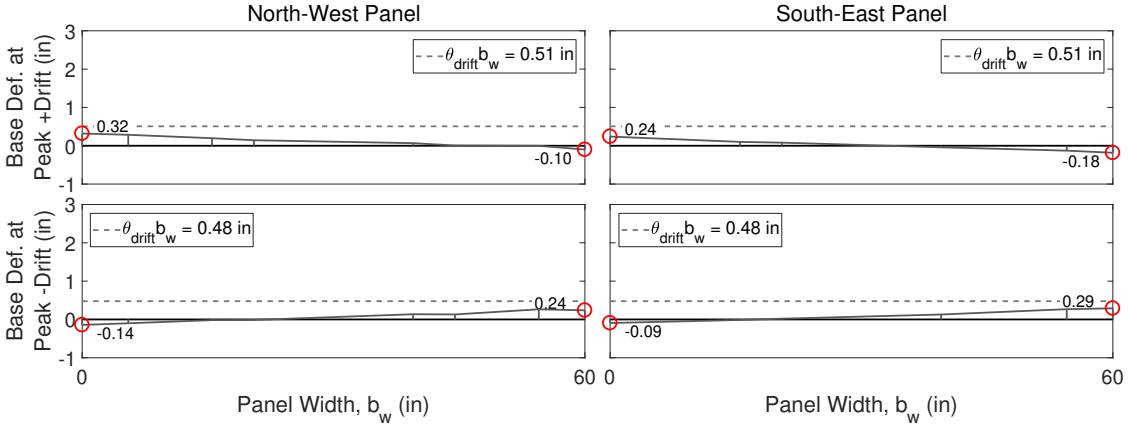

(g) Test 7 Imperial Valley SLE

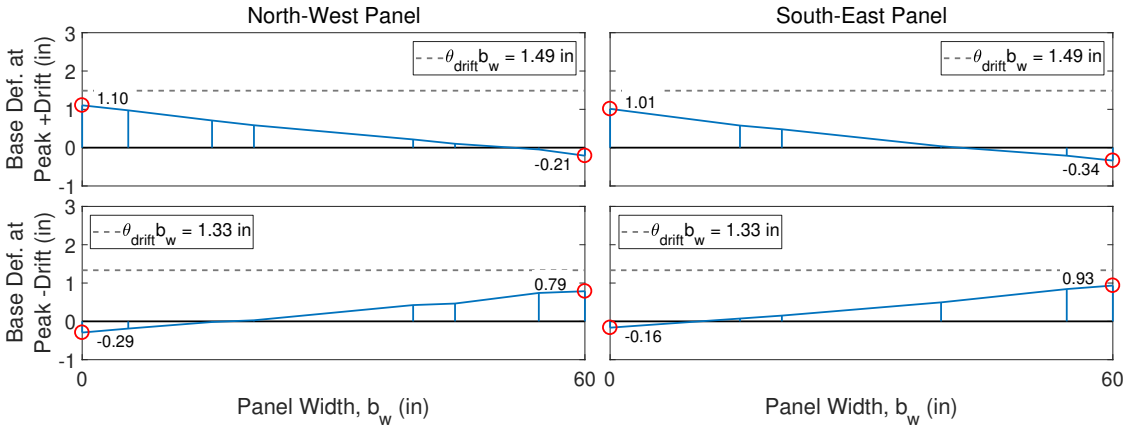

(h) Test 8 Northridge DBE

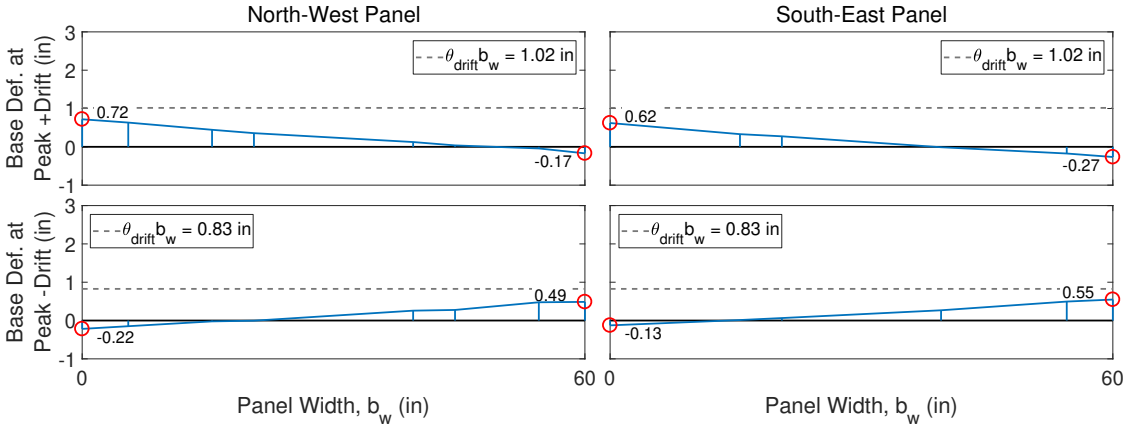

(i) Test 9 Loma Prieta DBE

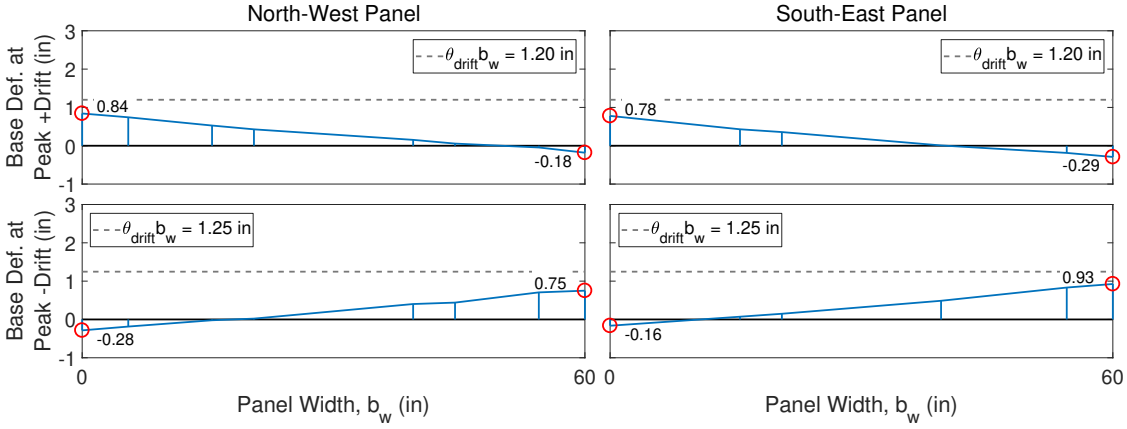

(j) Test 10 Superstition Hills DBE

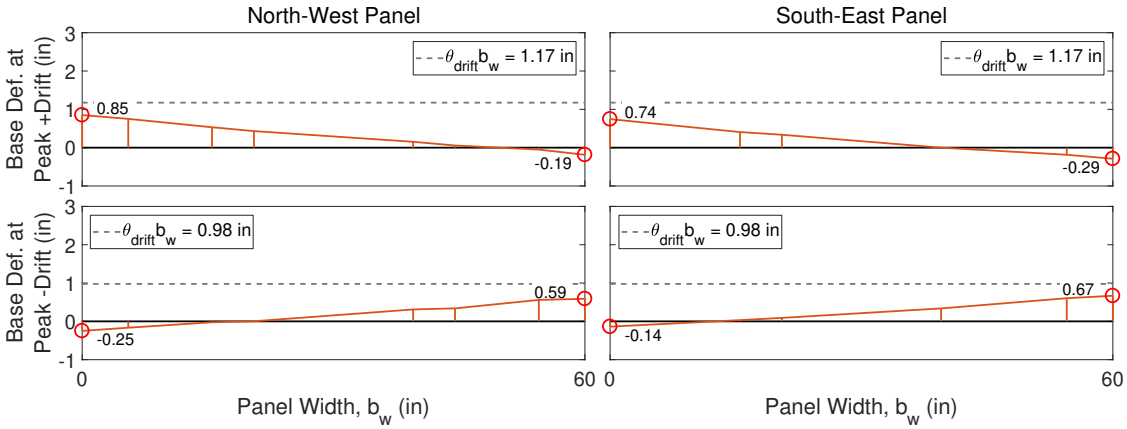

(k) Test 11 Loma Prieta MCE

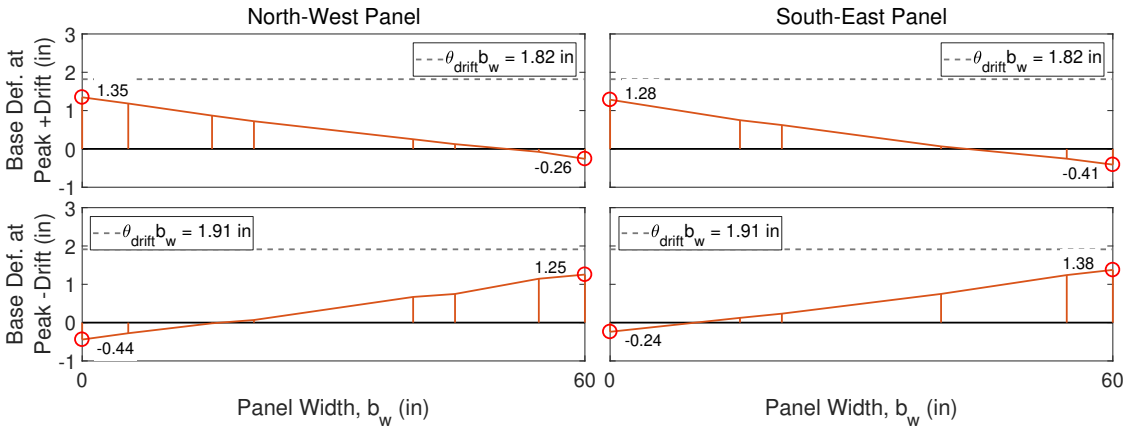

(l) Test 12 Northridge MCE

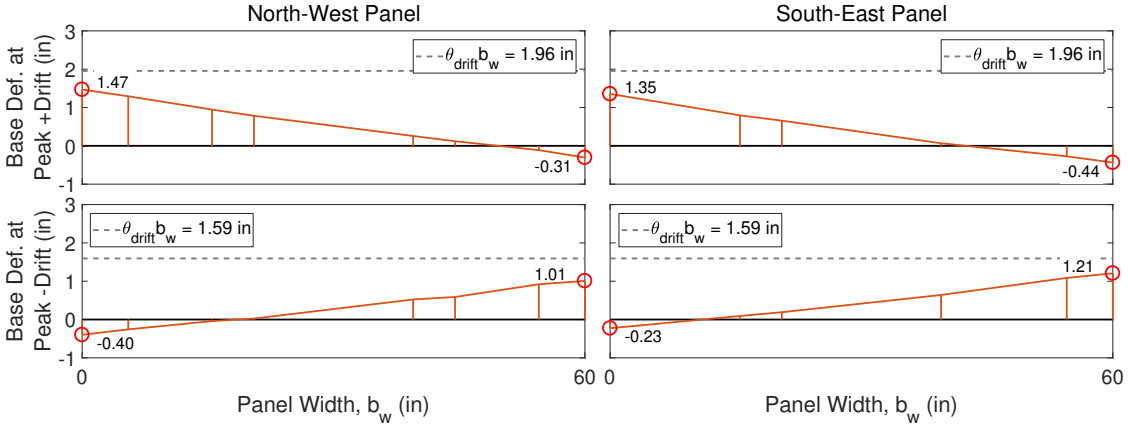

(m) Test 13 Superstition Hills MCE

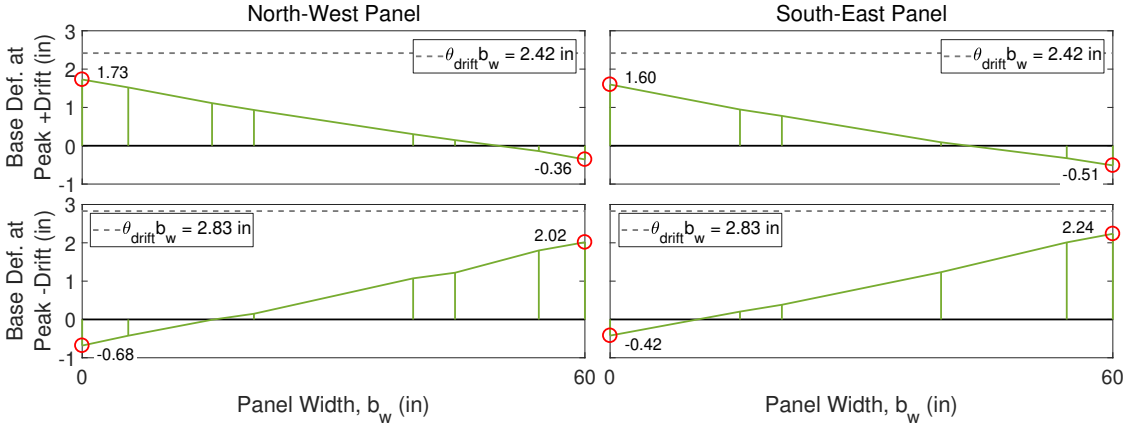

(n) Test 14 Northridge MCEx1.2

Figure B.6: Wall panel base deformation

B.7 UFP

Figure B.7 show the UFP force verses deformation hysteresis plots discussed in Section 6.8. Deformations across the UFPs were measured using string potentiometers and force data was determined using a calibrated steel model. The expected plastic yield force is also plotted for each hysteresis.

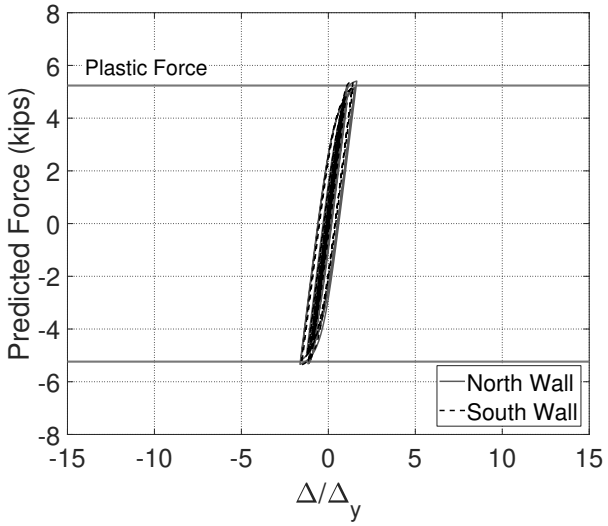

(a) Test 1 Loma Prieta SLE

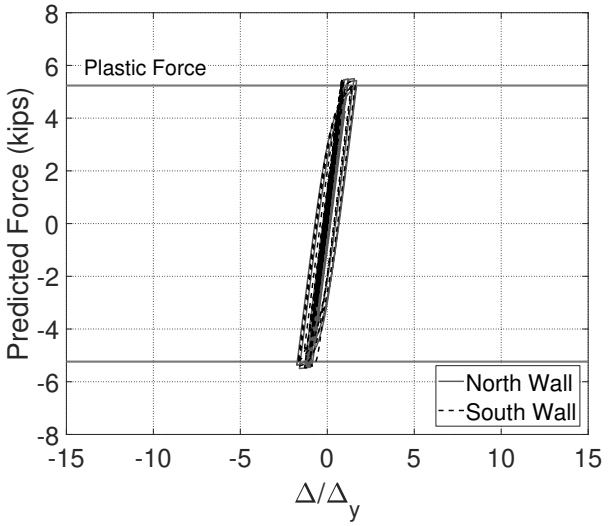

(b) Test 2 Loma Prieta SLE

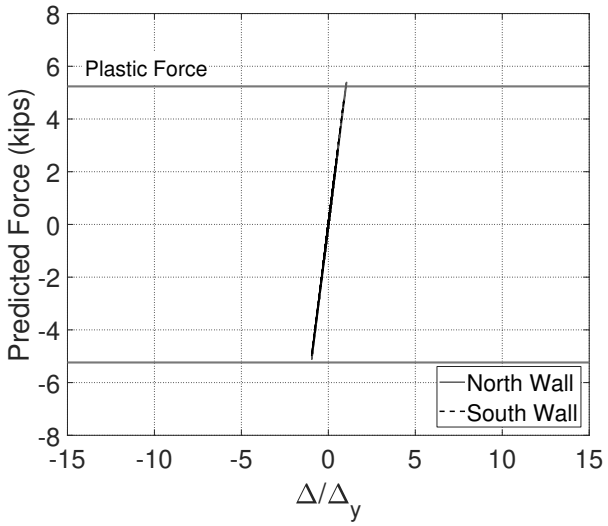

(c) Test 3 Northridge SLE

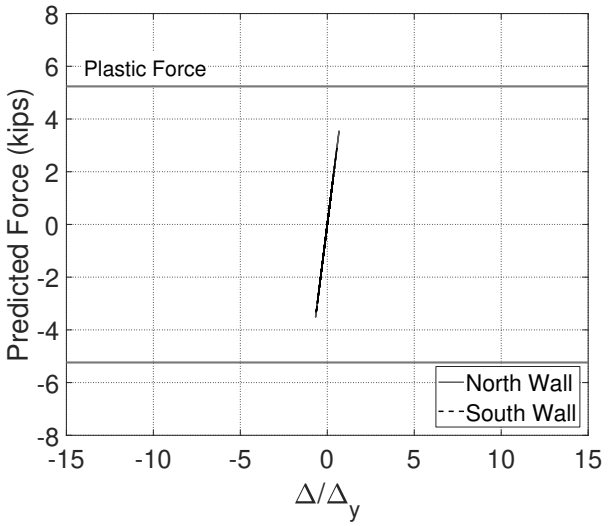

(d) Test 4 Superstition Hills SLE

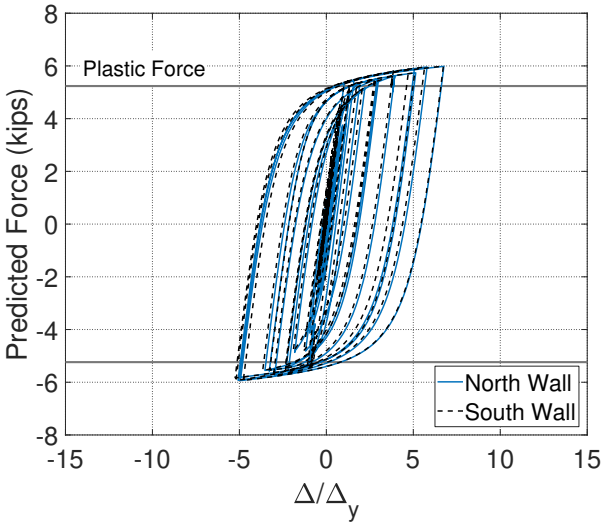

(e) Test 5 Northridge DBE

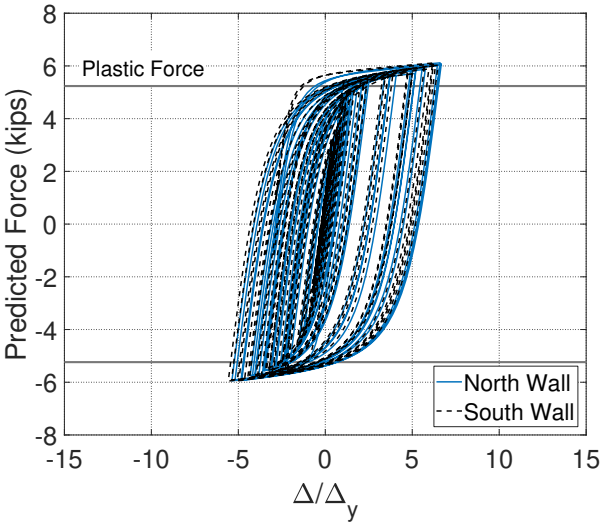

(f) Test 6 Northridge DBE

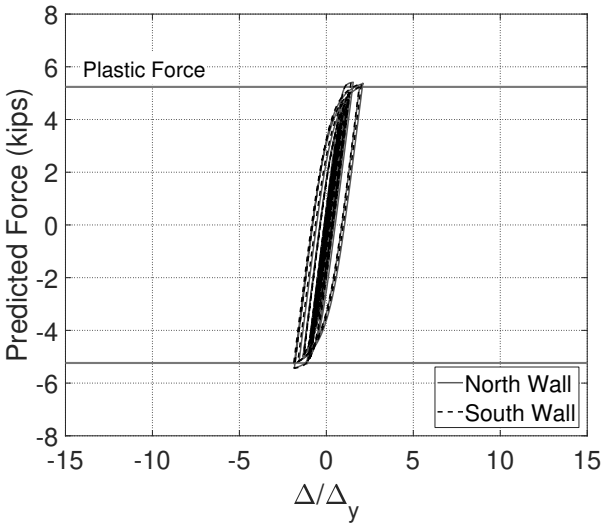

(g) Test 7 Imperial Valley SLE

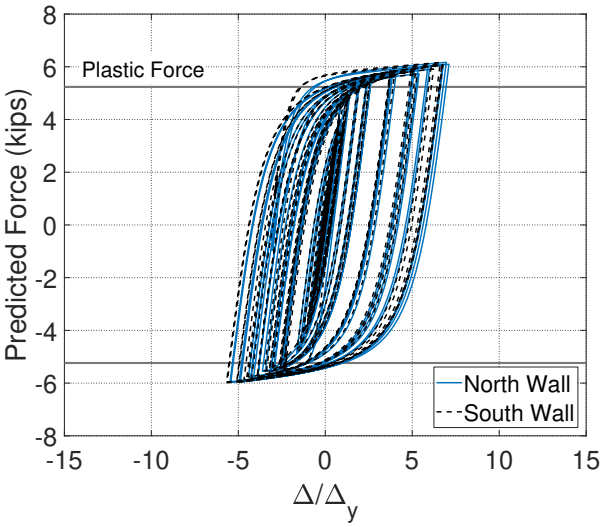

(h) Test 8 Northridge DBE

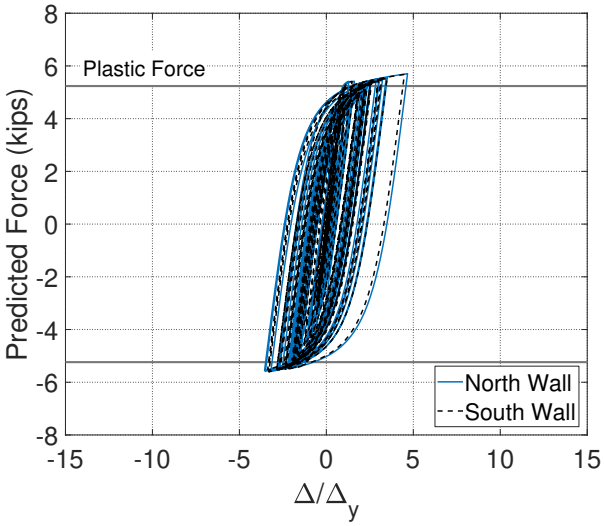

(i) Test 9 Loma Prieta DBE

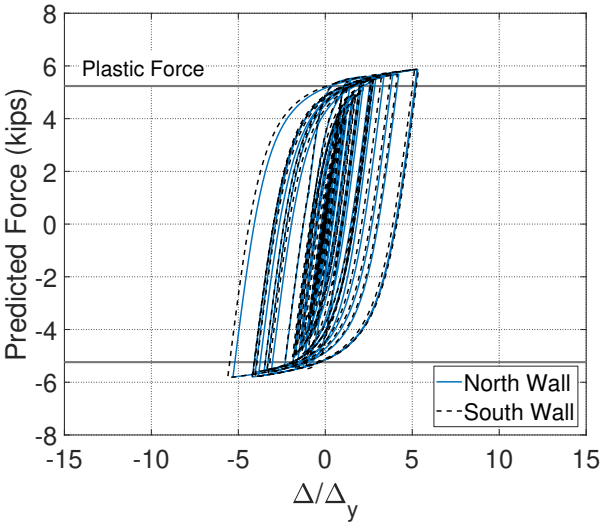

(j) Test 10 Superstition Hills DBE

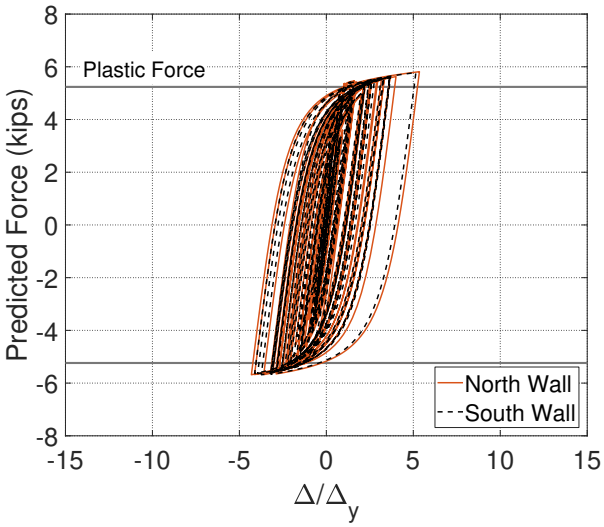

(k) Test 11 Loma Prieta MCE

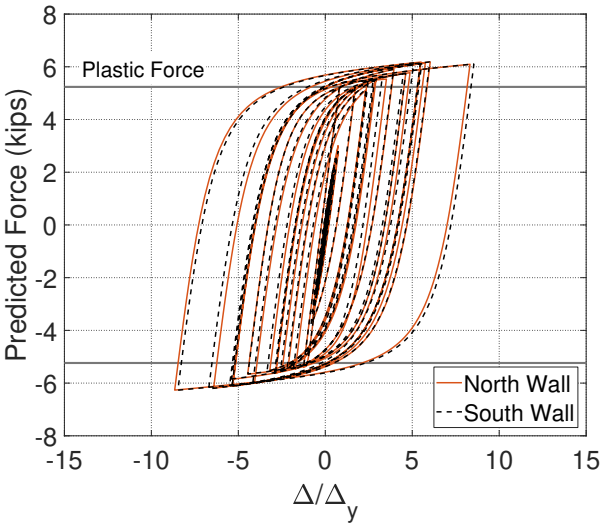

(l) Test 12 Northridge MCE

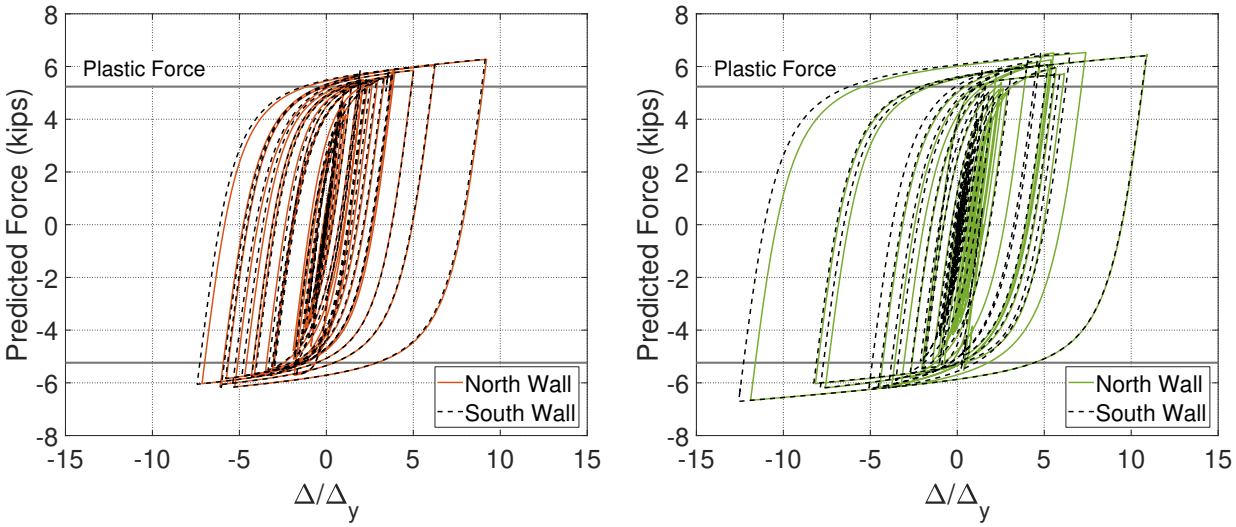

(m) Test 13 Superstition Hills MCE

(n) Test 14 Northridge MCEx1.2

Figure B.7: Predicted UFP hysteresis